Discovery and Manipulation of Individual Skyrmions in Ultrathin Magnetic Films

Dissertation
zur Erlangung des Doktorgrades
an der Fakultät für Mathematik, Informatik und Naturwissenschaften
Fachbereich Physik
der Universität Hamburg

vorgelegt von
M.Sc. Niklas Romming
geb. am 24.09.1988 in Neumünster

Hamburg
2017

Gutachter der Dissertation:
Prof. Dr. Roland Wiesendanger
PD Dr. Guido Meier
Dr. Vincent Cros

Zusammensetzung der Prüfungskommission:
Prof. Dr. Roland Wiesendanger
PD Dr. Guido Meier
Prof. Dr. Wolfgang Hansen
Prof. Dr. Stefan Heinze
Prof. Dr. Michael Thorwart

Vorsitzender der Prüfungskommission:
Prof. Dr. Wolfgang Hansen

Datum der Disputation:
20.12.2017

Vorsitzender des Promotionsausschusses PHYSIK:
Prof. Dr. Wolfgang Hansen

Leiter des Fachbereichs PHYSIK:
Prof. Dr. Michael Potthoff

Dekan der MIN-Fakultät:
Prof. Dr. Heinrich Graener

Abstract

Modern data storage technology is facing the inevitable obstacle that soon, the currently available storage capacities cannot simply be extended by a continued miniaturisation. Instead, fundamentally new approaches have to be found to accommodate the increasing amount of data generated each year. One possible candidate as information carrier in future spintronics devices is the magnetic skyrmion. These topologically stabilised, magnetic knots could e.g. be used in three-dimensional arrays of race-track-type memory devices that would increase the available storage density manifold and thereby overcome the above mentioned impediment. Whereas the observation of skyrmion lattices in bulk materials was reported before, the realisation of skyrmion-based devices requires individual skyrmions, which can be manipulated in a controlled fashion.

This thesis presents the discovery of nanoscale, interface-induced, isolated magnetic skyrmions, which were found in the ultrathin film system Pd/Fe/Ir(111) by (spin-polarised) scanning tunneling microscopy ((SP-)STM). It is demonstrated how (spin-polarised) currents from the STM tip can be used to write and delete them individually and in close vicinity to one another.

In addition, the high spatial resolution of SP-STM paired with the direct access to the sample spins was employed to investigate the size and shape of an isolated skyrmion as a function of external magnetic field. A novel analytical description for the skyrmion spin structure was introduced to connect these findings to the original micromagnetic model, which was used for predicting magnetic skyrmions, demonstrating excellent agreement. However, analysing slightly different PdFe systems in a similar manner showed that the simplified model fails; based on density functional theory results, this is attributed to the importance of the frustration of exchange interactions at different distances.

The investigation of further Pd_xFe and RhFe systems revealed the sensitive dependence of the magnetic properties of Fe/Ir(111) on the overlayer(s) and on the stacking order of the ultrathin film systems, emphasising the importance of atomic scale precision for the tailoring of magnetic states. The observed magnetic periodicities in these systems range from 1 to 15 nm, and additional skyrmions and skyrmion lattices with transition magnetic fields between <0.8 and >9 T were found. Due to the meta-stability of topologically distinct magnetic states at low temperature, novel skyrmionic spin structures are reported, which can be categorised into common and uncommon states using the concept of topology. At the island edges, SP-STM measurements revealed the theoretically predicted edge tilt induced by the Dzyaloshinskii-Moriya interaction.

In conclusion, this thesis covers some of the key aspects of fundamental research on the path to the realisation of skyrmion based devices, while hopefully inspiring further experimental and theoretical research in the developing field of skyrmionics.

Inhaltsangabe

Die heutige Technologie zur Datenspeicherung steht vor dem fundamentalen Problem, dass die verfügbare Speicherdichte schon bald nicht mehr allein durch Miniaturisierung erweitert werden kann. Stattdessen müssen grundlegend neue Ansätze gefunden werden, um dem steigenden, jährlich generierten Datenberg Herr zu werden. Ein möglicher Kandidat als Informationsträger in künftigen Spintronik-Anwendungen sind magnetische Skyrmionen. Diese topologisch stabilisierten, magnetischen Knoten könnten z.B. in dreidimensionalen Anordnungen von sog. Race-Track-Speichern zur Anwendung kommen und damit die erreichbare Speicherdichte um ein Vielfaches erhöhen. Skyrmionengitter wurden zwar bereits in Volumenmaterialien nachgewiesen, jedoch werden für die Realisierung von Skyrmionen-basierten Anwendungen einzelne Skyrmionen benötigt, die auf kontrollierte Weise manipuliert werden können.

In dieser Arbeit wird die Entdeckung von Grenzflächen-induzierten, isolierten magnetischen Skyrmionen auf Nanometer-Skala beschrieben, welche in dem Dünnfilm-System Pd/Fe/Ir(111) mittels (spin-polarisierter) Rastertunnelmikroskopie ((SP-)STM engl. (spin-polarised) scanning tunneling microscopy) nachgewiesen werden konnten. Es wird demonstriert, wie sie anhand (spin-polarisierter) Ströme aus der STM Spitze einzeln und in direkter Nachbarschaft zueinander geschrieben und gelöscht werden können.

Zusätzlich wurde die hohe laterale Auflösung von SP-STM, gepaart mit dem direkten Zugang zu den Proben-Spins, dazu genutzt, die Größe und Form eines isolierten Skyrmions als Funktion des externen Magnetfeldes zu untersuchen. Über die Einführung einer neuartigen, analytischen Beschreibung für die Spinstruktur von Skyrmionen konnten die Ergebnisse, in sehr guter Übereinstimmung, mit dem zur Vorhersage von Skyrmionen verwendeten mikromagnetischen Modell verbunden werden. Jedoch zeigte die Analyse leicht andersartiger PdFe Systeme, dass das simplifizierte Modell nicht ausreicht, was auf Grundlage von Ergebnissen aus Dichtefunktionaltheorie-Rechnungen auf die Bedeutung von Austauschfrustration zurück geführt werden konnte.

Mittels der Untersuchung weiterer Pd_xFe- und RhFe-basierter Systeme konnte die empfindliche Abhängigkeit der magnetischen Eigenschaften von Fe/Ir(111) von den Deckschichten und der Stapelfolge der Dünnfilmsysteme gezeigt werden, was die Bedeutung hoher Präzision auf atomarer Skala für maßgeschneiderte magnetische Zustände hervorhebt. Die beobachteten magnetischen Periodizitäten in diesen Systemen reichen von 1 bis 15 nm, wobei weitere Skyrmionen und Skyrmionengitter mit Übergangsfeldern zwischen < 0.8 und $>9\,\mathrm{T}$ entdeckt werden konnten. Aufgrund der Meta-Stabilität von topologisch unterschiedlichen magnetischen Zuständen bei tiefen Temperaturen wurden neue skyrmionische Zustände ausgemacht, welche nach ihrer Topologie in gewöhnliche und ungewöhnliche Zustände unterteilt werden können. An Inselrändern konnte mittels SP-STM-Messungen das theoretisch vorhergesagte Verkippen der Spins aufgrund der Dzyaloshinskii-Moriya-

Wechselwirkung nachgewiesen werden.

Insgesamt beantwortet diese Doktorarbeit mehrere Schlüsselfragen der Grundlagenforschung auf dem Weg zur Realisierung von Skyrmionen-basierten Anwendungen und eröffnet hoffentlich das Feld für weiterführende experimentelle und theoretische Forschung im aufstrebenden Gebiet der Skyrmionik.

Contents

List of Abbreviations vii

Introduction 1

1. Theoretical Background 5
   1.1. Magnetism and Magnetic Interactions . . . 5
      1.1.1. Magnetic Interactions in an Atomistic Model . . . 5
      1.1.2. Continuum Approximation of Magnetic Interactions . . . 8
      1.1.3. Micromagnetic Characteristics in Skyrmionic Systems . . . 9
      1.1.4. Numerical Fit Procedure . . . 13
   1.2. Scanning Tunnelling Microscopy and Image Simulation . . . 14
      1.2.1. Working Principle of STM . . . 14
      1.2.2. Simulation of (SP-)STM Images . . . 15
      1.2.3. Simplified Calculation of SP-STM-Images . . . 17

2. Experimental Set-up and Sample Preparation 21
   2.1. Chamber System and Microscopes . . . 21
   2.2. Sample Preparation . . . 21
      2.2.1. Ir(111) . . . 21
      2.2.2. Fe/Ir(111) . . . 22
      2.2.3. Pd/Fe/Ir(111) . . . 24
      2.2.4. Rh/Fe/Ir(111) . . . 25

3. Discovery and Manipulation of Individual Skyrmions 29
   3.1. Magnetic Field Dependent Phase Transitions in Pd/Fe/Ir(111) . . . 29
   3.2. Writing and Deleting Single Magnetic Skyrmions . . . 34
   3.3. Exploration of the Switching Mechanism . . . 37

4. Field-Dependent Size and Shape of Single Magnetic Skyrmions 53
   4.1. The Skyrmion Structure in Detail . . . 53
   4.2. Improvement of the Fit . . . 58
   4.3. Influence of the Material Parameters on the Magnetic Properties . . . 61
   4.4. Literature Overview: International Activities on Skyrmions . . . 62

5. Tuning Effect of Pd on Fe/Ir(111) 65
5.1. ML Pd in Two Stackings on fcc Fe . . . 65
5.2. Pd on hcp Fe: Increase of the Magnetic Period . . . 71
5.3. Pd on fcc Pd/fcc Fe: Skyrmion Lattice up to 7T . . . 71
5.4. Pd on hcp Pd/fcc Fe: Skyrmions at 9T . . . 74
5.5. Summary of Magnetic Systems of Pd/Fe/Ir(111) . . . 76

6. Novel Magnetic States: Topology and Edges 81
6.1. fcc Pd on fcc Fe/Ir(111) at Low Energy . . . 83
6.2. Confined ML hcp Pd/Fe/Ir(111) . . . 86
6.3. Confined DL Pd/Fe/Ir(111): The Target Skyrmion . . . 89
6.4. Comparison of Boundary Conditions . . . 92
6.5. Experimental Observation of the Edge Tilt . . . 94

7. Tuning Fe/Ir(111) with Rh 97
7.1. fcc Rh/Fe/Ir(111) . . . 97
7.2. hcp Rh/Fe/Ir(111) . . . 98
7.3. DFT Calculations . . . 104
7.4. Conclusions . . . 106

Summary 107

A. Methods 111
A.1. Estimation of Tip-Sample Distance and Electric Field . . . 111
A.2. Spin Dynamics Simulation Details . . . 111
A.3. Estimation of Saturation Magnetisation . . . 112
A.4. Different Error Weighting in Section 4.1 . . . 113
A.5. Error Estimation for A, D, K . . . 113

B. Triple Layer Fe/Ir(111) 115
B.1. Distorted Skyrmion Model . . . 115
B.2. "Zero-Current" Switching of Skyrmions . . . 116

C. Additional Figures and Data 119
C.1. Additional Data: Exploration of the Switching Mechanism . . . 121

List of Figures 126

References 127

List of Publications 141

List of Abbreviations

180°-**DW** 180°-domain wall

1D one-dimensional

2D two-dimensional

360°-**DW** 360°-domain wall

3D three-dimensional

AFM antiferromagnetic

DFT density functional theory

$\mathrm{d}I/\mathrm{d}U$ differential tunnelling conductance

DL double-layer

DMI Dzyaloshinskii-Moriya interaction

fcc face centered cubic

Fe/Ir(111) iron on iridium (111)

FFT Fast Fourier Transform

FM ferromagnetic

FvM Frank-van der Merwe

hcp hexagonal close-packed

HDD hard disk drive

IP in-plane

LDOS local density of states

MBE molecular beam epitaxy

ML monolayer

NCMR non-collinear magnetoresistance

NND nearest neighbor distance

OOP out-of-plane

Pd/Fe/Ir(111) palladium on iron on iridium (111)

Rh/Fe/Ir(111) rhodium on iron on iridium (111)

RKKY Ruderman-Kittel-Kasuya-Yosida

RT race-track

SkHE skyrmion Hall effect

SkX skyrmion lattice

SOC spin-orbit coupling

SP-STM spin-polarised scanning tunneling microscopy

SS spin spiral

StKr Stranski-Krastanov

STM scanning tunneling microscopy

STT spin-transfer-torque

TAMR tunneling anisotropic magnetoresistance

TL Fe/Ir(111) triple layer of iron on iridium (111)

TMR tunnel magnetoresistance

UHV ultra-high vacuum

VW Volmer-Weber

Introduction

Ever since the cognitive revolution about 70,000 to 30,000 years ago, when humankind started to form elaborate social structures, humans have been generating information that needed to be passed on to the next generation. With the evolvement of ever more complex societies, including kingdoms, empires and today's globalised community, the language of choice for passing on the information constantly had to improve. Whereas in the beginning, oral communication was sufficient, at the latest when having to keep tax records of a large kingdom, new ways of storing information (or data) had to be developed. Only about 5,000 years ago, when the Sumerians invented a data-processing method called "writing" for storing large amounts of mathematical data, it was possible to keep tax records of hundreds of thousands of individuals and thereby to sustain the first large kingdoms. The first "storage devices" used were clay tablets and the language to store information on these storage devices were two types of signs. One type for numbers and the other type representing people, animals, merchandise and so forth. [Harari, 2014]

With every new invention for storing a larger quantity of increasingly more complex information in faster ways - e.g. the printing of books in sophisticated languages - the total amount of data stored and available world-wide boosted. For instance, a modern standard laptop could easily store every single drawing, written word or number that was available in all the medieval libraries in the year 1500 AD, with still room to spare. However, in the early 21st century, keeping up with the amounts of data just generated by one family during numerous holidays in the form of high-resolution photos and videos can already reach the maximum capacity of modern storage devices.

The main language to store (digital) data nowadays is the binary code, consisting of bits with the possible states "0" and "1". Typically, 8 bits contribute to 1 byte. The total amount of digital data generated world-wide in the year 2016 was 16.1 zettabyte or 16.1×10^{21} byte, estimated to increase by an order of magnitude by the year 2025 to 163 zettabyte of generated data per year [Seagate, 2017]. Up to now, most of this vast amount of data is stored as collinear magnetic bits (representing "0" or "1" depending on their orientation) in storage devices called hard disk drives (HDDs). To cope with this flood of data, the capacity of modern HDDs has been increased over the last decades by packing the magnetic bits more and more densely, today reaching an areal density of nearly 1 TB/inch^2 [Shilov, 2016]. Inevitably, this miniaturisation will reach its limit due to conflicting material requirements known as the trilemma of magnetic recording

[Richter, 2007]: at some point it is impossible to make the magnetic bits any smaller while maintaining their thermal stability, easy switchability and a decent signal-to-noise ratio. Although approaching the limit is still being postponed by new improvements to magnetic recording techniques such as heat-assisted magnetic recording [Rottmayer *et al.*, 2006], the storage of information in two-dimensional (2D) arrays of magnetic bits needs to be replaced soon.

The magnetic skyrmion is one possible candidate as information carrier (the presence or absence of a skyrmion can be attributed to the bit states "1" or "0") in storage devices which make use of the third dimension. These solitonic magnetic whirls [Bogdanov and Yablonsky, 1989], essentially being 2D knots in a continuous magnetisation field, can be moved along a magnetic track by electric currents [Jonietz *et al.*, 2010; Yu *et al.*, 2012; Jiang *et al.*, 2015; Woo *et al.*, 2016]. Due to their nature as quasi-particles, information can thus be transferred without the need for any mechanically moving parts. Ideas have been proposed to use skyrmions in race-track-type storage devices [Parkin *et al.*, 2008; Fert *et al.*, 2013; Sampaio *et al.*, 2013; Zhang *et al.*, 2015b]. As opposed to HDDs, in which the read/write head needs to move over the bits, the write and read heads in such devices can be stationary, because the magnetic information can be moved along the tracks. This enables an arbitrary arrangement of the tracks, including an undulation in three-dimensional (3D) arrays. This way, the areal density of bits could be boosted manifold and continue to accommodate the flood of generated data in the future. Whereas magnetic skyrmion lattices were observed experimentally for the first time in 2009 [Mühlbauer *et al.*, 2009], the realisation of skyrmion-based devices requires individual skyrmions, which can be written and deleted in order to store information.

This thesis covers some key aspects of fundamental research about magnetic skyrmions in Fe-based ultrathin magnetic films on an Ir(111) single crystal. First, a short introduction about the relevant magnetic interactions and models, and about the working principle of (spin-polarised) scanning tunneling microscopy ((SP-)STM) - the experimental technique applied in this thesis - is given in Chapter 1, before introducing the experimental set-up and the sample preparation in Chapter 2, including a short overview of the observed nanoskyrmion lattice in Fe/Ir(111). Chapter 3 presents the first experimental observation of individual nano-scale skyrmions in a bilayer of PdFe on Ir(111). It is demonstrated, how skyrmions can be addressed individually and written and deleted in close vicinity to each other with the scanning tunneling microscopy (STM) tip. By analysing time-dependent switching signals as a function of the tunnelling parameters, the key aspects of the switching mechanism are identified. In Chapter 4, the thesis offers an in-depth exploration of the magnetic field dependent spin structure of skyrmions in Pd/Fe/Ir(111), combined with the comparison of high-resolution experimental data to the original model used for predicting skyrmions [Bogdanov and Yablonsky, 1989]. A literature overview about research related

to skyrmions is placed in Section 4.4 to also put the work in Chapters 3 and 4 in perspective. The connection of experimental observables to the micromagnetic model, yielding the relevant material parameters for skyrmion formation, is subsequently used to quantify the tuning effect of Pd adlayers on the magnetic properties of Fe/Ir(111) in Chapter 5. Also in the sample systems with a double-layer (DL) of Pd, magnetic skyrmions (with different properties) are discovered. The concept of topological charge is used in Chapter 6 to classify non-collinear magnetic structures as common skyrmionic structures and uncommon novel spin textures. The experimental observation of the tilting of spins at edges of magnetic samples in Section 6.5 may also be important for future race-track devices. Finally, the influence of an adlayer of Rh on the magnetic properties of Fe/Ir(111) is studied as a comparison to Pd/Fe/Ir(111) in Chapter 7.

Besides answering some fundamental questions about skyrmions and the tuning of interactions in thin films, the research presented in this thesis, including the discovery and manipulation of interface-induced isolated skyrmions, hopefully has the potential to inspire more investigations and developments on the path to a possible next generation of storage devices capable of coping with the flood of data generated by our rapidly evolving global community.

Chapter 1.

Theoretical Background

This thesis is about the magnetism in different combinations of the 3d and 4d transition metals Fe, Pd and Rh, grown as epitaxial ultrathin films on the (111)-surface of the 5d transition metal single crystal of Ir. All of the itinerant magnetic systems, investigated by (spin-polarised) scanning tunneling microscopy ((SP-)STM) in the following chapters, exhibit non-collinear magnetic ordering, which is a result of the coupling of magnetic moments via a variety of interactions that stem from relativistic and non-relativistic effects acting on the electrons of the system. Section 1.1 offers a brief overview of the relevant interactions[1] first in an atomistic model (Section 1.1.1), followed by the continuum approximation of the interactions (Section 1.1.2) and a section about important micromagnetic characteristics in non-collinear (skyrmionic) systems (Section 1.1.3). Section 1.2 presents a short introduction into the working principle of (SP-)STM (Section 1.2.1), including the description of a routine to simulate (SP-)STM-images (Section 1.2.2) and considerations about a simplified calculation of SP-STM-images (Section 1.2.3).

1.1. Magnetism and Magnetic Interactions

1.1.1. Magnetic Interactions in an Atomistic Model

The relevant interactions for the magnetic systems in this thesis will briefly be introduced in this section within an atomistic model. Especially important for this thesis is the frustration of exchange interactions in combination with the Dzyaloshinskii-Moriya interaction (DMI). Although magnetism of itinerant magnets originates from the (close to freely) moving electrons, their magnetic moments can safely be assumed as localised at the atom positions due to the accumulation of spin density around the atom. In the following, for simplicity the magnetism will be represented by spins $\vec{S}_i$ of length 1 at the atom positions $\vec{R}_i$.

[1] A detailed introduction to itinerant magnetism and interactions can be found in [Hubert and Schäfer, 2000; Blundell, 2001].

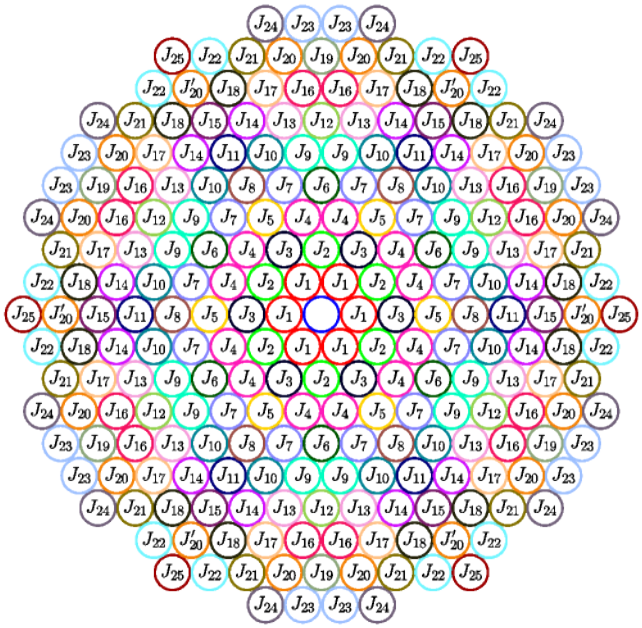

Figure 1.1.: Relative atom positions corresponding to exchange constants. J_{ij}, numbered by distance to central atom. J_{20} and J'_{20} possess the same distance to the central atom but different symmetries and therefore need to be treated separately.

Exchange Interaction

The Heisenberg exchange interaction is a quantum mechanical phenomenon that stems from the Coulomb repulsion between electrons, and from the Pauli exclusion principle. The associated energy, depending on the relative orientation of pairs of spins $\vec{S}_i$ and $\vec{S}_j$ can be expressed as:

$$E_{\text{ex}} = \sum_{i,j} -J_{ij}\vec{S}_i \cdot \vec{S}_j, \tag{1.1}$$

with the summation over all possible pairs of spins. For many magnetic systems, the exchange constants J_{ij} decay fast with the distance between the spins. For most magnetic systems, only the nearest-neighbour exchange plays a role and determines, whether they are ferromagnetically (FM) ($J_1 > 0$) or antiferromagnetically (AFM) ordered ($J_1 < 0$). Still, for a complete modelling of some magnetic systems, e.g. for small J_1, it is necessary to include J_{ij} up to several atomic distances (see Fig. 1.1). Above some distance, these J_{ij} do not originate from electron wavefunction overlap any more, but are mediated by conduction electrons in a Ruderman-Kittel-Kasuya-Yosida (RKKY)-type fashion [Ruderman and Kittel, 1954; Kasuya, 1956; Yosida, 1957].

It is easily imaginable that, as soon as e.g. J_1 and J_2 have a different sign, the magnetism becomes frustrated. If $|J_2| > |J_1|/4$, a FM or AFM arrangement of spins is no more

favourable, but instead the magnetic ground state can become a non-collinear spin spiral (SS) state. In a spin chain with the lattice constant a, the period λ of this SS simply depends on the sign and magnitude of J_1 and J_2 [Blundell, 2001, Eq. (5.32)]:

$$\lambda = \frac{2\pi a}{\arccos\left(-J_1/4J_2\right)} \tag{1.2}$$

The energy of this SS does neither depend on the plane of rotation nor on the rotational sense, when only considering Heisenberg exchange interactions.

Dzyaloshinskii-Moriya Interaction

The rotational sense starts to play a role for another interaction, the DMI, which stems from the antisymmetric part of the exchange energy and can provide a considerable contribution for a system with broken inversion symmetry and large spin-orbit coupling (SOC) [Dzyaloshinskii, 1957; Moriya, 1960]. A large SOC and therefore a large DMI-contribution is especially given for heavy elements like Ir. For the DMI between two spins, the energy can be written as:

$$E_{\mathrm{DM}} = \sum_{i,j} \vec{\mathrm{D}}_{ij} \cdot \left(\vec{S}_i \times \vec{S}_j\right), \tag{1.3}$$

where $\vec{\mathrm{D}}_{ij}$ is the material specific DM-vector. The spins prefer a perpendicular alignment to one another with the DM-vector pointing to the normal of their rotation plane. For the case of a (light) 3d element like Fe on a heavy substrate like Ir(111), the DM-vector can be assumed in-plane (IP) and perpendicular to the vector $\vec{R}_j - \vec{R}_i$ connecting the two spins $\vec{S}_i$ and $\vec{S}_j$ [Moriya, 1960; Fert, 1990; Crépieux and Lacroix, 1998]. This means, the DMI together with FM Heisenberg exchange leads to Neél-type cycloidal spin spirals with a rotation over the out-of-plane (OOP)-direction with the period (for a spin chain):

$$\lambda = \frac{2\pi a}{\arctan\left(\mathrm{D}_1/J_1\right)}, \tag{1.4}$$

in which a is the lattice constant.

Magnetocrystalline Anisotropy

Another energy contribution that originates from SOC and therefore tends to be larger for heavy elements, is the magnetocrystalline anisotropy. It can prefer certain spin orientations with respect to the crystal symmetry axes, and for the special case of a uniaxial anisotropy the energy equals:

$$E_{\mathrm{aniso}} = \sum_i -\mathrm{K}_i \cdot \left(S_i^{\mathrm{z}}\right)^2 \tag{1.5}$$

with the anisotropy constant $K_i > 0$ for an easy axis along the z-direction. This anisotropy energy then prefers OOP alignment of spins and tends to make SSs inhomogeneous, if K_i is of considerable strength. For an OOP easy axis, a SS rotates faster over the IP part and slower over the OOP part. If the anisotropy becomes large compared to the contributions from exchange interaction and DMI, the SS state is suppressed and large domains form.

Zeeman-Energy

The Zeeman-energy for the magnetic moments μ in an external magnetic field $\vec{B}$ is expressed as:

$$E_{\text{Zeeman}} = \sum_i -\mu \vec{S}_i \cdot \vec{B} \tag{1.6}$$

and favours parallel alignment of the spins with the magnetic field. A SS in a magnetic field can be distorted in such a way that the parts (anti-)parallel to $\vec{B}$ are (compressed) expanded.

1.1.2. Continuum Approximation of Magnetic Interactions

To calculate the magnetic energy of an ensemble of spins, it is necessary to sum up Eqs. (1.1), (1.3), (1.5) and (1.6). It is often only possible to find the energy minimum of a large spin ensemble by numerical calculations such as Monte-Carlo simulations. These calculations can quickly exceed the limits of analytical as well as numerical solving methods. To overcome these problems and to simplify the calculations, it is possible to use the continuum approximation of some of the interactions.

For small lateral changes in the magnetisation vector field $\vec{m}(\vec{r})$ and constant saturation magnetisation M_S ($|\vec{m}| = 1$), the Eqs. (1.1), (1.3), (1.5) and (1.6) can be approximated by [Bogdanov and Hubert, 1994b; Skomski *et al.*, 2005; Lin and Hayami, 2016]:

$$E_{\text{cont}} = \int_V \left[A\,(\nabla \vec{m})^2 + D w_{\text{DM}} - K_{\text{eff}} m_z^2 - B M_S m_z \right] d^3\vec{r}, \tag{1.7}$$

with the four magnetic material parameters A, D and K_{eff} being the exchange stiffness, DM-constant and effective uniaxial anisotropy constant[2], respectively. The four material parameters are the continuum analogues of the atomistic constants J_{ij}, D_{ij}, K_i and μ for M_S, respectively. The magnetic field B points along the z-direction. In the continuum case, this is now an integral over the volume V of the magnetic sample. w_{DM} represents the DMI energy functional and depends on the crystal symmetry class. For the thin film

[2] The effective anisotropy constant K_{eff} contains, additionally to the magnetocrystalline anisotropy, an effective term for the demagnetisation field. In extended thin films, the demagnetisation field can be included as an effective hard axis anisotropy term: $K_{\text{eff}} = K - K_d$, with $K_d = \mu_0 M_S^2/2$.

samples on the Ir(111)-crystal with interface DMI treated in this thesis, Eq. (1.7) simplifies to its 2D-formulation [Bogdanov and Yablonsky, 1989]:

$$E_{\text{cont}} = t \int_{Area} \Bigg\{ \overbrace{A \left[\left(\frac{\partial \vec{m}}{\partial x} \right)^2 + \left(\frac{\partial \vec{m}}{\partial y} \right)^2 \right]}^{\text{exchange energy}} + \overbrace{D \left(m_z \frac{\partial m_x}{\partial x} - m_x \frac{\partial m_z}{\partial x} + m_z \frac{\partial m_y}{\partial y} - m_y \frac{\partial m_z}{\partial y} \right)}^{\text{DM energy}} - \underbrace{K_{\text{eff}} m_z^2}_{\text{anisotropy energy}} - \underbrace{B M_{\text{S}} m_z}_{\text{Zeeman energy}} \Bigg\} \, \mathrm{d}x \, \mathrm{d}y, \tag{1.8}$$

with constant magnetisation along the z-direction and with the sample thickness t.

This simplified continuum approximation has the disadvantage that all J_{ij} are incorporated in one parameter, the exchange stiffness A. As a consequence, only a FM ground state favoured by the exchange interactions can be modelled by this approximation. As soon as the magnetic ground state of a system is a non-collinear SS state, resulting from frustration of exchange interactions, this model fails. Reproducing a certain spin spiral with this approximation will then result in an undesired overestimation of D.

There are some first attempts to incorporate a frustration of the exchange interactions in this approximation model [Leonov and Mostovoy, 2015; Lin and Hayami, 2016; Rózsa *et al.*, 2017; da Silva Oliveira *et al.*, 2017] with an additional parameter A_2 for the frustrated exchange. In principle, frustration can also play a role in the DMI [Menzel *et al.*, 2012; da Silva Oliveira *et al.*, 2017]. Nonetheless, this thesis will only use the well-established model in Eq. (1.8) to characterise the various skyrmionic systems and their underlying material parameters.

1.1.3. Micromagnetic Characteristics in Skyrmionic Systems

Using the model in Eq. (1.8) and radial representations thereof, it is possible to show that, for certain material parameter sets and magnetic fields, (meta-)stable, spatially localised, solitonic magnetic whirls with axial symmetry and fixed rotational sense exist as possible solutions, see Fig. 1.2a [Bogdanov and Yablonsky, 1989; Bogdanov and Hubert, 1994b,a; Rößler *et al.*, 2006, 2011; Wilson *et al.*, 2014]. They were initially named vortices but later called magnetic skyrmions, due to the resemblance of their stabilising mechanisms to parts of the Skyrme model in particle physics field theory [Skyrme, 1962; Braun, 1999; Bogdanov *et al.*, 2002]. A more thorough literature overview about skyrmions is given in Section 4.4.

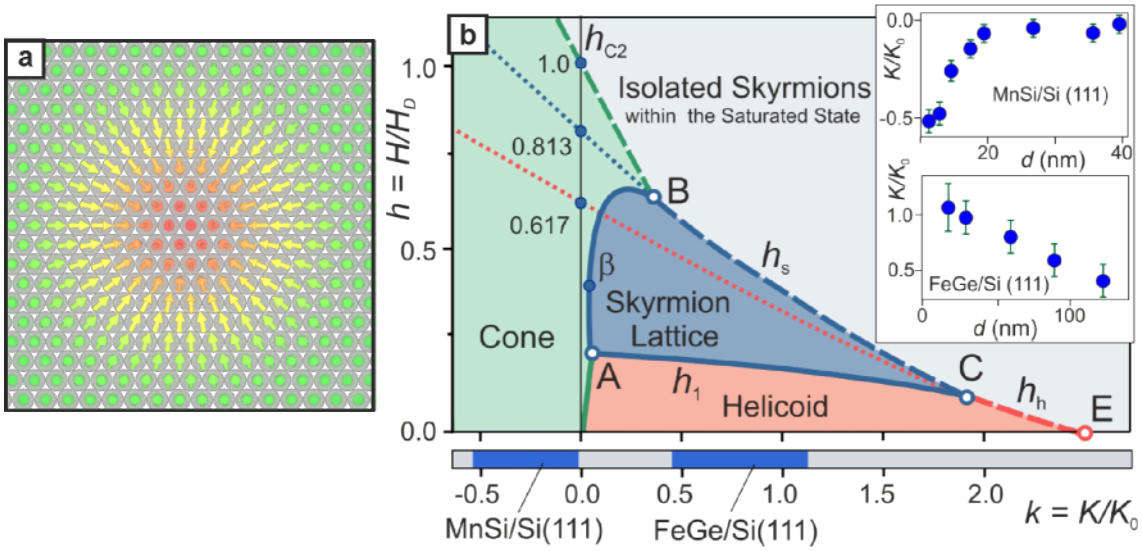

Figure 1.2.: Skyrmion and reduced phase diagram for skyrmionic systems. a Sketch of a Néel-type skyrmion. Each arrow represents an atomic spin. **b** Phase diagram for skyrmionic systems for reduced parameters, reprinted figure with permission from [Wilson *et al.*, 2014, Fig. 3]. Copyright (2014) by the American Physical Society. The values for $h_1\,(k)$ and $h_S\,(k)$ are given in Table C.1.

Phase Diagram and Transition Fields

Figure 1.2b shows a zero temperature phase diagram based on reduced parameters that was computed by [Wilson *et al.*, 2014]. To apply this phase diagram to a manifold of magnetic systems, the reduced parameters h and k are introduced:

$$k = \frac{K_{\text{eff}}}{K_0} = \frac{4AK_{\text{eff}}}{D^2} \tag{1.9}$$

$$h = \frac{B}{B_{\text{D}}} = B \cdot \frac{2AM_{\text{S}}}{D^2} \quad \Rightarrow \quad B = h \cdot \frac{D^2}{2AM_{\text{S}}} \tag{1.10}$$

Here k is the reduced anisotropy, which basically is a magnetic material parameter-based classification of any material in this phase diagram. h is directly proportional to the external magnetic field B, but also reduced with respect to the material parameters. It should be possible to classify any skyrmionic magnetic material, which is driven by FM exchange and DMI only (if frustrated exchange plays a significant role, the model will fail) in this phase diagram and thus find the calculated critical transition fields between the SS and the skyrmion lattice (SkX) state ($B_{\text{SS-Sk}}$), and between the SkX and the FM state ($B_{\text{Sk-FM}}$). They are represented in the diagram by h_1 and h_{S}, respectively. By manually extracting the characteristic points from Fig. 1.2b and linearly interpolating between the points A and C, and B and C, the critical phase transition fields can roughly be estimated to:

$$h_1(k) \approx -0.065 \cdot k + 0.22 \tag{1.11}$$

$$h_S(k) \approx -0.35 \cdot k + 0.64. \tag{1.12}$$

The resulting critical magnetic fields can be estimated, using Eqs. (1.9) and (1.10), as:

$$B_{SS-Sk} \approx \frac{1}{M_S}\left(-0.13 \cdot K_{eff} + 0.11 \cdot \frac{D^2}{A}\right) \tag{1.13}$$

$$B_{Sk-FM} \approx \frac{1}{M_S}\left(-0.70 \cdot K_{eff} + 0.32 \cdot \frac{D^2}{A}\right) \tag{1.14}$$

These equations only serve as a rough estimate for how the different material parameters influence the transition fields. For a more accurate numerical calculation of B_{SS-Sk} and B_{Sk-FM} and fits to experimental data, a cubic interpolation between more extracted values from Fig. 1.2b is used (see values in Table C.1).

Spin Spiral Profile and Period

Without an external magnetic field, the ground state of skyrmionic systems over a large range of k is the SS state (named "Helicoid" in Fig. 1.2b). The period of a SS, even with an applied magnetic field, can be calculated as [Bogdanov and Hubert, 1994b, Eq. (19)]:

$$\lambda = \frac{A}{D}\int_0^{2\pi} \mathrm{d}\theta \left[B \cdot \frac{AM_S}{D^2} \cdot (1-\cos\theta) + \frac{A}{2D^2} \cdot \left(K_{eff} + \mu_0 M_S^2\right) \cdot \sin^2\theta + C\right]^{-1} \tag{1.15}$$

with C being the solution of [Bogdanov and Hubert, 1994b, Eq. (20)]:

$$\int_0^{\pi} \mathrm{d}\theta \sqrt{B \cdot \frac{AM_S}{D^2} \cdot (1-\cos\theta) + \frac{A}{2D^2} \cdot \left(K_{eff} + \mu_0 M_S^2\right) \cdot \sin^2\theta + C} = \frac{\pi}{2}, \tag{1.16}$$

which can be found numerically. For the special case of $B = K_{eff} = 0$, Eq. (1.15) simplifies to $\lambda = 4\pi A/D$. The actual position-resolved spin spiral profile $\theta(\rho)$ (θ is the polar angle, ρ the spatial coordinate) can be calculated numerically by applying the fourth order Runge-Kutta-method [Runge, 1895; Kutta, 1901] on [Bogdanov and Hubert, 1994b, Eq. (18)]:

$$\frac{\mathrm{d}\theta}{\mathrm{d}\rho} = \sqrt{B \cdot \frac{AM_S}{D^2} \cdot (1-\cos\theta) + \frac{A}{2D^2} \cdot \left(K_{eff} + \mu_0 M_S^2\right) \cdot \sin^2\theta + C}, \tag{1.17}$$

scaling the resulting ρ by A/D.

Figure 1.3a shows the polar angle of such a calculated inhomogeneous SS profile and the atomistic 3D representation of the corresponding spin configuration for the material

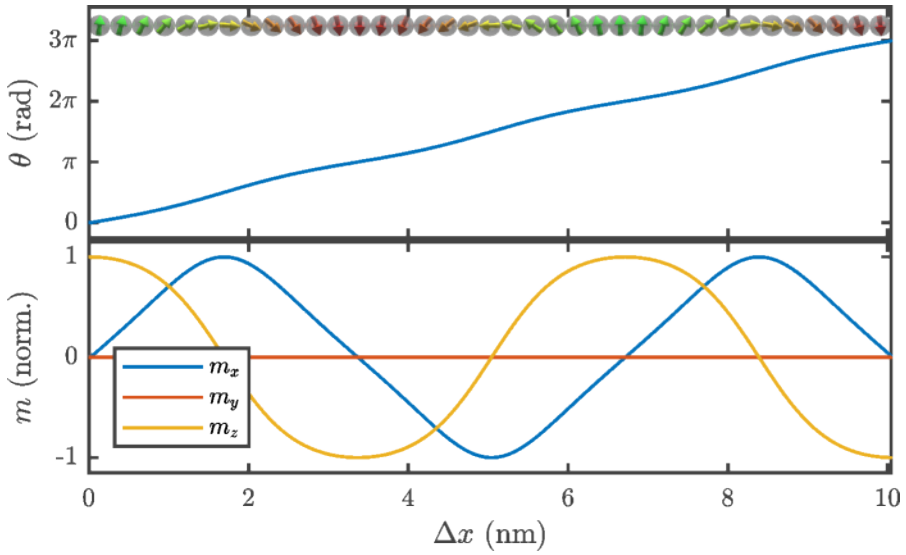

Figure 1.3.: Example of a spin spiral profile. **a** Polar angle θ of a typical zero field SS profile as obtained from the analytical formula Eq. (1.17). Material parameters from [Romming *et al.*, 2015] ($A = 2.0\,\mathrm{pJ\,m^{-1}}$, $D = 3.9\,\mathrm{mJ\,m^{-2}}$, $K = 2.5\,\mathrm{MJ\,m^{-3}}$, $M = 1.1\,\mathrm{MA\,m^{-1}}$). Rendered ball model spins show a side view of the spin spiral configuration of atomic spins with the Ir lattice constant $a = 2.715\,\text{Å}$. **b** Calculated magnetisation components of a SS profile in **a**.

parameters of hexagonal close-packed (hcp) Pd/Fe/Ir(111) obtained in [Romming *et al.*, 2015] (see also Chapter 4). Figure 1.3b shows the magnetisation components.

(360°-)Domain Walls

Other non-collinear magnetic structures that are regularly seen are domain walls. If the DMI is too small to form the SS state ($D < D_\mathrm{C} = 4\sqrt{AK_\mathrm{eff}}/\pi$ [Heide *et al.*, 2008; Rohart and Thiaville, 2013]), still domain walls between larger domains can form. For vanishing DMI, these domain walls can have both rotational senses. The magnetisation rotation is then given by [Hubert and Schäfer, 2000; Braun, 1994]:

$$\varphi_{180} = \arcsin\left(\tanh\frac{x}{w_0/2}\right) \tag{1.18}$$

with the domain wall width $w_0 = 2\sqrt{A/K_\mathrm{eff}}$. As soon as there is a considerable amount of DMI in thin films, a unique rotational sense is found without affecting the shape or width of the wall, given by Eq. (1.18) [Meckler *et al.*, 2012]. Upon application of an external magnetic field, the domains antiparallel to the field shrink, causing the domain walls to move closer to each other in pairs. Due to their unique rotational sense, they cannot simply annihilate each other, but instead join to one 360°-domain wall (360°-DW), of which the profile is then described by two walls at the positions $\pm c$ [Kubetzka *et al.*, 2003; Braun, 1994]:

$$\varphi_{360}(x,c,w) = \begin{cases} \sum\limits_{+,-} \left[\arcsin\left(\tanh\frac{x\pm c}{w/2}\right)\right] + \pi & |B_z > 0 \\ \sum\limits_{+,-} \left[\arcsin\left(\tanh\frac{x\pm c}{w/2}\right)\right] & |B_z < 0, \end{cases} \tag{1.19}$$

with the sign of w determining the rotational sense. For the only two parameters c and w a surprisingly simple exact solution exists that connects them to the magnetic material parameters [Kubetzka *et al.*, 2003; Braun, 1994]:

$$c = \frac{w}{2}\arcsin\left(\sqrt{\frac{2K_{\text{eff}}}{M_{\text{S}}B}}\right), \quad w = 2\sqrt{\frac{A}{K_{\text{eff}} + M_{\text{S}}B/2}}. \tag{1.20}$$

Also for skyrmionic systems with SS ground states ($D > D_{\text{C}}$), spin spiral fragments can remain at higher magnetic fields, which are the same as 360°-DW and can be described in the same way (see Section 5.1). It will be shown in Chapter 4, how the 360°-DW-profile in Eq. (1.19) can also be used to describe magnetic skyrmions.

1.1.4. Numerical Fit Procedure to Extract Material Parameters from Experiment

Having described several characteristic properties of skyrmionic systems in theory, the next step is to compare them to their experimental counterparts and use them to extract the magnetic material parameters A, D, K_{eff} and M_{S} in a fit. In the framework of this thesis, a flexible fitting procedure was developed that is used with a variety of known experimental input parameters χ_i (for example in Section 5.1 the spin spiral period λ and the domain wall parameters c_i and w_i at two magnetic fields). Together with their estimated absolute errors ξ_i they are compared to their theoretically calculated values Υ_i (here λ from Eq. (1.15) and c_i, w_i from Eq. (1.20)). A numerical fit is implemented by reducing the problem to the error-weighted total square deviations of experimental and theoretical values:

$$\mathcal{S}(\mathcal{P}) = \sqrt{\sum_{\chi}\left\{\sum_{i=1}^{N}\left(\chi_i - \Upsilon_i(\mathcal{P})\right)^2 \cdot \frac{w_i^2}{N^2}\right\}}, \tag{1.21}$$

with

$$w_i = \frac{1}{\xi_i}$$

as the chosen relative error-dependent weights of each summand. $\mathcal{P}$ represents the magnetic parameter sets, consisting of A, D, K_{eff}, M_{S} (and B_i). If there are N experimental values of one kind (e.g. 360°-DWs at two magnetic fields), these summands are divided by the number of values provided. This way, all parameters get the same weight within the total square deviations, irrespective of their magnitude or multitude. For example, the zero-field spin spiral period λ is equally important as a set of domain walls in several magnetic fields.

To get the magnetic material parameters from a set of experimental input values, first a set $\mathcal{P}$ is randomly picked within the range of the phase diagram that is reasonable ($k\,(\mathrm{A}) < k < k\,(\mathrm{E})$ in Fig. 1.2b). Equation (1.21) is then numerically minimised with respect to $\mathcal{P}$, using a *Nelder-Mead simplex method* as implemented in Matlab [MATLAB, 2016; Nelder and Mead, 1965; Lagarias *et al.*, 1998].

To estimate how the uncertainties of the experimental values influence the uncertainty of the resulting fitted material parameters, this procedure is repeated many times, but the experimental input parameters are randomly varied according to their error ξ_i before each run. This way, a distribution of each material parameter is obtained, of which the mean value and standard deviation can be calculated and used as the result.

1.2. Scanning Tunnelling Microscopy and Image Simulation

All experimental results in this work are based on measurements, acquired with STM. This section is dedicated to shortly[3] giving an overview of how (SP-)STM works and how (SP-)STM images of known (spin) structures can be simulated.

1.2.1. Working Principle of STM

The principle of STM is to bring a sharp metallic tip so close to the conducting sample surface that the electrons between tip and sample can tunnel through the gap between the tip apex atom and the nearest surface atoms (the gap is typically less than 1 nm wide), see Fig. 1.4a. When applying a bias voltage between tip and sample, the resulting net current is exponentially dependent on the distance between tip and sample, and proportional to the local density of states (LDOS) of both tip and sample, integrated from the Fermi energy up to the energy chosen by the applied bias voltage. If a magnetic tip is used (SP-STM), an additional dependency of the current on the spin-split LDOSs of tip and sample and the angle between tip and sample magnetisation appears, see schematic in Fig. 1.4b. The current in the typical range of pA to nA can be measured with a current amplifier. Any change in the electronic structure of the sample will be reflected in the (spin-split) LDOS and can thus be accessed by (SP-)STM. Therefore, several magnetoresistive effects can influence the tunnel current, depending on the tip and the bias voltage chosen: For magnetic tips, the tunnel magnetoresistance (TMR) [Heinze, 2006; Wiesendanger, 2009] produces a contrast depending on the relative orientation of tip and sample magnetisation direction (scalar projection) and on the net spin-polarisation of the current $\eta = (I_\uparrow - I_\downarrow)/(I_\uparrow + I_\downarrow)$.

[3] Because (SP-)STM is a well-known and standard technique by now, many assumptions and steps before coming to the conclusions in this section are skipped for simplicity. For complete descriptions of (SP-)STM theory, see for example Refs. [Bardeen, 1961; Binnig and Rohrer, 1982; Tersoff and Hamann, 1983, 1985; Chen, 1988, 1990; Wiesendanger *et al.*, 1990a,b; Chen, 1993; Wiesendanger, 1994; Heinze *et al.*, 1998; Wortmann *et al.*, 2001; Heinze, 2006; Wiesendanger, 2009, 2011].

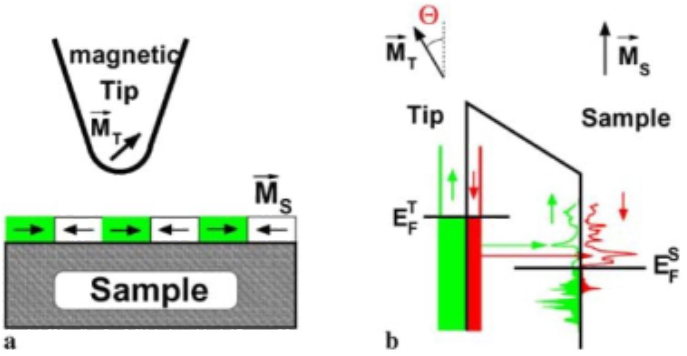

Figure 1.4.: SP-STM geometry and spin-split LDOS. a Geometry of the experimental set-up including the magnetisation directions of tip $\vec{M}_T$ and sample $\vec{M}_S$. **b** Sketch of the spin-dependent electronic structure of tip and sample. Extracted from [Heinze, 2006, Fig. 1] with permission of Springer.

The tunneling anisotropic magnetoresistance (TAMR) [von Bergmann *et al.*, 2012] results from changes in the LDOS due to SOC and can thus lead to a contrast between IP and OOP magnetised sample spins, irrespective of the magnetisation of the tip. Also accessible with a non-magnetic (or magnetic) tip is the non-collinear magnetoresistance (NCMR) [Hanneken *et al.*, 2015; Crum *et al.*, 2015; Kubetzka *et al.*, 2017], which results from changes in the LDOS due to a mixing of spin-up and spin-down bands for non-collinear structures. One way of acquiring an image of the sample surface is to scan the tip laterally over the sample while keeping the measured current constant via a feedback-loop that controls the z-position of the tip (constant-current mode). The recorded signal $z\,(x, y)$ represents the topography of the sample surface.

Another signal that can be recorded - via modulating the bias voltage with the Lock-In-technique - is the differential tunnelling conductance ($\mathrm{d}I/\mathrm{d}U$). Since the bias voltage is modulated in a small interval around the chosen constant bias voltage, the resulting change of the current is proportional to the LDOS of the sample at the location of the tip and at the energy chosen. This way, certain features of the electronic structure of the sample can be accessed separately. Maps of the $\mathrm{d}I/\mathrm{d}U$-signal can be recorded both in constant-height or in constant-current operation of the STM. Throughout this thesis, they are recorded simultaneously to constant-current topography images, unless stated otherwise.

1.2.2. Simulation of (SP-)STM Images

In 2006, Heinze showed how (SP-)STM images can be simulated from any (spin) structure [Heinze, 2006]. This section will give a detailed description how a fast and simple numerical procedure can be set up for calculating such images, also incorporating an approximation of the NCMR. As input, a list of spins with their normalised direction vectors $\vec{S}_i$ and their respective atom positions $\vec{R}_i$ are given. For an image with $a \times b$ pixels, the position of each

pixel has to be given as the position of the tip $\vec{R}_j^{\mathrm{T}}$, typically at a constant height z_0 above the atom positions. The current at each pixel I_j can then be calculated as:

$$I_j\left(\vec{R}_j^{\mathrm{T}}\right) = \sum_i I_i^{\mathrm{loc}} \cdot \exp\left(-2\kappa\left|\vec{R}_j^{\mathrm{T}} - \vec{R}_i\right|\right) \tag{1.22}$$

with the decay constant $\kappa = \sqrt{2m_e\Phi/\hbar^2}$. Here Φ is the work function with a typical value of $\Phi = 4.8\,\mathrm{eV}$, m_e is an electron's mass and $\hbar$ is the reduced Planck constant. Generally, the sum has to be evaluated over all atom positions, but can be limited to atoms in the near vicinity of $\vec{R}_j^{\mathrm{T}}$ to reduce computing time significantly. The exponential decay leads to negligible contributions from atoms further away (a cut-off distance of $3 \cdot z_0$ is used in this thesis). I_i^{loc} is the sum of local contributions to the tunnel current corresponding to the atom position $\vec{R}_i$, which only needs to be calculated once for each atom as:

$$I_i^{\mathrm{loc}} = I_0 \cdot \left(1 + \gamma_{\mathrm{P}} \cdot \vec{S}_i \cdot \vec{m}_{\mathrm{T}} + \gamma_{\mathrm{T}} \cdot S_i^{z2} + \gamma_{\mathrm{N}} \cdot \frac{\angle_i^{\mathrm{NN}}}{\pi}\right) \tag{1.23}$$

with γ_{P}, γ_{T} and γ_{N} as the prefactors of the current contributions caused by the TMR [Heinze, 2006; Wiesendanger, 2009], the TAMR [von Bergmann *et al.*, 2012] and the NCMR [Hanneken *et al.*, 2015; Crum *et al.*, 2015; Kubetzka *et al.*, 2017], respectively. Since the intensity of the NCMR scales approximately linearly with the mean angle of nearest neighbours [Kubetzka *et al.*, 2017], such a contrast is implemented in the simulations in a simplified way as $\angle_i^{\mathrm{NN}}/\pi$, which is the mean angle of $\vec{S}_i$ to its nearest neighbours, normalised by the maximum possible value π. For a fast numerical calculation of the whole image, it is advantageous to first calculate Eq. (1.23) once for all atoms i and then evaluate Eq. (1.22) for all pixels j, which can be done in parallel to decrease computing time.

The change in tunnel current as a function of the lateral tip position $\vec{R}_{\mathrm{T},\parallel}$ can be related to a corrugation in the height Δz by making use of the linear approximation of the exponential decay [Chen, 1993; Heinze, 2006]:

$$\Delta z\left(\vec{R}_{\mathrm{T},\parallel}\right) = \frac{I\left(\vec{R}_{\mathrm{T},\parallel}, z_0\right) - I_0\left(z_0\right)}{2\kappa I_0\left(z_0\right)}. \tag{1.24}$$

Here $I_0\left(z_0\right)$ is the much larger laterally constant spin-independent tunnel current, which can be chosen arbitrarily in the simulations. Choosing $I_0\left(z_0\right)$ as the constant current in the middle of a large film without magnetic contributions γ_k leads to $\Delta z = 0$ for no magnetic contributions (neglecting atomic corrugations).

Figure 1.5a shows a schematic top view of two skyrmion spin structures (see Sections 1.1.3 and 4.4), a larger one at low magnetic field and a smaller one at high field. Panels b-e show simulated STM images of these spin structures with the respective pre-

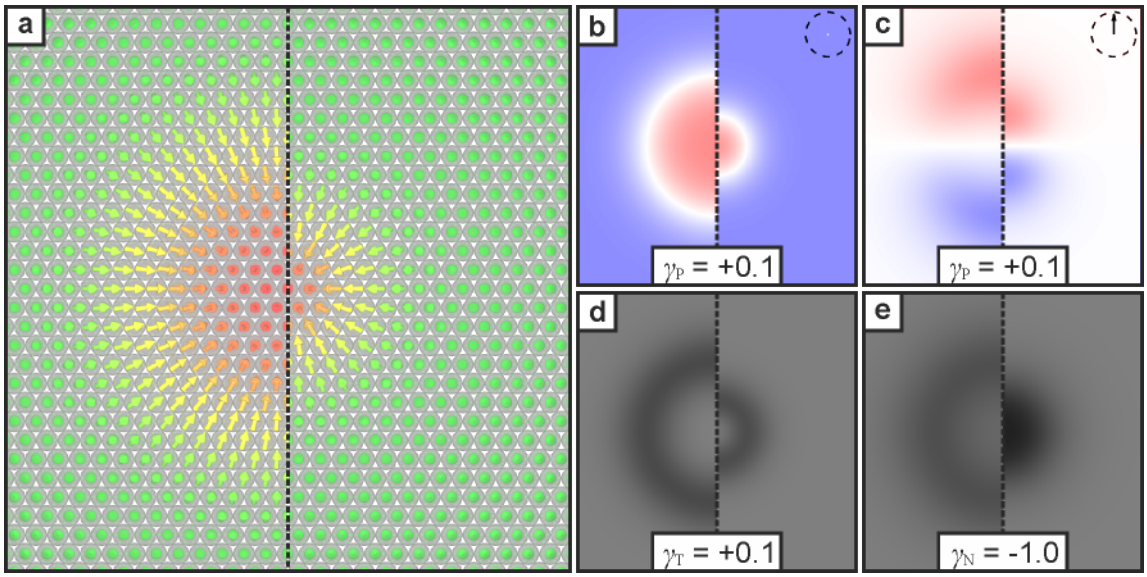

Figure 1.5.: Different magnetic STM contrasts. **a** Schematic top view of two skyrmion spin structures, a larger one at low magnetic field (left) and a smaller one at high field (right). **b-e** Simulated STM images according to Eqs. (1.22) to (1.24) as described in the text with all contrast mechanisms $\gamma_k = 0$ except the one indicated. $7 \times 7\,\mathrm{nm}$ images, $z_0 = 0.6\,\mathrm{nm}$. **b,c** SP-STM-contrast with tip direction as denoted in upper right corner. **d** TAMR-contrast. **e** NCMR-contrast (linear relation to mean angle between nearest neighbours). **b,c** Colour coded according to Fig. C.1b. **d,e** Colour coded according to Fig. C.1a.

factors γ_k as denoted. Spin-polarised STM images (γ_P) lead to a contrast between spins that are aligned parallel to the tip direction $\vec{m}_\mathrm{T}$, and spins that are aligned in the opposite direction. The TAMR (γ_T) leads to a contrast between IP and OOP aligned spins, whereas the NCMR (γ_N) is different between collinear and non-collinear spin structures [Hanneken *et al.*, 2015; Kubetzka *et al.*, 2017]. These last two contrasts can also be seen with a non-magnetic tip.

1.2.3. Simplified Calculation of SP-STM-Images

Since images simulated according to the previous section, are still time-consuming to calculate, throughout this thesis, SP-STM-images (based on the TMR) are often calculated in a simplified manner by calculating the local part of the signal as:

$$z\,(x,y) = z_0 + a \cdot \vec{m}_\mathrm{T} \cdot \vec{m}_\mathrm{S}\,(x,y)\,. \tag{1.25}$$

Here the sample magnetisation is defined as a vector field at the pixel positions projected onto a fixed tip direction. This calculation is much faster because there is no need to calculate the distances to neighbouring atoms, the exponential decay of each of the atoms and the sum. For the analysis of $\mathrm{d}I/\mathrm{d}U$ signals, z can be substituted by $\mathrm{d}I/\mathrm{d}U$. In principle, this simplified approach can lead to a systematic overestimation of the width of

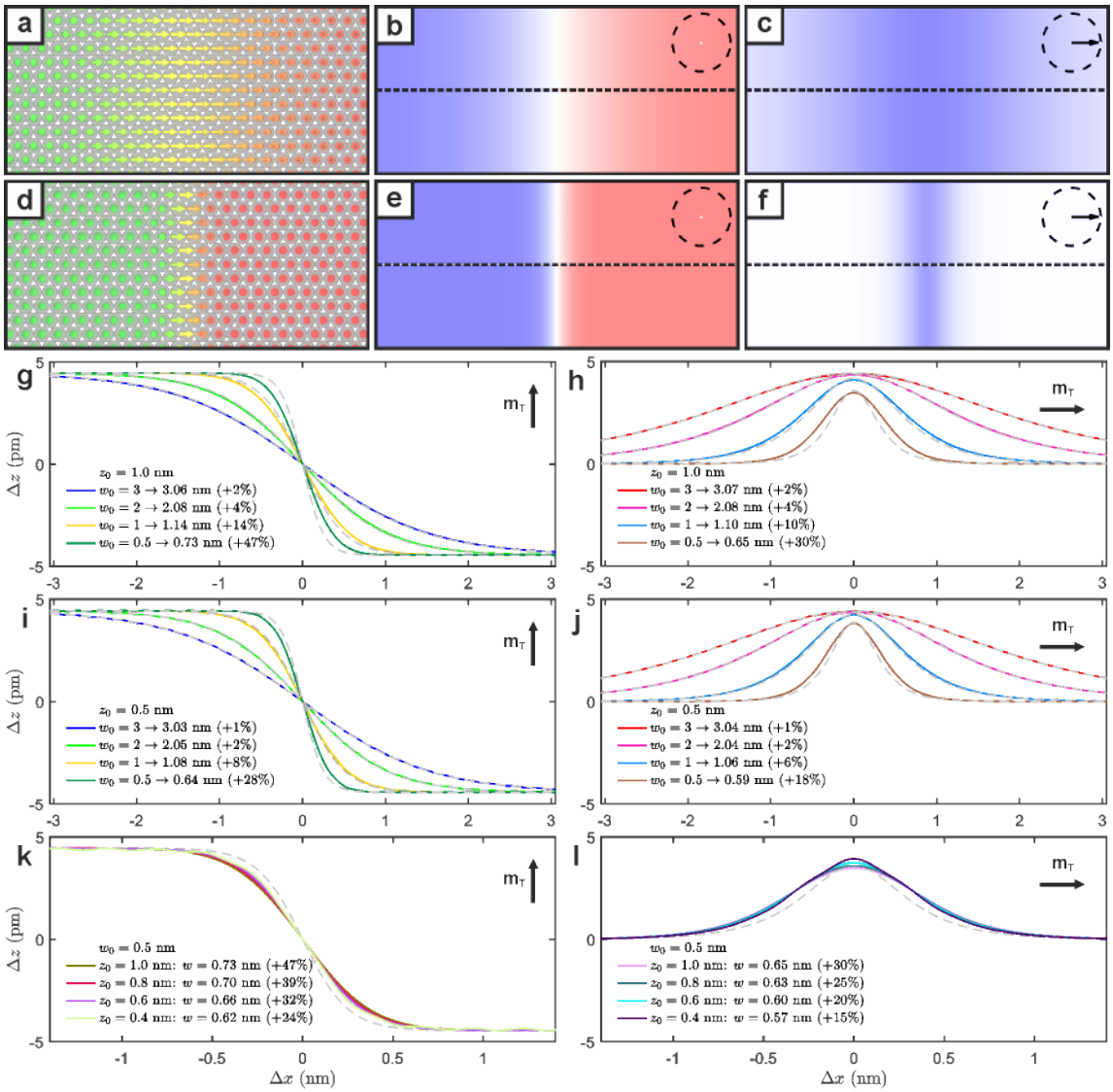

Figure 1.6.: Magnetic contrasts on 180°-domain walls. **a,d** Schematic top view of 180°-DWs as defined by Eq. (1.18) with $w_0 = 3\,\mathrm{nm}$ and $w_0 = 0.5\,\mathrm{nm}$, respectively. **b,c,e,f** Simulated SP-STM-images of the structures in **a** and **d** according to Eq. (1.22) (upper part of panels, $z_0 = 0.8\,\mathrm{nm}$, $\gamma_\mathrm{P} = +0.1$) and images, which are directly calculated using Eq. (1.25) (lower part of panels), tip directions as indicated. Colour code according to Fig. C.1b. **g-l** Line profiles taken from simulated SP-STM-images (solid lines) and directly calculated images (dashed grey lines) of 180°-DWs with domain wall widths w_0, tip-sample distance z_0 and the tip direction as indicated, $\gamma_\mathrm{P} = +0.1$. Labels show the apparent widths of the domain walls in the simulated images.

small magnetic structures, especially when their size approaches the distance between tip and sample, z_0.

To demonstrate this, Fig. 1.6 shows the overestimation effect using the example of 180°-DWs as defined by Eq. (1.18). Panels a and d show the spin structure of a Neél-type 180°-DW with the domain wall widths $w_0 = 3\,\mathrm{nm}$ and $w_0 = 0.5\,\mathrm{nm}$, respectively. Panels

b, c, e and f show simulated SP-STM-images of the structures according to Eq. (1.22) (upper part of panels) and images which are directly calculated using Eq. (1.25) (lower part of panels). For the wider 180°-DW, the images calculated either way appear the same (panels b and c), whereas for the narrower 180°-DW, the SP-STM-images are broadened compared to the direct images (panels e and f). This results from the sum over neighbouring atoms, which do not all have the same orientation, reflecting the (distance dependent) instrumental broadening.

Panels g-j show line profiles taken from simulated SP-STM-images (solid lines) and directly calculated images (dashed grey lines) of 180°-DWs with domain wall widths w_0 as indicated for a tip-sample distance $z_0 = 1.0\,\mathrm{nm}$ (g and h) and $z_0 = 0.5\,\mathrm{nm}$ (i and j). From the shift of the SP-STM profiles compared to the direct profiles, it can be concluded that the smaller the magnetic structure, the larger the deviation between the two methods and that the deviation is higher for an OOP tip compared to an IP tip for these IP domain walls. Panels k and l show that the overestimation effect decreases approx. linearly with decreasing tip-sample distance z_0.

The following conclusions can be made from this exemplary study of simulated SP-STM-images: As long as the magnetic length scale of the spin structure is longer than twice the tip-sample distance, the systematic error of the simplified calculation of SP-STM-images via Eq. (1.25) is negligible (approx. 5 %). Generally, for smaller spin structures, smaller tip-sample distances should be used, i.e. a lower bias voltage and higher current set-point should be chosen. For typical tip-sample distances of 4 to 8 Å, any spin structure smaller than 1 nm should be analysed using the full STM simulation to prevent an overestimation of its size.

Chapter 2.

Experimental Set-up and Sample Preparation

2.1. Chamber System and Microscopes

The samples investigated in this thesis were prepared under ultra-high vacuum (UHV) conditions ($p_{\text{base}} < 1 \times 10^{-10}$ mbar) in a UHV chamber system that was described elsewhere [Witt *et al.*, 1997; Menzel, 2011; Hanneken, 2015]. It consists of several chambers, each serving specific purposes. This way, contaminations from some procedures like electron beam heating or Ar-sputtering do not have an influence on the pressure in the chamber, in which clean materials are deposited by molecular beam epitaxy (MBE).

Once a sample is prepared as desired, it can be transferred into one of the two available low temperature STMs. One operates at approx. 8 K and provides a maximal magnetic field of $|B| < 2.5$ T, perpendicular to the sample surface [Pietzsch *et al.*, 2000]. The other one can be cooled down to a minimal temperature of approx. 1.3 K but is usually operated at 4.2 K for the work presented in this thesis. A maximal magnetic field of $|B| < 9$ T can be applied, also in the OOP direction. Both low temperature STMs possess a mechanism for exchanging the tip *in-situ*. Therefore, a variety of tips can be used for different kinds of investigations. For instance, W tips can be used for non-spin-polarised measurements or Fe-coated W tips for spin-polarised measurements, in which the tip magnetisation direction can be controlled via the external magnetic field. For tips with a fixed magnetisation direction independent of the applied magnetic field and a negligible stray field, Cr-coated W-tips or bulk Cr tips can be utilised [Kubetzka *et al.*, 2002; Schlenhoff *et al.*, 2010]. Most measurements in this thesis were conducted using a bulk Cr tip, unless stated otherwise.

2.2. Sample Preparation

2.2.1. Ir(111)

All samples studied in this thesis are based on the Ir(111) crystal, which was initially cleaned and depleted of carbon contamination by repeated annealing cycles in an oxy-

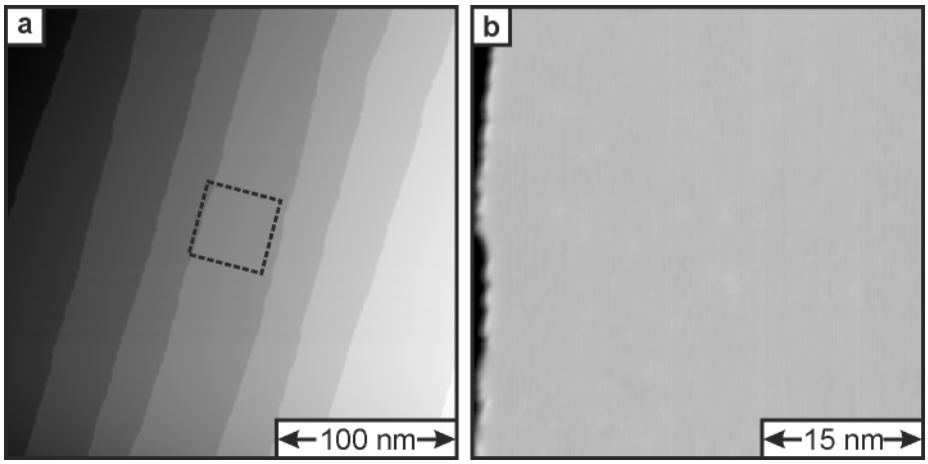

Figure 2.1.: Clean Ir(111)-substrate. a,b STM constant-current topography images of a typical Ir(111) substrate after the cleaning procedure as described in the text. **b** Image taken along rectangle indicated in **a**. Bulk Cr tip, $T = 4.2\,\mathrm{K}$, **a**: $U = +1\,\mathrm{V}$, $I_{\mathrm{set}} = 750\,\mathrm{pA}$, **b**: $U = +30\,\mathrm{mV}$, $I_{\mathrm{set}} = 3\,\mathrm{nA}$.

gen atmosphere of p_{O_2} in the range of 10^{-6} to $10^{-7}\,\mathrm{mbar}$. During the cycles the crystal temperature was continuously increased via electron beam heating to $T_{\mathrm{max}} \approx 1800\,\mathrm{K}$. To get rid of surface contaminations, the crystal was sputtered with Ar-ions ($U_{\mathrm{acc}} = 800\,\mathrm{V}$ at $p_{\mathrm{Ar}} \approx 9 \times 10^{-5}\,\mathrm{mbar}$ and a sputtering rate of around 3 ML/min) for approx. 10 min. Subsequently, the sample was annealed to about 1600 K for about 90 s to restore a smooth surface.

Such a clean Ir(111) substrate exhibits atomically flat terraces, separated by 1 ML high step edges, see Fig. 2.1. Depending on the substrate quality and the position on the crystal, the terraces can vary in width between a few nm and several hundred nm. Once, the Ir(111) crystal is sufficiently clean and free of carbon contaminations in a depletion zone near the surface, the initial annealing in an oxygen atmosphere need not be repeated for every preparation procedure.

2.2.2. Fe/Ir(111)

Each sample preparation in this thesis starts with Ar-sputtering and subsequent annealing of the Ir(111) crystal to about 1600 K for about 90 s. After a transfer of the sample to the evaporation chamber, lasting about 5 min, 0.7 to 1.0 ML of Fe was deposited by a standard electron-beam evaporator onto the warm surface at around 0.6 ML/min. Metal on metal growth is known to exhibit three main growth modes: (1) Volmer-Weber (VW) growth, i.e. 3D island growth; (2) Frank-van der Merwe (FvM) growth, i.e. layer-by-layer growth, and (3) Stranski-Krastanov (StKr) growth, i.e. 3D islands on top of one or a few epitaxial layers [Bauer, 1982]. The terrace size, the substrate temperature and the deposition rate can have an influence on the sample morphology. On the one hand, at a low deposition rate,

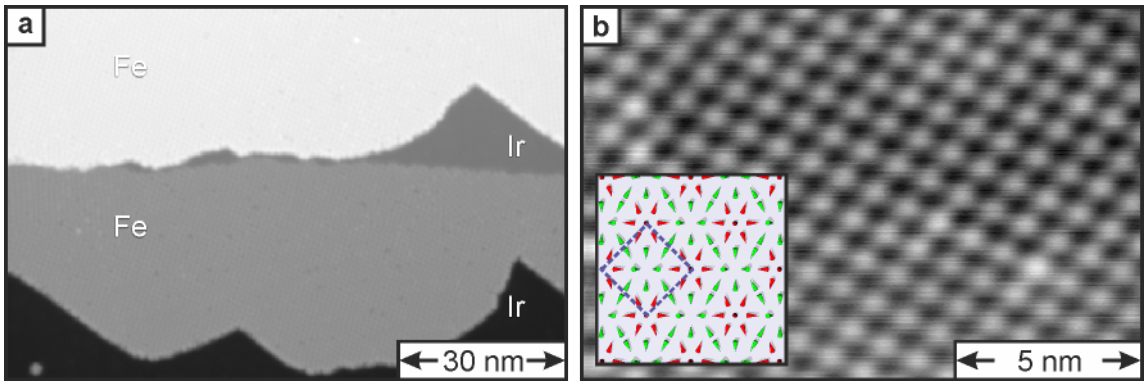

Figure 2.2.: Nanoskyrmion lattice in fcc Fe/Ir(111). a,b SP-STM constant-current images of a typical Fe/Ir(111) sample with approx. 0.8 ML fcc Fe. The inset in **b** shows the (commensurate) spin model of the nanoskyrmion lattice as derived in [Heinze *et al.*, 2011]. $I_{\text{set}} = 1\,\text{nA}$, $T = 4.2\,\text{K}$, **a**: $U = +50\,\text{mV}$, **b**: $U = +30\,\text{mV}$.

atoms arrive on the surface individually. If they are mobile at the substrate temperature, they randomly move around until they reach a step edge and get bound by the available substrate neighbours. In this step-flow growth, the adatoms mostly continue the same stacking as the sample. On the other hand, if more atoms arrive simultaneously and have more space for movement before reaching a step edge, they can bind with each other until they become stationary and thus form an island anywhere on a terrace and possibly in a different stacking than at a step edge.

Density functional theory (DFT) calculations showed that the hcp stacking of Fe is energetically preferred on the Ir(111) surface [von Bergmann *et al.*, 2007]. Section 5.2 shows such hcp Fe islands with a hexagonal nanoskyrmion lattice as ground state [von Bergmann *et al.*, 2015]. Nonetheless, the mobility of the Fe on the Ir(111) surface leads mostly to self-organised step flow growth in a FvM growth mode. The first layer of Fe then grows pseudomorphically, continuing the face centered cubic (fcc) stacking of the substrate [von Bergmann *et al.*, 2006], see Fig. 2.2a.

The magnetic state of fcc Fe/Ir(111) was previously shown by Heinze *et al.* to be a square nanoskyrmion lattice with a magnetic unit cell of $1\,\text{nm} \times 1\,\text{nm}$, see Fig. 2.2b. The system is characterised by a flat spin spiral energy dispersion driven by frustration of exchange interactions with a considerable amount of DMI originating from the Fe/Ir-interface. Since the dispersion is so flat, other higher order exchange interactions such as the biquadratic and the 4-spin-interaction also play a role in forming the highly non-collinear ground state, which does not react to external magnetic fields up to 9 T. [Heinze *et al.*, 2011; von Bergmann *et al.*, 2014]

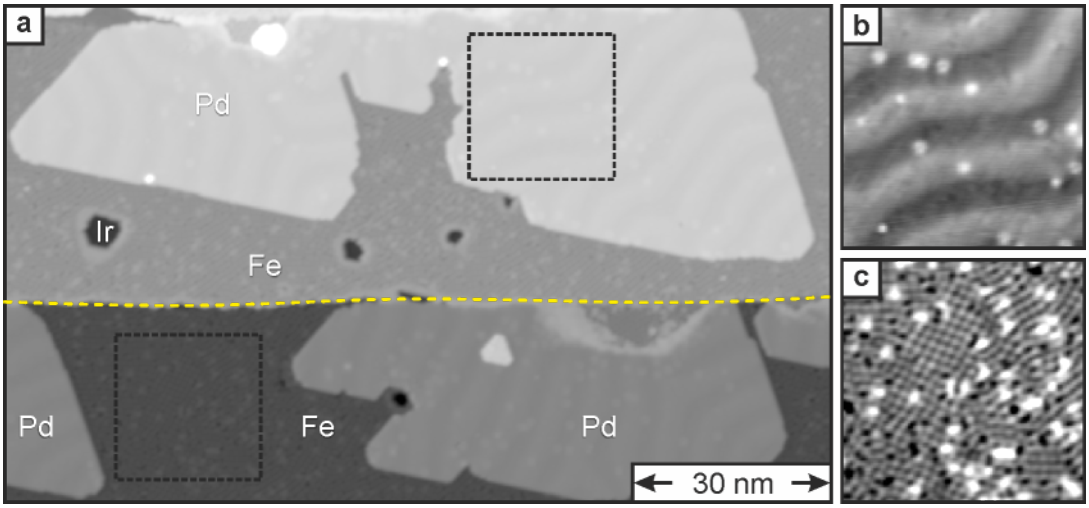

Figure 2.3.: Sample preparation of Pd/Fe/Ir(111). **a** SP-STM constant-current image of a Pd/Fe/Ir(111) sample, prepared as described in the text. The Pd islands are fcc stacked. The dashed yellow line marks a buried Ir step edge. **b,c** Zoom-ins of the image in **a** along the dashed rectangles with the contrast adjusted to ±20 pm. Bulk Cr tip, $T = 4.2\,\mathrm{K}$, $B = 0\,\mathrm{T}$, $U = +20\,\mathrm{mV}$, $I_{\mathrm{set}} = 300\,\mathrm{pA}$.

2.2.3. Pd/Fe/Ir(111)

In this thesis, one or two adlayer(s) of non-magnetic Pd or Rh are used to fine-tune the magnetic interactions in Fe/Ir(111). For this, a standard sample preparation of Fe/Ir(111) as described in the previous section is continued by subsequently depositing the desired amount of the respective element by MBE.

Figure 2.3 shows an SP-STM image of a Pd/Fe/Ir(111) sample with approx. 0.5 ML of Pd evaporated in direct subsequence to the Fe deposition. On the Fe/Ir(111) in Fig. 2.3, the nanoskyrmion lattice is visible similarly to Fig. 2.2, although the domains are much smaller (seemingly due to the defects). The stripes on the Pd islands in Fig. 2.3 result from the SS ground state, which will be described in Section 3.1.

Mostly, the Pd also exhibits FvM growth in either stacking and forms islands consisting of a single atomic layer with only small DL islands on top. Based on atomic resolution STM images, it is possible to identify the stacking of Pd by their relative $\mathrm{d}I/\mathrm{d}U$ signals [Hanneken, 2015]. For instance, at $U = +700\,\mathrm{mV}$, the fcc stacking always appears brighter in $\mathrm{d}I/\mathrm{d}U$-maps than the hcp stacking. The assignment of the Pd stacking throughout this thesis is based on those previous results. On a sample prepared as described above, the fcc stacking occurs with much higher probability.

Besides the three main growth modes described above, modified growth modes due to interfacial alloying or intermixing are possible [Rousset *et al.*, 1992; Pleth Nielsen *et al.*, 1993; Saßmannshausen, 2016]. Indications for intermixing can be seen in the zoom-ins in Fig. 2.3 as the clearly visible bright defects. These are attributed to single Pd atoms in

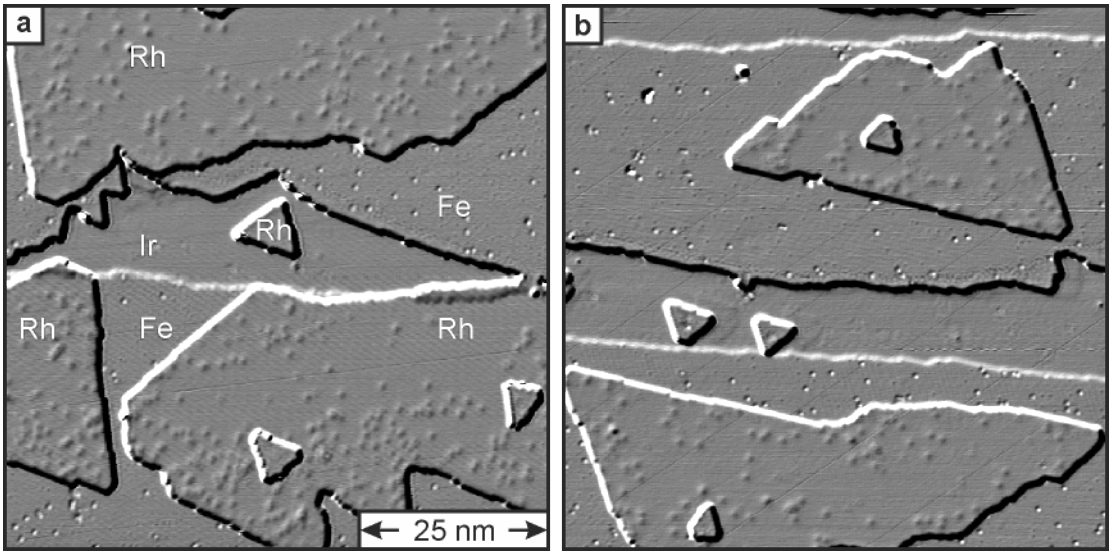

Figure 2.4.: Rh/Fe/Ir(111) - defects due to intermixing. **a,b** Topography maps of Rh/Fe/Ir(111) samples prepared as described in the text (Differentiated in x- and $-y$-direction). Rh deposited 5 min (a) and 20 min (b) after the Fe deposition. W tip, $T = 8\,\mathrm{K}$, **a**: $U = +700\,\mathrm{mV}$, $I_{\mathrm{set}} = 2\,\mathrm{nA}$, **b**: $U = +600\,\mathrm{mV}$, $I_{\mathrm{set}} = 1.5\,\mathrm{nA}$.

the Fe layer or Fe atoms in the Pd layer [Hanneken *et al.*, 2016]. Jonas Saßmannshausen showed that the tendency for intermixing is element- and temperature-dependent. For the example of Pb on Fe/Ir(111), a disordered, alloyed phase is obtained when depositing Pb at room temperature, whereas a temperature of 140 K during the deposition leads to highly ordered growth of Pb on the iron [Saßmannshausen, 2016]. To reduce intermixing effects for Pd or Rh on Fe/Ir(111), it is sufficient to let the sample cool down at room temperature for about 1 h before depositing the desired amount of Rh or Pd.

If many but small islands are required, additional cooling before and during the deposition leads to even less mobility and more nucleation centres for islands. Because of this reduced mobility of Rh and Pd at lower temperature, the resulting islands may not develop the desired size and shape. This can be overcome by slightly heating the sample after the deposition. Hence, the islands become mobile again and can reshape to the energetically most preferred shape, which often includes long and straight edges along the high symmetry directions. During this post-annealing process, intermixing is suppressed, because the Rh or Pd is already bound in islands. Such well-defined, small Pd islands with little intermixing can be seen in Chapter 6.

2.2.4. Rh/Fe/Ir(111)

The preparation of Rh/Fe/Ir(111) samples is similar to the preparation of Pd/Fe/Ir(111) samples as described in the section above. After the preparation of step-flow grown Fe/Ir(111) as described above, roughly half a ML of Rh is deposited subsequently.

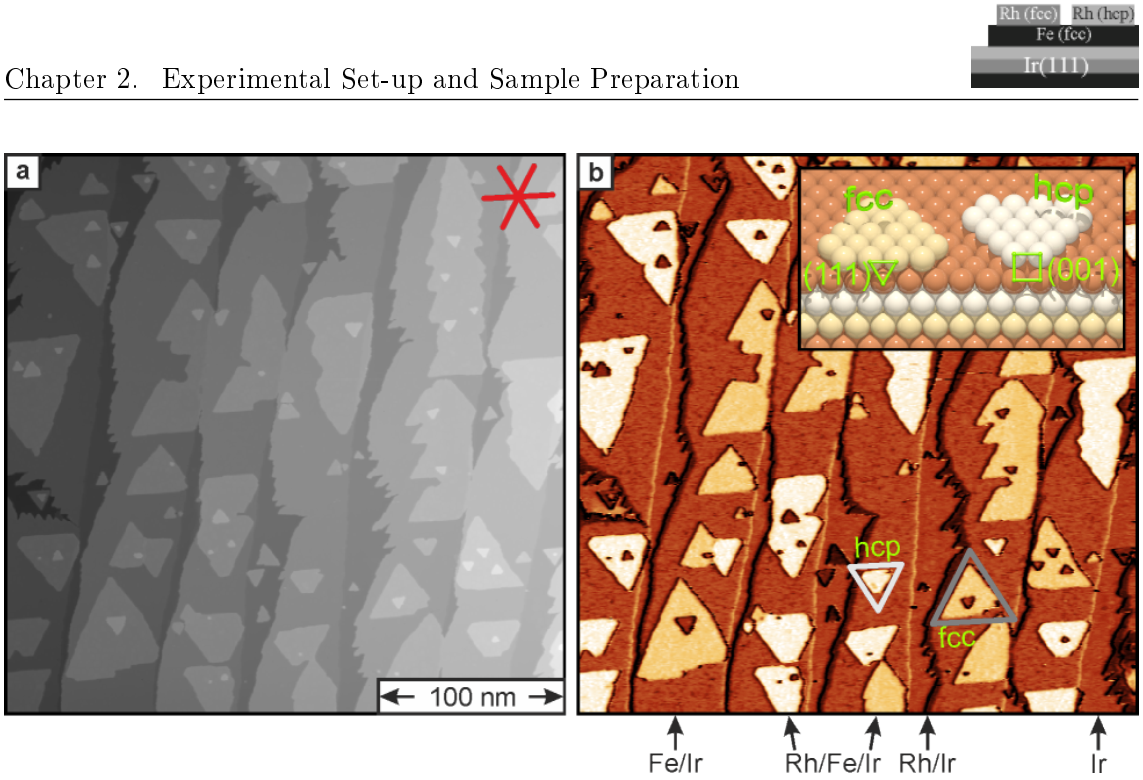

Figure 2.5.: Stacking of Rh/Fe/Ir(111). **a** STM constant-current topography image of a typical Rh/Fe/Ir(111) sample with approx. 0.8 ML Fe and 0.4 ML Rh. Red lines mark the $\langle 1\bar{1}0 \rangle$ directions (close-packed rows), as obtained from straight island edges. **b** $\mathrm{d}I/\mathrm{d}U$-map recorded simultaneously to the image shown in **a**. Inset shows a ball model sketch of triangular fcc and hcp Rh/Fe islands. Different edge coordinations are indicated by the triangle and rectangle. W tip, $T = 8\,\mathrm{K}$, $U = +500\,\mathrm{mV}$, $I_{\mathrm{set}} = 750\,\mathrm{pA}$, $U_{\mathrm{mod}} = 50\,\mathrm{mV}$.

Figure 2.4 shows differentiated topography maps of such Rh/Fe/Ir(111) samples, with the Rh deposited 5 min (a) and 20 min (b) after the Fe deposition. Comparing the number of defects due to intermixing in Fig. 2.4a to the amount of defects in Fig. 2.3 indicates that the tendency to intermix with the Fe is higher for Rh than for Pd. Comparing Fig. 2.4a to Fig. 2.4b suggests that the intermixing is reduced for a lower temperature during the deposition of Rh. Besides the slightly different tendency to intermix, the morphology of the Rh/Fe/Ir(111) samples is similar to the one of Pd/Fe/Ir(111) samples: The Rh exhibits mostly growth of ML islands with small DL islands on top.

Figure 2.5a shows the topography and Fig. 2.5b a simultaneously recorded differential tunnelling conductance ($\mathrm{d}I/\mathrm{d}U$)-map of a Rh/Fe/Ir(111) sample. At this bias voltage, the Fe and Ir have a similar $\mathrm{d}I/\mathrm{d}U$-signal. However, there are two clearly distinguishable contrast levels for the Rh islands on the Fe stripes, accompanied by triangular shapes either pointing up or down. This indicates pseudomorphic growth and the different levels are caused by the electronic difference due to the two possible stackings of the Rh. Their triangular and not hexagonal island shapes are caused by the two inequivalent types of edges ((001)-like and (111)-like), see inset of Fig. 2.5b. The two edge types possess different diffusion energies [Müller *et al.*, 2005]; this leads to a preference of one type of edge. As evident from the inset in Fig. 2.5b, straight island edges can be used to determine the

crystallographic $\langle 1\bar{1}0 \rangle$ directions (or close-packed rows), which are marked by red lines in Fig. 2.5a. The fact that we observe both stackings with similar probability indicates similar energies of the two stackings. To assign the stackings of Rh to either fcc or hcp, we have to consider island shapes and, since it was not possible to determine the stacking directly from atomic resolution on the Rh, make two assumptions. (i) We assume that the Rh connected to the Fe on the Ir surface continues the fcc stacking of the Fe. The same $\mathrm{d}I/\mathrm{d}U$-signal, as obtained for these fcc Rh stripes, is obtained on freestanding, up-pointing islands of Rh on Ir, which are thus also fcc. Down-pointing Rh/Ir islands with higher $\mathrm{d}I/\mathrm{d}U$-signal are hcp-stacked. (ii) The fcc (hcp) Rh islands on the Fe prefer the same type of edge as on the Ir and thus also point up (down). Based on these two assumptions, we conclude that the fcc (hcp) Rh/Fe/Ir(111) islands in Fig. 2.5b correspond to a lower (higher) $\mathrm{d}I/\mathrm{d}U$-signal at $U = +500\,\mathrm{mV}$. This knowledge is used to assign the Rh stacking throughout Chapter 7.

Chapter 3.

Discovery and Manipulation of Individual Skyrmions

After the first prediction of magnetic skyrmions, see Section 1.1.3 and Chapter 4, in 1989 [Bogdanov and Yablonsky, 1989], they were first observed experimentally as a lattice phase in 2009 using neutron scattering on the helical magnet B20 compound MnSi [Mühlbauer *et al.*, 2009]. Subsequently, these magnetic skyrmion lattices were also investigated in real space [Yu *et al.*, 2010], including observations of individual skyrmions (called diluted skyrmion lattice phase by Yu *et al.*) in a helical magnet [Yu *et al.*, 2010; Pfleiderer and Rosch, 2010].[1] This chapter is dedicated to the first observation of interface-induced magnetic skyrmions in the sample system of ultrathin PdFe films on Ir(111). Whereas the exact spin structure of isolated magnetic skyrmions will be explored in more detail in Chapter 4, this chapter focusses on the ability of the STM tip to manipulate skyrmions individually and independently, in close vicinity to one another. Different contributions playing a role in the switching process are investigated performing repetitive switching experiments in Section 3.3. Parts of the results in this chapter originate from my master thesis [Romming, 2013] and were published in the collaborative work [Romming *et al.*, 2013].

3.1. Magnetic Field Dependent Phase Transitions in Pd/Fe/Ir(111)

As shown in Chapter 2, well-defined islands of Pd can be grown pseudomorphically on a clean Fe/Ir(111) sample by MBE. It will be shown in this chapter and especially in Chapter 5, that Pd, being a non-magnetic material in its elementary form, gets polarised by the Fe [Weber *et al.*, 1991] and significantly influences the magnetic interactions in the resulting PdFe bilayer. Using a bulk Cr tip for SP-STM measurements on a Pd/Fe/Ir(111) sample, prepared as described in Chapter 2, leads to the observation of stripe patterns on the Pd islands with a period of $\lambda \approx 6\,\mathrm{nm}$, see Fig. 3.1a,g. Upon application of an ex-

[1] A more thorough literature overview of international publications about skyrmions is given in Section 4.4, also putting the work presented in this chapter and in Chapter 4 into perspective.

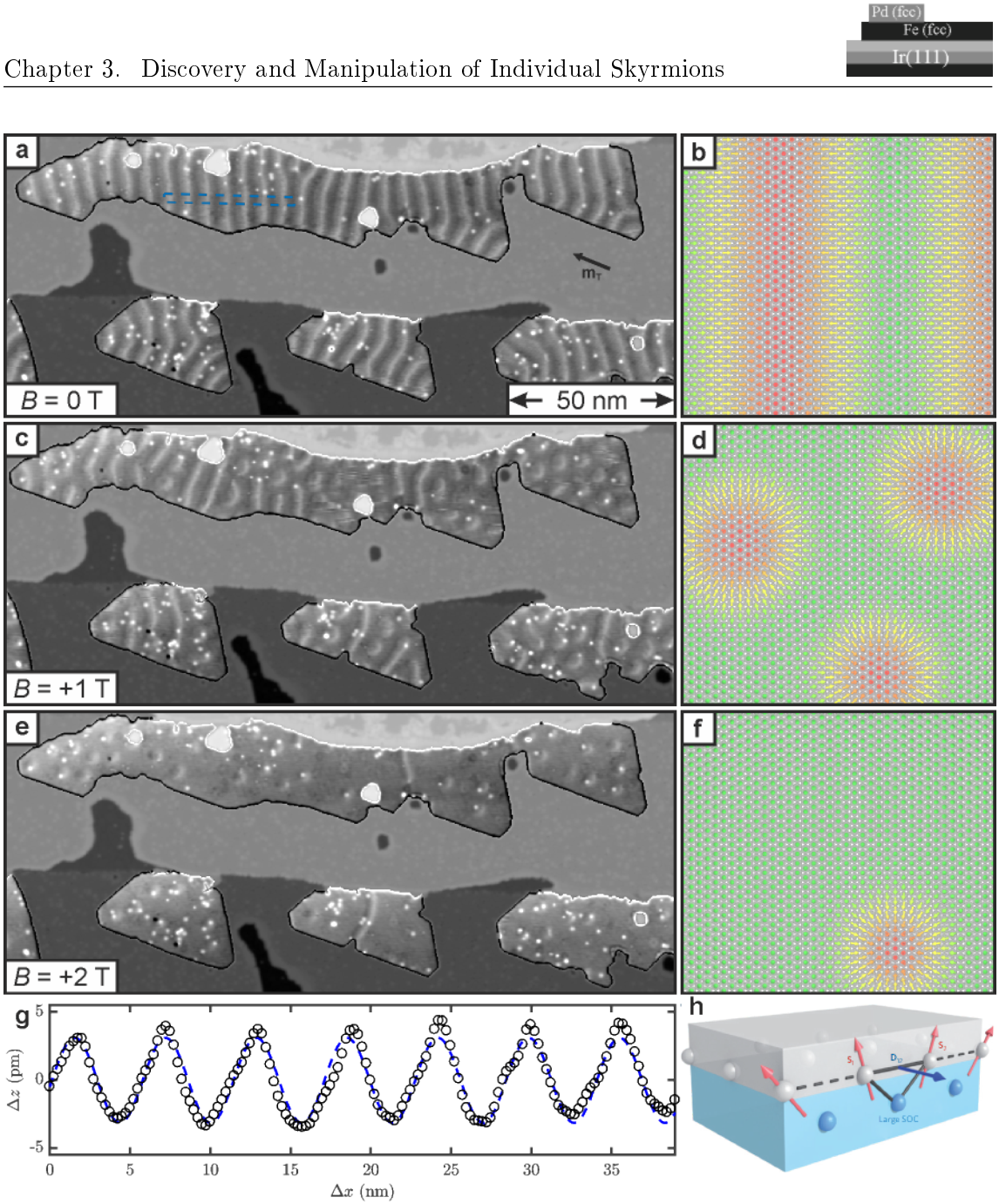

Figure 3.1.: Magnetic field dependence of Pd/Fe/Ir(111). a,c,e SP-STM images of fcc stacked Pd islands on Fe/Ir(111) with the contrast adjusted locally to ±15 pm. Bulk Cr tip with canted magnetisation direction mostly IP as depicted by the arrow in **a**, $T = 4.2\,\mathrm{K}$, $U = +50\,\mathrm{mV}$, $I_{\mathrm{set}} = 500\,\mathrm{pA}$. **b,d,f** Sketches of a spin spiral, SkX and FM with a single skyrmion, respectively. Spins have actual atomic distances. **g** Line profile along dashed rectangle in **a**. Dashed line is a cosine-fit as guide to the eye. **h** Sketch of DMI at the interface between a ferromagnetic metal (grey) and a metal with a strong SOC (blue). The DMI vector D_{12} related to the triangle composed of two magnetic sites and an atom with a large SOC is perpendicular to the plane of the triangle, reprinted by permission from Macmillan Publishers Ltd: [Fert *et al.*, 2013, Fig. 1f], copyright (2013).

ternal magnetic field B, perpendicular to the surface, the observed structure changes, see Fig. 3.1c, demonstrating its magnetic origin. Figure 3.1c, recorded at $B = +1\,\mathrm{T}$, permits additional observations: Upon the application of an external magnetic field, areas parallel to the field expand, separated by single stripes and round entities, which all show a lower spin-polarised signal on their left side and a higher signal on their right side for this tip. This can only be explained for a tip with an IP magnetisation component and proves that the rotation of the local magnetisation direction has a unique rotational sense. The only interaction known for imposing a unique rotational sense on non-collinear magnetic structures is the DMI, see Section 1.1.1, [Dzyaloshinskii, 1957; Moriya, 1960]. Since it originates from spin–orbit scattering of electrons in an inversion-asymmetric crystal field, it becomes especially important for magnetic thin films on heavy substrates [Fert, 1990; Fert *et al.*, 2013]. From symmetry considerations, it can be deduced that the Dzyaloshinskii-Moriya-vector must be IP and perpendicular to the connecting line between interacting spins, see Fig. 3.1h [Moriya, 1960; Fert, 1990; Fert *et al.*, 2013]. The resulting spin structures therefore have a Néel-type, cycloidal character. Although the rotational sense cannot be deduced from this data, DFT calculations [Dupé *et al.*, 2014] and experiments using a vector magnetic field [Schmidt *et al.*, 2016] showed that it is as sketched in Fig. 3.1b,d,f.

From these considerations and in comparison to earlier work [Bode *et al.*, 2007; Ferriani *et al.*, 2008; Meckler *et al.*, 2009], the origin of the periodic stripe pattern in the Pd islands without an applied magnetic field is assumed to be a cycloidal SS, see sketch in Fig. 3.1b. This explanation of the periodic stripes in SP-STM images with cycloidal SSs also matches the observation of varying corrugation amplitudes for different propagation directions, recorded with an IP tip, see Fig. 3.1a. A propagation of the spin spirals parallel to the tip direction leads to the maximal contrast, a propagation perpendicular to the tip direction leads to a vanishing projection of the sample spins onto the tip direction and thus to no contrast in the SP-STM image. The deduced magnetisation direction of the tip in the plane is marked by the arrow in Fig. 3.1a. From the fact that the bright and the dark parts in the SP-STM images are not symmetric, see e.g. Fig. 3.1c,e, it can be deduced that the tip must also have a (small) OOP magnetisation component.

With the knowledge about the tip's spin direction, the direction of the magnetic field and the fact that the spin structure must have a Néel-type character with a unique rotational sense, it is possible to also find out what the observed magnetic structures at higher magnetic field must resemble. The left-over stripes in Fig. 3.1c and e are attributed to 360°-DWs, see Section 1.1.3, and the round entities must be magnetic skyrmions with their center pointing opposite to the external magnetic field, see see sketch in Fig. 3.1d and f. Whereas Fig. 3.1c at $B = +1\,\mathrm{T}$ shows a mixed phase of 360°-DWs and a SkX (see sketch in Fig. 3.1d), at $B = +2\,\mathrm{T}$ (Fig. 3.1e) most of the PdFe island is aligned ferromagnetically along the magnetic field with a small number of individual magnetic skyrmions present,

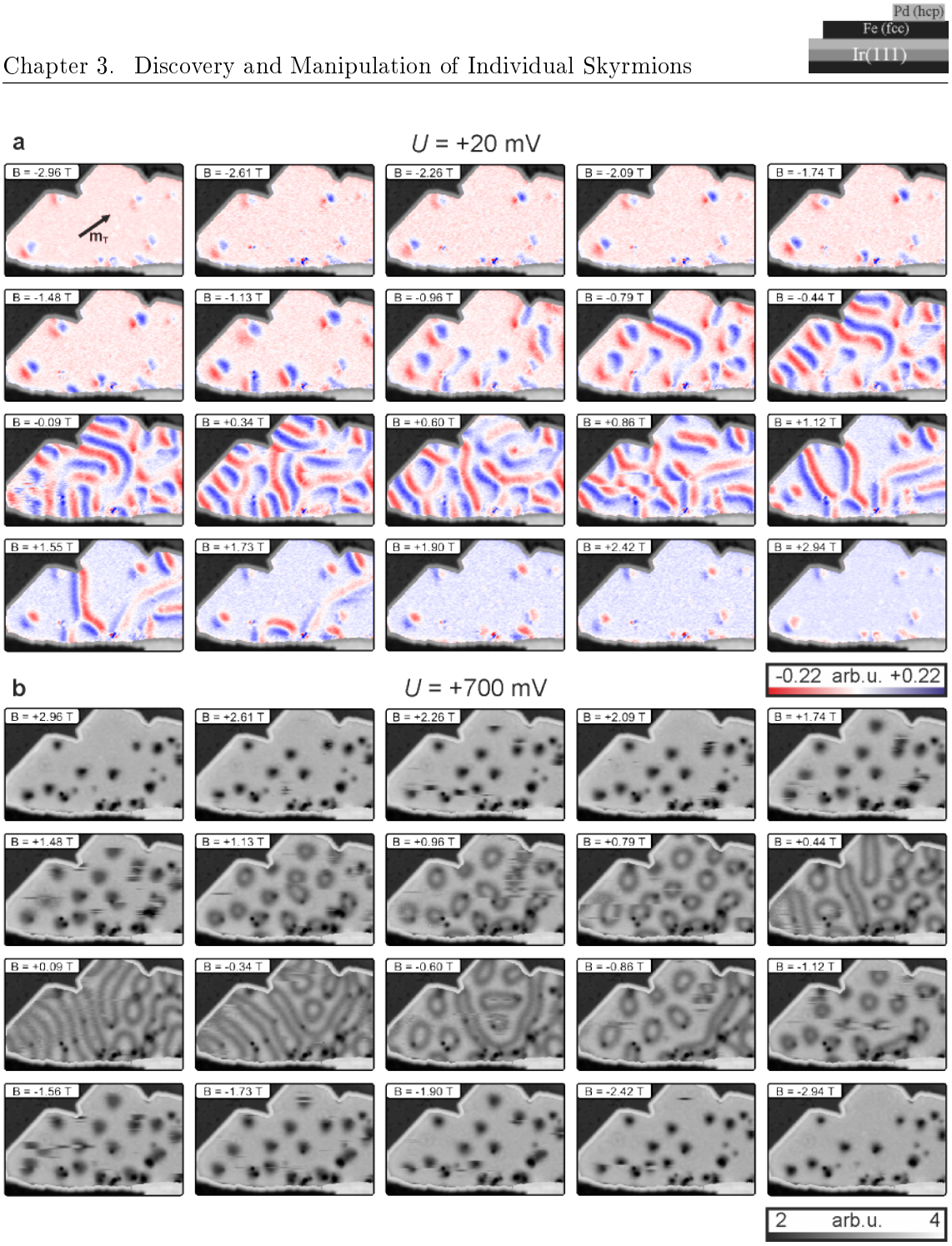

Figure 3.2.: Influence of bias voltage in Pd/Fe/Ir(111). a SP-STM based difference $\mathrm{d}I/\mathrm{d}U$ image series (calculated by subtracting the non-magnetic reference image (mean of data at highest positive magnetic field and data at highest negative magnetic field)) taken during a continuous sweep of the magnetic field from $B = -3.0\,\mathrm{T}$ to $B = +3.0\,\mathrm{T}$ at approx. 87 mT/image. Bulk Cr tip with canted magnetisation direction mostly IP as depicted by the arrow in the first image, $U = +20\,\mathrm{mV}$, $I_{\mathrm{set}} = 2\,\mathrm{nA}$, $U_{\mathrm{mod}} = 2.4\,\mathrm{mV}$. **b** Series of $\mathrm{d}I/\mathrm{d}U$-maps of the same island during another sweep of the magnetic field from $B = +3.0\,\mathrm{T}$ to $B = -3.0\,\mathrm{T}$, recorded with the same tip, but at a higher bias showing the NCMR contrast. $U = +700\,\mathrm{mV}$, $I_{\mathrm{set}} = 2\,\mathrm{nA}$, $U_{\mathrm{mod}} = 40\,\mathrm{mV}$. The duration of one complete sweep was about 9 h. The Pd island shown here is hcp stacked, see Section 2.2.3. $T = 4.2\,\mathrm{K}$.

mostly pinned at defects in the film (see sketch in Fig. 3.1f). The exact spin structure of the isolated skyrmions, which are observed for the first time in this sample, will be investigated in more detail in Chapter 4. More details on the phase transition field between the SS, SkX and FM phase and on other characteristic differences, depending on the stacking of the Pd, will be presented in Chapter 5.

The main focus of this chapter is the controlled manipulation of the particle-like, isolated skyrmions with the STM tip. For that, it is necessary to have the ability to perform non-disturbing measurements of the sample on the one hand, and to efficiently influence the magnetic structure on the other hand. Figure 3.2 shows the magnetic field dependent evolution of the magnetic structure in one hcp PdFe island during two separate, continuous sweeps of the external magnetic field between $\pm 3\,\mathrm{T}$. The upper series of images was taken with a low bias voltage of $U = +20\,\mathrm{mV}$ after sweeping the field down to $B = -3\,\mathrm{T}$, whereas the lower series was recorded using a higher bias voltage of $U = +700\,\mathrm{mV}$ directly after the upper series with the same tip. Two main differences are important when regarding the images: (i) The images of the low bias series are dominated by the spin-polarised signal that originates from the projection of the sample spins and the fixed spin direction of the tip (TMR), whereas in the high bias series the contrast is caused by a difference in non-collinearity due to the NCMR, see Section 1.2. The skyrmions thus appear in a doughnut-like shape at low $|B|$ and as dark dots at higher $|B|$. It should be noted here that due to the exact knowledge of the skyrmion size and shape as a function of magnetic field, which will be shown in Chapter 4, it was possible to distinguish this novel magnetoresistance NCMR from the TAMR [Hanneken *et al.*, 2015; Hanneken, 2015; Kubetzka *et al.*, 2017]. (ii) The low bias series in Fig. 3.2a depicts mostly undisturbed, stable magnetic structures with only occasional switching events, which are caused by the changing magnetic field, visible as abrupt changes between scan lines. On the contrary, the high bias series in Fig. 3.2b shows many of these switching events of skyrmions, even in the course of single images. This demonstrates the significant influence of the scanning tip on the magnetic structures at high bias, because the chosen voltage is the only tunnel parameter changed between the two series.

As a result of the manipulating effect of the tip at high bias, another key difference between the two series becomes apparent. Whereas at high bias, the magnetic structures qualitatively resemble each other at $\pm B$ for equal $|B|$, at low bias considerable hysteresis effects can be observed. For instance at low bias, at $|B| \approx 1.1\,\mathrm{T}$ the PdFe island exhibits single skyrmions in a FM background ($B = -1.13\,\mathrm{T}$) when coming from high $|B|$. At $B = +1.12\,\mathrm{T}$ (coming from zero field), the image shows a mixed phase of 360°-DWs, single skyrmions and the FM background. During the whole series, no SkX appears. At high bias, the corresponding images both qualitatively depict the same magnetic state with several skyrmions in the FM background, suggesting vanishing hysteresis. Similar examples can be

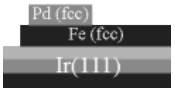

found at different magnetic fields. This can be explained by a finite energy barrier between the different magnetic states that is not overcome at the low temperature of $T = 4.2\,\mathrm{K}$ and while applying low bias voltage, but the application of high bias provides a scheme for overcoming energy barriers between the topologically different states (see Chapter 6 for a more detailed discussion of the topology of skyrmionic magnetic states). Generally, the number of skyrmions during the high bias series in Fig. 3.2b is higher than at low bias voltage in Fig. 3.2a.

3.2. Writing and Deleting Single Magnetic Skyrmions

This combination of hysteresis at low temperature leading to meta-stable magnetic states and the ability to overcome energy barriers and therefore manipulate skyrmions by high bias voltage applied to the tip is now used in a more controlled fashion to create skyrmions individually and localised. For this, the upper Pd island shown in Fig. 2.3a is first brought into a FM state by ramping the magnetic field up to $+3\,\mathrm{T}$ (Fig. 3.3a) and then to a meta-stable mostly FM state by setting the magnetic field to $B = +1.8\,\mathrm{T}$.

The resulting magnetic state is shown in Fig. 3.3c. Most of the PdFe island is ferromagnetically aligned with the magnetic field with only very few skyrmions left, pinned at clearly visible defects. The local potential landscape of the skyrmion state and the FM state can be pictured as an asymmetric double well potential as depicted in Fig. 3.3b. Of the two states, which are separated by an energy barrier, the skyrmion state (1) is favoured at lower magnetic fields, whereas at higher magnetic fields, the FM state (0) is preferred[2]. If the available energy by thermal fluctuations or by the STM tip is not sufficient to overcome this barrier, meta-stable configurations do not decay. Starting from Fig. 3.3c, the tip is sequentially positioned at the locations of the circles depicted in Fig. 3.3c and the bias voltage is ramped up while keeping the current constant. The resulting $\mathrm{d}I/\mathrm{d}U$ spectroscopy curves, consisting of the up-sweep (blue lines) and down-sweep (red lines) of the bias, are shown in Fig. 3.3e. Whereas in the first bias-sweep, there is no change detectable between the up- and down-sweep, in the second sweep, a clear jump in the differential tunnelling conductance is visible in the down-sweep. The subsequently recorded image in Fig. 3.3f shows that the origin of this jump is the creation of a skyrmion at the position of the second bias-sweep. Additionally, another skyrmion was created, which now resides above the position of the first bias sweep. A possible explanation for this is that also during the first sweep, a skyrmion was created but it immediately moved away from the

[2] The preferred state does not necessarily need to be the energetically lower state due to the asymmetry of the potential landscape. It was shown in collaboration with Hagemeister *et al.* that a considerable difference in attempt frequencies of the two switching directions (e.g. due to the different entropies of the two states) can make them equally probable, despite a difference in the energies of the states [Hagemeister *et al.*, 2015].

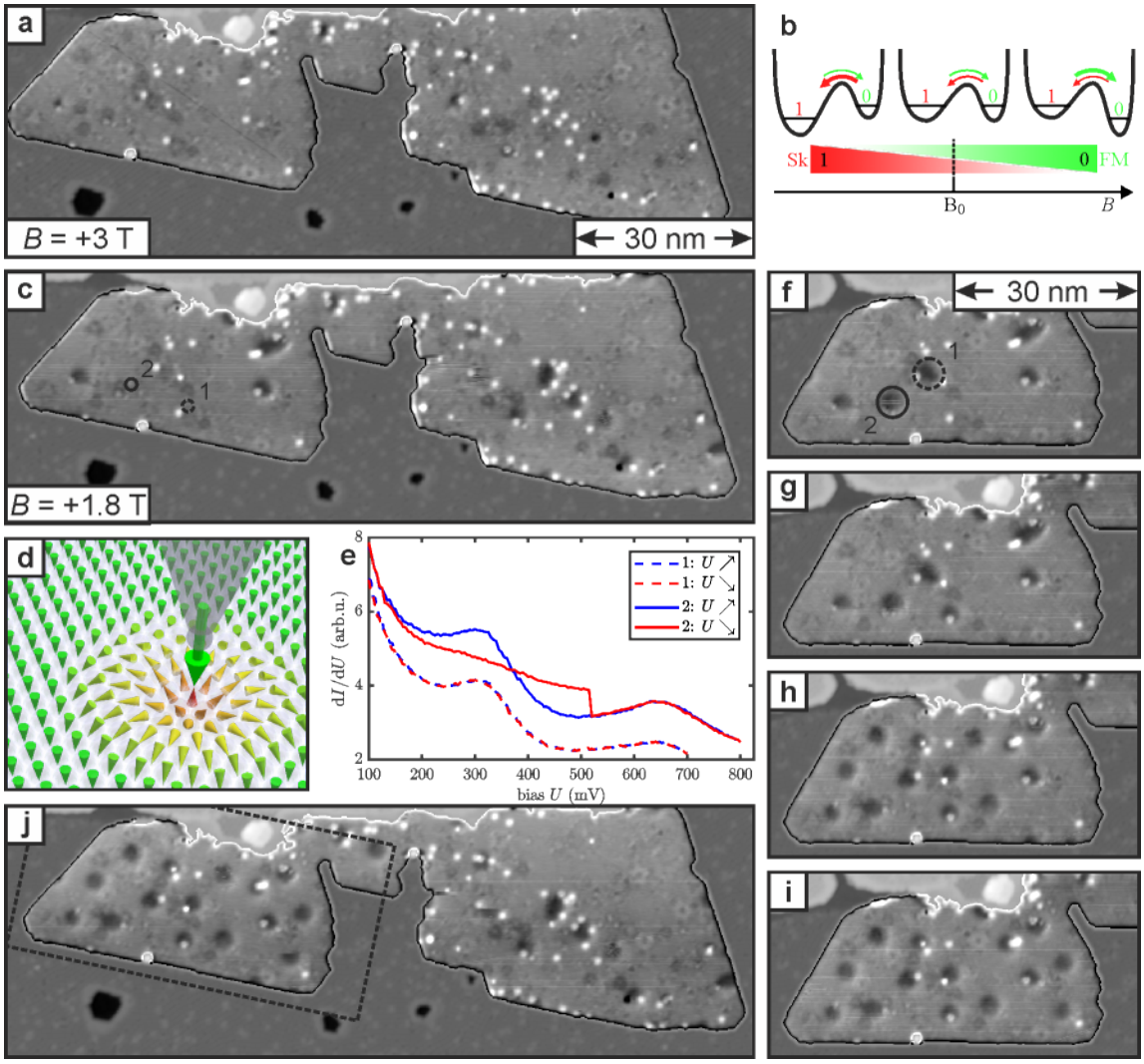

Figure 3.3.: Writing single skyrmions in Pd/Fe/Ir(111). **a,c,f-j** SP-STM images with the contrast adjusted locally to ±15 pm. **f-i** are taken along dashed rectangle in j. Bulk Cr tip with mostly OOP alignment, $T = 4.2\,\mathrm{K}$, $I_{\mathrm{set}} = 1\,\mathrm{nA}$, $U = +70\,\mathrm{mV}$, **a**: $U = +20\,\mathrm{mV}$, **c**: $U = +100\,\mathrm{mV}$. **b** Sketch of the potential landscape of skyrmion and FM. **d** Sketch of the SP-STM tip located over a magnetic skyrmion. **e** $\mathrm{d}I/\mathrm{d}U$ spectroscopy curves ($I = 1\,\mathrm{nA}$), consisting of the up-sweep (blue line) and down-sweep (red line) of the bias. The tip was positioned at the corresponding circles marked in **c**. Spectrum 2 is vertically shifted by $+1\,\mathrm{arb\,u}$. $U_{\mathrm{stab}} = +100\,\mathrm{mV}$, $U_{\mathrm{mod}} = 15\,\mathrm{mV}$. The circles in **f** mark the corresponding written skyrmions.

tip position to the pinning defects above. Due to the low time-resolution of the STM, the creation was not captured in the corresponding spectroscopy curve.

In between the subsequent image series in Fig. 3.3g-i, similar bias sweeps were performed at various positions on the island with similar spectra (not shown). The result is the controlled population of that part of the island with several skyrmions. Figure 3.3j shows

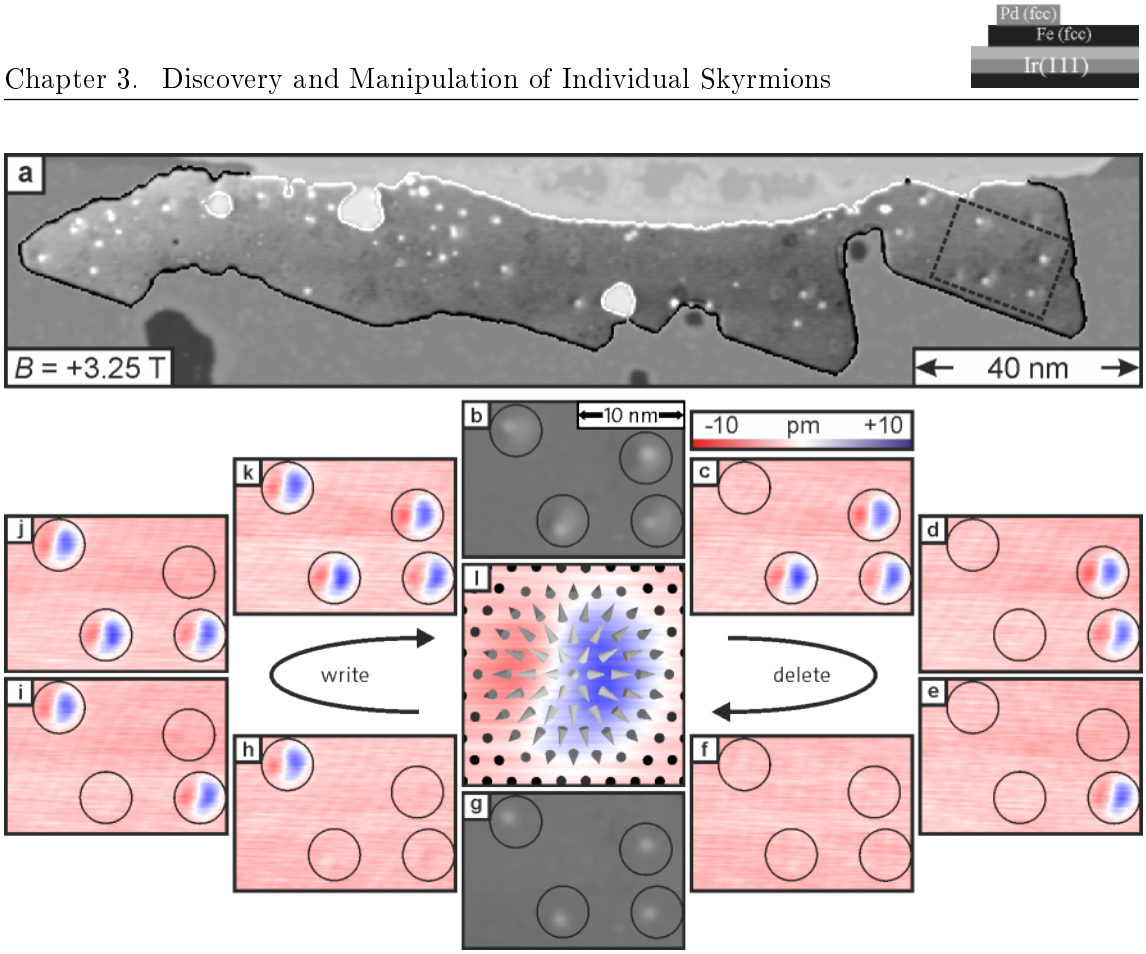

Figure 3.4.: Writing and deleting single magnetic skyrmions. **a** SP-STM image of an fcc Pd island on fcc Fe/Ir(111) with the contrast adjusted locally to ±15 pm. Bulk Cr tip with mostly IP alignment, $T = 4.2\,\mathrm{K}$, $I_{\mathrm{set}} = 500\,\mathrm{pA}$, $U = +100\,\mathrm{mV}$. **b** SP-STM image of the area marked in **a** with four defects, each hosting one skyrmion marked by a circle containing about 270 surface atoms. $I_{\mathrm{set}} = 1\,\mathrm{nA}$, $U = +250\,\mathrm{mV}$. **c-f,h-k** Sequences of difference SP-STM images (with respect to **g**, subsequently shifted in z to equalise the absolute maximal and minimal contrast) showing the selective annihilation and creation of the four skyrmions. **g** Same area as in **b**, but without skyrmions. **l** Schematic spin configuration with distances twice the atomic lattice, superimposed on the experimental data. Figure adapted from [Romming *et al.*, 2013, Fig.3].

the same area of the sample as in Fig. 3.3c, but after the sequence of writing skyrmions within the area, marked by the dashed rectangle. As evident from the unchanged state of the magnetic structure in the rest of the island, skyrmions were only created within the marked part of the island, where a higher bias was applied between tip and sample. This also demonstrates the absence of the spontaneous creation of skyrmions by thermal fluctuations during the writing sequence, which lasted about 3 hours.

For the use of skyrmions in storage devices, they need to be written, but also deleted in a controlled fashion. To have both the skyrmion and FM states meta-stable, a higher magnetic field is needed, compare Fig. 3.3b. Figure 3.4 shows how writing and deleting can be done at a fixed magnetic field by voltage/current ramps. The island that was also shown in

Fig. 3.1 up to a magnetic field of +2 T, is now depicted in Fig. 3.4a at $B = +3.25\,\mathrm{T}$. Most of the island is aligned ferromagnetically with the external magnetic field, except for a few isolated skyrmions located at atomic defects. Figure 3.4b shows a closer view of the area marked by the dashed rectangle in Fig. 3.4a with four pinning defects, each hosting one skyrmion. By locally injecting higher energy electrons during voltage sweeps with the tip held stationary inside the encircled areas, any desired skyrmion configuration for the four pinning sites can be generated. In the series of difference SP-STM images in Fig. 3.4c-f, the skyrmions are annihilated one by one until no skyrmion is present (Fig. 3.4g). Skyrmions are then created in a different sequence until the starting configuration is restored (Fig. 3.4h-k). The voltage sweeps were performed between +250 mV and +750 mV at a constant height, simultaneously causing an increase in current, which - as will be shown in the next section - leads to a more efficient manipulation of the magnetic state.

3.3. Exploration of the Switching Mechanism

So far it was shown that non-disturbing measurements of skyrmions are possible using low bias and current, whereas they can be manipulated at higher bias voltage and current. To disentangle the different contributions to the switching process, measurements were performed as a function of bias voltage U, tunnel current I and applied magnetic field B. While keeping the lateral tip position stationary via atom tracking at a defect hosting a skyrmion, see Tip#1 in Fig. C.2, the time-dependent tip height z and $\mathrm{d}I/\mathrm{d}U$-signal can be recorded. Due to the continuous, probabilistic switching between the two states, the time-dependent $\mathrm{d}I/\mathrm{d}U$ signals resemble a telegraph noise signal, see Fig. 3.5a,c. The signals, typically consisting of more than 1000 switching events, can be analysed regarding their asymmetry by fitting two Gauss-curves to the histogram graphs of the data, see Fig. 3.5b,d:

$$R(x) = \frac{a_1}{\sigma_1\sqrt{2\pi}} \cdot \exp\left(-\frac{(x-\mu_1)^2}{2\sigma_1^2}\right) + \frac{a_0}{\sigma_0\sqrt{2\pi}} \cdot \exp\left(-\frac{(x-\mu_0)^2}{2\sigma_0^2}\right) \tag{3.1}$$

with the prefactors a_i, variances σ_i^2 and expectation values μ_i. The relative occupation of the skyrmion state (skyrmion probability) can be calculated as:

$$P_{\mathrm{Sk}} = \frac{a_1}{a_1 + a_0} \tag{3.2}$$

or by simply counting all the datapoints of the normalised telegraph signal higher than 0.5 (N_{Sk}) and lower than 0.5 (N_{FM}):

$$P_{\mathrm{Sk}} = \frac{N_{\mathrm{Sk}}}{N_{\mathrm{Sk}} + N_{\mathrm{FM}}} \tag{3.3}$$

Another characteristic property that can be extracted from the telegraph signals is the

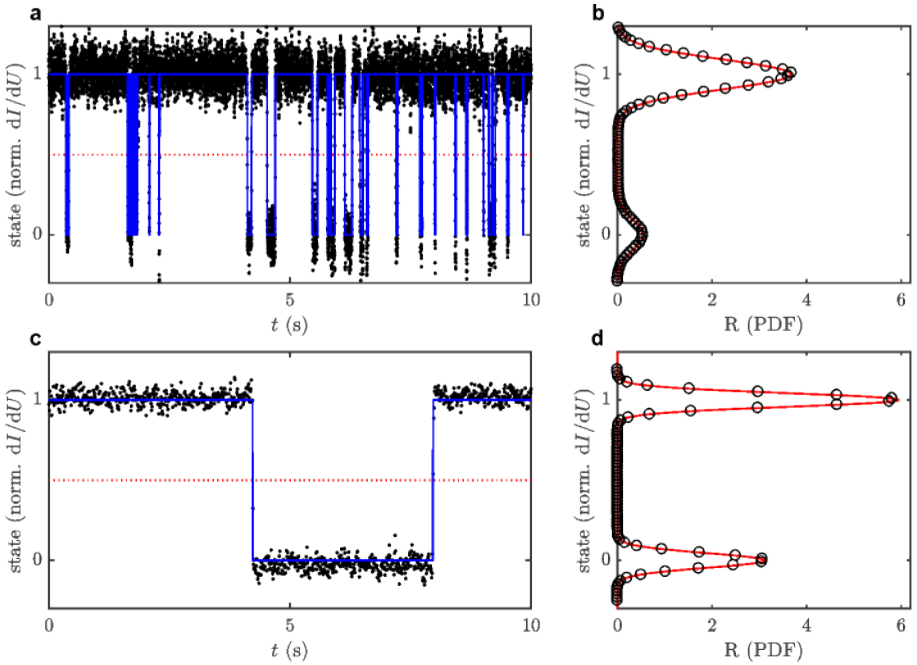

Figure 3.5.: Exploration of the switching mechanism: telegraph noise. a,c Time-dependent switching signal, recorded on a defect hosting a skyrmion in fcc Pd/Fe/Ir(111), see Tip#1 in Fig. C.2, at $U = +750\,\mathrm{mV}$ (a) and $U = +400\,\mathrm{mV}$ (c), $I_{\mathrm{set}} = 300\,\mathrm{nA}$, $T = 4.2\,\mathrm{K}$, $B = +2.7\,\mathrm{T}$. Data shows 10 s excerpts of the whole recording time (a: 303 s, 1382 switching events, c: 3102 s, 1019 switching events). **b,d** Normalised histograms of **a** and **c**, respectively. PDF: estimate of the Probability Density Function (integral of data points equals 1). Solid red lines are fits with Eq. (3.1). States (0) and (1) correspond to the FM and the skyrmion state, respectively.

mean lifetime of the two states $\bar{\tau}$, which represents the average duration the magnetic state is in one of the two states before a switching event occurs. For this, the number of switching events N_{sw} is counted as the number of crossings of the center value 0.5 (horizontal red lines in Fig. 3.5a,c), leading to the relation:

$$\bar{\tau} = \frac{T}{N_{\mathrm{sw}} - 1} \tag{3.4}$$

with the recording time of the telegraph signal between the first and the last switching event T. The mean switching rate $\bar{f}$ is calculated as:

$$\bar{f} = \frac{1}{\bar{\tau}} \tag{3.5}$$

Several observations can be made regarding the U- and I-dependent changes of the mean switching rate $\bar{f}$. Figure 3.6a shows the increase of $\bar{f}$ as a function of the bias voltage U at a constant current of $I_{\mathrm{set}} = 300\,\mathrm{nA}$ and a magnetic field of $B = +2.7\,\mathrm{T}$. For a better comparability, all of the data points from this data set, which were collected with one tip on one skyrmion, are colourised according to the bias U, see colour bar in Fig. 3.6.

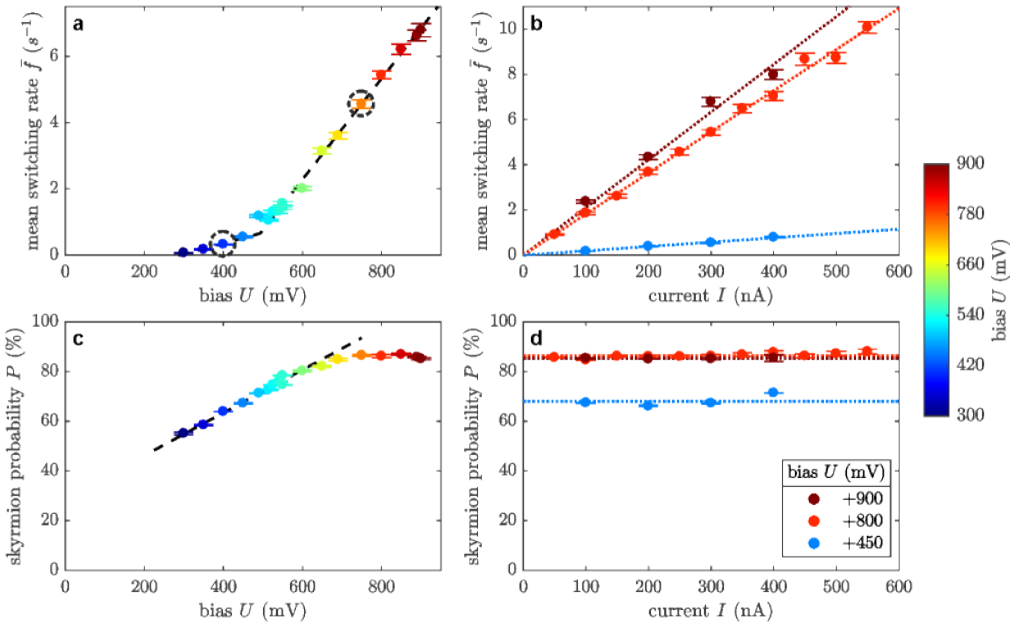

Figure 3.6.: Exploration of the switching mechanism: U and I dependence. a,b Mean switching rate $\bar{f}$ as a function of U at constant $I_{\mathrm{set}} = 300\,\mathrm{nA}$ and as a function of I at three constant values of U, respectively. **c,d** The corresponding skyrmion probabilities P. All data points were extracted from respective time-dependent switching signals, recorded on one defect hosting a skyrmion in fcc Pd/Fe/Ir(111), see Tip#1 in Fig. C.2. $\bar{f}$ according to Eq. (3.5), P according to Eq. (3.3). The circled data points in **a** are extracted from the data shown in Fig. 3.5. Dashed lines in **a** and **c** are linear guides to the eye. Coloured, dotted lines in **b** and **d** serve as guides to the eye for constant bias voltages. $T = 4.2\,\mathrm{K}$, $B = +2.7\,\mathrm{T}$.

Starting from the first data point with enough statistics within a reasonable amount of time at $U = +300\,\mathrm{mV}$, the switching rate first increases slowly with U before increasing with a higher slope and approximately linearly above $U \approx +500\,\mathrm{mV}$. Figure 3.6b shows the mean switching rate at three chosen bias voltages as a function of the tunnel current I, recorded with the same tip. The switching rates scale approximately linearly with I, with different slopes depending on the bias voltage U (see dotted lines in Fig. 3.6b), suggesting on average a constant yield per electron to activate a switching event for a given bias voltage.

The average switching yield per electron Υ can be calculated as:

$$\Upsilon = \frac{\bar{f}}{I \cdot \left(6.24 \times 10^{18}\,\mathrm{electrons/Coulomb}\right)} \tag{3.6}$$

and represents the average probability for each tunnelling electron to result in a switching event. In other words, $1/\Upsilon$ is the average number of electrons tunnelling before a switching event occurs. Figure 3.7a shows the data points from Fig. 3.6b, now represented as $\Upsilon(I)$. The dotted lines are constant values as a guide to the eye, suggesting that Υ is mostly

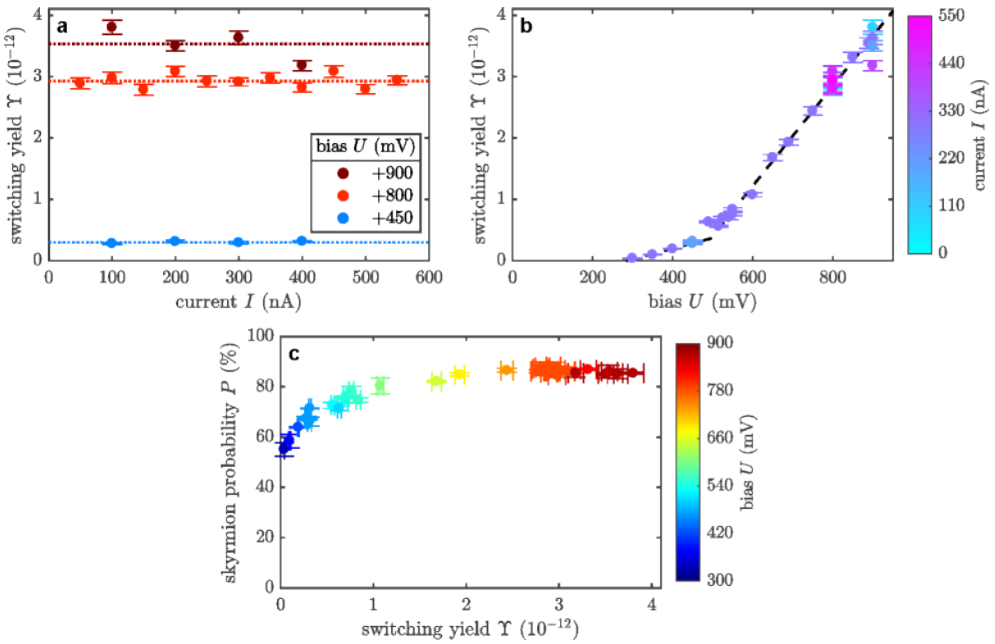

Figure 3.7.: Exploration of the switching mechanism: switching yield ϒ. a Mean switching yield ϒ as a function of I at three constant values of U. **b** ϒ as a function of U for the full data set of Fig. 3.6. **c** The corresponding skyrmion probabilities P of the complete data set plotted as a function of ϒ. All data points were extracted from respective time-dependent switching signals, recorded on one defect hosting a skyrmion in fcc Pd/Fe/Ir(111), see Tip#1 in Fig. C.2. ϒ according to Eq. (3.6), P according to Eq. (3.3). Coloured, dotted lines in **a** serve as guides to the eye for constant bias voltages. Dashed lines in **b** are linear guides to the eye. $T = 4.2\,\mathrm{K}$, $B = +2.7\,\mathrm{T}$.

constant for all I at each voltage. Figure 3.7b shows the two data sets of Fig. 3.6a and b combined in one graph, represented as the switching yield $\Upsilon(U)$, colourised with the value of the current I. The increase of the switching yield with bias voltage can be divided into two linear regimes separated at $U \approx +500\,\mathrm{mV}$, as suggested by the dashed line in Fig. 3.7b. The switching yield seems to mainly depend on U with an additional small scattering within the uncertainties with respect to I. Especially when regarding the switching yield as a function of the injected electrical power $I \cdot U$, Fig. 3.8a, it can be concluded that the main parameter responsible for activating the switching process is the bias voltage U, whereas the power $I \cdot U$ is not a decisive value. I simply increases the number of electrons available per time to activate a switching event and thereby increases the mean switching rate.

In addition to the change of the mean switching rate as a function of U and I, also a change of the skyrmion probability P as a function of the tunnel parameters is observed. Figure 3.6c and d show the skyrmion probability as a function of bias voltage and current, respectively. Once again, the bias voltage U is the decisive parameter that changes the skyrmion probability from just above 50 % at $U = +250\,\mathrm{mV}$ to over 80 % at $U > +700\,\mathrm{mV}$.

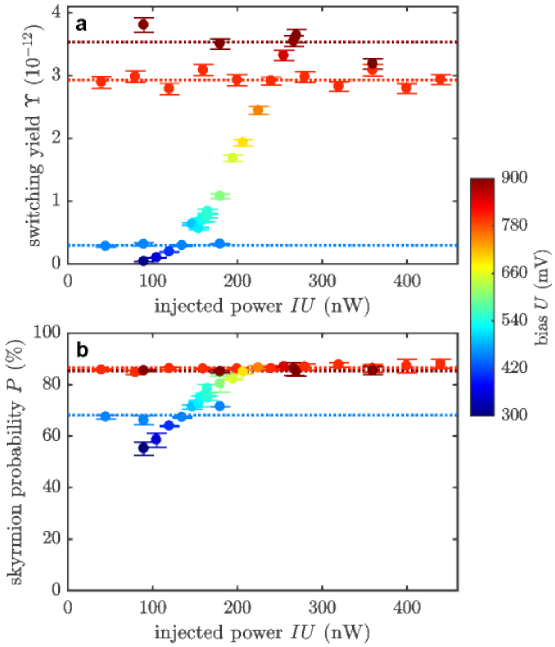

Figure 3.8.: Exploration of the switching mechanism: injected power $I \cdot U$. **a** Mean switching yield Υ as a function of the injected power $I \cdot U$ for the full data set of Fig. 3.6. **b** The corresponding skyrmion probabilities P as a function of $I \cdot U$. All data points were extracted from respective time-dependent switching signals, recorded on one defect hosting a skyrmion in fcc Pd/Fe/Ir(111), see Tip#1 in Fig. C.2. Υ according to Eq. (3.6), P according to Eq. (3.3). Coloured, dotted lines in **a** serve as linear guides to the eye for constant bias voltages. $T = 4.2\,\mathrm{K}$, $B = +2.7\,\mathrm{T}$.

The skyrmion probability first increases approximately linearly for $U \lesssim +500\,\mathrm{mV}$ before saturating to a value of $P \approx 85\,\%$. A change of the current leaves the skyrmion probability (nearly) constant at the value defined by the voltage as suggested by the horizontal dotted lines in Fig. 3.6d. Also looking at both data sets together as function of power IU in Fig. 3.8b corroborates the observation that the skyrmion probability is set by the applied bias voltage and (mostly) independent of the current. Figure 3.7c shows a monotonous correlation of P and Υ, suggesting that a higher switching yield per electron also leads to a higher skyrmion probability.

As mentioned before, the local potential landscape can be tuned with the external magnetic field, see Fig. 3.3b, leading to a preference of the skyrmion state at lower magnetic field and of the ferromagnetic state at higher field. This effect manifests in the skyrmion probability as a function of external magnetic field. Figure 3.9c shows $P(B)$ for $U = +600\,\mathrm{mV}$ and $U = -600\,\mathrm{mV}$ at $I = 100\,\mathrm{nA}$, i.e. for fixed energy of the injected electrons $|eU|$ and magnitude of the current $|I|$ but for two current directions[3]. As expected, the skyrmion probability decreases with increasing magnetic field for both current

[3] The data in Fig. 3.9 is recorded with a different tip, on another stacking and skyrmion. Nonetheless, the observed trend is expected to be the same for the skyrmion and tip investigated above.

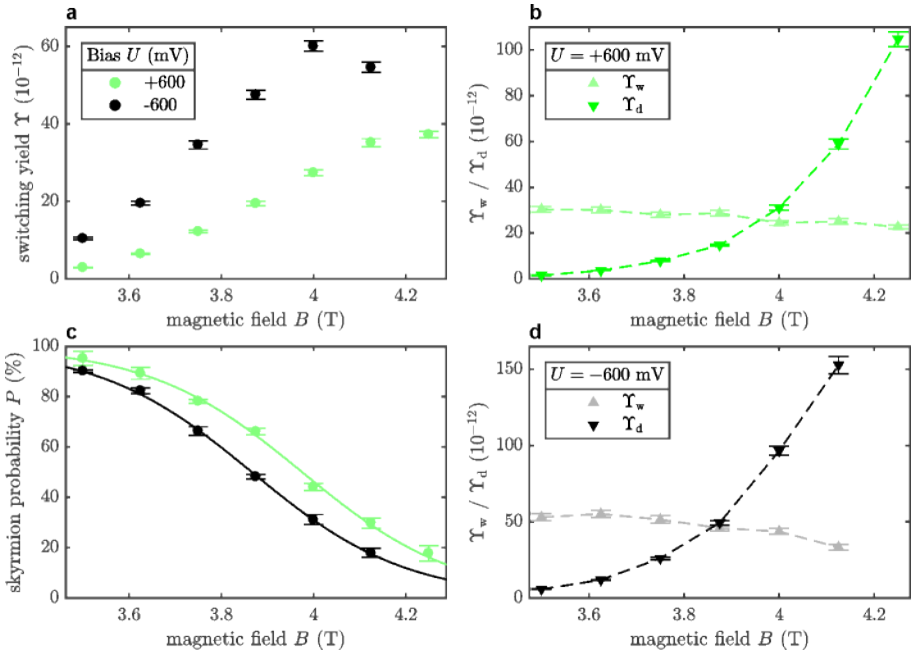

Figure 3.9.: Exploration of the switching mechanism: B-dependence. a,c Mean switching yield Υ and skyrmion probability P as a function of magnetic field B for the two bias voltages indicated, $I = 100\,\mathrm{nA}$. All data points were extracted from respective time-dependent switching signals, recorded on one defect hosting a skyrmion in hcp Pd/Fe/Ir(111), see Tip#2 in Fig. C.2. Υ according to Eq. (3.6), P according to Eq. (3.3). Solid lines in **c** are fitted hyperbolic tangent functions. **b,d** The skyrmion writing and deletion yields Υ_w and Υ_d as a function of magnetic field, calculated from Eqs. (3.7) and (3.8) for the data points shown in **a** and **c**. Bulk Cr tip, $T = 4.2\,\mathrm{K}$.

directions, and we find that it follows the shape of a hyperbolic tangent function, see fitted lines. More importantly, the data points show a uniform shift of $\Delta B \approx 100\,\mathrm{mT}$ upon current direction reversal. So once again, the skyrmion probability is different for different applied bias voltage or in this case different current direction. The maximum difference in P at a constant magnetic field for the two current directions is $\Delta P\,(B = 3.9\,\mathrm{T}) \approx 18\,\%$.

Another observation is that the mean switching yield increases with magnetic field and that it differs to a great extent for the two chosen bias voltages or current directions, see Fig. 3.9a. The mean switching yield is on the order of 1.5 to 3 times higher for $U = -600\,\mathrm{mV}$ than for $U = +600\,\mathrm{mV}$. The mean switching yield Υ contains the different yields for skyrmion creation and annihilation. The respective values (skyrmion writing yield Υ_w and skyrmion deletion yield Υ_d) can be calculated, analogous to Eq. (3.6), from the mean switching rate $\bar{f}$ (Eq. (3.5)) and the skyrmion probability P (Eq. (3.3)) via:

$$\Upsilon_{\mathrm{w}} = \frac{\bar{f}}{2I \cdot (1-P) \cdot \left(6.24 \times 10^{18}\,\mathrm{electrons/Coulomb}\right)} \tag{3.7}$$

$$\Upsilon_{\mathrm{d}} = \frac{\bar{f}}{2I \cdot P \cdot \left(6.24 \times 10^{18}\,\mathrm{electrons/Coulomb}\right)} \tag{3.8}$$

These state-resolved switching yields are shown in Fig. 3.9b,d for the two bias voltages, respectively. It can directly be seen that Υ_{w} and Υ_{d} scale differently with the magnetic field and that the increase of $\Upsilon(B)$ in Fig. 3.9a mostly results from the increase of the skyrmion deletion yields Υ_{d}. The different curve shapes for the two switching directions are not surprising, because the two respective origin states, FM and skyrmion, are distinctively different. On the one hand, the magnetic starting configuration of the writing process, the FM alignment of spins, does not significantly change with the magnetic field, which matches the mostly constant (only slightly decreasing) curve shape of the skyrmion writing yields Υ_{w} in Fig. 3.9b,d. On the other hand, the origin state of the deletion process, the skyrmion configuration, considerably responds to changes of the magnetic field. As will be investigated in more detail in Chapter 4, the size of the skyrmion roughly decreases with $1/B$. Possibly as a result, the skyrmion deletion yields Υ_{d} increase greatly in Fig. 3.9b,d. In other words, a higher magnetic field leads to a drastic decrease of the skyrmion stability.

To understand the qualitatively different behaviour of the two switching directions, Monte Carlo simulations were performed in collaboration with Hagemeister *et al.*. It was found that the different stabilities of the FM and the skyrmion configuration result from a different field dependence of the activation energies. Additionally, the attempt frequencies for the two switching directions vary considerably, resulting in an asymmetric potential landscape as schematically shown in Fig. 3.3b. The shallower slope of the potential well in the skyrmion state, representing a lower attempt frequency, leads to an additional stabilisation of the skyrmion. [Hagemeister *et al.*, 2015]

Regarding the previous paragraphs, the experimental observations can be summarised in the following way:

- The mean switching yield per electron Υ is determined by the applied bias voltage U. On average every 10^{10} to 10^{14} tunnelling electrons, a switching event occurs for the parameter range investigated. Higher positive U leads to a higher Υ in two linear regimes with different slopes. It can also be different for $\pm U$, meaning it does not simply depend on the energy of the injected electrons $|eU|$.

- Also the directionality of the switching process, represented as the skyrmion probabil-

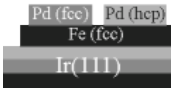

ity, crucially depends on U and can vary by about 30 % in the bias range investigated. For one set of $\pm U$, it was also shown that the sign inversion of U and with it the current direction leads to a change in skyrmion probability.

- The tunnel current I only changes the average switching rate $\bar{f}$ but not the switching yield Υ or the skyrmion probability P to a significant extent.
- The external magnetic field B influences the skyrmion probability, leading to less skyrmion probability for higher magnetic fields.
- Also the switching yield depends on the magnetic field, with generally a higher yield for higher magnetic field. This mainly results from an increased skyrmion deletion yield, whereas the skyrmion writing yield stays mostly constant.

In principle, several contributions may activate the switching process between the two states FM (0) and skyrmion (1), of which the following are considered as possible explanations here:

(i) **Thermal fluctuations** caused by the substrate electrons, which may randomly activate a switching process.

(ii) Local **Joule heating** of the sample due to the electrical power injected by the tunnel current from the STM tip can also heat up the sample locally and thus lead to thermally activated switching.

(iii) **Nonthermal excitations** from the scattering of the injected electrons.

Additionally, a number of effects can break the symmetry of the switching process and add a preferred directionality:

(iv) The **Oersted field** generated by the tunnel current with its chirality could prefer or decrease skyrmion creation.

(v) Similar to the external magnetic field, which tunes the local potential landscape, a local **stray field** of the tip may influence the preferred state.

(vi) The local **electric field** due to the applied bias voltage between tip and sample may alter the magnetic interactions locally and thus distort the potential landscape, leading to either a change of the barrier height [Sonntag *et al.*, 2014] or also to changes of the energies of inequivalent states like skyrmion and ferromagnet [Hsu *et al.*, 2017].

(vii) **Spin-transfer-torque (STT)** as a known mechanism to provide a preferred directionality in magnetic switching processes can occur when spin-polarised electrons interact with the sample.

(viii) Differences in the **local density of states (LDOS)** of the two states may lead to different yields for the two switching directions.

Using the available data presented above and additional deduced parameters, some of the effects (i) to (viii) can be identified or excluded as major contributions to the switching process:

(i) Thermal Fluctuations

The thermal stability of the skyrmions at $T = 4.2\,\mathrm{K}$ was already demonstrated in Fig. 3.3c vs. j. During 3 hours of manipulation in the left side of the island, the undisturbed part of the island on the right side remained unchanged. Additionally, the average switching rate $\bar{f}$ as a function of U and I, see Fig. 3.6a and b, approaches 0 for $U, I \to 0$. This leads to the conclusion that thermal noise can be neglected as the origin of the switching process at $T = 4.2\,\mathrm{K}$.

(ii) Joule Heating

Joule heating of the local environment of the skyrmion via the injected tunnel current leading to thermal switching can be excluded as a major activation process because of the following reasoning: If Joule heating was important here, the resulting temperature increase should linearly depend on I at a constant voltage [Bat'ko and Bat'ková, 2005]. For similar tunnelling experiments on Fe-islands, it was shown that the temperature increases on the order of $1.6\,\mathrm{K\,\mu A^{-1}}$ [Krause *et al.*, 2011]. Although, this effect could be higher in Pd/Fe/Ir(111), it is assumed that the temperature will not rise above $T = 8\,\mathrm{K}$ in the U- and I-range used here. Because skyrmions will later be shown to still be stable at $T = 8\,\mathrm{K}$, see e.g. Fig. 5.1, switching rates of up to $10\,\mathrm{s^{-1}}$ cannot be due to Joule heating, which is therefore neglected as a major contribution in the switching process.

(iii) Nonthermal Excitations

When electrons with a certain energy and spin tunnel between tip and sample, several processes for the relaxation of both energy and spin can occur, including elastic or inelastic electron-phonon or electron-electron interactions [Schlenhoff, 2013]. Besides the electron-phonon processes, which were already ruled out as the main mechanisms in (i) and (ii), electron-electron processes can take place, e.g. in the form of magnon generation, spin-flip scattering or other scattering processes including hot electrons [Plihal *et al.*, 1999]. Which of the relaxation processes contributes predominantly can crucially depend on the involved states and the energy of the tunnelling electrons [Plihal *et al.*, 1999; Echenique *et al.*, 2000; Schlenhoff, 2013]. The dependence of the switching yield on the bias voltage, see Fig. 3.7b, therefore suggests that some forms of electron-electron scattering processes, which start

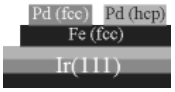

above a certain electron energy, are responsible for the activation of the observed switching processes.

(iv) Oersted Field

In principle, the Oersted field generated by the tunnel current can have an influence on magnetic switching processes [Krause *et al.*, 2007]. With its clock-wise or counter-clockwise orientation around the flow of current depending on the current direction, it is imaginable that it can also stabilise or destabilise the skyrmion vs. the FM state, especially when the tunnel current is not injected in the center of the skyrmion position. Because the Oersted field is proportional to the current, this directional effect should, however, result in a change of the skyrmion probability P as a function of I. As such a change is not observed, see Fig. 3.6d, the Oersted field is excluded as a major contribution adding a directionality to the switching process.

(v) Stray Field of the Tip

Hanneken showed that even antiferromagnetic bulk Cr tips may have local stray fields at the sample on the order of $\approx 100\,\mathrm{mT}$ for close distances of $< 6\,\text{Å}$ [Hanneken, 2011]. Because the distance of tip and sample changes depending on both U and I, the stray field could in principle explain the observed changes of the skyrmion probability with the experimental parameters. To test this hypothesis, Fig. 3.10a and c show the switching yield and the skyrmion probability for the complete data set of Fig. 3.6 as a function of the estimated tip-sample distance d, respectively.[4] If the stray field was the dominating effect determining the directionality of the switching process, there should be a clear dependence of $P(d)$, irrespective of U or I. As there are multiple values of P for one d visible in Fig. 3.10c, the effect of the stray field of the tip is negligible.

(vi) Electric Field

Changes in electric fields can alter the magnetic interactions in metallic thin films e.g. due to changes in the interlayer distance or by spin-dependent screening of the electric field [Matsukura *et al.*, 2015]. Such alterations of the magnetic interactions have for example been observed in Fe islands on tungsten and molybdenum single crystals [Sonntag *et al.*, 2014] or in the triple layer of iron on iridium (111) (TL Fe/Ir(111)) [Hsu *et al.*, 2017], each leading to changes of the switching process via tuning of the local potential landscape. In principle, changes in the electric field could hence also be responsible for the change of switching yield or skyrmion probability. As a crude approximation, the electric field at the sample below the tip can be described in the plate-capacitor model as:

[4] See Appendix A.1 for the estimation of the tip-sample distance d.

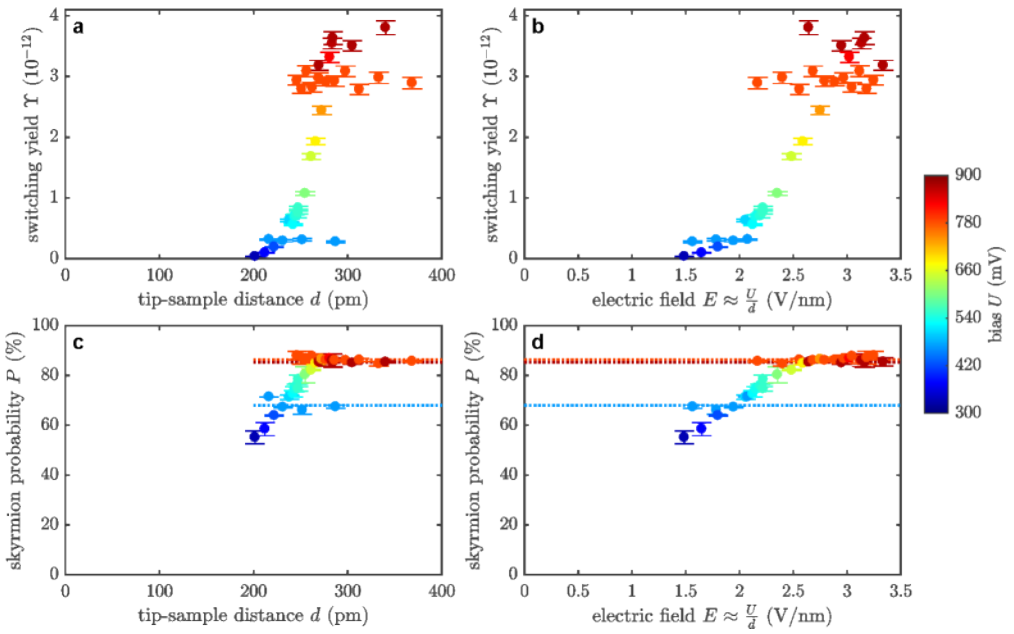

Figure 3.10.: Exploration of the switching mechanism: d and E. a,c Mean switching yield Υ and skyrmion probability P as a function of the estimated tip-sample distance d (see Appendix A.1) for the full data set of Fig. 3.6. **b,d** The corresponding values as a function of estimated electric field E (see Appendix A.1). All data points were extracted from respective time-dependent switching signals, recorded on one defect hosting a skyrmion in fcc Pd/Fe/Ir(111), see Tip#1 in Fig. C.2. Υ according to Eq. (3.6), P according to Eq. (3.3). Coloured, dotted lines in **c,d** serve as linear guides to the eye for constant bias voltages. $T = 4.2\,\mathrm{K}$, $B = +2.7\,\mathrm{T}$.

$$E \approx \frac{U}{d} \tag{3.9}$$

with an estimated tip-sample distance $d(U, I)$ as described in Appendix A.1. To test the hypothesis, Fig. 3.10b and d show the two parameters Υ and P for the complete data set in Fig. 3.6 as a function of electric field. Once again, there are multiple possible values of Υ and P possible for one value of the electric field, leading to the exclusion of the electric field as a major contribution for the observed changes.

(vii) Spin-Transfer-Torque

The macroscopic spin-torque effect is proportional to the spin-polarisation factor of the tunnel current $\eta = (I_\uparrow - I_\downarrow)/(I_\uparrow + I_\downarrow)$, with $I_\uparrow$ and $I_\downarrow$ being the up and down spin-polarised parts of the current, respectively, and depends on the current direction [Slonczewski, 1996; Krause, 2008]. The observed shift of the magnetisation curves upon inversion of the current direction in Fig. 3.9b therefore is a typical indication for the presence of STT [Khajetoorians *et al.*, 2013]. In the limit of small bias voltages, the net spin-polarisation of the tunnel current can safely be assumed constant due to a negligible change of the LDOS in a

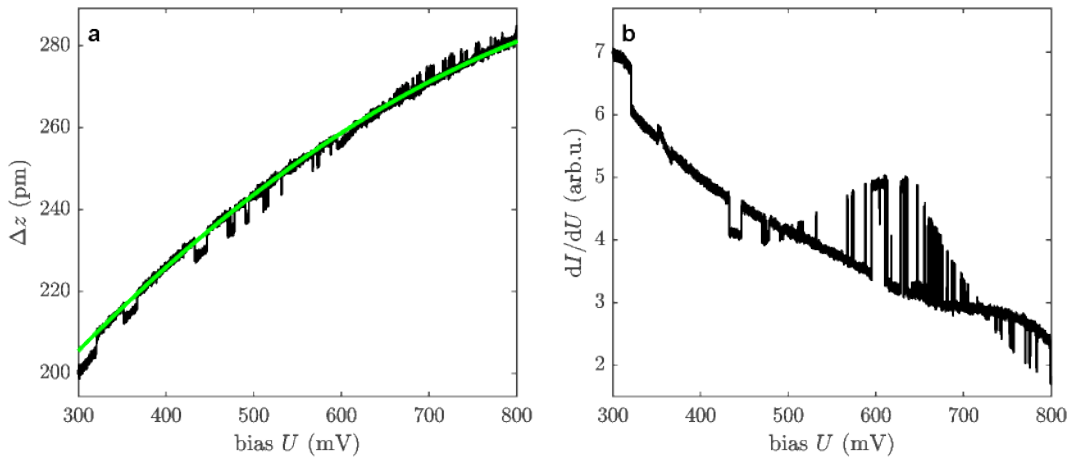

Figure 3.11.: z-spectroscopy for constant current. **a,b** Relative tip height Δz and the differential tunnelling conductance during a constant current sweep of the bias from $U_s = +300\,\mathrm{mV}$ to $U_e = +800\,\mathrm{mV}$ with the tip positioned over the defect shown in Fig. C.2 (Tip#1) (same tip and position as complete data set in Fig. 3.6). Solid green line in **a** depicts the value of z in the skyrmion state, as a guide to the eye. Sweep recording duration: 50 s, $I_{set} = 300\,\mathrm{nA}$, $U_{mod} = 10\,\mathrm{mV}$, $T = 4.2\,\mathrm{K}$, $B = +2.7\,\mathrm{T}$.

small region around the Fermi energy. Due to the conservation of angular momentum during the interaction of the tunnelling electrons with the sample magnetisation, a transfer of spin angular momentum can lead to a reversal of the magnetisation with a preferred directionality depending on the net spin-polarisation and on the direction of the current [Berger, 1996; Slonczewski, 1996; Krause *et al.*, 2007; Khajetoorians *et al.*, 2013]. However, for higher bias voltages, as used here, the spin-split LDOS of the sample and the tip can in principle have an arbitrary distribution regarding the energy and the tip-sample distance. The net spin-polarisation of the tunnel current can vary and even invert sign depending on the chosen tunnel current I and bias U, rendering the STT a possible explanation for the bias-dependent change of P.

A good test of the proposed STT mechanism being responsible for the bias dependent directionality of the switching process would thus be correlating the skyrmion probability $P(U)$ with the bias-dependent spin-polarisation of the tunnel current. As described in Section 1.2, also the TMR-based signal strength $\Delta z\,(\vec{m}_{\uparrow\downarrow})$ is proportional to the spin-polarisation η of the tunnel current. The directional STT-effect should thus correlate with the change in z between skyrmion and FM state.

Figure 3.11a shows the z-signal during a slow sweep of the bias voltage, recorded on the defect, hosting a skyrmion; Fig. 3.11b shows the simultaneously recorded differential tunnelling conductance-signal. Due to the high current of $I_{set} = 300\,\mathrm{nA}$ and the slow sweep rate, the magnetic state is continuously switching between the skyrmion and the FM state, resulting in a telegraph signal superimposed on the general shapes of $z\,(U)$ and $\mathrm{d}I/\mathrm{d}U\,(U)$. As a guide to the eye, the z-value in the skyrmion state is marked by the solid green line in

Fig. 3.11a. The bias dependent signal strength, here defined as $S_z(U) = z_{\mathrm{FM}}(U) - z_{\mathrm{Sk}}(U)$, changes as a function of U and has a point of sign inversion at $U_{\mathrm{inv}} \approx +630\,\mathrm{mV}$.

If the magnetic signal was purely a result of the TMR, the spin-polarisation of the tunnel current η could be extracted from the signal strength $S_z(U)$. However, it is now known that in the investigated bias range, another magnetoresistive effect, the NCMR, plays a crucial role [Hanneken *et al.*, 2015; Hanneken, 2015; Crum *et al.*, 2015; Kubetzka *et al.*, 2017]. As the NCMR results from a change of the LDOS of the sample due to a mixing of spin up- and down-channels in non-collinear magnetic structures, it can also lead to a bias dependent change of the signal strength $S_z(U)$, independent of the spin-polarisation of the tunnel current. Due to the lack of appropriate data, the bias-dependent spin-polarisation of the current hence cannot be extracted. Although it still serves as a good explanation, the STT as the main effect responsible for the directionality of the switching process can therefore neither be validated nor ruled out. The large variation of the LDOS, manifesting in the $\mathrm{d}I/\mathrm{d}U$-signal as a function of U in Fig. 3.11b, however, inspires the suggestion of a new effect based on variations in the LDOS, which will be described in the next paragraphs.

(viii) Differences in the LDOS

As mentioned in the previous paragraphs, the measured $\mathrm{d}I/\mathrm{d}U$ signal is known to be significantly altered in the bias range investigated here due to the NCMR. The NCMR-effect is essentially a magnetoresistive imaging mechanism in STM that changes with the degree of non-collinearity of the sample magnetisation, see schematic drawing in Fig. 3.12a. It was shown that the NCMR-related difference in tunnelling conductance originates from a change of the band structure of Pd/Fe/Ir(111) due to a mixing of spin-up and spin-down bands [Hanneken *et al.*, 2015; Hanneken, 2015; Crum *et al.*, 2015; Kubetzka *et al.*, 2017]. A different band structure leads to a different LDOS, which leads to qualitatively different $\mathrm{d}I/\mathrm{d}U(U)$-spectra for the skyrmion state and the FM state, see spectra in Fig. 3.12a, which were taken from [Kubetzka *et al.*, 2017].

Also the spectrum in Fig. 3.12c, recorded with the same tip and on the same defect as used for the recording of the complete data set in Fig. 3.6, looks qualitatively similar to the reference spectra in Fig. 3.12a, and the general shapes of the skyrmion state and the FM state can be identified, see annotations in Fig. 3.12c. Figure 3.12d shows the $I(U)$-spectrum, simultaneously recorded with the $\mathrm{d}I/\mathrm{d}U$-spectrum in Fig. 3.12c, also enabling the identification of both states in the $I(U)$-spectrum, see annotations in Fig. 3.12d. As the magnetic state switches during the up-ramp and down-ramp of U (marked as $U \nearrow$ and $U \searrow$ in Fig. 3.12c and d), both configurations can be accessed in one graph for a given tip height and at the same bias voltages. As evident from Fig. 3.12d, not only the $\mathrm{d}I/\mathrm{d}U$-spectra but also the $I(U)$-spectra have a qualitatively different shape for the two states. Below $U_{\mathrm{inv}} \approx +630\,\mathrm{mV}$, the skyrmion state leads to a larger current than the FM

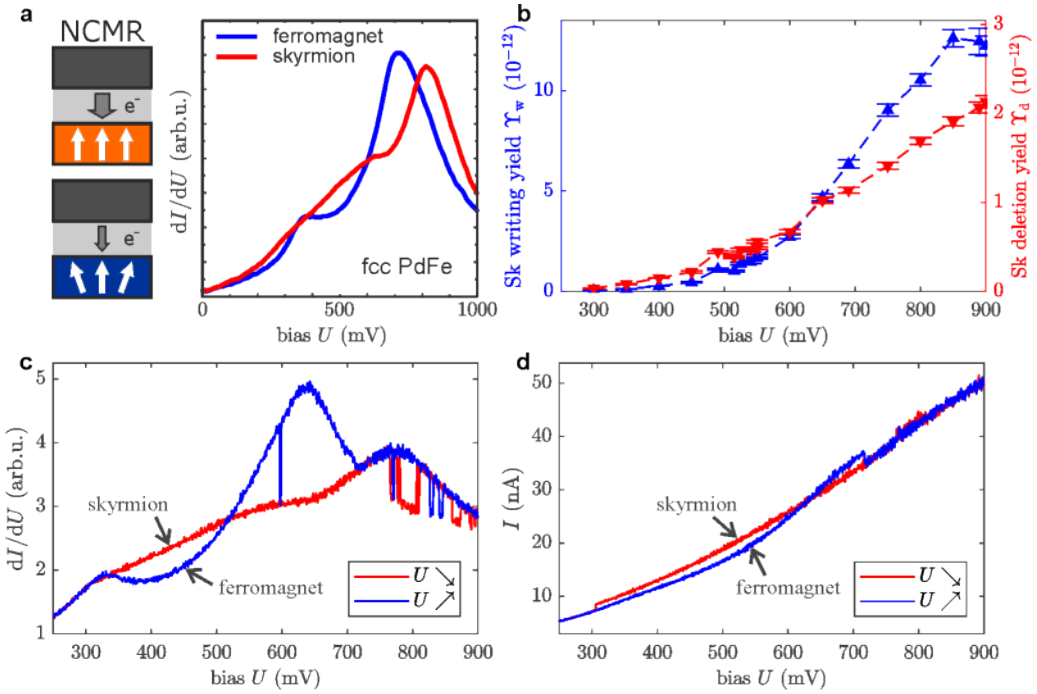

Figure 3.12.: Different LDOS of skyrmion and ferromagnet. **a** Schematic drawing for the NCMR and its manifestation in spectra of the differential tunnelling conductance as a function of sample bias U. Both adapted from [Kubetzka *et al.*, 2017, Fig.2]. Spectra are taken in the center of a skyrmion and in the FM background of an fcc Pd/Fe/Ir(111)-island, respectively. $U_{\mathrm{stab}} = -1\,\mathrm{V}$, $I_{\mathrm{stab}} = 1\,\mathrm{nA}$, $U_{\mathrm{mod}} = 7\,\mathrm{mV}$, $B = -2.5\,\mathrm{T}$, $T = 4.2\,\mathrm{K}$. **b** The skyrmion writing and deletion yields Υ_{w} and Υ_{d} as a function of bias voltage, calculated from Eqs. (3.7) and (3.8) for the data points shown in Fig. 3.6a and c. **c,d** The differential tunnelling conductance and the current, recorded during a constant-height sweep of the bias from $U_{\mathrm{s}} = +900\,\mathrm{mV}$ to $U_{\mathrm{e}} = +250\,\mathrm{mV}$ and back with the tip positioned over the defect shown in Fig. C.2 (Tip#1, same tip and position as complete data set in Fig. 3.6). $U_{\mathrm{stab}} = +900\,\mathrm{mV}$, $I_{\mathrm{stab}} = 50\,\mathrm{nA}$, $U_{\mathrm{mod}} = 10\,\mathrm{mV}$, $B = -2.8\,\mathrm{T}$, $T = 4.2\,\mathrm{K}$.

state, whereas, due to a bend in the FM curve around $U_{\mathrm{bend}} \approx +500\,\mathrm{mV}$, above U_{inv} the FM state results in a larger current. The skyrmion curve generally exhibits a more steady increase in current.

Naturally, as the different tunnelling conductances for the skyrmion and the FM state originate in locally different LDOSs of the sample (see explanation of the NCMR above), fundamentally different states of the sample can contribute to the tunnelling process at a certain bias voltage, depending on the magnetic state of the sample at the time of the tunnelling. Depending on the nature of these states and the respective relaxation paths of the tunnelling electrons (see e.g. considerations to contribution (iii)), different switching yields are conceivable for skyrmion creation and annihilation.

Figure 3.12b shows the direction-resolved switching yields calculated via Eqs. (3.7) and (3.8) from the values of $\bar{f}$ and P shown in Fig. 3.6a and c. The respective y-scales were adapted to have them artificially cross at $U = U_{\mathrm{inv}}$ for didactic purposes. This way, the

resemblance of the curve shapes of $\Upsilon_{w,d}$ to the shapes of $I_{FM,Sk}(U)$ is most pronounced.[5] Surprisingly, the $I_{FM}(U)$-curve has a similar shape as the curve for the skyrmion writing yield $\Upsilon_w(U)$ and the $I_{Sk}(U)$-curve resembles the curve for the skyrmion deletion yield $\Upsilon_d(U)$. This means that the writing yield seems to have a connection to the FM state, which is the state from which the writing process also starts, and vice versa for the deletion yield.

Based on these observations and on similar observations with another tip-apex (see Appendix C.1), I propose here that besides the possible explanation with STT, a new effect may play a crucial role in switching skyrmions in Pd/Fe/Ir(111) using an STM tip. Apparently, this effect is related to the bias-dependent LDOS of the sample and can influence the switching yield depending on which electronic states contribute to the tunnel process. Due to the significant alteration of the LDOS in the skyrmion state with respect to the FM state, this influence can behave differently in the two inequivalent magnetic states skyrmion and ferromagnet, because of the NCMR. This would thus be another possible explanation for the observed change of the preferred directionality of the switching process P with U.

If this new effect is indeed responsible for the observed bias-dependent directionality of the switching mechanism, some intriguing, possible applications of the effect are imaginable. Without the need for a magnetic tunnel junction, skyrmions could be preferably written or deleted with a non-magnetic tunnel junction just by the choice of the right bias voltage. Assuming the possible arbitrary design of the band structure of the magnetic system, a device could be built that incorporates the writing, deleting and read-out of skyrmions in a single tunnel junction at three different bias voltages U_w, U_d and U_r. At U_w, the skyrmion deletion yield would need to be suppressed, at U_d, the skyrmion writing yield, and at U_r both. Depending on the control over the electronic states responsible, this could be realised without the need for high (spin-polarised) currents.

[5] If the magnetic field for the data set had been chosen appropriately, this crossing at $U = U_{inv}$ would have occurred naturally (for $P(U = U_{inv}) = 50\,\%$). Figure C.5d shows a similar data series, recorded with a different tip apex on a different defect and at a different magnetic field, confirming similar shapes of the $I_{FM,Sk}(U)$-curves.

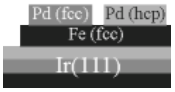

Summary of the Switching Mechanism

The analysis of measurements of the telegraph noise, caused by the repeated switching of the magnetic state in Pd/Fe/Ir(111) at different bias voltages U, tunnel currents I and magnetic fields B, yielded two main experimental observations. The mean switching rate $\bar{f}$ depends on both U and I, but only U determines the switching yield per electron. The directionality of the switching process, represented as the skyrmion probability P, is significantly changed depending on U (and B). Two possible explanations are proposed for these observations:

(1) A nonthermal activation of the switching process via higher-energy electrons (iii), paired with an additional directionality imposed by STT (vii). This is also the explanation, stated in [Romming *et al.*, 2013].

(2) The two inequivalent states FM and skyrmion possess a distinctively different LDOS. This could lead to an asymmetric switching process caused by the different electronic states participating in the tunnel process and their corresponding relaxation paths, depending on the bias U and the current magnetic state of the system (viii).

With the data available, it is not entirely clear which of the two possible explanations is the correct one. Appendix C.1 offers another data set, recorded with a different tip apex and on a different fcc Pd/Fe/Ir(111) island, corroborating the observations and conclusions made here, but also without identifying one of the two possible explanations. It remains to be explored by future experiments and theoretical considerations, whether the new effect may indeed play an important role in the switching of magnetic skyrmions.

Chapter 4.

Field-Dependent Size and Shape of Single Magnetic Skyrmions

In Section 1.1.3, skyrmions are described as spatially localised, solitonic magnetic whirls with axial symmetry and fixed rotational sense (sketch in Fig. 4.1a) [Bogdanov and Yablonsky, 1989; Bogdanov and Hubert, 1994a,b; Rößler *et al.*, 2011]. In the previous chapter, the discovery of individual skyrmions and their manipulation was reported without explicitly analysing their internal structure. This chapter is dedicated to investigating the spin structure of skyrmions in Pd/Fe/Ir(111) in detail and to connecting the experimental findings to the micromagnetic model described in Section 1.1.2. Section 4.1 is based on [Romming *et al.*, 2015].

4.1. The Skyrmion Structure in Detail

Figure 4.1b shows a ML Pd/Fe/Ir(111)-island in an external magnetic field of $B = -1.5\,\mathrm{T}$, exhibiting several circular skyrmions and three 360°-DW sections, see Section 1.1.3, remaining from the spin spiral phase. Due to the use of an OOP sensitive SP-STM tip, the axisymmetric character of the skyrmions becomes directly evident. When an IP sensitive SP-STM tip is used, the appearance of the skyrmions changes: now two lobes with maximal and minimal spin-polarised current flow are imaged per skyrmion (Fig. 4.1c) as a result of a positive or negative projection of the local magnetisation direction of the skyrmion onto the spin direction of the tip. When tip and sample magnetisation directions are orthogonal to each other, the spin-polarised contribution to the tunnel current, and thus the magnetic signal, vanishes: for the image in Fig. 4.1c this is true close to the center of the skyrmion and above and below the center. The four skyrmions in the sample area of Fig. 4.1c appear identical, which is always the case for all skyrmions imaged with a given SP-STM tip. This implies that they exhibit indeed a unique rotational sense. According to the symmetry selection rules of the DMI, these interface-induced skyrmions are expected to be cycloidal (sketch in Fig. 4.1a) [Moriya, 1960; von Bergmann *et al.*, 2014], in agreement with recent DFT calculations and Monte Carlo simulations for this system [Dupé *et al.*,

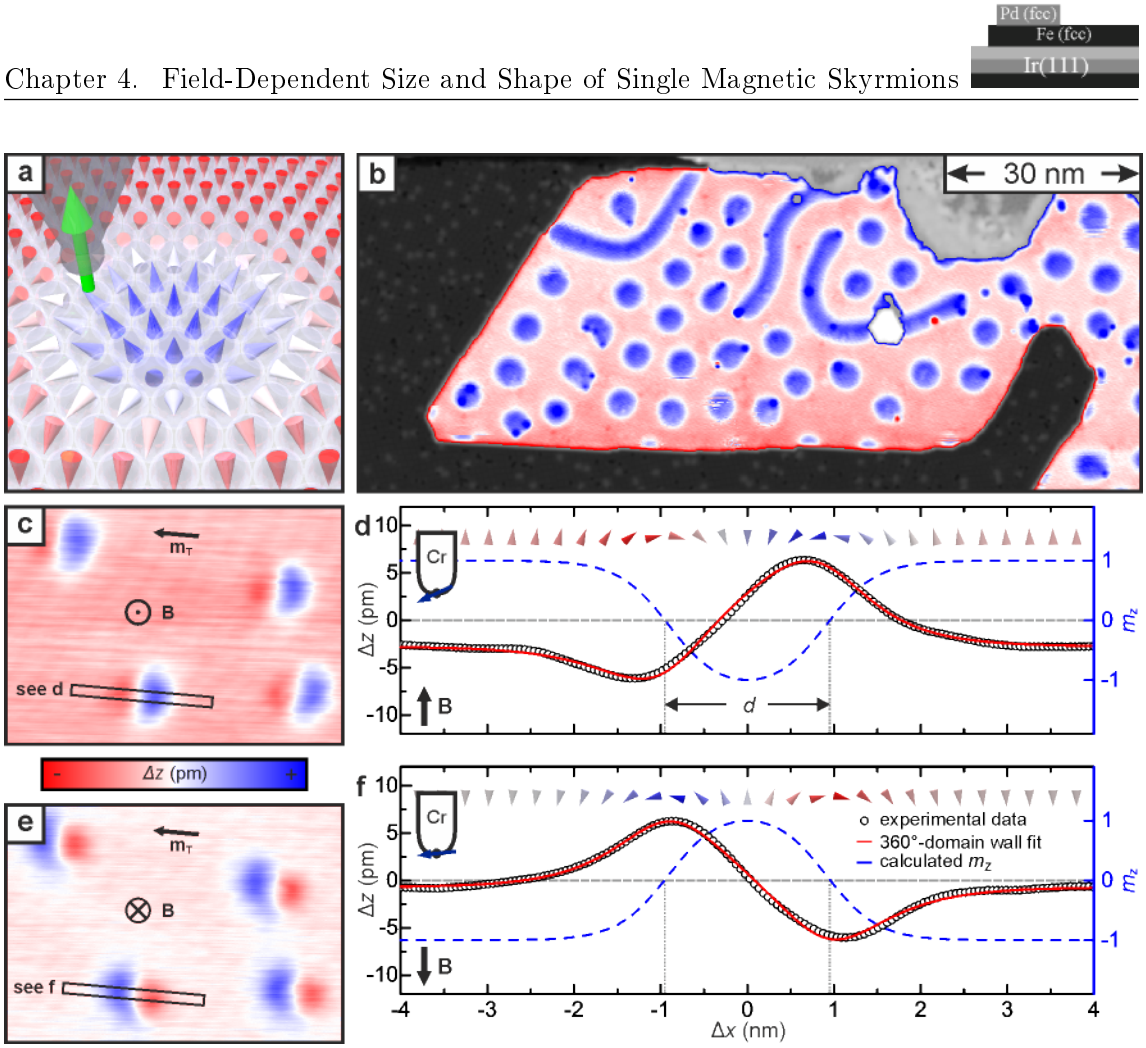

Figure 4.1.: Spin structure of an individual skyrmion in PdFe/Ir(111). **a** Sketch of the experimental setup of a spin-polarised STM tip probing a magnetic skyrmion. **b** Constant-current SP-STM image measured with OOP sensitive magnetic tip; each blue circular entity is a skyrmion. $U = +200\,\mathrm{mV}$, $I = 1\,\mathrm{nA}$, $T = 2.2\,\mathrm{K}$, $B = -1.5\,\mathrm{T}$. **c,e** Magnetic signal (an image of the same area without skyrmions was subtracted) of four skyrmions measured with an in-plane magnetisation of the tip, $\vec{m}_T$, revealing a two-lobe structure. $U = +250\,\mathrm{mV}$, $I = 1\,\mathrm{nA}$, $T = 4.2\,\mathrm{K}$. **d,f** Line profiles across a skyrmion along the rectangles in **c**, **e**, respectively, and fits with Eqs. (1.19) and (1.25) (**d** $c = (0.90 \pm 0.01)\,\mathrm{nm}$, $w = (1.18 \pm 0.02)\,\mathrm{nm}$; **f** $c = (0.91 \pm 0.01)\,\mathrm{nm}$, $w = (1.17 \pm 0.01)\,\mathrm{nm}$) and corresponding calculated out-of-plane magnetisation m_z. The sketches show spins with atomic distance, colourised according to the SP-STM contrast. **e** Same area as in **c** with inverted magnetic field; due to the preserved rotational sense, the contrast is inverted. Measurements conducted together with Dr. André Kubetzka and Christian Hanneken, Univ. Hamburg.

2014]. When the external magnetic field, which induces the skyrmions, is applied in the opposite direction, the contrast of the two lobes of the skyrmions is inverted (Fig. 4.1e) since each spin in the sample is inverted while the spin structure of the anti-ferromagnetic tip remains unchanged, providing an additional proof of the unique rotational sense caused by the DMI. The four skyrmions in Fig. 4.1c and e appear at identical positions due to pinning at atomic defects.

To characterise the size and the shape of a skyrmion we take height profiles across

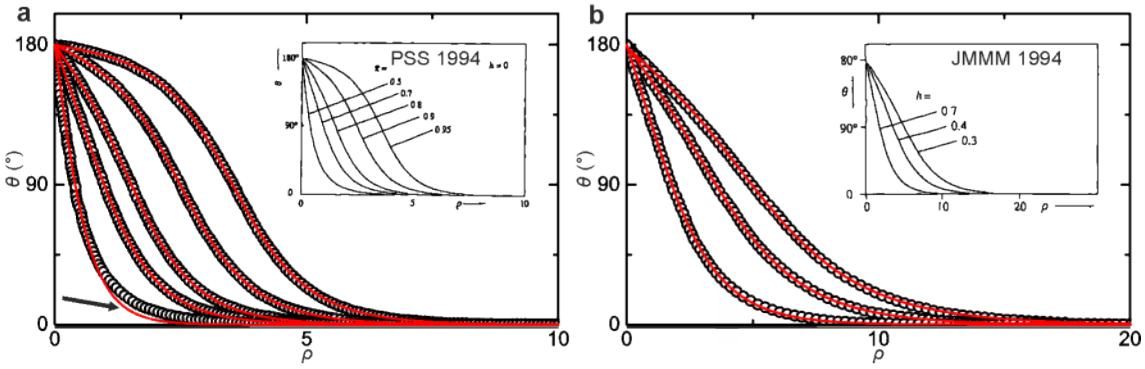

Figure 4.2.: Comparison of proposed skyrmion profile with numerical calculations. **a** Circles: numerically obtained magnetisation profiles of an isolated skyrmion for different values of $\pi D/\left(4\sqrt{AK}\right)$ in zero magnetic field (graphically extracted from ref. Bogdanov and Hubert [1994a]), solid red lines: fits with Eq. (4.1). The arrow points to a deviation of the analytical and the numerical profile for $\pi D/\left(4\sqrt{AK}\right) = 0.5$. **b** Circles: numerically obtained magnetisation profiles for zero effective anisotropy for different magnetic fields (graphically extracted from ref. Bogdanov and Hubert [1994b]), solid red lines: fits with Eq. (4.1). Insets show original graphs from refs. Bogdanov and Hubert [1994a,b].

the center (see black rectangles in Fig. 4.1c and e). Since there is no exact analytical expression to describe skyrmion profiles, we approximate the cross-section of a skyrmion using a standard 360°-DW profile [Braun, 1994; Kubetzka *et al.*, 2003], Eq. (1.19):

$$\varphi_{360}(x,c,w) = \begin{cases} \sum\limits_{+,-}\left[\arcsin\left(\tanh\frac{x\pm c}{w/2}\right)\right] + \pi & |B_z > 0 \\ \sum\limits_{+,-}\left[\arcsin\left(\tanh\frac{x\pm c}{w/2}\right)\right] & |B_z < 0, \end{cases} \tag{4.1}$$

The good agreement between experimental data and fit, see black data points and red fit lines in Fig. 4.1d and f, justifies the chosen description. Furthermore, a comparison to numerically calculated skyrmion profiles leads to the conclusion that Eq. (1.19) is an excellent approximation for a wide range of material parameters and field values (Fig. 4.2). From Eq. (1.19) it is straightforward to determine the perpendicular magnetisation component $m_z(x)$, see blue dashed lines in Fig. 4.1d, f, and the diameter of the skyrmion d, which we define as the diameter of the circle with $m_z = 0$. Exploiting the axial symmetry[1], the spin structure of an isolated skyrmion in two dimensions is then described by:

$$\vec{S}(x,y) = \begin{pmatrix} -\sin\left(\varphi_{360}(\rho,c,w)\right)\cdot x/\rho \\ -\sin\left(\varphi_{360}(\rho,c,w)\right)\cdot y/\rho \\ \cos\left(\varphi_{360}(\rho,c,w)\right) \end{pmatrix}, \tag{4.2}$$

[1] In the framework of this thesis, the model was also extended to distorted skyrmions in the TL Fe/Ir(111), see Appendix B.1.

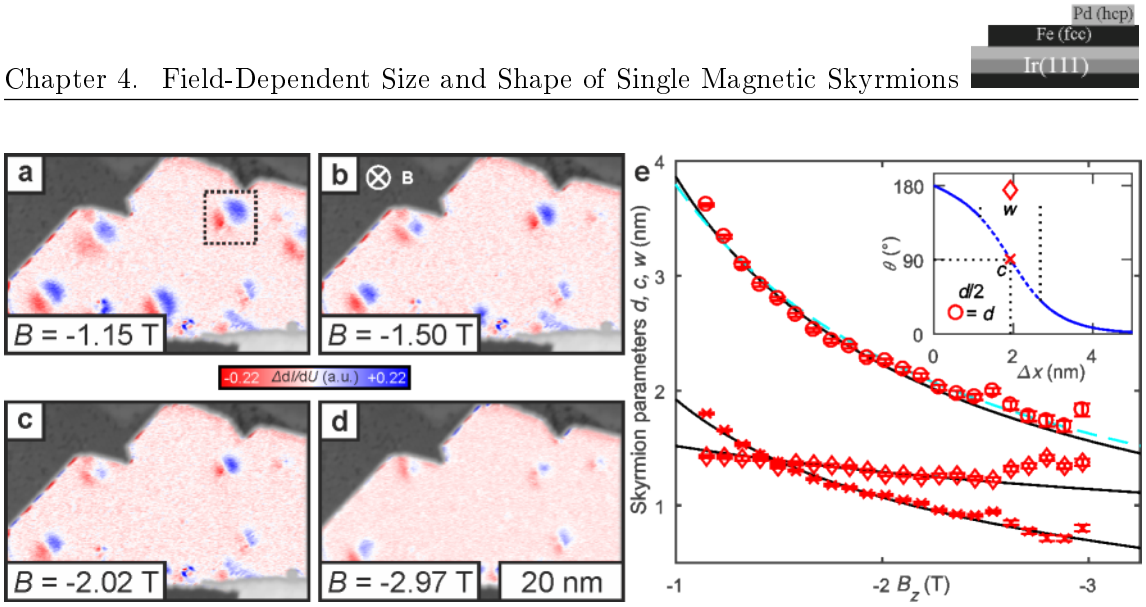

Figure 4.3.: Evolution of the size and shape of skyrmions in PdFe/Ir(111) as a function of external magnetic field. a-d Magnetic signal of SP-STM differential conductance maps (calculated by subtracting the non-magnetic reference image (mean of data at highest positive magnetic field and data at highest negative magnetic field)) with IP magnetised tip, combined with a gray-scale image of the topography at the magnetic fields as indicated (the full data set can be found in [Romming *et al.*, 2015, supplemental online material]). $U = +20\,\mathrm{mV}$, $I = 3\,\mathrm{nA}$, $U_{\mathrm{mod}} = +2.4\,\mathrm{mV}$, $T = 4.2\,\mathrm{K}$. **e** The size and shape of the skyrmion indicated by the box in **a** is evaluated by a fit with Eqs. (1.25) and (4.2) as a function of magnetic field. Inset shows geometrical meaning of c and w and of d, which is numerically calculated; dashed blue line is a fit to d with $1/(B - B_0)$. Solid black lines are obtained theoretically for the fitted set of material parameters A, D, and K (see text). Error bars correspond to the standard deviation of fit parameters.

in which φ_{360} is the 360°-DW description (Eq. (1.19)) and $\rho = \sqrt{x^2 + y^2}$ is the radial distance from the center of the skyrmion located at the origin. Note that within this model the spin structure of the skyrmion is fully determined by only two parameters, c and w.

The impact of external magnetic fields on the size and shape of a skyrmion becomes evident in field-dependent SP-STM experiments: Fig. 4.3a-d show the identical area of an hcp Pd/Fe/Ir(111)-island imaged at different external magnetic field strengths. The colour scale resembles the magnetic contribution to maps of $\mathrm{d}I/\mathrm{d}U$, and the use of an IP sensitive tip leads again to the two-lobe appearance of the skyrmions. The decrease of the skyrmion size with increasing field can be directly seen in the displayed image sequence (the full data set can be found in [Romming *et al.*, 2015, supplemental online material]). For a quantitative analysis we fit a single isolated skyrmion (black box in Fig. 4.3a) with our two-dimensional skyrmion model and obtain the characteristic parameters c, w, and thus also d and $\vec{m}\,(x, y)$.

The evolution of these parameters with external field is shown in Fig. 4.3e. The diameter of the skyrmion roughly scales with $1/(B - B_0)$, see dashed blue line, in agreement with numerical calculations [Bogdanov and Hubert, 1994a; Wilson *et al.*, 2014]. While in the investigated field range, the diameter changes by more than a factor of two, the effect

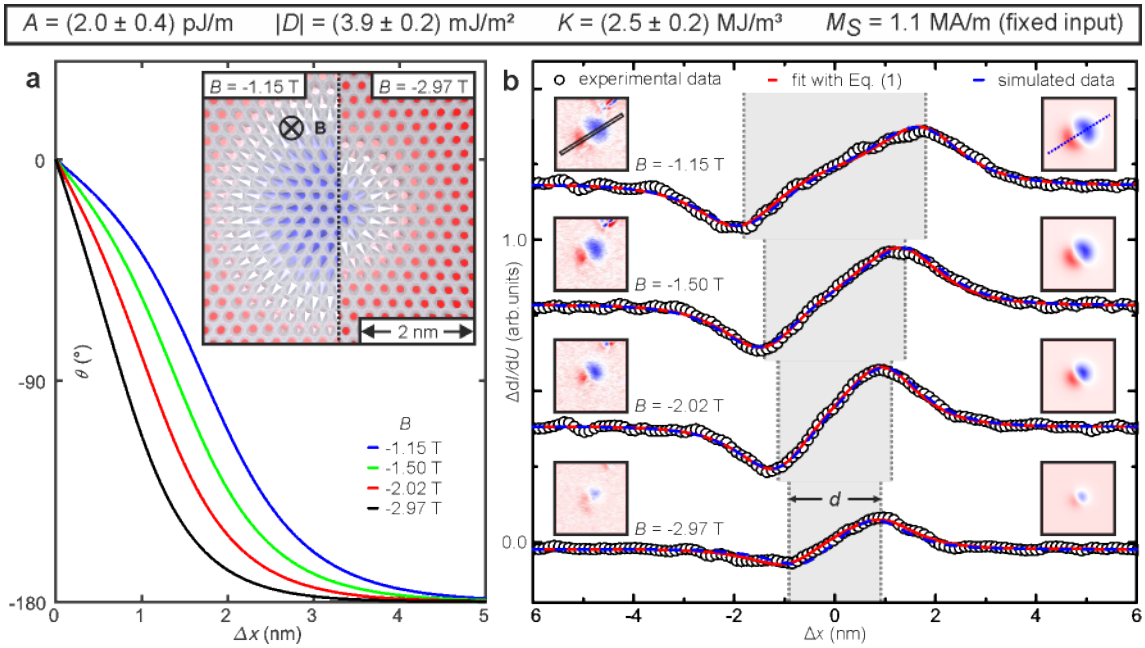

Figure 4.4.: Validation of material parameters via micromagnetic simulations. **a** Internal spin structure of the skyrmion as described by Eq. (1.19) for the field values indicated. Inset shows the visualisation of spins with atomic distance as parametrised by Eq. (4.2); c, w given by fits in Fig. 4.3e. **b** Comparison of experimental and simulated height profiles across an individual skyrmion (box in insets) for several magnetic field values, and a fit with Eq. (1.19). Left and right insets show SP-STM experimental data from Fig. 4.3a-d and micromagnetic simulations, based on the derived material parameters, respectively. The colour scale of the simulations is adapted to reproduce the experimental data.

on the width of the transition region is only about 25 %. Consequently, as can be seen in Fig. 4.4a, the skyrmion shape changes qualitatively with magnetic field, leading to a significant decrease in the number of spins with a component opposite to the magnetic field. This results from a subtle balance of all energies involved, where the Zeeman energy leads to a compressing force and the DMI stabilises skyrmions against collapse to the ferromagnetic state.

To assess these underlying interactions for the hcp biatomic PdFe layer in the framework of micromagnetic continuum theory, we establish a connection to the standard micromagnetic energy functional (Eq. (1.8)), rewritten in cylindrical coordinates [Bogdanov and Yablonsky, 1989; Bogdanov and Hubert, 1994a,b; Wilson *et al.*, 2014; Bogdanov and Hubert, 1999; Rohart and Thiaville, 2013]:

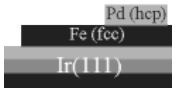

$$E_{\mathrm{cont}} = 2\pi t \int_0^\infty \Bigg\{ \overbrace{A\left[\left(\frac{\mathrm{d}\theta}{\mathrm{d}\rho}\right)^2 + \frac{\sin^2\theta}{\rho^2}\right]}^{\text{exchange energy}} + \overbrace{D\left[\frac{\mathrm{d}\theta}{\mathrm{d}\rho} + \frac{\sin\theta\cos\theta}{\rho}\right]}^{\text{DM energy}} - \underbrace{K\cos^2\theta}_{\text{anisotropy energy}} - \underbrace{BM_{\mathrm{S}}\cos\theta}_{\text{Zeeman energy}} \Bigg\} \rho\,\mathrm{d}\rho, \tag{6.2}$$

with the exchange stiffness A, DMI constant D, uniaxial effective anisotropy constant K, and saturation magnetisation M_S as the material dependent parameters. B_z is the external out-of-plane magnetic field and t is the film thickness. From DFT calculations [Dupé *et al.*, 2014], we estimate $M_S \approx 1.1\,\mathrm{MA\,m^{-1}}$ (see Appendix A.3). The magnetisation profile $\theta(\rho)$ is given by our experimentally verified skyrmion model, Eq. (4.1). Now for each set of A, D, K, B the energy functional can be minimised with respect to c and w. These theoretical curves $c(B)$ and $w(B)$ are fitted to the experimentally obtained values for $c(B)$ and $w(B)$ via an error weighted[2] least square fit with A, D, K as fitting parameters (Fig. 4.3e). The solid lines are the calculated values of d, c, w for $A = (2.0 \pm 0.4)\,\mathrm{pJ\,m^{-1}}$, $D = (3.9 \pm 0.2)\,\mathrm{mJ\,m^{-2}}$ and $K = (2.5 \pm 0.2)\,\mathrm{MJ\,m^{-3}}$ as a function of magnetic field[3] (best fit). These parameters are in the range expected for thin-film systems [Dupé *et al.*, 2014; Simon *et al.*, 2014a], and the agreement of c and w obtained from theory with those from a fit to the experimental data is evident.

To demonstrate that these derived material parameters can be used to accurately reproduce the experimental data, we performed micromagnetic simulations[4] [Rohart and Thiaville, 2013; OOMMF, 2016]. Figure 4.4b shows height profiles across an isolated skyrmion at four different magnetic field values. The SP-STM data (black circles), the skyrmion fit with Eq. (1.19) (red line), and the height profile across the skyrmion in a micromagnetic simulation (blue dashed) nicely coincide, and the real-space agreement between experimental data and simulation is demonstrated in the insets to Fig. 4.4b.

4.2. Improvement of the Fit

Despite the good agreement of the micromagnetic simulations with the experimental data, the material parameters in the previous section were derived from the size and shape of one single skyrmion during one magnetic field sweep from $B = -3\,\mathrm{T}$ to $B = -1\,\mathrm{T}$. In this

[2] The error weighting in this fit was different from the one described in Eq. (1.21). See Appendix A.4.
[3] For a detailed discussion on these error bars, see Appendix A.5.
[4] The micromagnetic simulations were performed on a disc with a diameter of 50 nm and a thickness of 4.08 Å, using a lateral cell size of 1 Å × 1 Å. A central skyrmion was relaxed at every field step with a Runge-Kutta evolver at $T = 0\,\mathrm{K}$.

section, the fitting procedure is extended to more experimental input parameters such as the zero-field spin spiral period λ and the size and shape of a SS segment (360°-DW).

It is known that defects in and on the PdFe film can influence the size and shape of skyrmions quite significantly [Hanneken *et al.*, 2016]. The local area of the skyrmion investigated in the previous section contains at least one clearly visible defect and possibly several subsurface defects or inhomogeneities that define the position of the skyrmion and have an influence on the size and shape. Also at large $|B|$, the skyrmion position starts to fluctuate, leading to a smeared-out contrast and a misestimation of the values for c and w. As mentioned in Section 1.2.3, the approximation of the spin-polarised signal via Eq. (1.25) additionally leads to a systematic overestimation of c and w at large $|B|$. All this leads to uncertain inputs to the fitting procedure and therefore a possible miscalculation of the magnetic material parameters.

To demonstrate the variability of the skyrmion size and shape, Fig. 4.5a shows the skyrmion parameters of the same skyrmion, but now as the mean value of the forward and backward scan direction and also during a later time of the sweep from $B = +1\,\mathrm{T}$ to $B = +3\,\mathrm{T}$. The main difference between the two sets is that going from $B = -3\,\mathrm{T}$ to $B = -1\,\mathrm{T}$, the skyrmion size increases, whereas going from $B = +1\,\mathrm{T}$ to $B = +3\,\mathrm{T}$, the skyrmion starts large and decreases in size. As evident from the spread between the respective values at negative field and at positive field, the skyrmion appears not to have exactly the same size and shape for both directions. A reason could be the skyrmion moving either on a fast time scale, leading to a smeared-out contrast in the STM images, or on a slow time scale, leading to a slightly different skyrmion position with possibly slightly different magnetic interactions.

To make the fit more accurate and reproduce the behaviour of the complete system also at lower magnetic fields, now all the skyrmion c- and w-values from both field and scan directions are included in the fit up to only $|B| < 2.45\,\mathrm{T}$. Skyrmion parameters above this value are excluded due to their unreliability (dimmed colour in Fig. 4.5a). Additionally, the zero field SS period λ as obtained from a sine fit in Fig. 4.5b,c and the domain wall parameters c and w of the 360°-DW in Fig. 4.5d,e are added as input parameters to the fit procedure described in Eq. (1.21). Similar to the fit comparing the skyrmion size and shape to calculated values of c and w via Eq. (6.2), these additional experimental input parameters are compared to the calculated values via Eqs. (1.15) and (1.20), respectively. The resulting fit minimising Eq. (1.21) yields these material parameters for hcp Pd/Fe/Ir(111):

$$A = (1.95 \pm 0.29)\,\mathrm{pJ\,m^{-1}}, \quad D = (3.86 \pm 0.55)\,\mathrm{mJ\,m^{-2}}, \quad K = (2.50 \pm 0.74)\,\mathrm{MJ\,m^{-3}},$$

with the saturation magnetisation $M_\mathrm{S} = 1.1 \times 10^6\,\mathrm{A\,m^{-1}}$ once again fixed as input. These material parameters correspond to an effective reduced anisotropy value of $k = 1.28 \pm 0.19$ (Eq. (1.9)). The material parameters obtained here agree well with the ones obtained by

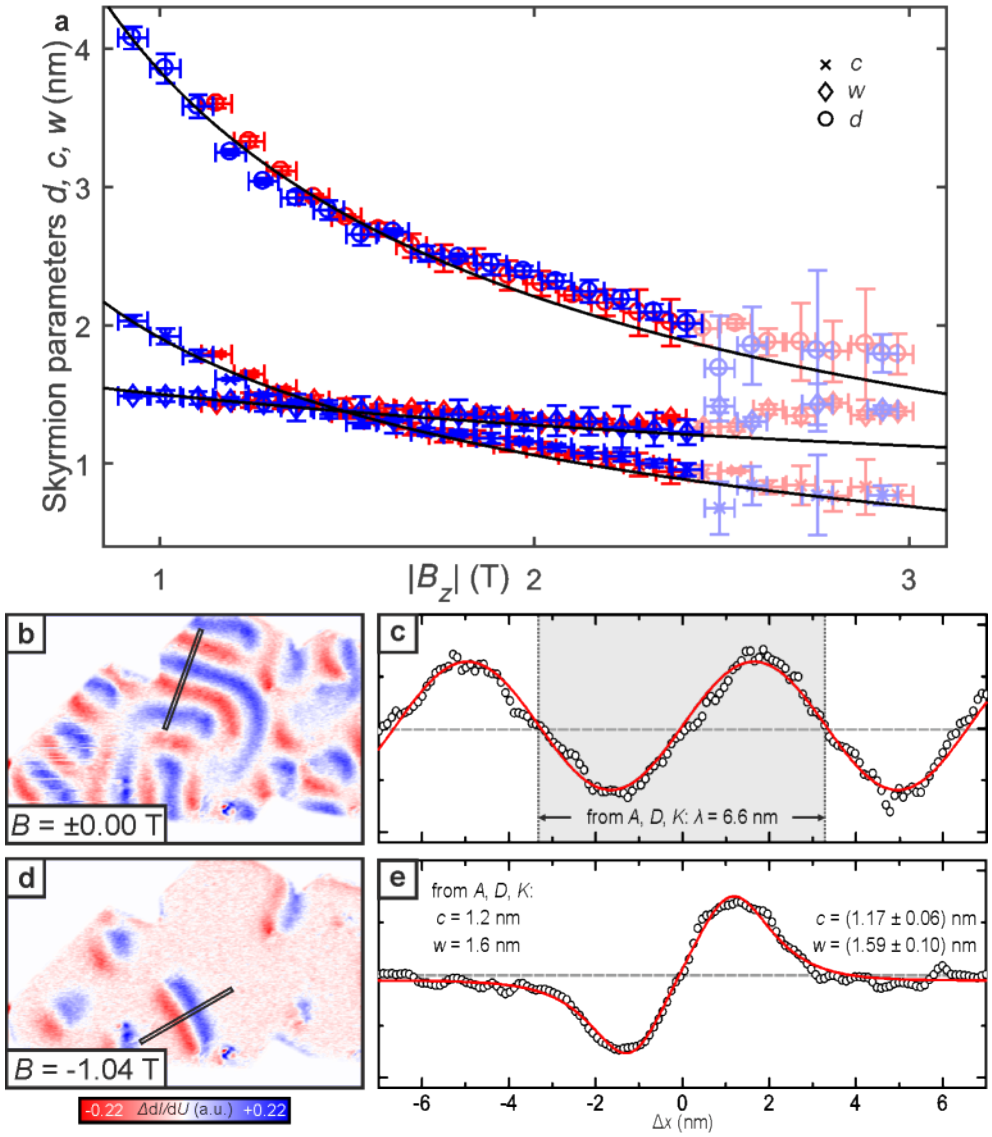

Figure 4.5.: Uncertainty of the material parameter fit. a The size and shape of the skyrmion indicated by the box in Fig. 4.3a is evaluated by a fit with Eqs. (1.25) and (4.2) as a function of magnetic field. Each data point is the mean value of the forward and the backward scan direction. Blue colour corresponds to positive field values, red indicates negative magnetic field values. **b,d** Magnetic signal of SP-STM $\mathrm{d}I/\mathrm{d}U$ maps (calculated by subtracting the non-magnetic reference image (mean of data at highest positive magnetic field and data at highest negative magnetic field)) with IP magnetised tip ($U = +20\,\mathrm{mV}$, $I = 3\,\mathrm{nA}$, $U_{\mathrm{mod}} = +2.4\,\mathrm{mV}$, $T = 4.2\,\mathrm{K}$) at the magnetic fields as indicated. **c,e** Line profiles along the respective rectangles in **b,d**. Solid line in **c** is a sine-fit as guide to the eye. Solid line in **e** is a fit with Eqs. (1.19) and (1.25).

the simpler procedure above using only the skyrmion size and shape and a different error weighting procedure[5].

[5] See Appendix A.4.

This extension of the fit procedure originally used in [Romming *et al.*, 2015] to other experimental input parameters, besides the skyrmion size and shape, now paves the path to also estimate material parameters for other magnetic systems, as will be shown in Chapter 5.

4.3. Influence of the Material Parameters on the Magnetic Properties

For future investigations and applications of isolated skyrmions, it is desirable to accurately tune their size and shape, as well as further properties, such as the transition fields or zero field SS period λ, according to the respective requirements. Should it be possible to individually tune each of the magnetic material parameters in a desired direction, it is imperative to know their impact on those properties.

To demonstrate the influence of changing the material parameters individually, Figs. 4.6a-d show the skyrmion parameters as a function of magnetic field for the same magnetic material parameters A, D, K and M as for hcp Pd/Fe/Ir(111) but with one of them decreased (red values) or increased (blue values), respectively: The skyrmion diameter d decreases when increasing any of the parameters except for D, for which, in contrast, a raise leads to quite a big increase of d. This is counter-intuitive because an increase of D leads to a reduction of the SS period λ. It can be explained, though, by the fact that the bigger an isolated skyrmion, the more spins are non-collinear, thus the more DMI-energy can be gained. For the parameter c, the same behaviour as for d can be observed. Regarding w, the impact of a change in any parameter is only comparably small. An increase of A or D leads to an increase of w, whereas an increase of K or M leads to a decrease of w.

The SS period λ is also influenced by changing the material parameters. As expected, A and D have the biggest (reciprocal) impact, whereas K and M only influence λ marginally, but both the same way. An increase of A, K or M decreases both transition magnetic fields, whereas an increase of D leads to a raise of the transition fields. The reduced anisotropy k (Eq. (1.9)) is increased by both an increase of A or K. An increase of D reduces k and a change of M does not have an influence on k. This is obvious when looking at Eq. (1.9).

Many suggestions for future applications of skyrmions involve FM strips of magnetic material in a so-called racetrack-geometry with single isolated skyrmions imprinted at arbitrary positions [Fert *et al.*, 2013; Iwasaki *et al.*, 2013; Zhang *et al.*, 2015b,c; Müller, 2017]. For simplification of the experimental requirements, the ground state at zero magnetic field should be FM. This corresponds to a value of $k > k(\mathbf{E}) = 2.5$ in Fig. 5.7. To realise such a magnetic system, starting from the parameters of hcp Pd/Fe/Ir(111), A and K can be increased to raise k.

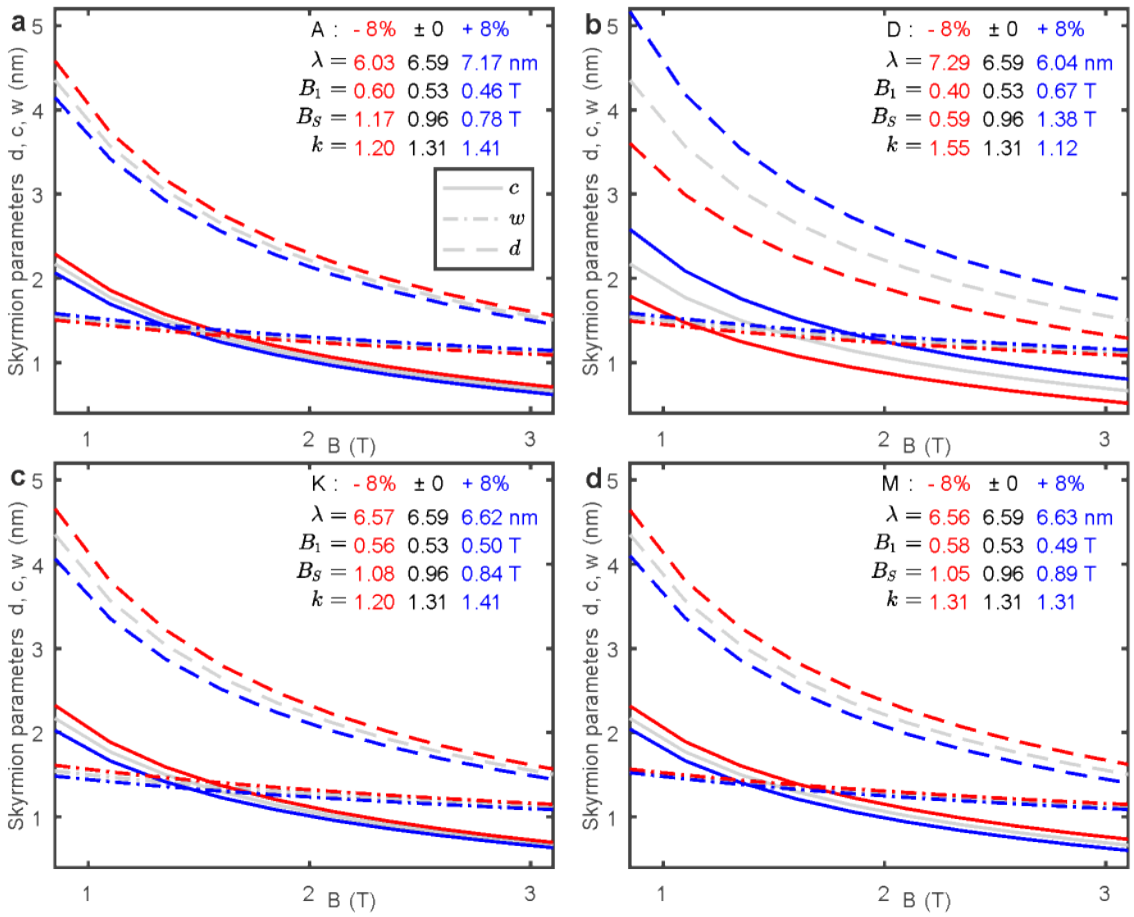

Figure 4.6.: Influence of the material parameters on the size and shape of an isolated skyrmion. Theoretically obtained curves for the skyrmion size and shape by minimising the energy of Eq. (6.2) with Eq. (4.2) with respect to c and w for each set of A, D, K, M and B. Reference values (black) correspond to $A = 1.95\,\mathrm{pJ\,m^{-1}}$, $D = 3.86\,\mathrm{mJ\,m^{-2}}$, $K = 2.50\,\mathrm{MJ\,m^{-3}}$, $M_\mathrm{S} = 1.1 \times 10^6\,\mathrm{A\,m^{-1}}$.

4.4. Literature Overview: International Activities on Skyrmions

After the initial theoretical predictions of magnetic skyrmions starting in 1989, they were first observed experimentally as a lattice phase in 2009 by Mühlbauer *et al.* using neutron scattering on the helical magnet B20 compound MnSi. Subsequently, many more observations of skyrmions in various types of systems were reported, including samples with chiral crystal structure [Yu *et al.*, 2010, 2011, 2012; Jonietz *et al.*, 2010; Münzer *et al.*, 2010; Adams *et al.*, 2012; Schulz *et al.*, 2012; Seki *et al.*, 2012; Milde *et al.*, 2013; Leonov *et al.*, 2016], magnetic thin film and multilayer systems [Heinze *et al.*, 2011; Fert *et al.*, 2013; Romming *et al.*, 2013, 2015; Jiang *et al.*, 2015; Boulle *et al.*, 2016; Moreau-Luchaire *et al.*, 2016; Woo *et al.*, 2016; Hsu *et al.*, 2017], polar magnets [Kezsmarki *et al.*, 2015] and

antiskyrmions in tetragonal Heusler compounds [Nayak *et al.*, 2017]. Depending on the sample symmetry and the resulting directions of the DMI-vectors, the skyrmions are either of Bloch- or of Néel-type. The samples investigated in this thesis are thin film systems on a single crystal. The DMI in such systems prefers Néel-type rotations of spins (see also Section 1.1.1).

Many possible applications of magnetic skyrmions in storage and computing technology have been predicted up to now [Kang *et al.*, 2016; Fert *et al.*, 2017], including race-track (RT)-type storage devices [Parkin *et al.*, 2008; Fert *et al.*, 2013; Sampaio *et al.*, 2013; Zhang *et al.*, 2015b], skyrmion based logic gates [Zhang *et al.*, 2015a] or skyrmion based transistors [Zhang *et al.*, 2015c]. On the path to realising such proposed devices, many prerequisites have been proven experimentally up to now, such as their possible creation and annihilation by currents [Romming *et al.*, 2013; Büttner *et al.*, 2017b], electric field [Hsu *et al.*, 2017] or heat [Finazzi *et al.*, 2013], their existence at room temperature [Chen *et al.*, 2015; Jiang *et al.*, 2015; Moreau-Luchaire *et al.*, 2016; Woo *et al.*, 2016; Soumyanarayanan *et al.*, 2017] and the possibility for lateral manipulation by electric currents [Jonietz *et al.*, 2010; Yu *et al.*, 2012; Jiang *et al.*, 2015; Woo *et al.*, 2016]. A promising candidate for the all-electrical detection of skyrmions is the NCMR [Hanneken *et al.*, 2015; Crum *et al.*, 2015; Kubetzka *et al.*, 2017].

For the ultimate design of small skyrmions needed in such devices that are stable at room temperature, ideally without an external magnetic field, it is imperative to be able to tune each involved material parameter and to develop fast theoretical models to predict the resulting properties of the skyrmions. Also in this area, quite a few advancements have been made, including the tailoring of the chirality of domain walls [Chen *et al.*, 2013], tuning the SOC strength [Shibata *et al.*, 2013] or the strength of the DMI [Soumyanarayanan *et al.*, 2017]. It was proposed by Dupé *et al.* to tune the exchange and DMI in multilayer stacks separately by changing certain interfaces individually [Dupé *et al.*, 2016]. Parts of the work shown in this chapter and in [Romming *et al.*, 2015] (together with its subsequent confirmation by [Boulle *et al.*, 2016]) inspired the development of a fast analytical model to screen the full phase diagrams of isolated skyrmions depending on six material parameters [Büttner *et al.*, 2017a].

Chapter 5.

Tuning Effect of Pd on Fe/Ir(111): Many Stacking Possibilities

As shown in the previous chapters, adding Pd on top of Fe/Ir(111) leads to pseudomorphic growth of nicely shaped islands with significantly different magnetic states than observed in Fe/Ir(111). This chapter focuses on the additionally altered magnetism in different stacking possibilities of Pd on Fe/Ir(111). To roughly quantify the tuning effect of the Pd on the magnetism of Fe/Ir(111), the flexible fit procedure introduced in the previous chapter and in Section 1.1.2 is applied to the characteristic magnetic properties available. The following section first describes the magnetic states of the two possible stackings of Pd on fcc Fe/Ir(111), validating the new approach at the example of hcp Pd on fcc Fe/Ir(111). Then, a short section about Pd on hcp Fe/Ir(111) follows, finished by two sections about the DL Pd on fcc Fe/Ir(111). The magnetism of all the different combinations of Pd and Fe on Ir(111) differs significantly regarding the periodicity, transition magnetic fields and magnetic material parameters and their characteristic properties are summarised in Section 5.5.

5.1. ML Pd in Two Stackings on fcc Fe

Similar to the growth of Rh/Fe/Ir(111), see Section 2.2.4, also Pd can grow in the two possible stackings on fcc Fe/Ir(111). Figure 5.1a shows a 3D view of SP-STM data of a sample area exhibiting elongated stripes of both stackings of Pd on fcc Fe/Ir(111), colourised with the simultaneously recorded, spin-resolved $\mathrm{d}I/\mathrm{d}U$-map. On both terraces, the Fe exhibits step-flow growth, continuing the fcc stacking of the Ir(111)-sample [von Bergmann *et al.*, 2006]. The well-known nanoskyrmion lattice with its square symmetry is easily recognisable, cf. Chapter 2 and [Heinze *et al.*, 2011]. On the Pd, the different $\mathrm{d}I/\mathrm{d}U$-signals of the upper and lower island are caused by the altered electronic structure due to a different stacking of the pseudomorphically grown Pd. In comparison with previous work showing atomic resolution [Hanneken, 2015], the brighter (darker) contrast on the upper (lower) island can be attributed to the hcp (fcc) stacked Pd, see also Fig. 5.1b. This assignment

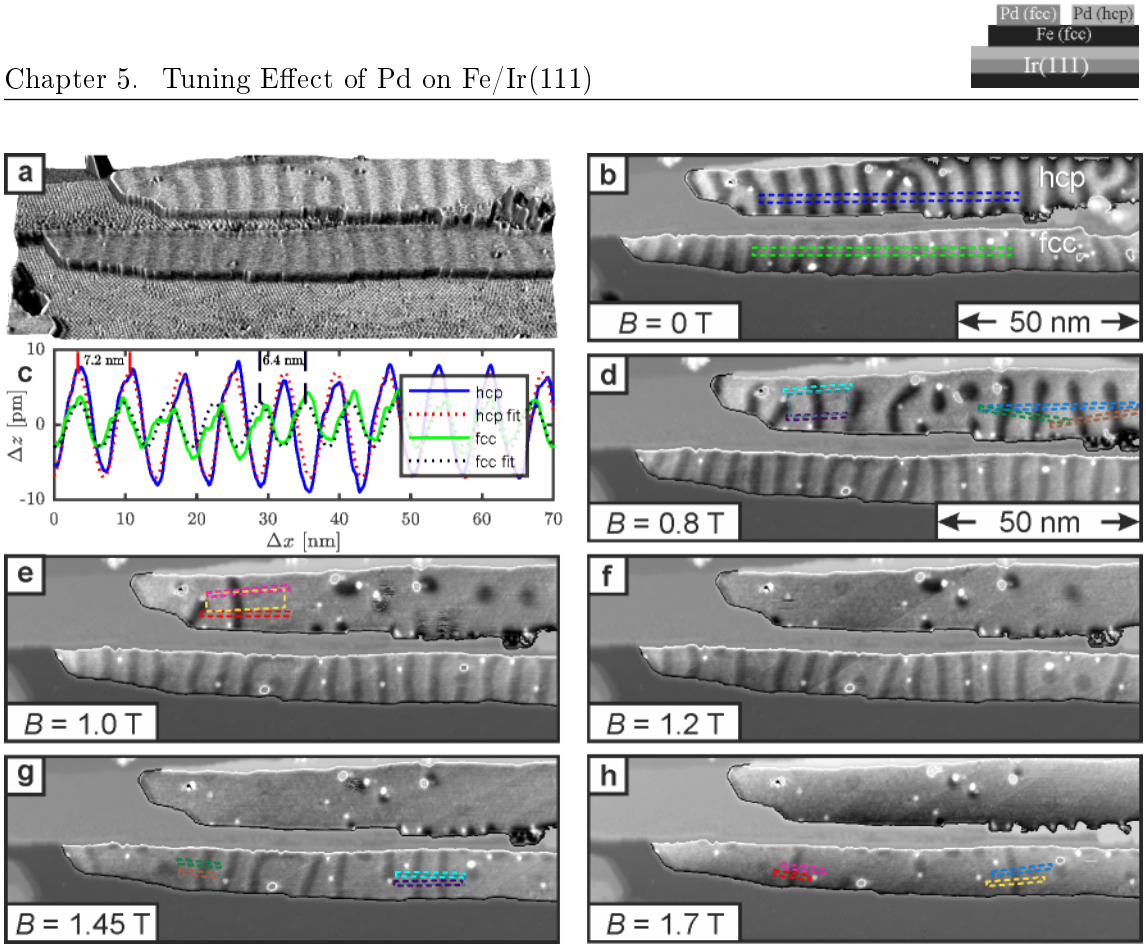

Figure 5.1.: Magnetic field dependent evolution of ML Pd/Fe(fcc). a 3D view of a constant-current SP-STM-image (same data as in **b**) colourised with the simultaneously recorded, spin-resolved dI/dU-map ($U_{mod} = 1\,mV$). **b,d-h** Constant-current SP-STM images with the contrast adjusted locally to $\pm 15\,pm$. Image **g** was creep-corrected by subtracting a parabolic plane. Cr-bulk tip, $T = 8\,K$, $U = +12\,mV$, $I_{set} = 1\,nA$. **c** Line profiles taken along dashed rectangles in **b**; linear trends were removed. Dotted lines are cosine-fits as guide to the eye. Dashed rectangles in **d-h** indicate the positions of line profiles shown in Fig. 5.3.

agrees with the fact that the lower (fcc) island is directly connected to the fcc Fe on the terrace above.

All images that are shown in Fig. 5.1 are recorded with the tunnel parameters of $U = +12\,mV$, $I_{set} = 1\,nA$. Under these conditions, the STM tip is expected to have a negligible effect on the magnetic structures, see Chapter 3 and [Romming *et al.*, 2013]. Figure 5.1b shows an SP-STM image of the sample without an applied external magnetic field. On both islands (stackings), a periodic modulation along the long directions [Schmidt *et al.*, 2016] of the islands is visible. The magnetic periodicities are about $(7.2 \pm 0.4)\,nm$ and $(6.4 \pm 0.3)\,nm$ for the hcp and fcc stacking, respectively. These modulations were previously shown to be caused by cycloidal SSs in the PdFe bilayer, see previous chapters and [Romming *et al.*, 2013; Dupé *et al.*, 2014; Simon *et al.*, 2014b].

Upon application of an external magnetic field of $B = 0.8\,T$ perpendicular to the sample surface (Fig. 5.1d), the magnetism of the two stackings responds differently. Whereas

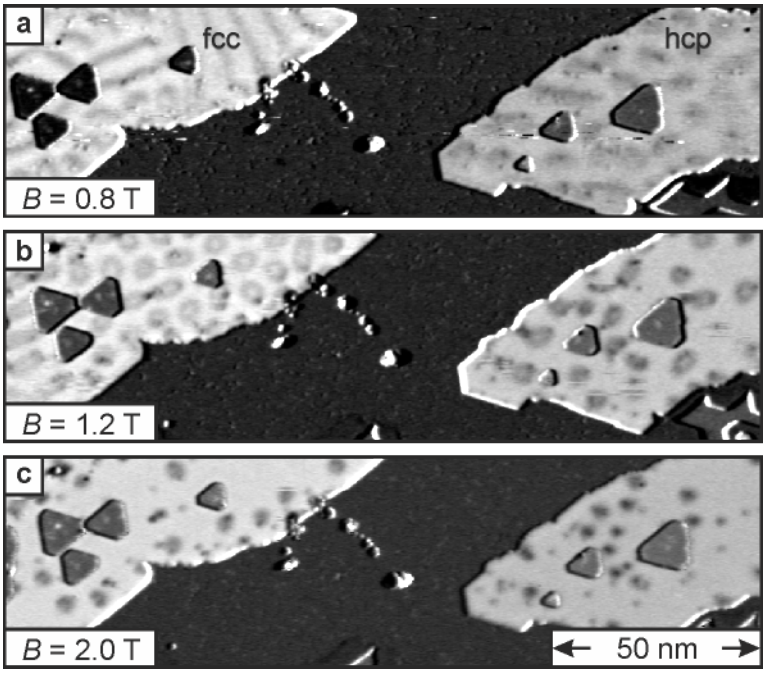

Figure 5.2.: ML Pd/Fe(fcc) at higher bias. a-c $\mathrm{d}I/\mathrm{d}U$-maps recorded simultaneously to constant-current images (not shown). Cr-bulk tip, $T = 8\,\mathrm{K}$, $I_{\mathrm{set}} = 1\,\mathrm{nA}$, $U_{\mathrm{mod}} = 30\,\mathrm{mV}$, **a:** $U = +600\,\mathrm{mV}$, **b,c:** $U = +700\,\mathrm{mV}$.

in the hcp stacking, the SS locally transforms into skyrmions with a few remaining SS fragments, in the fcc stacking, the SS state remains stable while changing its shape (bright areas parallel to the field expand, other areas shrink). These trends are continued with increasing magnetic field (Fig. 5.1e-h). The magnetic state in the hcp stacking exhibits no spiral fragments at 1.2 T, and only individual skyrmions, pinned at defects, at 1.45 T. For the fcc stacking, the first skyrmions appear at 1.0 T, and still two spiral fragments are left at 1.7 T. This leads to the conclusion that the critical fields for phase transitions from the SS state to the SkX ($B_{\mathrm{SS-Sk}}$) and from the SkX to the FM ($B_{\mathrm{Sk-FM}}$) state are lower for hcp stacking than for fcc stacking. However, the results for the SS period and the transition fields in Fig. 5.1 could be qualitatively and quantitatively different from extended films or larger islands due to the narrow elongated stripe shape of the island. Edge related effects and a change of the effective anisotropy due to a reduced stray field can have a considerable influence on the magnetic structure.

The absolute values of the critical fields are difficult to extract from the experiments because the transitions between the different magnetic phases are hindered at low temperature due to pinning, energy barriers related to topology (see Chapter 6) and due to confinement. Since the images in Fig. 5.1 are taken at low bias, also the tunnelling electrons cannot push the magnetic state towards its thermodynamic equilibrium. Figure 5.2 shows two other islands of Pd/Fe/Ir(111) (hcp stacking for the right one, fcc stacking for

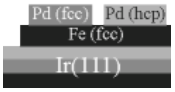

the left one), imaged at higher bias ($U \geq +600\,\mathrm{mV}$) and therefore significantly influenced by the STM tip, see Chapter 3 and [Romming *et al.*, 2013]. This can in principle change the magnetic state at a certain field by exciting the state and pushing it over potential barriers, resulting from confinement, pinning or topology. Also the extracted transition fields from higher bias measurements can be misleading such as the manipulation by the tip can have a preferred directionality, see Chapter 3. The transition fields would then be systematically over- or underestimated.

Nonetheless, together with the low bias measurements, the phase transition fields can be estimated from Fig. 5.2 for both stackings of Pd/Fe/Ir(111). As evident from Fig. 5.2a, at $B = 0.8\,\mathrm{T}$, the fcc island is still mostly in the SS state, whereas the hcp island has fully completed a transition to the SkX state ($B^{\mathrm{hcp}}_{\mathrm{SS-Sk}} \leq 0.8\,\mathrm{T}$). At $B = 1.2\,\mathrm{T}$, Fig. 5.2b, the fcc stacking exhibits a dense SkX. The transition field for SS to SkX for fcc Pd is therefore estimated to be at roughly $B^{\mathrm{fcc}}_{\mathrm{SS-Sk}} = 1\,\mathrm{T}$ (also comparing with Fig. 5.1e). The SkX in the hcp stacking is already diluted to a certain extent, indicating a transition to the mostly FM state with individual skyrmions at around $B^{\mathrm{hcp}}_{\mathrm{Sk-FM}} \leq 1.2\,\mathrm{T}$. For fcc, this transition happens above 1.2 T. Figure 5.1f, which is also recorded at $B = 1.2\,\mathrm{T}$, shows a similar magnetic state of the hcp island, but the fcc stacking is still mostly in the SS state. The last image, Fig. 5.2c, shows a mostly FM state with single skyrmions for both islands. It is visible that a moderately large number of skyrmions remain, pinned at the considerable amount of defects for this sample preparation. The transition field from SkX to FM state with single skyrmions is estimated to be around $B^{\mathrm{fcc}}_{\mathrm{Sk-FM}} = 1.4$ to $1.7\,\mathrm{T}$ for the fcc stacking. The single, pinned skyrmions can survive up to quite high magnetic fields above 3 T [Hanneken *et al.*, 2016], as was seen in the previous chapters.

Estimation of the Material Parameters

As described in Sections 1.1.3 and 4.2, it is possible to estimate the micromagnetic material parameters A, D and K from the zero-field spin spiral period λ (shown in Fig. 5.1c) and the shape of 360°-DWs in an external magnetic field; the saturation magnetisation M_{S} has to be chosen separately as a fixed input to the fitting procedure[1]. Figure 5.3 shows several line profiles across 360°-DWs taken along the dashed rectangles in Fig. 5.1. To extract their size and shape with sufficient accuracy, combinations of Eqs. (1.19) and (1.25) were fitted to all the 360°-DWs at each magnetic field simultaneously. During this fit, the tip polar angle θ, the amplitude a and the characteristic 360°-DW-parameters c and w were shared, whereas their lateral ($x_{0,i}$) and vertical shifts ($z_{0,i}$) were left free. Thus the influence of

[1] The fit also converges for any M_{S} to equivalent sets of different values, depending on the initial set of parameters. To get values that are comparable between different systems, M_{S} is chosen for all the Pd and Fe based systems as $M_{\mathrm{S}} = 1.1 \times 10^6\,\mathrm{A\,m^{-1}}$, see Appendix A.3.

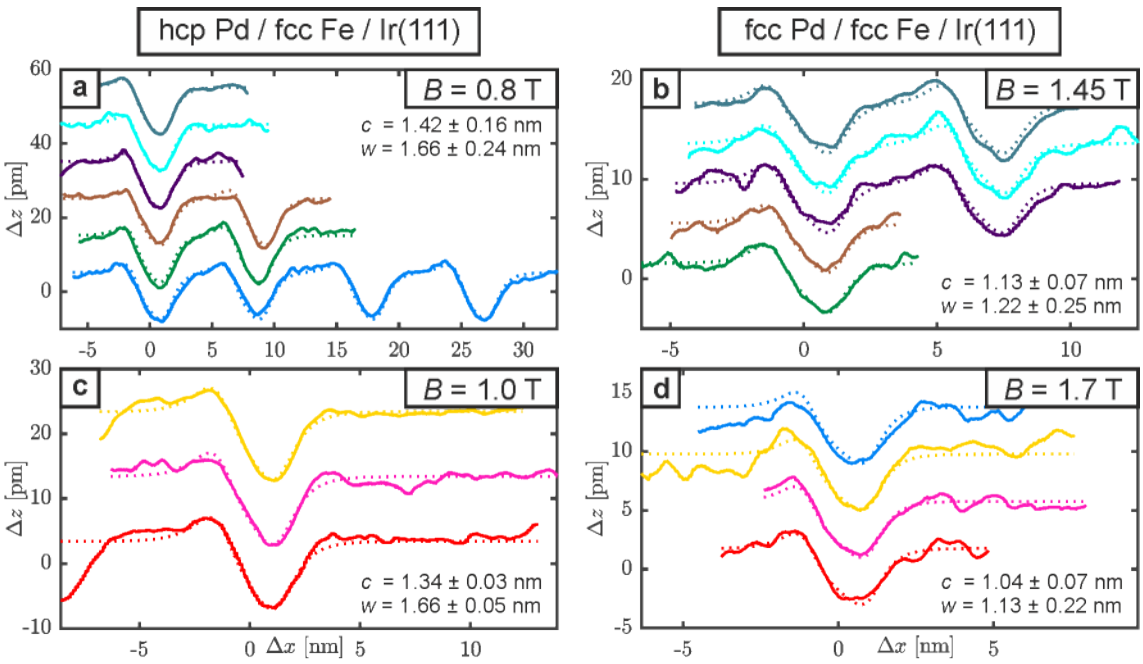

Figure 5.3.: Line profiles of 360°-DWs in the ML Pd/Fe(fcc). a-d Solid lines: Line profiles taken along the respectively coloured dashed rectangles in Fig. 5.1. Line profiles are shifted vertically by multiples of 10 pm (hcp Pd) or 4 pm (fcc Pd) and laterally to align the centres of the first domain walls for better visibility. Dashed lines: simultaneous fits for each magnetic field with sums of Eq. (1.19) combined with Eq. (1.25). During the fits, the tip polar angle θ, the amplitude a and the characteristic 360°-DW-parameters c and w were shared, whereas their lateral ($x_{0,i}$) and vertical shifts ($z_{0,i}$) were left free.

single defects is minimised and the parameters c and w are the ones that describe the complete set of 360°-DWs at one magnetic field best.

The resulting 360°-DW-parameters c and w, as shown in Fig. 5.3, are used together with the zero-field spin spiral period λ, as shown in Fig. 5.1c, as input values for a fitting procedure according to Eq. (1.21). The resulting magnetic material parameter sets are:

$$\begin{aligned} \text{hcp}: \quad & A = (2.6 \pm 0.2)\,\text{pJ m}^{-1}, \quad D = (4.7 \pm 0.4)\,\text{mJ m}^{-2}, \quad K = (3.2 \pm 0.4)\,\text{MJ m}^{-3} \\ \text{fcc}: \quad & A = (3.1 \pm 0.7)\,\text{pJ m}^{-1}, \quad D = (6.6 \pm 2.0)\,\text{mJ m}^{-2}, \quad K = (8.0 \pm 4.0)\,\text{MJ m}^{-3}, \end{aligned}$$

with $M_\text{S} = 1.1 \times 10^6\,\text{A m}^{-1}$ being fixed as input. This results in reduced material parameters (as defined in Eq. (1.9)) of $k = 1.5 \pm 0.2$ and $k = 2.4 \pm 0.5$ for hcp and fcc Pd, respectively. As evident from the comparably large uncertainties, these results can only serve as a rough estimate of the material specific parameters. Nonetheless, the comparison of the values for hcp Pd/Fe/Ir(111) with the ones obtained in Chapter 4 validates this approach to estimate material parameters from the zero-field SS period and the size and shapes of 360°-DWs in magnetic fields (360°-DWs were also used in [Kubetzka *et al.*, 2003] to estimate magnetic material parameters).

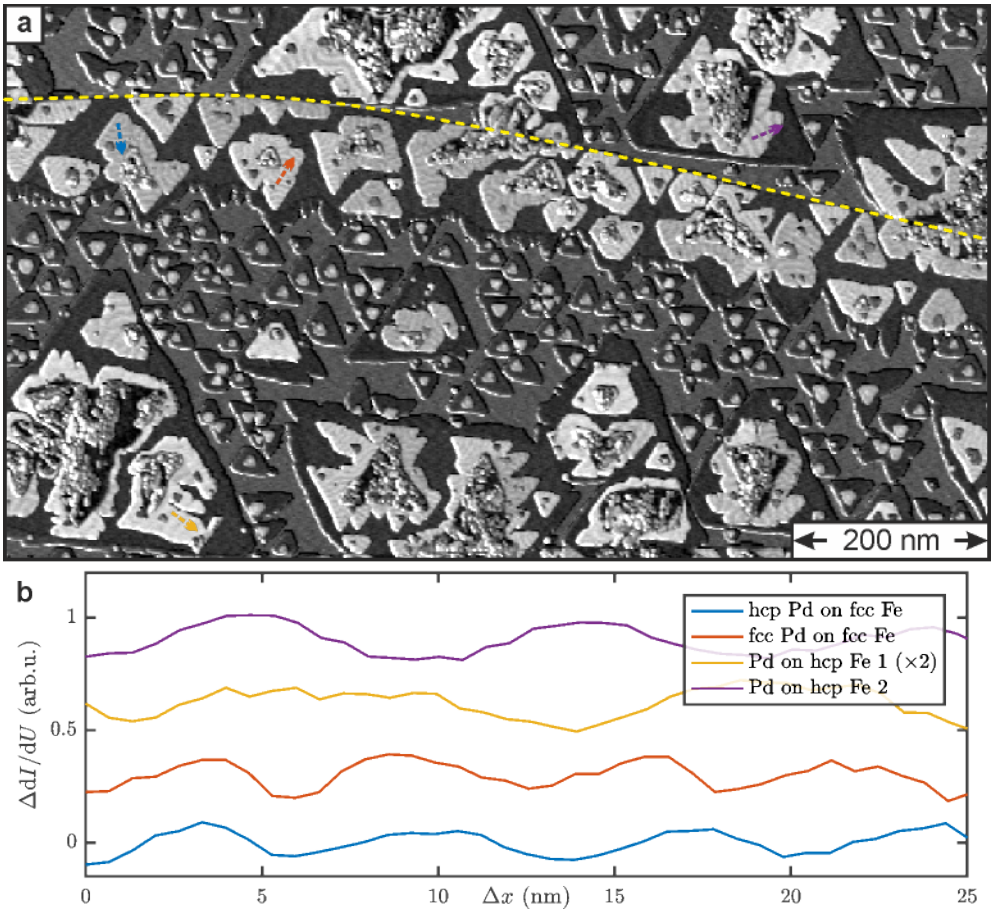

Figure 5.4.: Pd on hcp Fe. a dI/dU-map of Pd/Fe/Ir(111)-sample with fcc and hcp Fe areas. $T = 4.2\,\mathrm{K}$, $I_{\mathrm{set}} = 300\,\mathrm{pA}$, $U = +700\,\mathrm{mV}$, $U_{\mathrm{mod}} = 70\,\mathrm{mV}$. Dashed yellow line marks an Ir step edge. **b** Line profiles taken along the dashed arrows in **a** coloured accordingly, vertically offset by multiples of 0.3 arb.u., Yellow line was scaled by a factor of 2.

One way to assess whether it is reasonable to use the material parameters and with them the applied model to describe a certain skyrmionic system, is to classify them with respect to the phase diagram, as derived by Wilson *et al.* As obvious from the marked k-ranges in Fig. 5.7, the model works well to describe hcp Pd, because the k-range indicates a part of the phase diagram, in which the typical phase transitions are expected (SS, SkX, FM). The respective transition fields can be estimated, following Section 1.1.3, to $B_{\mathrm{SS-Sk}} = (0.53 \pm 0.11)\,\mathrm{T}$ and $B_{\mathrm{Sk-FM}} = (0.85 \pm 0.27)\,\mathrm{T}$, which is in reasonable agreement with the experimental observations ($B^{\mathrm{hcp}}_{\mathrm{SS-Sk}} \leq 0.8\,\mathrm{T}$, $B^{\mathrm{hcp}}_{\mathrm{Sk-FM}} \leq 1.2\,\mathrm{T}$).

In contrast, for the fcc stacking the obtained k-range is above the area, in which SkXs are expected and also in parts above the area, in which SS ground states are expected, in general. This is a strong indication that this model - including only exchange, DMI and anisotropy - is not sufficient for capturing all characteristic properties of fcc Pd/Fe/Ir(111).

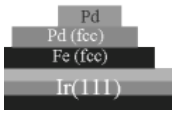

5.2. Pd on hcp Fe: Increase of the Magnetic Period

Besides the previously treated fcc growth of Fe at Ir step edges, the Fe can also grow in hcp stacking (see also Chapter 2), leading to another two possible stacking combinations of Pd/Fe/Ir(111). Figure 5.4 shows the dI/dU-map of a large overview of a particular sample preparation of PdFe on an Ir(111)-crystal with, in this area, very large terraces (one visible step edge is marked by the dashed yellow line). Due to kinetic growth of Fe and Pd, these large terraces lead to a different sample morphology (see Chapter 2). At the upward step edge, marked by the dashed yellow line in Fig. 5.4, there is a stripe of fcc step-flow grown Fe. Further away from this step edge, many Fe islands have formed. Since the Fe is not forced by the fcc Ir edge to continue this stacking, the Fe islands can grow in either possible stacking, resulting in hcp (here up-pointing triangular shapes) and fcc islands (here down-pointing triangular shapes) of various sizes. The magnetic ground state of the hcp Fe/Ir(111) is known to be a hexagonal nanoskyrmion lattice [von Bergmann *et al.*, 2015]. On top of the Fe, there are islands of Pd visible. As known from the previous section, the Pd also grows in both stackings on the fcc Fe. The well-known SS ground state with roughly 6 to 8 nm periodicity can be seen as modulations in the SP-STM-image (Fig. 5.4), despite the low resolution.

In addition to the already known magnetic system Pd on fcc Fe on Ir(111), there are islands of Pd on hcp Fe visible in Fig. 5.4a. It is already evident from the image that the magnetic periodicities on these islands are larger. By looking at several line profiles taken from a number of islands, see Fig. 5.4b, the magnetic periodicity of both stackings of Pd on hcp Fe can be estimated to approximately 10 nm and 15 nm for the two stackings of Pd, respectively. Compared to Pd on fcc Fe, this change could be explained by e.g. an increase of the exchange stiffness or a decrease of the effective DMI. Unfortunately, there is no additional data on this stacking combination of Pd on hcp Fe. Therefore, the two possible magnetic systems of Pd on hcp Fe are not investigated in more detail in this work and no magnetic material parameters can be estimated. Since the occurrence of large hcp Fe patches on a regularly stepped Ir(111)-crystal is quite rare, the following sections focus on Pd on fcc Fe only.

5.3. Pd on fcc Pd/fcc Fe: Skyrmion Lattice up to 7T

As seen on some of the previously shown Pd/Fe/Ir(111) islands, also the second layer of Pd grows pseudomorphically, adding more possibilities for tuning the magnetism in Fe/Ir(111). Figure 5.5a shows the topography of a Pd/Fe/Ir(111) sample at high Pd coverage, deposited shortly after Fe, therefore at elevated temperature. This leads to the growth of hexagonal to triangular Pd islands on fcc Pd on fcc Fe. The stacking of the second layer of Pd is unknown in this case, although the island shapes suggest that mostly one energetically

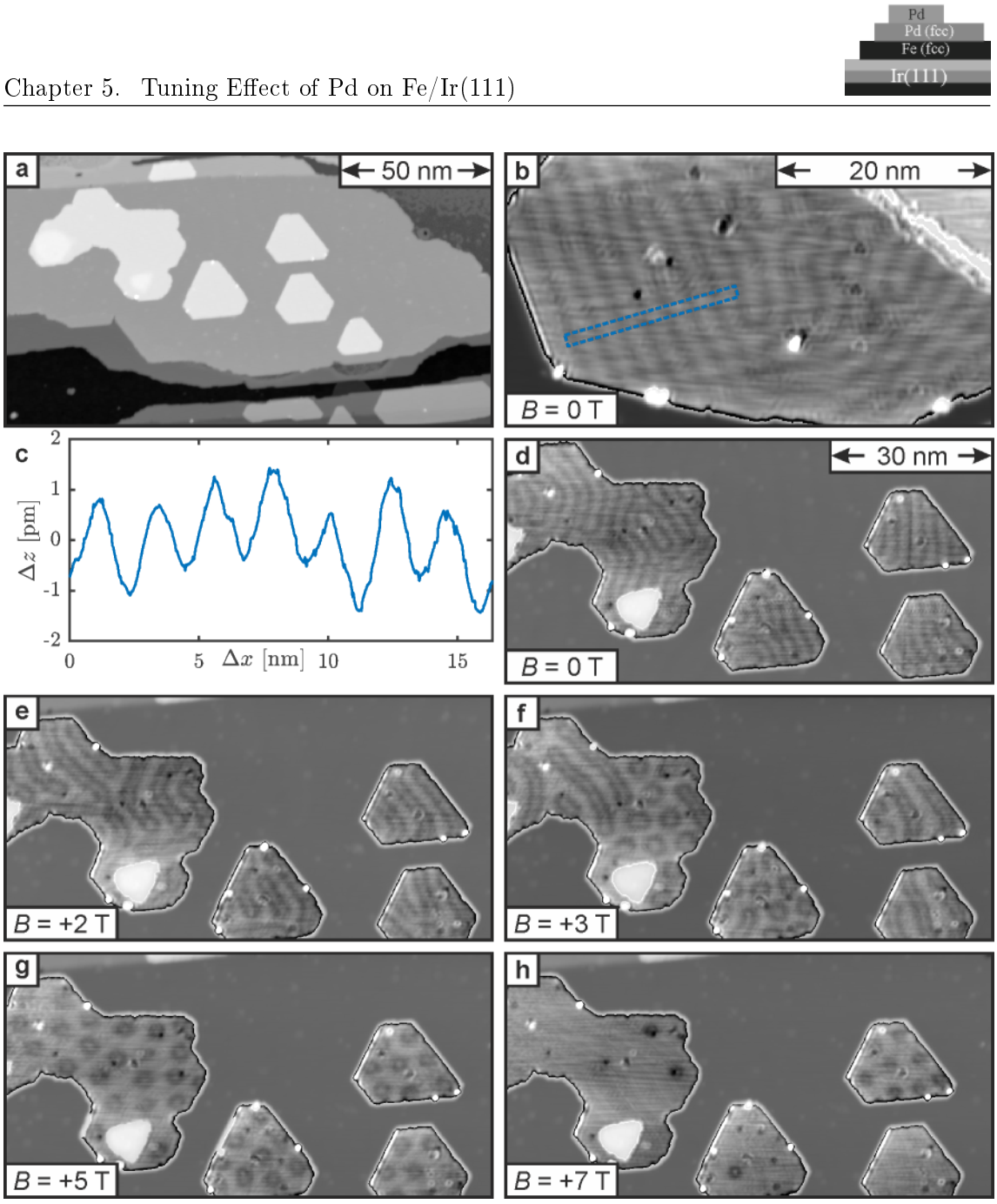

Figure 5.5.: Magnetic field dependent evolution of Pd on Pd(fcc)/Fe(fcc). **a** Topography overview STM image of a Pd/Fe/Ir(111)-sample. **b** Topography image with contrast adjusted locally to ±10 pm. Gauß-filtered in y-direction with $\sigma = 1.2$ Å. **c** Line profile taken along dashed rectangle in **b**. **d-h** Topography images with contrast adjusted locally to ±10 pm. Gauß-filtered in y-direction with $\sigma = 1.2$ Å. $T = 4.2$ K, $I_{\text{set}} = 1$ nA, **a:** $U = +50$ mV, **b:** $U = +30$ mV, **d-h:** $U = +50$ mV.

preferred stacking occurs[2]. Figures 5.5d-h show three small and one larger DL Pd island at different out-of-plane magnetic fields B. The magnetic states are imaged using the NCMR-contrast [Hanneken *et al.*, 2015; Kubetzka *et al.*, 2017]. This can be easily identified in

[2]The small patches of higher height in the large DL island are attributed to the less common other stacking.

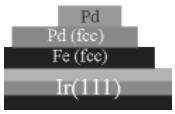

Fig. 5.5e, as - upon application of a magnetic field - the stripe pattern develops a periodicity with twice the period of the pattern in Fig. 5.5b,d, which is an expected observation for spin spirals in magnetic field, imaged with the NCMR. The parts of the SS, which are (close to) parallel to B, expand and the antiparallel parts compress. Therefore, the SS locally becomes less or more non-collinear, hence attenuating or enhancing the NCMR, respectively. Lower signal in the $\mathrm{d}I/\mathrm{d}U$-maps can therefore be attributed to a higher degree of non-collinearity. A homogeneous SS with the same magnetisation gradient over the whole period would not produce a periodic NCMR-signal without magnetic field, since the degree of non-collinearity is constant. Therefore, one can conclude from Fig. 5.5b-d that the SS is inhomogeneous, thus being influenced by some considerable effective anisotropy. From the fact that the bright parts (without magnetic field) grow/shrink upon application of an out-of-plane magnetic field, these can be attributed to the more slowly rotating out-of-plane areas of the SS. This leads to the conclusion that the anisotropy is of the easy-axis out-of-plane type. The magnetic period of the SS is twice the visible periodicity of the NCMR signal, therefore $\lambda_{\mathrm{DLPd}} \approx 4.6\,\mathrm{nm}$, see Fig. 5.5c. At $B = 3\,\mathrm{T}$, Fig. 5.5f, the transition field to the SkX state is reached and the first typical doughnut shaped skyrmions appear (when imaged with the NCMR). At least up to a field of 5 T, the SkX prevails, showing a mostly hexagonal order (disturbed by defects), Fig. 5.5e. Between 5 and 7 T, the magnetic structure undergoes a phase transition to FM alignment of most spins except for few single skyrmions, pinned at defects and for the remaining SkX in the upper right island, Fig. 5.5h. This is probably induced by an increased hysteresis effect in smaller islands and will be discussed in more detail in section 6.3.

Once again, it is attempted to estimate the magnetic material parameters from the experimental observations. This time, there is no TMR-contrast of 360°-DWs or skyrmions in magnetic field, but only NCMR-based data, which cannot be used in a straightforward way to extract their size and shape. Therefore, different characteristic values are used as input for the fitting procedure based on Eq. (1.21), i.e. the zero field spin spiral period $\lambda = (4.6 \pm 0.3)\,\mathrm{nm}$ and the phase transition fields $B_{\mathrm{SS-Sk}} = (3.0 \pm 0.6)\,\mathrm{T}$ and $B_{\mathrm{Sk-FM}} = (6.0 \pm 1.2)\,\mathrm{T}$. As mentioned in Section 5.1, the accurate values for the transition fields are difficult to extract without systematic errors, meaning the results from this fit are less trustworthy. With these experimental observations as input, the fit converges to two solutions, one in the k-range between points **A** and **B**, and one between points **B** and **C** in Fig. 1.2b. With the same saturation magnetisation as for the MLs Pd/Fe/Ir(111)[3], the material parameters result to:

[3] Of course, the mean saturation magnetisation of the DL Pd on Fe is significantly different from the ML Pd on Fe. Nonetheless, M_{S} only has a scaling effect in this fit. The fit converges for an arbitrarily chosen M_{S}, with the same k but scaled A, D and K. For a better comparability and since most of the magnetic moment is located at the Fe, M_{S} is kept the same here.

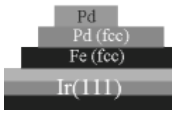

Pd on fcc Pd, $k = 0.09 \pm 0.07$:

$A = (4.1 \pm 1.0)\,\mathrm{pJ\,m^{-1}}$, $D = (12 \pm 2)\,\mathrm{mJ\,m^{-2}}$, $K = (0.55 \pm 0.12)\,\mathrm{MJ\,m^{-3}}$

Pd on fcc Pd, $k = 1.1 \pm 0.4$:

$A = (5.8 \pm 2.0)\,\mathrm{pJ\,m^{-1}}$, $D = (16 \pm 5)\,\mathrm{mJ\,m^{-2}}$, $K = (14 \pm 8)\,\mathrm{MJ\,m^{-3}}$

To decide which of the two solutions is the better one to describe the experiment, more input parameters would be needed. Despite the large uncertainties of these parameters, the following conclusions can be made: Although the fit converges within the reasonable k-range of Fig. 5.7, the large D and also its large change compared to the ML fcc Pd on Fe serve as an indication that the simple model is also insufficient to describe the system Pd on fcc Pd/Fe/Ir(111) completely.

5.4. Pd on hcp Pd/fcc Fe: Skyrmions at 9T

In this section, islands of the second layer of Pd grown on hcp Pd on fcc Fe/Ir(111) are studied. Figure 5.6a shows the dI/dU-map of a sample preparation with a large coverage of Pd. Besides the previously shown fcc ML Pd, there are also areas of hcp stacked Pd possible in such samples, as seen as the large, dark ML area on the left side of Fig. 5.6a. The brighter area on the right corresponds to fcc Pd/Fe/Ir(111). It will be shown in this section that the magnetism of the DL Pd differs significantly depending on the stacking of the underlying ML Pd. The stacking of the second layer of Pd is once again unknown in this case, although the island shapes and the dI/dU-contrast in Fig. 5.6a also suggest that mostly one stacking occurs.

Figure 5.6c shows an SP-STM image of several DL Pd islands on hcp Pd without an external magnetic field. By looking at the line profile (Fig. 5.6b), which was taken on the largest of the islands (rectangle in Fig. 5.6c), the magnetic period can be estimated to around 3.4 nm. As done previously, together with the magnetic field evolution, the period can be used to identify the material parameters that are changed by the adlayer.

In Fig. 5.6d, a change of the magnetic structure towards a SkX is starting to appear at $B = 1.5\,\mathrm{T}$. This is already roughly twice the value for the phase transition field of the ML hcp Pd. After scanning the same area with $U = +700\,\mathrm{mV}$ (not shown), the transition to a skyrmion lattice is nearly complete (Fig. 5.6e). The approximated phase transition field $B_{\mathrm{SS-Sk}} \approx 1.5\,\mathrm{T}$ could be under- or overestimated due to directed tip-mediated effects (see Chapter 3 and Section 5.1). Also the following images in Fig. 5.6f-h show skyrmions in the DL islands at magnetic fields of $B = 3\,\mathrm{T}$, $7\,\mathrm{T}$ and $9\,\mathrm{T}$. Only at $B = 9\,\mathrm{T}$ (Fig. 5.6h), the skyrmion density seems to decrease, which indicates an approach of the second phase transition field at $B_{\mathrm{Sk-FM}} > 9\,\mathrm{T}$. This is a remarkably high value compared to previous experimental results on skyrmionic systems.

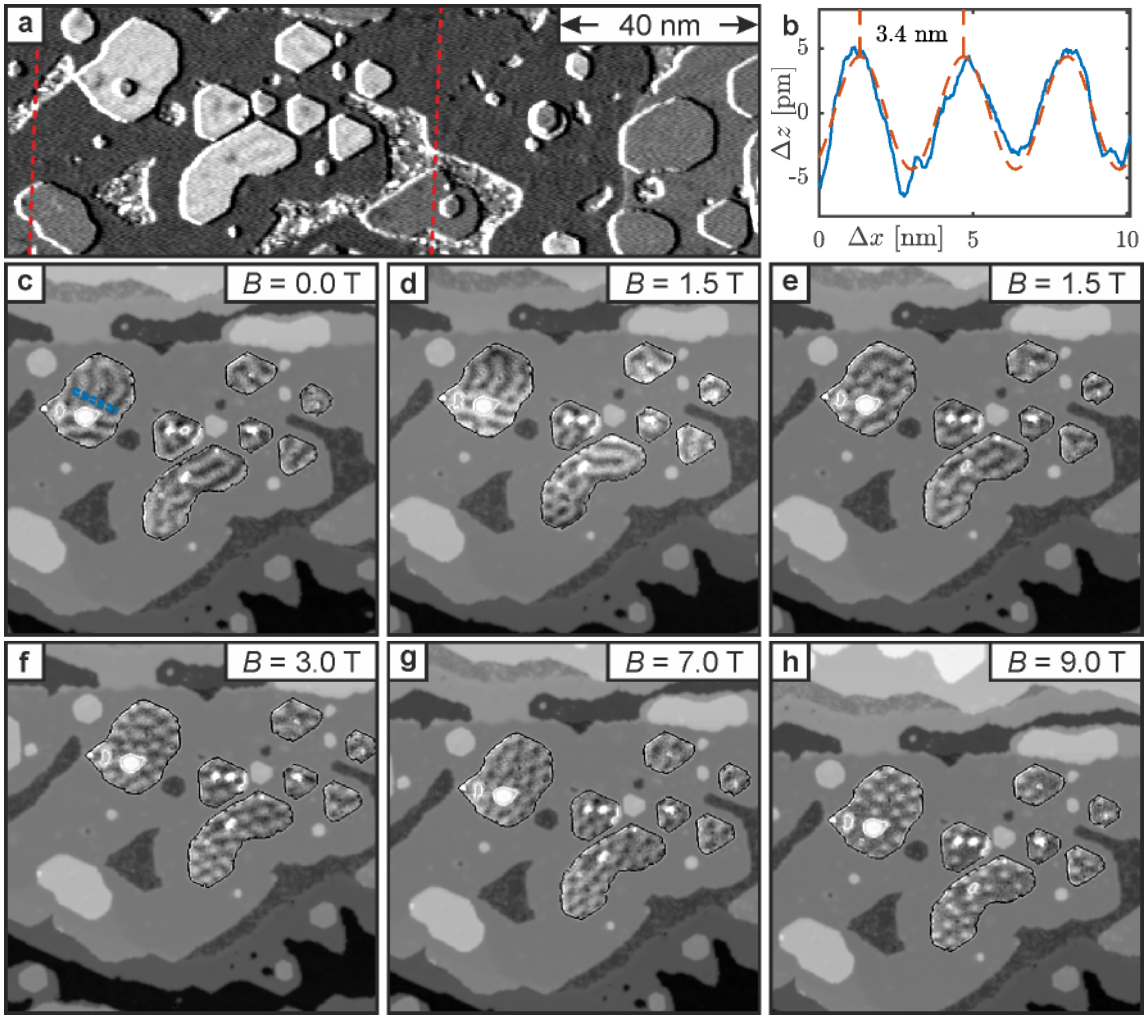

Figure 5.6.: Magnetic field dependent evolution of Pd on Pd(hcp)/Fe(fcc). a $\mathrm{d}I/\mathrm{d}U$-map ($U_{\mathrm{mod}} = 17\,\mathrm{mV}$) of Pd/Fe/Ir(111)-sample, red dashed rectangle indicates scan area of images **c-h**. **b** Line profile taken along dashed rectangle in **c** (blue solid line). Red dashed line is a cosine-fit as guide to the eye. **c-h** SP-STM images with contrast adjusted locally to ±15 pm. Cr-bulk tip, $T = 4.2\,\mathrm{K}$, $I_{\mathrm{set}} = 1.5\,\mathrm{nA}$, **a:** $U = -170\,\mathrm{mV}$, **c-h:** $U = +12\,\mathrm{mV}$.

The large magnetic field range, in which the SkX is stable and the high transition field $B_{\mathrm{Sk-FM}} > 9\,\mathrm{T}$ can be used to further estimate the tuning effect of the second layer of Pd. Similar to the fitting procedure in the previous section, the zero field spin spiral period $\lambda = (3.4 \pm 0.3)\,\mathrm{nm}$ and the phase transition fields $B_{\mathrm{SS-Sk}} = (1.5 \pm 0.4)\,\mathrm{T}$ and $B_{\mathrm{Sk-FM}} = (9 \pm 1)\,\mathrm{T}$ are used to estimate the magnetic material parameters. The fit terminates at $k = 0.32 \pm 0.10$, which seems to be the position of the maximum field range of the SkX in Fig. 5.7, for all random start parameters. Nonetheless, the large spread between the transition fields cannot be reproduced within this model. The closest fit is $B_{\mathrm{SS-Sk}} = (2.3 \pm 0.3)\,\mathrm{T}$ and $B_{\mathrm{Sk-FM}} = (7.4 \pm 0.8)\,\mathrm{T}$ for:

$$\begin{array}{ll} \text{Pd on hcp Pd:} & A = (1.8 \pm 0.4)\,\mathrm{pJ\,m^{-1}}, \quad D = (6.7 \pm 0.9)\,\mathrm{mJ\,m^{-2}}, \\ \text{(not converged)} & K = (2.0 \pm 0.2)\,\mathrm{MJ\,m^{-3}} \end{array}$$

The failure of the fit to converge for these experimental input parameters suggests that the simple model including only A, D, K and M is also not sufficient to describe the system Pd on hcp Pd/Fe/Ir(111).

5.5. Summary of Magnetic Systems of Pd/Fe/Ir(111), Applicability of the Micromagnetic Model

As seen in the previous sections, the stackings of both the Fe layer as well as the additional Pd layer(s) play an important role in fine-tuning the magnetism of the resulting sample system. Although one ML of Fe on the Ir(111)-crystal is common to all of the magnetic systems shown in this chapter, their characteristic properties vary widely. Also in the sample systems with a DL Pd, skyrmions/SkXs were discovered, even up to a magnetic field of 9 T. For a better overview, the main properties of the PdFe based systems obtained from experiments are summarised in Table 5.1.

magnetic system on Ir(111)	λ (nm)	$B_{\mathrm{SS-Sk}}$ (T)	$B_{\mathrm{Sk-FM}}$ (T)	section
hcp Pd / fcc Fe	7.2 ± 0.4	0.8	≤ 1.2	5.1
fcc Pd / fcc Fe	6.4 ± 0.3	1.0	1.4-1.7	
Pd / hcp Fe	$10 - 15$	–	–	5.2
Pd / fcc Pd / fcc Fe	4.6 ± 0.3	3.0 ± 0.6	6.0 ± 1.2	5.3
Pd / hcp Pd / fcc Fe	3.4 ± 0.3	1.5 ± 0.4	$> 9 \pm 1$	5.4

Table 5.1.: Summary of magnetic systems based on Pd and Fe on Ir(111). Characteristic magnetic properties for the Pd and Fe based systems as obtained from experiments in this chapter.

Several observations can be made when comparing the different systems of Pd/Fe/Ir(111). The spin spiral period, for example, ranges from 3.4 to 15 nm. There is no systematic dependence of the period on the stackings of neither Pd nor Fe. Whereas for the ML, the period is longer for the hcp stacked Pd, for the DL, the fcc stacked Pd has the longer magnetic period. Since the spin spiral period depends on the (frustrated) exchange and the strength of the DMI, at least one of these interactions has to be different for the different systems. Since the DMI is expected to stem mostly from the interface between Fe and the Ir-crystal [Fert and Levy, 1980; Crépieux and Lacroix, 1998; Finco *et al.*, 2016], it should only be different for Pd on hcp Fe/Ir(111). The other systems all share the same interface

between the fcc Fe and the Ir-crystal and should thus all have a similar size of the DMI[4]. Hence, the main tuning effect is expected to be via the effective exchange interaction.

magnetic system on fcc Fe/Ir(111)	inputs	k	A ($\mathrm{J\,m^{-1}}$)	D ($\mathrm{J\,m^{-2}}$)	K ($\mathrm{J\,m^{-3}}$)
hcp Pd	Sk	1.3 ± 0.2	2.0 ± 0.4	3.9 ± 0.2	2.5 ± 0.2
	λ, DW, Sk	1.28 ± 0.19	1.95 ± 0.29	3.86 ± 0.55	2.50 ± 0.74
	λ, DW	1.5 ± 0.2	2.6 ± 0.2	4.7 ± 0.4	3.2 ± 0.4
fcc Pd	λ, DW	2.4 ± 0.5	3.1 ± 0.7	6.6 ± 2.0	8.0 ± 4.0
Pd / fcc Pd	λ, B_T	0.09 ± 0.07	4.1 ± 1.0	12 ± 2	0.6 ± 0.1
		1.1 ± 0.4	5.8 ± 2.0	16 ± 5	14 ± 8
Pd / hcp Pd	λ, B_T	0.32 ± 0.10	1.8 ± 0.4	6.7 ± 0.9	2.0 ± 0.2

Table 5.2.: Summary of material parameters of PdFe based systems. Results of the fitting procedures according to Eq. (1.21) with the inputs as shown (λ: SS period Eq. (1.15); DW c, w: 360°-DW Eq. (1.20); Sk c, w: skyrmion size and shape Eq. (6.2); B_T: magnetic phase transition fields Eqs. (1.13) and (1.14)). Green k-value marks a converged fit to a reasonable result that also describes other characteristic properties well. Orange k-values indicate satisfactory convergence of the fit but unreasonable results, concerning other characteristic properties. Red k-value denotes the fit's failure to reproduce the input experimental parameters.

Table 5.2 shows a summary of the different fitting procedures applied in this chapter and the previous one, and their results for the reduced anisotropy k (Eq. (1.9)), effective exchange stiffness A, DMI strength D and effective anisotropy constant K. As can be seen from the magnetic material parameters, all of the parameters change significantly depending on the sample system. Especially the large change in D cannot be real due to the above stated reasons.

Within the model applied in this chapter, which was originally used by Bogdanov and Yablonsky to predict the existence of skyrmions, the exchange constant A can only describe effective ferromagnetic exchange interactions. The model cannot describe spin spirals driven by frustrated exchange or complex shapes of spin spiral energy dispersions (only parabolic shapes are possible, see below). Depending on which magnetic characteristic is used as input to the fit and how frustrated exchange influences this magnetic property, the effect of the frustrated exchange will lead to a misestimation of any of the material parameters. For instance, in the model, the zero field spin spiral period λ depends, besides A, mostly on D, see Eq. (1.15). Therefore, D would be the parameter that is overestimated to compensate for frustrated exchange. Considering a 360°-DW, only A, K and M

[4] In principle, the Pd adlayer(s) can also contribute to the DMI directly or can indirectly lead to a change in DMI due to a different hybridisation of the Fe and the Ir or a different interlayer relaxation. Here, these changes are considered minor and not sufficient to describe a change in λ by a factor of two.

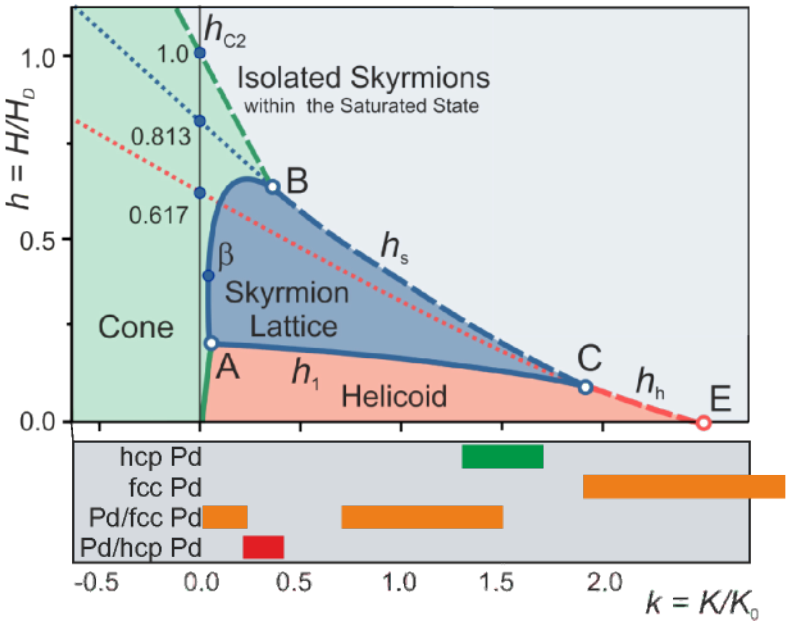

Figure 5.7.: Phase diagram by Wilson *et al.* – adapted version of Fig. 1.2b. The coloured bars at the bottom indicate the obtained k-range from fits to experimental input parameters with Eq. (1.21) (see text). Adapted with permission from [Wilson *et al.*, 2014]. Copyrighted by the American Physical Society.

determine the magnetic field dependent size and shape (see Eq. (1.20)). Should there be frustration of exchange interactions in the magnetic system, either of the three parameters will be estimated falsely.

Another observation when comparing the different magnetic systems in Table 5.1 is the large spread in the magnetic fields for the phase transitions. These depend on the depth of the spin spiral energy minimum compared to the Zeeman-energy. In reality, the depth of the spin spiral energy minimum and with it the transition fields are determined by a combination of frustrated exchange interactions and the DMI. Within the applied model, this depth can again only be increased by an increase of D. Large transition fields, caused by frustration of exchange, therefore again lead to an overestimation of D or cannot be explained at all, as seen for Pd on hcp Pd/Fe/Ir(111).

Summarising the tuning effect of Pd on a ML of Fe/Ir(111), it was shown that (1) the stacking of the Fe and the Pd is very important and can change the magnetic characteristics to a significant extent. (2) All of the investigated magnetic systems exhibit a spin spiral ground state, and it was shown for all but Pd on hcp Fe/Ir(111) that they undergo phase transitions to the SkX and the FM state. (3) The model originally proposed by Bogdanov and Yablonsky to describe skyrmionic systems is not sufficient for describing all of the systems coherently. For hcp Pd, the model produces reasonable results and can describe the magnetic characteristics investigated here. As shown in Chapter 4, it can also describe

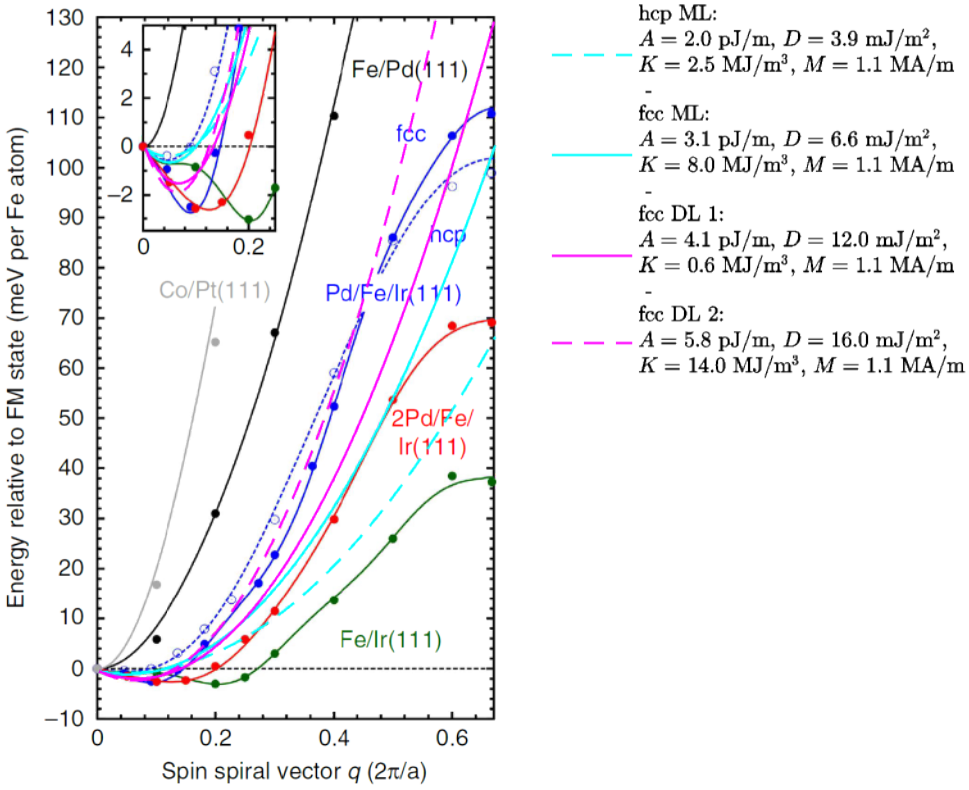

Figure 5.8.: Comparison of the model with spin spiral dispersion calculations. Energy dispersion of homogeneous SSs including SOC along the high-symmetry direction $\bar{\Gamma} - \bar{K}$ with respect to the FM state, performed by the group of Prof. Stefan Heinze, Univ. Kiel, reprinted by permission from Macmillan Publishers Ltd: [Dupé *et al.*, 2014, Fig. 4], copyright (2014). The additional parabolic graphs represent the calculated energy dispersion for a homogeneous SS in the micromagnetic model by Eq. (5.1) with the micromagnetic parameters of the various PdFe-layers as indicated.

skyrmions at higher magnetic field. For fcc Pd, the model converges to values outside the range where SkXs are expected although there is clear experimental evidence for skyrmions. The material parameters obtained for Pd on fcc Pd are within the reasonable range of the phase diagram, but the values of D and K are unexpectedly high. Finally, the observed phase transitions for Pd on hcp Pd were not reproducible by the model.

This leads to the conclusion that at least one interaction mechanism, which is not included in the micromagnetic model, plays an important role in these systems. As it is known from DFT calculations [Dupé *et al.*, 2014, 2016; Simon *et al.*, 2014b; Romming *et al.*, 2016], a possible missing element in the model is the frustration of exchange interactions, which also leads to a SS ground state without the need for DMI. This becomes particularly clear when looking at the energy dispersion of homogeneous SSs as obtained by DFT calculations, see Fig. 5.8. Besides the spin spiral energies from DFT and their corresponding fitted curves with an extended Heisenberg model up to the 10^{th} neighbour,

the calculated energy dispersions for the material parameters obtained in this and the previous chapter are added to the graph. Within the micromagnetic model, the energy of a homogeneous spin spiral is calculated as:

$$E_{\mathrm{SS/Fe}} = \left(Aq^2 - Dq + \frac{K}{2} \right) \cdot \frac{\sqrt{3}a^2 t}{2} \tag{5.1}$$

per Fe-atom. Obviously, within this model only parabolic energy dispersions are possible. A is responsible for the pitch of the parabola, whereas D shifts it towards the down-right direction and K only adds a vertical offset. Whereas the energy dispersions within the simple model can describe the SS energies of FM systems like Co/Pt(111) or Fe/Pd(111) well, other shapes of energy dispersions cannot be reproduced sufficiently, see Fig. 5.8. It may well be possible that the energy minimum and its close vicinity are captured by the micromagnetic model, but the shape at higher q and thereby higher angles between neighbours significantly differs from the energies obtained by DFT. Also a minimum at any $q \neq 0$ can only be produced within the micromagnetic model by D. If the minimum is produced, contrarily, by e.g. frustration of exchange interactions, it will be falsely interpreted as a large DMI within the micromagnetic model.

Figure 5.8 and additional calculations from [Dupé *et al.*, 2014; Simon *et al.*, 2014b] show that indeed frustration of exchange interactions plays a decisive role for the systems investigated in this chapter, except for hcp Pd/Fe/Ir(111), in which it plays less of a role. It is therefore not surprising that the micromagnetic model works well for hcp but not for fcc Pd/Fe/Ir(111) or the DL systems.

Chapter 6.

Novel Magnetic States: Topology and Edges

Besides spin spirals and skyrmions, there are several other magnetic structures with interesting geometric and topological properties made up of combinations of skyrmions. One concept to classify non-collinear spin structures and to distinguish between different ones, is topology. The characteristic topological charge Q of a spin structure, which is essentially a measure of the magnetisation curvature and the 2D equivalent of the one-dimensional (1D) winding number, can be defined as:

$$Q = -\frac{1}{4\pi}\int_A \vec{m}\cdot\left(\frac{\partial\vec{m}}{\partial x}\times\frac{\partial\vec{m}}{\partial y}\right)dxdy. \tag{6.1}$$

Here A is the area of interest, $\vec{m}$ is the normalised magnetisation vector and x, y are the lateral spatial coordinates. Please note that for simplicity, the sign is inverted, compared to the standard definition, to have $Q = +1$ ($Q = -1$) for a regular skyrmion in a field-polarised surrounding along $+z$ ($-z$)-direction. This way, a Q with the same sign as the magnetic field refers to a regular or naturally occurring skyrmionic state with the core pointing opposite the field, whereas the opposite sign indicates an uncommon state.

Although this definition of topological charge originates in the description of continuous magnetisation vector fields, it can be adapted to discrete lattices of spins, such as a hexagonal arrangement of spins in Pd/Fe/Ir(111). Any three neighbouring spins are chosen in a counter-clockwise order (e.g. $\vec{m}_i$ in Fig. 6.1a). The topological charge emerging from the three neighbouring spins is equivalent to the signed area of the spherical triangle with the corners $\vec{m}_1$, $\vec{m}_2$ and $\vec{m}_3$ on the unit sphere [Berg and Lüscher, 1981; van Oosterom and Strackee, 1983] (see Fig. 6.1b). The calculation of this area, which is equal to the solid angle spanned by the three spins, can be facilitated by considering a plane triangle at some arbitrary point in space [van Oosterom and Strackee, 1983] (see Fig. 6.1b). The solid angle Ω can then be calculated for the three normalised spins $\vec{m}_{1,2,3}$ via the relation:

$$\tan\left(\frac{\Omega}{2}\right) = \frac{\vec{m}_1\cdot(\vec{m}_2\times\vec{m}_3)}{1+\vec{m}_1\cdot\vec{m}_2+\vec{m}_1\cdot\vec{m}_3+\vec{m}_2\cdot\vec{m}_3} \tag{6.2}$$

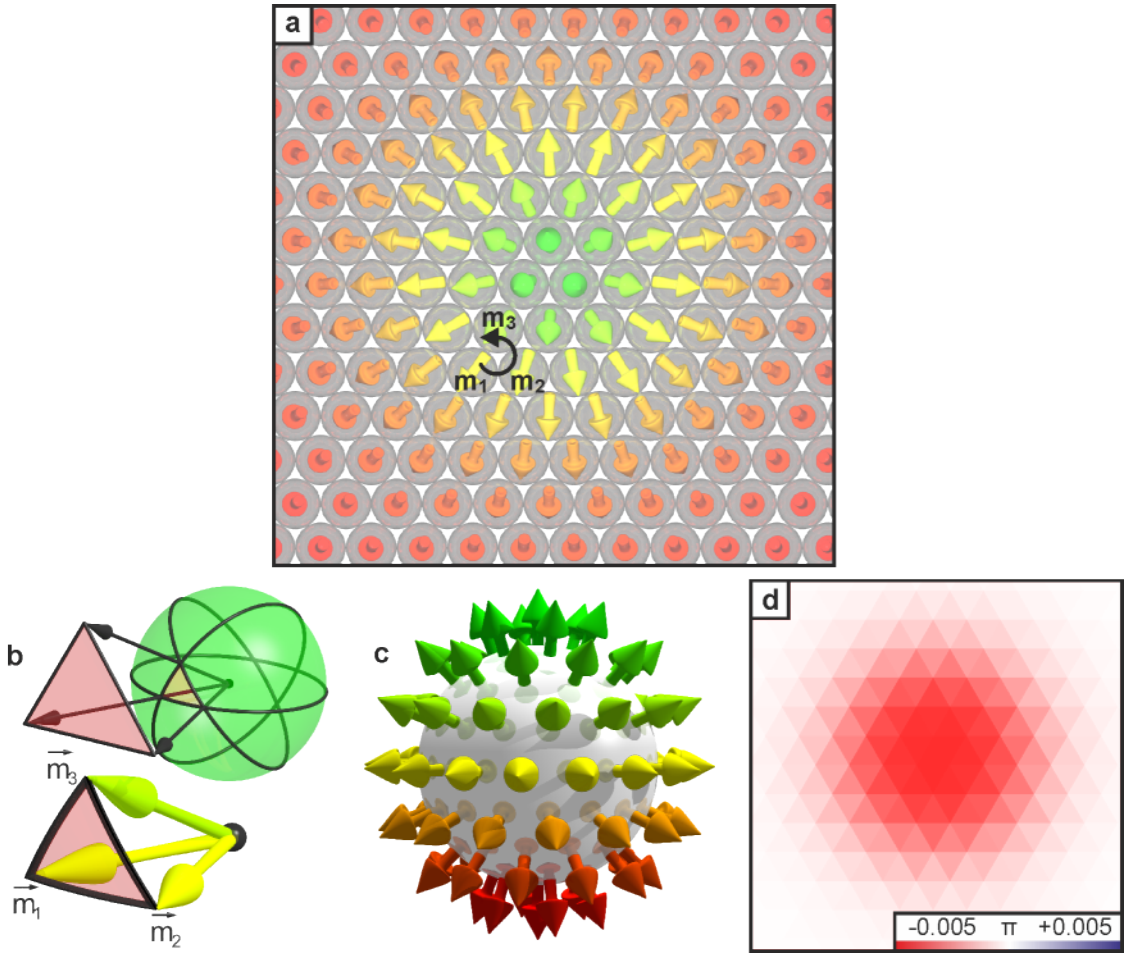

Figure 6.1.: The concept of topology in discrete magnetism. **a** Schematic 3D top view of a skyrmion made up of discrete atomic spins. **b** Schematic 3D view of three spins spanning a spherical triangle, which corresponds to the solid angle between them. The calculation of the area of the spherical triangle can be facilitated by looking at a plane triangle at an arbitrary point in space; inspired by [van Oosterom and Strackee, 1983, Fig. 1]. **c** Artistic 3D representation of the "unit sphere" of discrete spins. **d** Map of the topological charge density of the spins in panel **a** as defined by Eq. (6.3).

The topological charge corresponding to the three neighbouring spins thus equals to:

$$Q\left(\vec{m}_1, \vec{m}_2, \vec{m}_3\right) = -\frac{1}{2\pi} \arctan2\left(N, D\right), \tag{6.3}$$

with N and D the numerator and denominator of Eq. (6.2) [van Oosterom and Strackee, 1983]. Similarly to skyrmions in continuum descriptions, the topological charge of a regular skyrmion in an extended FM film results in integer values of ± 1, because the complete unit sphere of possible spin directions (Fig. 6.1c) is covered. This discrete model for topological charge can now also be used to describe the topological charge of a small island with open boundaries. Here, uncompensated topological charges at the edges can lead to non-integer

values for the net topological charge of the spin structure of the island.

Figure 6.1d shows such a map of the topological charge density of the skyrmion spin structure depicted in Fig. 6.1a. The topological charge between three neighbouring spins is represented by a coloured triangle spanned by the spin positions.

In principle, so-called topological protection does not exist for real magnetic systems. It is even debated, whether it exists in the continuum description of magnetism: although the local energy density diverges when for example skyrmions are collapsed to a Bloch-point, the associated total energy is finite [Feldtkeller, 1965; Büttner *et al.*, 2017a]. Whenever the topology of an extended magnetic system changes, such a local point of highly non-collinear spins (similar to a Bloch-point) has to form, resulting in a higher energy or potential barrier associated with the interactions involved [Cortés-Ortuño *et al.*, 2017]. Instead of topological protection, it is therefore reasonable to speak of topological energy barriers or potential barriers related to topology.

6.1. fcc Pd on fcc Fe/Ir(111) at Low Energy

In Chapter 5, the different magnetic systems have mostly been looked at in their thermodynamic equilibrium or excited state. Once the magnetic system is deprived of the energy needed to overcome e.g. topological barriers, a magnetic field induced transition of, for example, spin spirals to a SkX will be suppressed. This can be achieved by cooling the sample to even lower temperatures and using non-disturbing tunnelling parameters (low bias and current, see Chapter 3). Figure 6.2 shows topography images of fcc Pd islands on fcc Fe at a temperature of $T = 2\,\mathrm{K}$, recorded at low bias voltages. Images **a** and **b** show the same island at magnetic fields of $B = 0\,\mathrm{T}$ and $+1.75\,\mathrm{T}$, respectively. At the latter magnetic field, the system is expected to be in the SkX to FM state (see Section 5.1). Contrary to that, only very few single skyrmions are visible and still individual 360°-DWs, see Section 1.1.3, are present, pinned to defects and edges. This can be explained by the different topology of spin spirals ($Q = 0$) and skyrmions ($Q = \pm 1$). To make a transition from one to the other, topological charge has to be created (annihilated), meaning locally, spins have to become highly antiparallel (Bloch-point) and thus exchange and DMI have to be paid. If the available energy from the thermally excited electron bath of the sample or from tunnelling electrons is not sufficient to overcome this barrier, skyrmions are not created or annihilated in an extended film.

This barrier to create topological charge is lower at edges of the magnetic film [Cortés-Ortuño *et al.*, 2017]. Here, it is possible to continuously wind the magnetic structure without the need for a Bloch point. Figures 6.2c and d respectively show the spin structure and topological charge density of a 360°-DW terminating at an open boundary, just before depinning by a magnetic field. The DMI induces a tilting of spins at an island edge or

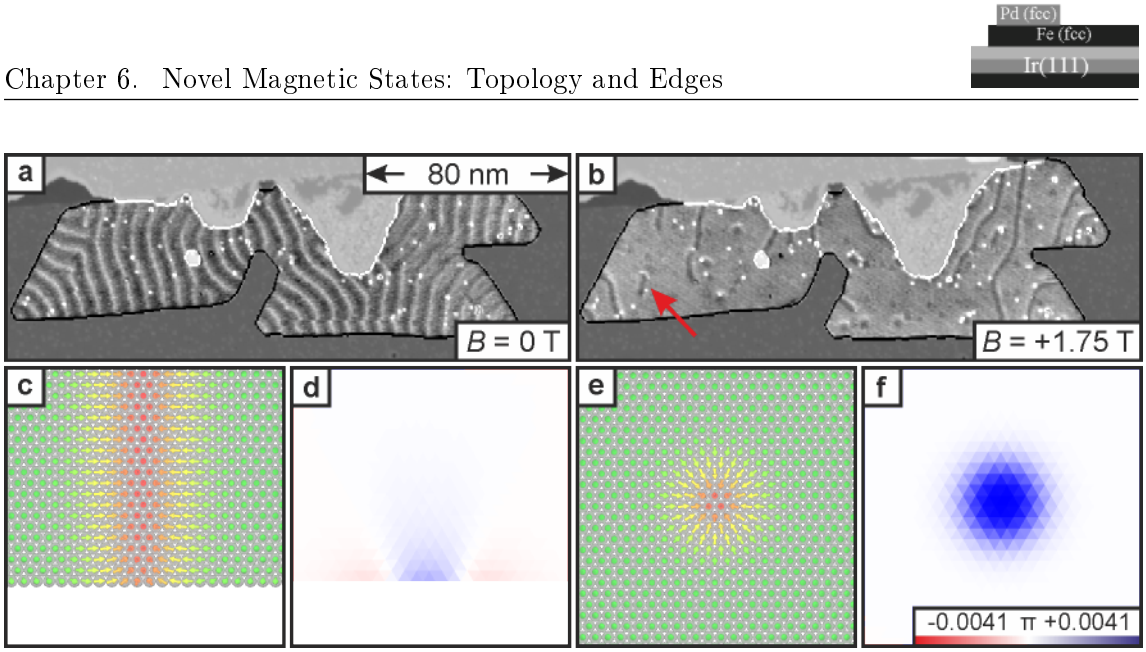

Figure 6.2.: Pd(fcc)/Fe(fcc) at 2K: Meta-stable states at low T. a,b SP-STM images with the contrast adjusted locally to ±10 pm. Measurements conducted together with Dr. André Kubetzka, Univ. Hamburg. Cr-bulk tip, $T = 2.2\,\mathrm{K}$, $I_{\mathrm{set}} = 1\,\mathrm{nA}$, $U = +100\,\mathrm{mV}$. **c** Schematic 3D top view of a simulation performed by the group of Prof. Hans Fangohr, Univ. Southampton of a PdFe island with one 360°-DW between two straight edges at $B = +3.3\,\mathrm{T}$ (details in Appendix A.2). **d** Map of the topological charge density of the spins in **c**, calculated according to Eq. (6.3). **e** Simulation as in **c** but at $B = +3.4\,\mathrm{T}$ after depinning of the 360°-DW from the edges. **f** Map of the topological charge density of the spins in **e**, similar to **d**.

open boundary [Rohart and Thiaville, 2013]. This is simply due to missing atoms on the other side, which would compensate this effect. It is evident from Fig. 6.2c and d that, in combination with the external magnetic field, this edge tilt starts to form a skyrmion-like termination of the 360°-DW. As soon as the critical magnetic field for depinning 360°-DWs from island edges is overcome, a single 360°-DW can detach from two edges, creating enough topological charge in the process to form one single skyrmion, Fig. 6.2e, f. For a real sample with inhomogeneities and pinning defects, it is also imaginable that the 360°-DW only detaches from one side and then annihilates at the other side. This can explain the direct transition of the SS in Fig. 6.2a to a mostly ferromagnetic alignment with very few skyrmions present in Fig. 6.2b.

Also in Fig. 6.2b, a section of a 360°-DW pinned between two defects is visible (red arrow). Such a segment already has the same topological charge as a skyrmion and can be seen as the transition snapshot of a single 360°-DW depinning from two edges before contracting to one skyrmion.

A similar suppression of the expected phase transitions can also be seen in Fig. 6.3a and b. Once again, the temperature is reduced to $T = 2\,\mathrm{K}$ and the bias voltage is chosen to a comparably low value of $U = +200\,\mathrm{mV}$. Figure 6.3a shows the Pd/Fe island at $B = -1.5\,\mathrm{T}$ after scanning it at higher bias of $U = +1\,\mathrm{V}$; thereby mostly pushing its magnetic state to the SkX, see Chapter 3. Figure 6.3b, shows the same island, but at $B = +1.5\,\mathrm{T}$ closely

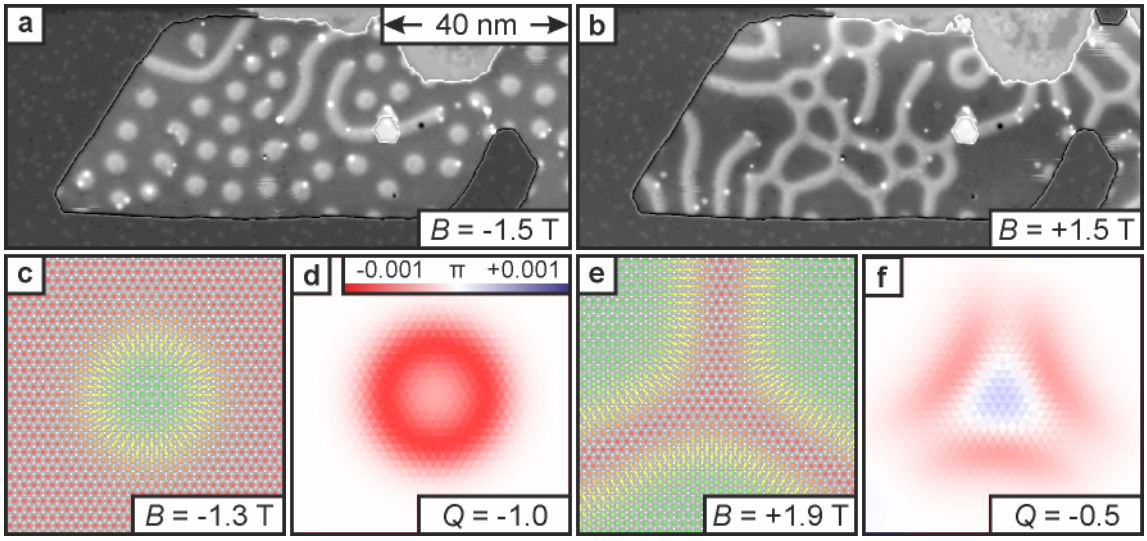

Figure 6.3.: Pd(fcc)/Fe(fcc) at 2K: Spin spiral junctions. a,b SP-STM images with contrast adjusted locally to ±20 pm. Before **a**, the area was scanned with up to +1 V and 5 nA. In between the images, the field was swept up. Measurements conducted together with Dr. André Kubetzka, Univ. Hamburg. Cr-bulk tip: the tip magnetisation reversed with the magnetic field, because there was probably a cluster at the apex of the tip with a net magnetic moment. $T = 2.2\,\mathrm{K}$, $I_{\mathrm{set}} = 1\,\mathrm{nA}$, $U = +200\,\mathrm{mV}$. **c** Schematic 3D top view of simulation performed by the group of Prof. Hans Fangohr, Univ. Southampton of a PdFe island with one skyrmion at $B = -1.3\,\mathrm{T}$ (details in Appendix A.2). **d** Map of the topological charge density of the spins in **c**, calculated according to Eq. (6.3). **e** Simulation of a PdFe island at $B = +1.9\,\mathrm{T}$, similar to **c** but started from a 5-skyrmion configuration at $B = -2.5\,\mathrm{T}$. **f** Map of the topological charge density of the spins in **e**, similar to **d**.

after changing the magnetic field, without disturbing the magnetic state by tunnelling with higher bias than $U = +200\,\mathrm{mV}$. The tip magnetisation reversed with the magnetic field and therefore shows areas parallel to the magnetic field as dark areas in both images. The resulting magnetic structure in Fig. 6.3b differs considerably from the one in a. Instead of skyrmions, the island is dominated by a network of 360°-DWs enclosing areas of spins parallel to the magnetic field.

This, once again, likely has its origin in the topology of the different magnetic states. The SkX in Fig. 6.3a possesses an integer topological charge of $Q = -1$ for every skyrmion in the island with $B = -1.5\,\mathrm{T}$, see Fig. 6.3c and d. A direct transition to a corresponding SkX at positive magnetic field, i.e. $B = +1.5\,\mathrm{T}$, would need a change in topological charge of $\Delta Q = +2$ for each skyrmion in the lattice. This process is similarly hampered, since the energy needed to overcome the potential barriers between the topologically different states is not supplied. Instead, the island in Fig. 6.3b develops a combination of topological-charge-less 360°-DWs and junctions of 360°-DWs with $Q = -0.5$, see Fig. 6.3e and f. Since there is no regular skyrmion with $Q = +1$ visible in Fig. 6.3b, the net topological charge in the island can be safely estimated to still be negative and therefore topologically closer to

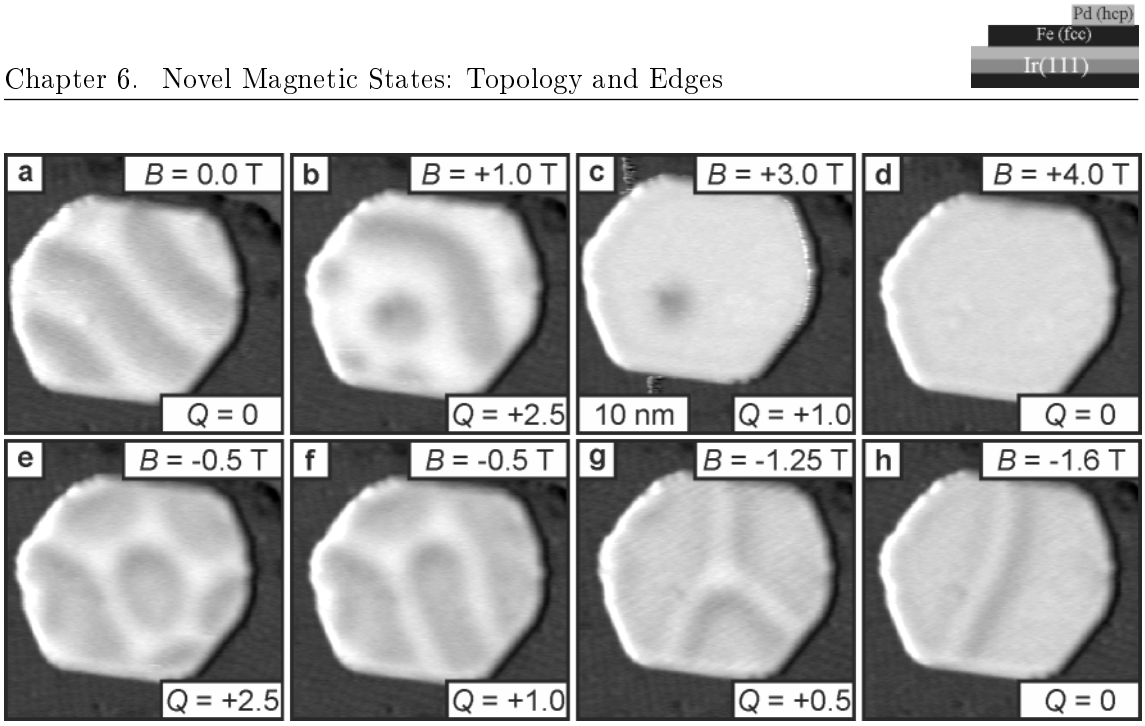

Figure 6.4.: Confined Pd(hcp)/Fe(fcc). Spin-resolved dI/dU-maps of an hcp Pd island on an fcc Fe/Ir(111) sample at different magnetic fields. Contrasts for all images are adjusted to the same values of [0.6 2.6] arb.u. Cr-bulk tip, $T = 4.2\,\mathrm{K}$, $I_{\mathrm{set}} = 1\,\mathrm{nA}$, $U = +610\,\mathrm{mV}$, $U_{\mathrm{mod}} = 38\,\mathrm{mV}$. The values for the topological charge Q were estimated from comparing the images to magnetic states in Fig. 6.5 and neglecting edge tilt.

the SkX at negative field than to a regular SkX expected at $B = +1.5\,\mathrm{T}$ in thermodynamic equilibrium. Both these measurements at reduced U and T suggest that most topological transitions take place at the island edges.

6.2. Confined ML hcp Pd/Fe/Ir(111)

The relative influence of island edges compared to the interior becomes more important when looking at small islands of Pd/Fe/Ir(111). To get well defined results that are reproducible by simulations, it is advantageous to look at regularly shaped hcp Pd islands on fcc Fe, since for this stacking, the magnetic material parameters are known from previous experiments (see [Romming *et al.*, 2015] and Chapter 4), and Chapter 5 suggests that this system is well described within the continuum model. This way, spin-dynamics simulations are expected to yield results that describe the experiments well. A well-defined growth of the desired islands is possible by the right combination of temperatures during the preparation process (see Chapter 2).

Figure 6.4 shows spin-resolved dI/dU-maps of one nearly hexagonal hcp Pd/Fe/Ir(111)-island at different magnetic fields. Since a Cr-bulk tip was used and the images are recorded at a bias of $U = +610\,\mathrm{mV}$, which is close to the main NCMR-peak [Hanneken *et al.*, 2015], the contrast visible is governed by a combination of TMR and NCMR. Due to the considerable bias voltage, the sample is prone to be influenced by the STM tip during

scanning, see Chapter 3 and [Romming *et al.*, 2013]. This can be seen in Fig. 6.4e and f, which are both recorded at the same magnetic field, but the magnetic structure changed in the meantime due to tip-mediated effects.

Figure 6.4a shows the magnetic virgin state of the island with a SS running in a diagonal direction, having a SS period of about 6 nm. From Section 5.1, the propagation direction of the SS $\vec{q}$ would be expected to run parallel to the longest edges or along one of the high symmetry directions [Schmidt *et al.*, 2016]. Obviously, this is not the case here, but instead the SS seems to bend to accommodate the many edges and corners in the close vicinity. It is also conceivable that this particular propagation direction is a result of the relation between the SS wavelength and the island diameter.

Figures 6.4b-d show the evolution of the magnetic state with changing magnetic field up to $B = +4\,\mathrm{T}$, including a mixed state of 360°-DW, a single skyrmion and incomplete skyrmions at the edges (Fig. 6.4b), a single skyrmion (Fig. 6.4c) and the FM state (Fig. 6.4d). Figures 6.4e, f show the magnetic state after passing through zero magnetic field at $B = -0.5\,\mathrm{T}$. Just like in Section 6.1, the magnetic structure is dominated by a network of 360°-DWs and their junctions, and is thus expected to have topological charge of $Q > 0$. This will be discussed in more detail below. With increasing $|B|$ to $B = -1.25\,\mathrm{T}$ and $B = -1.6\,\mathrm{T}$, the magnetic state transforms to one junction of three 360°-DWs and then to a single 360°-DW, respectively.

Figure 6.5 shows the results of atomistic simulations performed by the group of Prof. Hans Fangohr, Univ. Southampton (see Appendix A.2 for methods) for the island shape seen in the experiment, with different starting configurations and at different magnetic fields. Since the island of Pd/Fe/Ir(111) is surrounded by Fe/Ir(111), which exhibits a highly non-collinear nanoskyrmion lattice state on the length-scale of 1 nm, the potential magnetic coupling to the Fe/Ir(111) is neglected for simplicity (open boundaries are used). Any changing magnetic material parameters due to a different LDOS near island edges are also neglected. For each configuration, the Figure shows the spin alignment and the corresponding local topological charge density. As evident from the topological charge values Q, the sum of all topological charges does not need to be an integer value, when open boundaries are involved. For example the FM island in Fig. 6.5e, f should be topologically trivial, i.e. have the topological charge of $Q = 0$. But instead there is a residual value of $Q = -0.15$, which is due to the tilting of spins at the island edges, which is induced by the uncompensated DMI at open boundaries. This is also the cause for $Q = +0.90 < 1$ for the single skyrmion in Fig. 6.5c, d. This shows that the topological charge, induced by the edge tilt, possesses the opposite sign of the topological charge of a regular single skyrmion in a field-polarised surrounding. This is also corroborated by the negative topological charge of the FM alignment in Fig. 6.5e, f along the $+z$-direction.

Neglecting small ($|Q| < 0.2$) contributions induced by the edge tilt, it is possible to

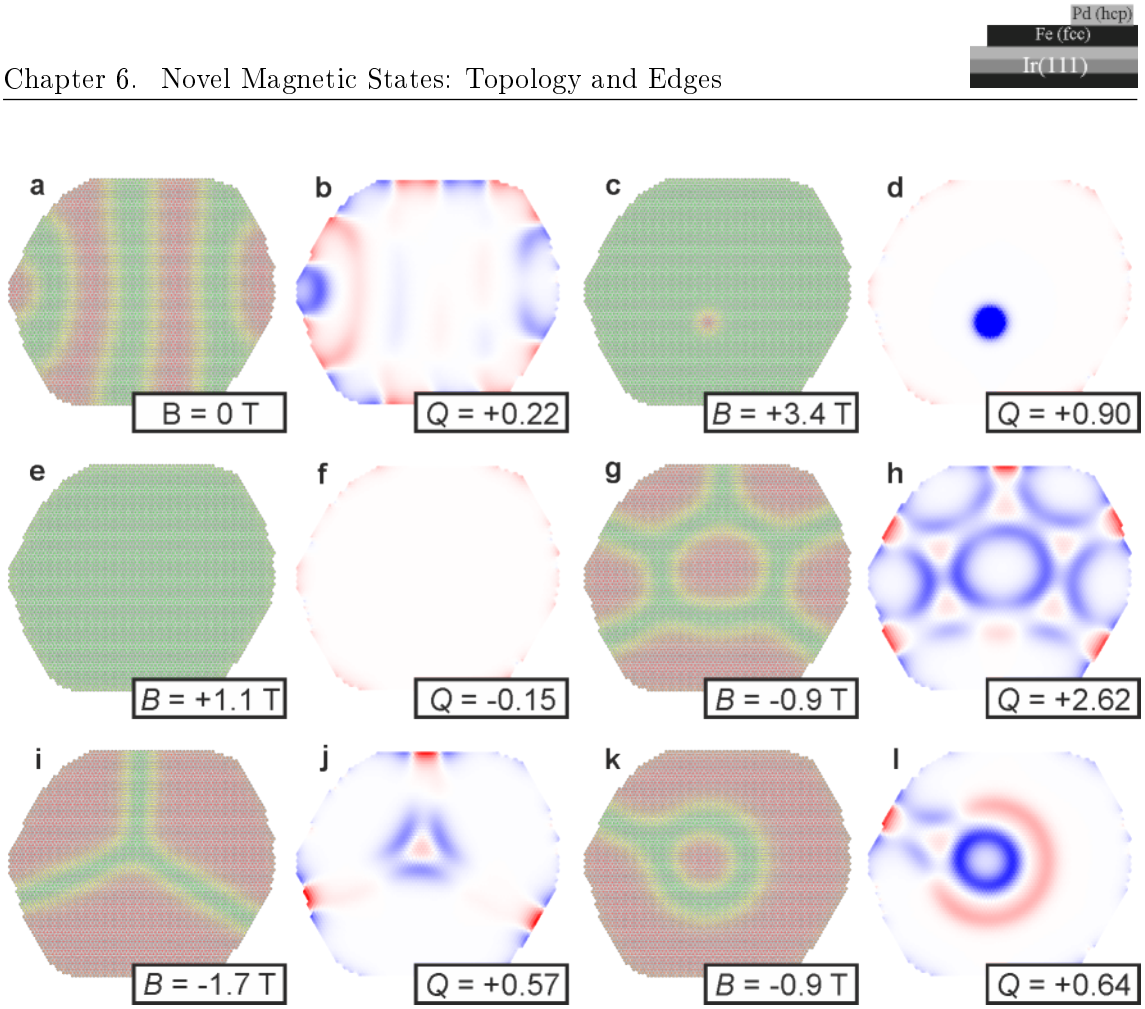

Figure 6.5.: Pd(hcp)/Fe(fcc): Topological charge of simulated magnetic states. **a,c,e,g,i,k** Schematic 3D top views of simulated magnetic states (performed by the group of Prof. Hans Fangohr, Univ. Southampton, details in Appendix A.2) at different magnetic fields with different histories and start configurations. **b,d,f,h,j,l** Maps of the topological charge density of the spins in **a,c,e,g,i,k**, respectively, calculated according to Eq. (6.3). Blue/red contrast adjusted to $\pm 0.0008\,\pi$ (colour code according to Fig. C.1b).

discuss the different magnetic states in Fig. 6.5, which are similar to some of the states in Fig. 6.4, regarding their topology. The magnetic structure in Fig. 6.5g, h, which resembles qualitatively the one in Fig. 6.4e, possesses a topological charge of roughly $Q \approx +2.5$. This can be explained by simply counting the 5 triple-junctions of 360°-DWs with a topological charge of $Q = +0.5$ each. Another way to look at this structure is to regard the 360°-DWs as the FM surrounding along $+z$-direction (green area in Fig. 6.5g) and then count one skyrmion in the center with $Q = +1$ and 5 fractions of skyrmions around the outside with $Q \approx +\frac{3}{10}$ each. Similarly, the magnetic structure in Fig. 6.5i, j can (topologically) be seen as one triple-junction with $Q = +0.5$ or as 3 skyrmion fractions with $Q \approx +\frac{1}{6}$ each.

Interestingly, the lollipop-shaped spin structure in Fig. 6.5k, l has the same topological charge as the triple junction, although it contains a skyrmion in the center. This can be understood if the center skyrmion with $Q = +1$ is seen as embedded in a larger skyrmion

with $Q = -1$. They compensate the topological charge of each other except for $-\frac{1}{2}$ topological charge, which is transferred from the outer skyrmion via the 360°-DW to the island edge and lost there. Another way to look at it, is to once again count the triple-junction of 360°-DWs with $Q = +0.5$ and regard the green ring on the right side as one bent 360°-DW with $Q = +0$. If a 360°-DW is not straight, but bent around a corner, topological charge is gained on one side, but compensated by a loss on the other side, see Appendix B.1. With this knowledge, it is possible to assign estimates of the topological charge to the magnetic structures observed in the experiments as shown in the labels of Fig. 6.4, without calculations.

Except for the unusual SS direction, confinement of the ML Pd did not lead to significantly new magnetic states compared to the previous measurements in more extended islands. They provide, however, a good model system to directly compare high-resolution experimental data with real-space atomistic simulations, and most of the characteristic states that are observed experimentally can be reproduced by the simulations. The concept of topological charge provides an appropriate method to classify magnetic states into common states like skyrmions ($\mathrm{sgn}\,(Q) = \mathrm{sgn}\,(B)$) and uncommon states like domain wall networks ($\mathrm{sgn}\,(Q) \neq \mathrm{sgn}\,(B)$), with Q as defined in Eq. (6.1) or (6.3). It is observed that the uncommon states usually appeared after an inversion of the magnetic field via a sweep through zero.

6.3. Confined DL Pd/Fe/Ir(111): The Target Skyrmion

Another system exhibiting well defined, confined structures is the DL Pd on Fe/Ir(111). Besides the different magnetic material parameters (see Chapter 5), the main difference to the previous section is the surrounding of these islands being Pd/Fe/Ir(111) instead of Fe/Ir(111). This is discussed in more detail in Section 6.4. Figure 6.6 shows the same area at the same magnetic field of $B = +3\,\mathrm{T}$, imaged with the NCMR contrast, see also Section 5.3, but with different histories. Before Fig. 6.6a, the magnetic field was swept up from $B = 0\,\mathrm{T}$. Figure 6.6b, on the contrary, is recorded directly after sweeping down the magnetic field from $B = +7\,\mathrm{T}$, c and d are recorded subsequently. Between a and c, no major change in the magnetic state is visible, whereas between images b and d, small changes occurred (in the large island). The changes may be explained by either a delayed relaxation of the magnetic state towards its thermodynamic equilibrium or a non-negligible influence of the STM tip with tunnelling parameters of $U = +50\,\mathrm{mV}$, $I_{\mathrm{set}} = 1\,\mathrm{nA}$. When comparing the magnetic states of the bigger island to the ones of the smaller islands, it becomes apparent that hysteresis is more pronounced in the small islands. In Fig. 6.6c, the two right islands still show the SS state, whereas in Fig. 6.6d, they are FM. In the big island, contrarily, the mixed state of spin spirals with skyrmions prevails for both images.

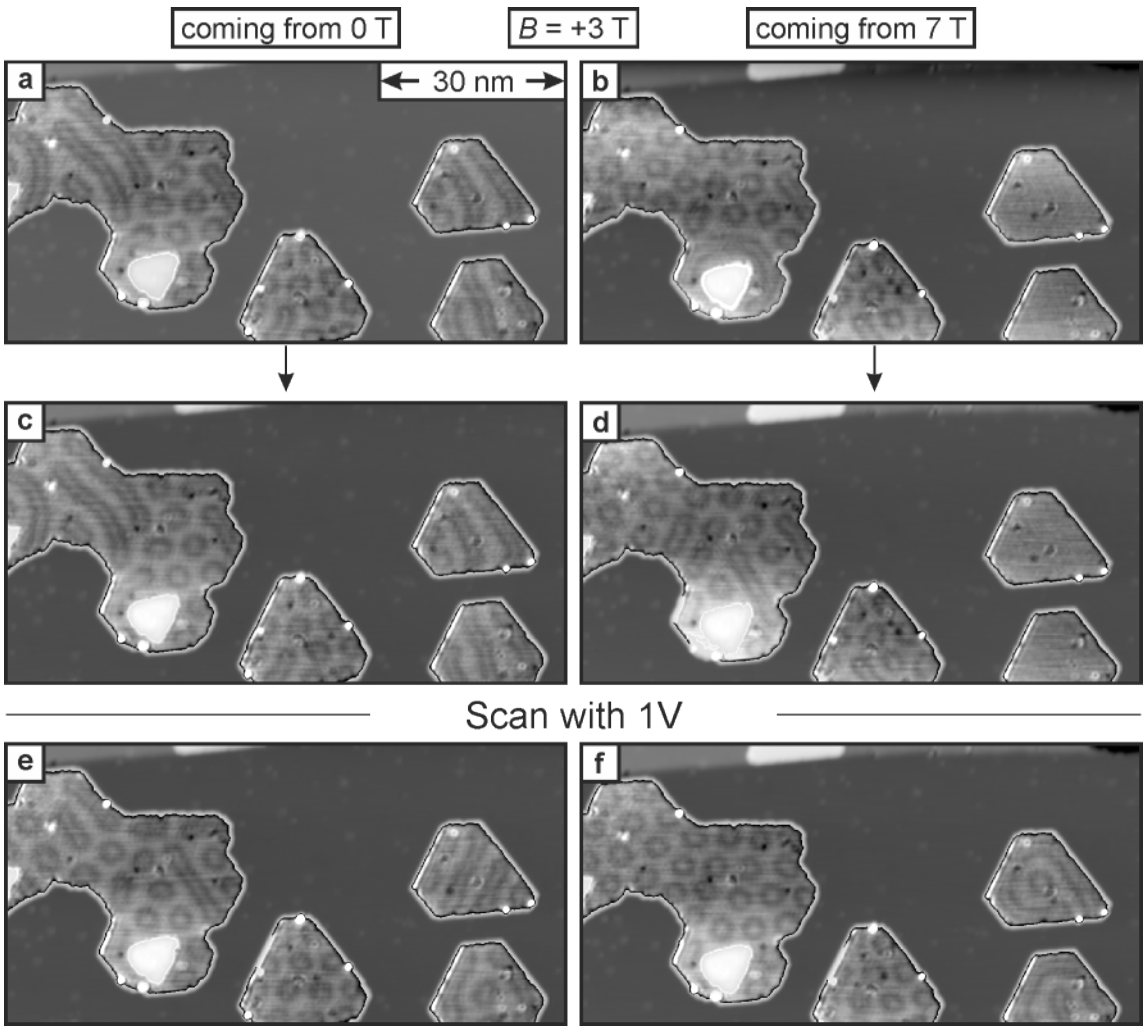

Figure 6.6.: Pd on Pd(fcc)/Fe(fcc): Discovery of the target skyrmion. a-f STM images of Pd islands on fcc Pd/Fe/Ir(111) with contrast adjusted locally to ±10 pm. Gauß-filtered in y-direction with $\sigma = 1.2$ Å, creep corrected by subtracting a parabolic plane fit. Cr-bulk tip, $T = 4.2$ K, $I_{\mathrm{set}} = 1$ nA, $U = +50$ mV, $B = +3.0$ T for all images. Panel **a** is identical to Fig. 5.5f. Between images **c,d** and **e,f**, respectively, the area was scanned with $U = +1$ V, $I_{\mathrm{set}} = 3$ nA (not shown).

Figures 6.6e and f are recorded following c and d, respectively, but only after a scan of the same area with $U = +1$ V, $I_{\mathrm{set}} = 3$ nA (not shown). The application of higher energy tunnelling electrons is known to affect the magnetic state of a sample, see Chapter 3 and [Romming *et al.*, 2013; Hsu *et al.*, 2017], which is also obvious from the comparison of images c to e or d to f. The big island and the central island are transformed more towards the pure SkX state for both starting conditions, whereas in the small islands different transitions are visible. Starting from the SS state (the two right islands in Fig. 6.6c), the propagation direction in the upper island is rotated, whereas the lower island undergoes a transition to a so-called target-skyrmion-like state (explained in the next paragraph).

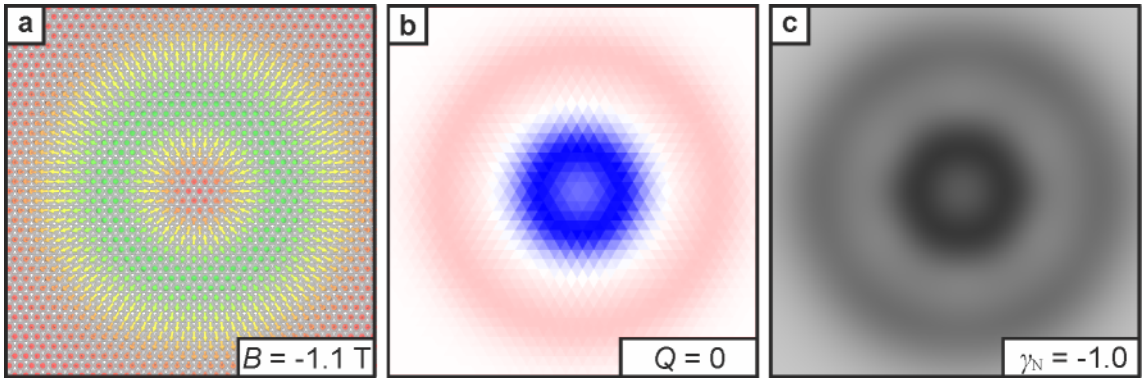

Figure 6.7.: Topological charge and STM contrast of a target skyrmion. **a** Schematic 3D top view of simulated atomic spins (simulated by the group of Prof. Hans Fangohr, Univ. Southampton, details in Appendix A.2) started from a manually defined target skyrmion state. **b** Map of the topological charge density of the spins in **a**, calculated according to Eq. (6.3). Blue/red contrast adjusted to $\pm 0.0015\,\pi$ (colour code according to Fig. C.1b). **c** STM simulation (see Section 1.2.2) of the NCMR contrast (approximated by a linear dependence on mean angle to nearest neighbours) of the spins in **a**; $z_0 = 0.8\,\mathrm{nm}$.

Starting from the FM state (two right islands in Fig. 6.6d), both islands transform to a state very similar to a target skyrmion.

The target skyrmion [Leonov *et al.*, 2014; Beg *et al.*, 2015; Liu *et al.*, 2015] or multi-π-skyrmion [Bogdanov and Hubert, 1999; Rohart and Thiaville, 2013] is a skyrmion-like magnetic structure with additional radially symmetric windings of the spins. The special case with two full windings across the center, the 2π-skyrmion, also called the skyrmionium [Komineas and Papanicolaou, 2015; Zhang *et al.*, 2016], can be seen in Fig. 6.7a. Originally predicted as another solution of the radially symmetric micromagnetic energy functional that was also used to investigate skyrmions [Bogdanov and Hubert, 1994b, 1999], the novel magnetic structures were also found by micromagnetic simulations both in confined nanostructures [Rohart and Thiaville, 2013; Leonov *et al.*, 2014; Beg *et al.*, 2015; Liu *et al.*, 2015] as well as in extended films [Komineas and Papanicolaou, 2015; Zhang *et al.*, 2016]. Additionally, first experimental evidence of the existence of skyrmioniums was given by Finazzi *et al.* [Finazzi *et al.*, 2013].

These topologically trivial magnetic structures, skyrmioniums, are said to have special properties regarding their dynamics under STT influence [Komineas and Papanicolaou, 2015; Liu *et al.*, 2015; Zhang *et al.*, 2016]. Compared to skyrmions as data carriers in proposed racetrack-like memory devices, target skyrmions possess some advantages. Skyrmions are prone to the skyrmion Hall effect (SkHE) and experience an additional acceleration perpendicular to the current direction, which is caused by its integer topological charge $Q = \pm 1$. Target skyrmions with $Q = 0$ (skyrmioniums), on the contrary, are made up of one skyrmion with $Q = \mp 1$ embedded in one skyrmion with $Q = \pm 1$, thus being topologically trivial, see Fig. 6.7b, and not susceptible to the SkHE. Instead, a target

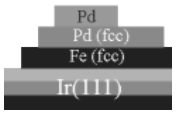

skyrmion moves along the track in a straight line, without significant deformation for low current and with a stretching deformation along the perpendicular direction at high current [Zhang *et al.*, 2016]. Furthermore, it was shown by Zhang *et al.* that, for current applied perpendicular to the plane, the target skyrmion moves significantly faster than a skyrmion [Zhang *et al.*, 2016]. It was predicted by Komineas and Papanicolaou [2015] that the skyrmionium acquires a momentum when moved by STT and carries on without current.

Figure 6.7c shows an NCMR-simulation of the target skyrmion as depicted in Fig. 6.7a. Originating from the easy-axis anisotropy, the spins rotate faster over the in-plane direction, leading to an increased NCMR-contrast and thus to the ring-like contrast seen in the experiment. The simulated image does not agree with the experiments (Fig. 6.6e, f) completely, because in the experiment, there are no perfect target skyrmions, but rather lollipop-like spin structures like in Fig. 6.5k. It remains unclear from this set of experimental data whether the center of the structure points along the magnetic field or in the opposite direction. It is more likely, though, that the outer ring points along the field, then a ring of spins with the opposite direction follows and the center points along the field again. This way the largest number of spins is aligned with the magnetic field direction, thus gaining the most Zeeman-energy. Also, the outer ring would then be parallel to the mostly FM surrounding Pd/Fe/Ir(111). The observation of target-skyrmion-like structures in the DL Pd on Fe/Ir(111) might therefore be facilitated by the existing boundary conditions, which is discussed in more detail in the next section.

6.4. Comparison of Boundary Conditions

As mentioned above, the two systems Pd/Fe/Ir(111) and DL Pd on Fe/Ir(111) differ from one another not only in their magnetic material parameters, but, when it comes to confinement, also in their boundary conditions. This is simply a result of the different materials surrounding the respective island. Whereas the DL system is surrounded by extended areas of Pd/Fe/Ir(111) with its corresponding phase transitions, the ML Pd is surrounded by the highly non-collinear nanoskyrmion lattice, which does not change its state upon application of an external magnetic field. Since the magnetic period of the nanoskyrmion lattice of about 1 nm is small compared to the magnetic period of Pd/Fe/Ir(111) of about 7 nm, the surrounding is assumed being non-magnetic (no net magnetic moment on the length scale of interest), leading to no significant coupling of the ML Pd/Fe/Ir(111) to the surrounding Fe/Ir(111)[1]. These edges are simply modelled by open boundaries. Assuming

[1] It should be noted that FM islands can couple to the nanoskyrmion lattice, leading to certain orientations of the nanoskyrmion lattice with respect to the island and with a net magnetic moment at the edge [Hagemeister *et al.*, 2016]. It is, however, more likely that the FM Pd/Fe/Ir(111)-island is imposing this alignment onto the Fe/Ir(111) than vice versa.

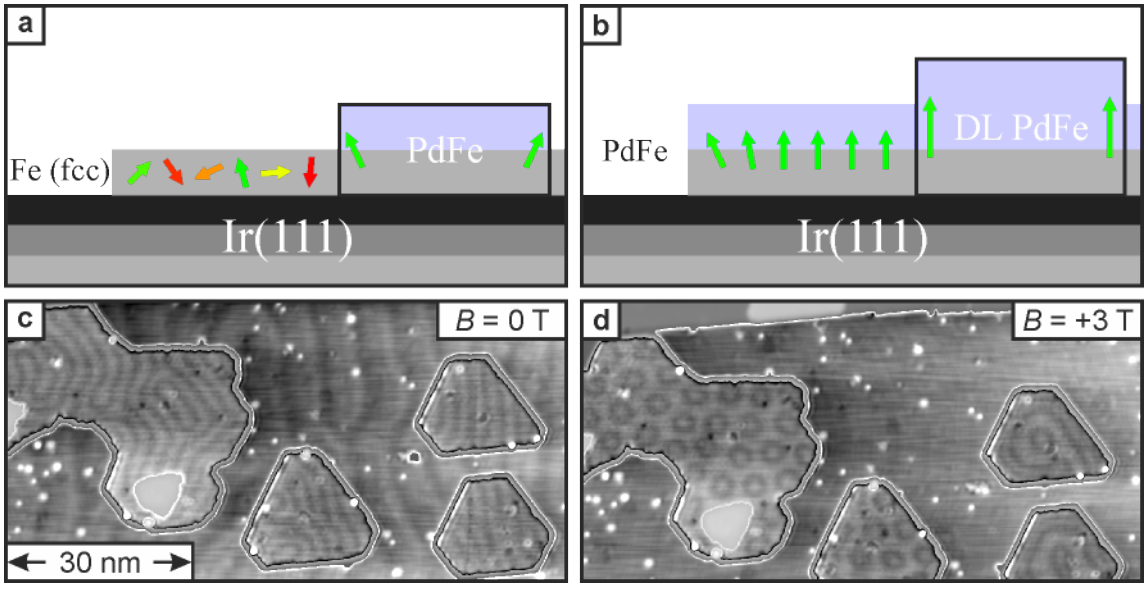

Figure 6.8.: The role of edge conditions for the existence of target skyrmions. **a** Sketch of the surrounding magnetic material of PdFe-islands (nano-skyrmion lattice in fcc Fe/Ir(111)). **b** Sketch of the changed situation for the DL island surrounded by PdFe, which is FM in a high external magnetic field. **c,d** (SP-)STM topography images of fcc Pd/Fe/Ir(111) with DL islands on top with the contrast adjusted locally to ±10 pm. Gauß-filtered in y-direction with $\sigma = 1.2$ Å. Cr-bulk tip, $T = 4.2$ K, $I_{\text{set}} = 1$ nA, $U = +50$ mV.

constant magnetic material parameters over the whole island, the spins are expected to tilt at the open boundary edges [Rohart and Thiaville, 2013; Beg *et al.*, 2015; Hagemeister, 2016], gaining DMI-energy, see Fig. 6.8a and Section 6.5. The edge tilt at open boundaries also leads to a preferred propagation direction of the spin spirals in Pd/Fe/Ir(111) parallel to edges [Hagemeister, 2016].

For the DL Pd on Fe/Ir(111), on the contrary, the surrounding Pd/Fe/Ir(111) undergoes several phase transitions. Without magnetic field, it exhibits a SS with a similar period (≈ 7 nm) as the DL Pd on Fe/Ir(111) with a period of roughly 4.5 nm. Figure 6.8c shows indications for a general trend of the spin spirals in the ML and in the DL to run parallel to each other. This is probably caused by a coupling of the two different spin spirals with similar periods at the interface between ML and DL Pd/Fe/Ir(111). At an external magnetic field of +3 T, the surrounding Pd/Fe/Ir(111) is mostly FM, see Fig. 6.8d. Any spin at the island boundaries that is not aligned with the FM surrounding along the external magnetic field will lead to an increase in energy, thus imposing a FM boundary condition on the islands, see Fig. 6.8b. Any non-collinear ordering along the edges (e.g. SS propagating along the edge or half a skyrmion at the edge) is therefore unfavoured by the boundary condition. However, target-skyrmion-like states as in the two right islands in Fig. 6.8d can satisfy this boundary condition if the outer ring is pointing along the external magnetic field. It can be speculated that this FM boundary condition is actually

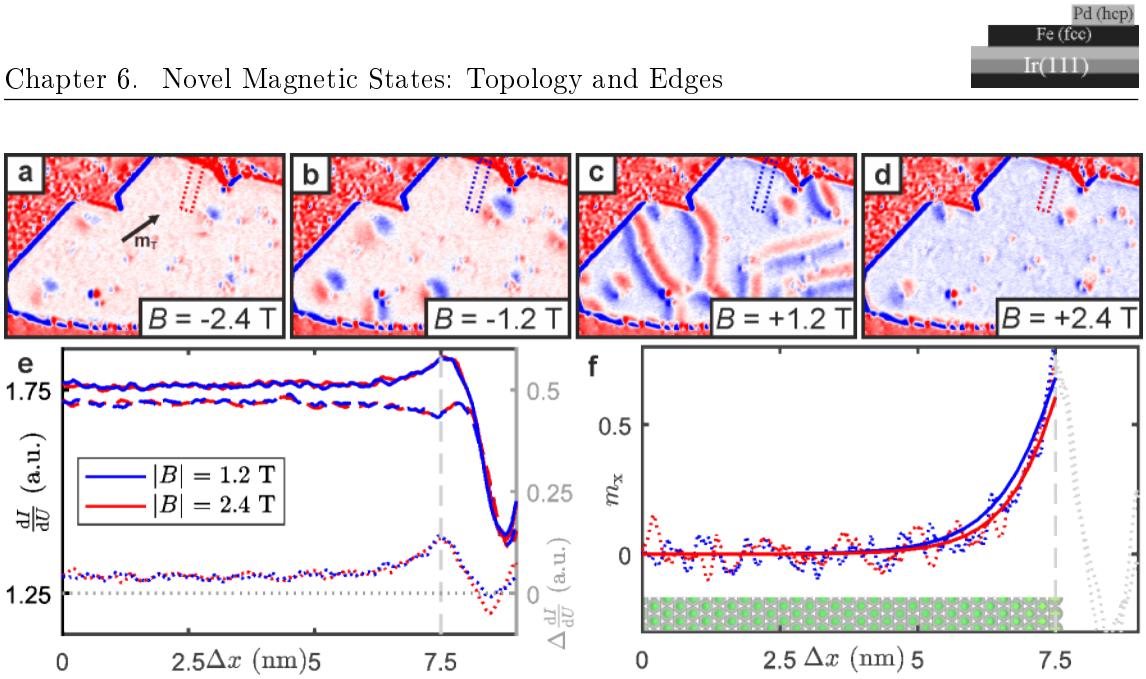

Figure 6.9.: Edge tilt in hcp Pd/Fe/Ir(111). **a-d** Spin-resolved $\mathrm{d}I/\mathrm{d}U$ maps of a Pd/Fe/Ir(111)-island (forward scan direction). **e** Line profiles along the dotted rectangles in **a-d** (solid lines: positive magnetic field, dashed lines: negative magnetic field). Dotted lines show the respective difference between line profiles taken at positive and at negative magnetic field. **f** Calculated magnetisation component along the profile direction m_x as dotted lines. For the calculation of m_x, the tip direction is given by the 2D fits to the skyrmion with the polar angle $\theta_\mathrm{T} = 78°$ and the azimuthal angle $\varphi = 35°$ (see also arrow in **a**). The profiles are chosen along $\alpha = 75°$. The solid lines represent the m_x-component of simulated data by the group of Prof. Hans Fangohr, Univ. Southampton (see Appendix A.2) of a Pd/Fe/Ir(111)-island with an open boundary (inset shows top view representation of spins at $B = 1.2\,\mathrm{T}$, corresponding to the blue solid line).

the reason for the observation of target-skyrmion-like states in the DL Pd but not in the ML Pd on Fe/Ir(111) system.

6.5. Experimental Observation of the Edge Tilt

For magnetic systems with considerable DMI, it is known from theoretical calculations that spins tilt at island edges (see inset in Fig. 6.9f), due to the uncompensated DMI at open boundaries (see Section 6.2 and e.g. Refs. [Rohart and Thiaville, 2013; Hagemeister, 2016]). The data recorded during the magnetic field sweep of Chapter 4 with an IP tip permits a high resolution experimental observation of this DMI-induced tilting of spins at island edges.

Figure 6.9a-d shows four exemplary raw data $\mathrm{d}I/\mathrm{d}U$ maps from the magnetic field sweep shown in Fig. 4.3 and in [Romming *et al.*, 2015]. Figure 6.9e shows line profiles over the edge of the Pd/Fe/Ir(111)-island, taken along the rectangles marked in Fig. 6.9a-d, at positive (solid lines in Fig. 6.9e) and at negative magnetic field (dashed lines in Fig. 6.9e). The difference between data at positive magnetic field and data at negative magnetic field is shown as dotted lines, representing the magnetic signal, while the electronic and

structural contrasts cancel. Figure 6.9f displays the calculated magnetisation component m_x along the profile direction as dotted lines. The solid lines in Fig. 6.9f represent the m_x-component of simulated data by the group of Prof. Hans Fangohr, Univ. Southampton (see Appendix A.2) of a Pd/Fe/Ir(111)-island with an open boundary (inset shows top view representation of spins at $B = 1.2\,\mathrm{T}$, corresponding to the blue solid line). Although the simulations do not include a possible change of the magnetic material close to the edge due to a change of the electronic structure, the agreement with the experimental profiles is remarkable. As evident from the profiles and the calculated magnetisation component m_x, DMI indeed leads to a considerable tilting of spins at open boundaries of up to $\gtrapprox 30°$ with respect to the surface normal. The negligible difference between the profiles at $B = 1.2\,\mathrm{T}$ and $B = 2.4\,\mathrm{T}$ shows the comparably small influence of the external magnetic field on the edge tilt.

Chapter 7.

Tuning Fe/Ir(111) with Rh

In the previous chapters, the impact of Pd overlayers on the magnetic state of Fe/Ir(111) was discussed. For comparison, the second element used here to tune the magnetic state of Fe/Ir(111) is Rh. This chapter describes the magnetism of both stackings of Rh on Fe individually, starting with fcc. Since the magnetism of hcp RhFe seems to be more complicated, the corresponding section offers spin-resolved and spin-averaged measurements, an analysis of observed Moiré patterns as well as a possible explanation for a propagation of the periodic magnetic structure in a non-high-symmetry direction. Finally, the underlying magnetic interactions in Rh/Fe/Ir(111) are briefly discussed in the context of spin spiral dispersion calculations obtained from DFT by the group of Prof. Stefan Heinze, Univ. Kiel.

7.1. fcc Rh/Fe/Ir(111)

As shown in Section 2.2.4, Rh islands of both stackings grow pseudomorphically on Fe/Ir(111). Figure 7.1a shows an SP-STM measurement of an fcc Rh/Fe/Ir(111) island with a cosine-like modulation with $\lambda_{\mathrm{fcc}} \approx 1.5\,\mathrm{nm}$ period, Fig. 7.1c, which is a typical indication for homogeneous spin spirals (see Fig. 7.1b), imaged with SP-STM [Wiesendanger, 2009; von Bergmann *et al.*, 2014]. As visible in the overview image (Fig. 7.1d), this modulation occurs in the three possible rotational domains with the propagation direction $\vec{q}$ strictly along the $\langle 11\bar{2} \rangle$ directions. The spin spirals are expected to be cycloidal due to the interface-induced DMI [von Bergmann *et al.*, 2014] (sketch in Fig. 7.1b, also cf. Section 1.1.1). In Fig. 7.1d, we find different magnetic signal amplitudes for different propagation directions, which is consistent with SSs and means that the tip has an in-plane component [Hsu *et al.*, 2016]. It should be noted that there is an apparent correlation between the overall island shapes and the preferred propagation direction of the spin spirals along the longer direction of the islands, comparable to the preferred propagation direction of the spin spirals in Pd/Fe/Ir(111), possibly caused by a coupling to the island edges [Romming *et al.*, 2013; Schmidt *et al.*, 2016]. The magnetic structure does not respond to fields of $B = 9\,\mathrm{T}$ [Romming, 2013]. Compared to the magnetism of Fe/Ir(111), the fcc Rh adlayer changes the square nanoskyrmion lattice state to a cycloidal spin spiral with an increased period

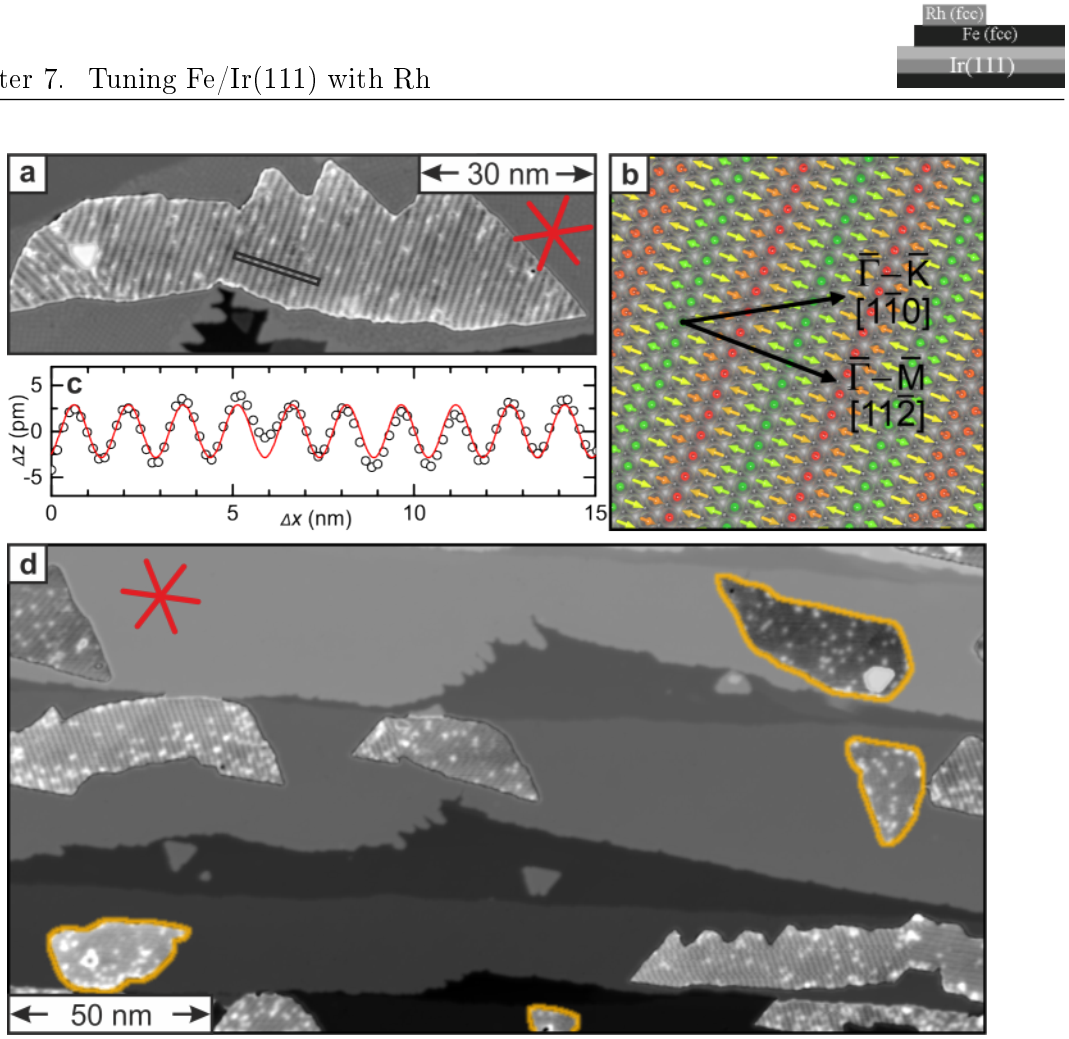

Figure 7.1.: Magnetism of fcc Rh/Fe/Ir(111)-islands. **a** SP-STM constant-current image of an fcc Rh/Fe/Ir(111)-island measured with a magnetic Cr-tip (contrast level adjusted locally to ±20 pm). Red lines mark the $\langle 1\bar{1}0\rangle$ directions (close-packed rows), as obtained from straight island edges ($T = 8\,\mathrm{K}$, $U = +30\,\mathrm{mV}$, $I_{\mathrm{set}} = 1.0\,\mathrm{nA}$). **b** Sketch of a homogeneous, cycloidal SS with $\lambda_{\mathrm{fcc}} = 1.5\,\mathrm{nm}$ along the $\bar{\Gamma} - \bar{\mathrm{M}}$ i.e. the $[11\bar{2}]$ direction. **c** Line profile along the rectangle in **a**. Solid line is a fit with a cosine-function as a guide to the eye. **d** SP-STM constant-current image with an in-plane magnetised Fe/W tip, contrast levels adjusted locally on the Rh/Fe/Ir(111)-islands to ±20 pm, orange rims mark the hcp-islands. Red lines mark the $\langle 1\bar{1}0\rangle$ directions (close-packed rows), as obtained from straight island edges ($T = 8\,\mathrm{K}$, $U = 600\,\mathrm{mV}$, $I_{\mathrm{set}} = 1.5\,\mathrm{nA}$.)

of 1.5 nm (compared to 1 nm in Fe/Ir(111)). A possible explanation could be that the higher-order exchange interactions are suppressed or negligible due to a deep spin spiral energy minimum.

7.2. hcp Rh/Fe/Ir(111)

Regarding hcp Rh/Fe/Ir(111) islands (Fig. 7.2), also periodic stripes with a slightly different period of ($\lambda_{\mathrm{hcp}} \approx 1.1\,\mathrm{nm}$) are visible, but it becomes directly evident that the magnetic structure differs from the one in fcc islands in several aspects: The propagation direction

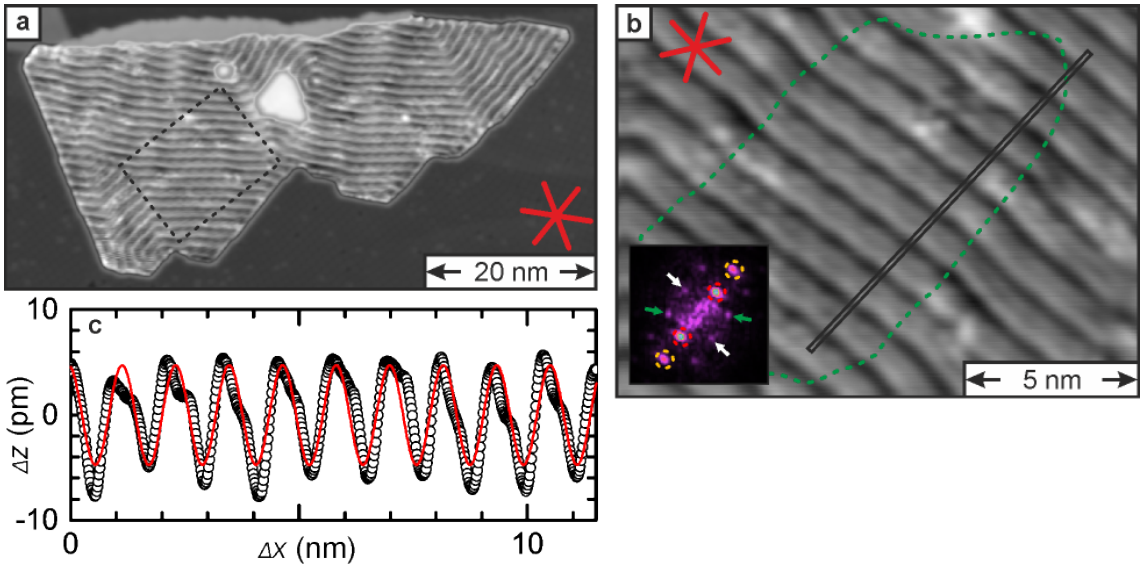

Figure 7.2.: Magnetism of hcp Rh/Fe/Ir(111)-islands. **a** SP-STM image of an hcp Rh/Fe/Ir(111)-island measured with a mostly OOP magnetic Cr-tip (contrast level adjusted locally to ±20 pm). **b** Zoom-in to the area marked by the dashed rectangle in **a**. The area enclosed by the green dotted line exhibits one singular tilted domain. Inset shows a $4\,\mathrm{nm}^{-1} \times 4\,\mathrm{nm}^{-1}$ cut-out of the FFT of the data in **b**. Red dotted circles mark spots caused by SP-STM contrast, yellow dotted circles mark spots caused by an electronic contrast. Additional spots, indicated by arrows, are caused by a beating of the electronic contrast with the atomic lattice. **c** Line profile along the rectangle in **b**. Solid line is a fit with a cosine-function as a guide to the eye. Red lines in **a,b** mark the $\langle 1\bar{1}0 \rangle$ directions (close-packed rows), as obtained from straight island edges. ($T = 8\,\mathrm{K}$, **a** $U = -30\,\mathrm{mV}$, $I_{\mathrm{set}} = 1.5\,\mathrm{nA}$; **b** $U = -5\,\mathrm{mV}$, $I_{\mathrm{set}} = 3.0\,\mathrm{nA}$)

seems to be more flexible; it is not strictly along the $\langle 11\bar{2} \rangle$ directions and varies locally. The nature of the periodic signal significantly differs from a cosine-like shape (profile in Fig. 7.2c). As also evident from the FFT of the data in Fig. 7.2b (inset), the image includes, in addition to the SP-STM signal (red dotted circles), a modulation in the same direction (yellow dotted circles), with half the period of the SP-STM signal. This could be induced by either TAMR or for inhomogeneous spin structures by NCMR or a variation of the polarisation [Al-Zubi *et al.*, 2011] (see also below). Also, there are additional modulations visible in different directions (arrows) with a period of about $\lambda_{\mathrm{b}} = 1\,\mathrm{nm}$, which are so far unexplained. Regarding the preferred propagation direction with respect to the island shapes, there is a tendency for the propagation direction to be roughly perpendicular to the long direction of hcp islands (observed also in several other islands, not shown) as opposed to the trend in the fcc islands. This suggests a different coupling of the magnetic structure to the island edges for the two stackings.

To disentangle the various periodic signals, we separate the non-spin-polarised from the spin-polarised part of the signal by using a non-magnetic tungsten tip (see Fig. 7.3). As expected, the spin-polarised signal with $\lambda_{\mathrm{hcp}} \approx 1.1\,\mathrm{nm}$ vanishes, but the shorter period with

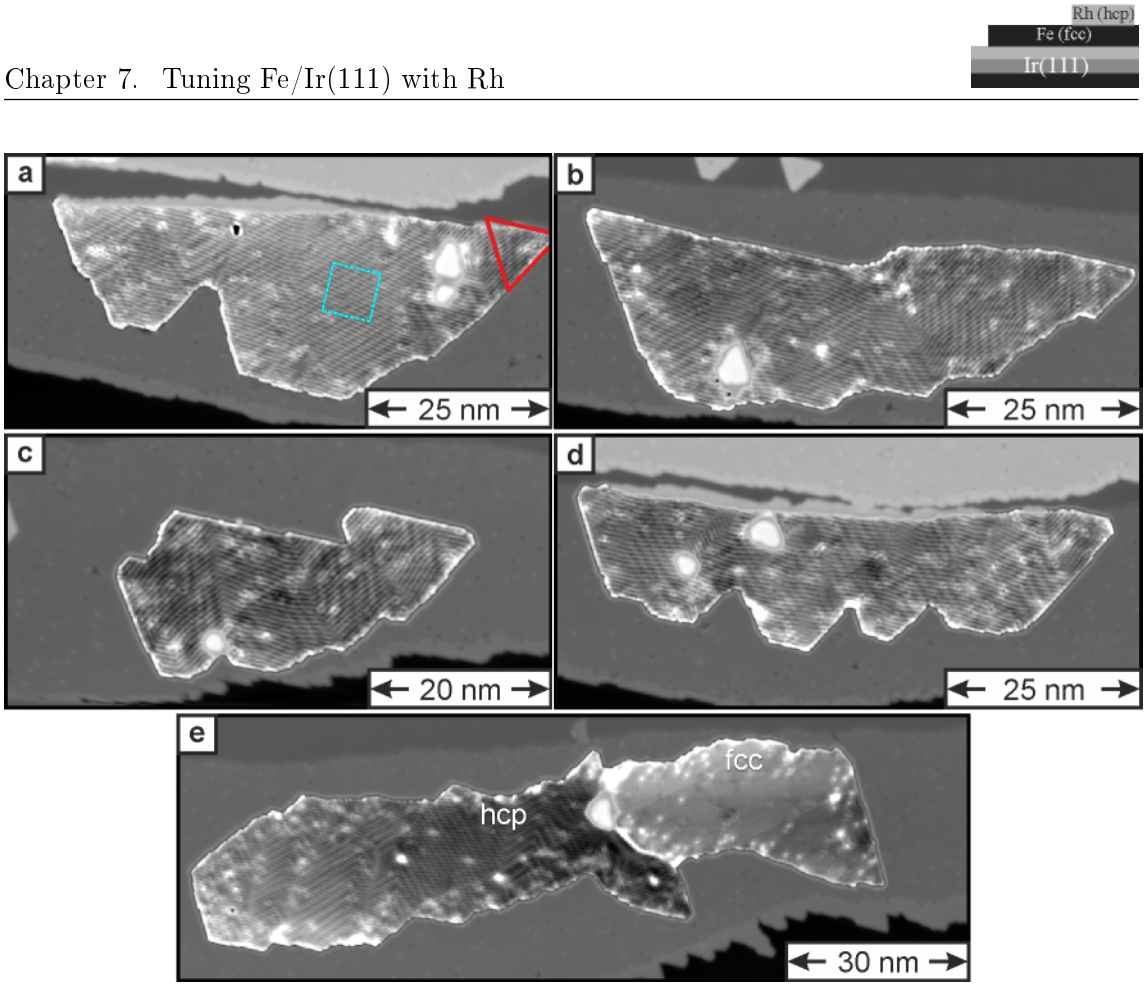

Figure 7.3.: hcp Rh/Fe/Ir(111)-islands with a non-magnetic tip. a-d STM-images of hcp Rh/Fe/Ir(111) with a non-magnetic W-tip. Dashed rectangle marks the area of zoom-in in Fig. 7.4a. Red triangle in **a** depicts close-packed rows. Note that **a-d** are recorded at the same angle with respect to the crystallographic axes. **e** STM-image of a mixed hcp (left) and fcc (right) Rh/Fe/Ir(111)-island with a non-magnetic W-tip. Contrast levels adjusted locally on the Rh/Fe/Ir(111)-islands to ±15 pm. Tunnel parameters: $T = 8\,\mathrm{K}$, $U = +30\,\mathrm{mV}$, **a-d**: $I_{\mathrm{set}} = 1.5\,\mathrm{nA}$; **e**: $I_{\mathrm{set}} = 1.0\,\mathrm{nA}$.

$\lambda_{\mathrm{e}} = \lambda_{\mathrm{hcp}}/2 \approx 5.5\,\text{Å}$ remains, with the additional modulation with $\lambda_{\mathrm{b}} \approx 1\,\mathrm{nm}$ in a different direction. The electronic contrast with λ_{e} can originate from different changes in the LDOS, depending on the underlying magnetic structure. It is possible that the periodic magnetic structure is also a homogeneous cycloidal SS as observed in fcc Rh/Fe/Ir(111). Then the electronic contrast with λ_{e} could be caused by the TAMR-contrast (cf. Section 1.2.2), which is linked to the spin alignment with respect to a quantisation axis. Also, the magnetic structure could be an inhomogeneous SS, which can induce modulations of the LDOS by the varying degree of non-collinearity (NCMR) or by a varying polarisation of the Rh-atoms induced by the neighbouring Fe-atoms [Al-Zubi *et al.*, 2011].

Regardless of the origin of the electronic contrast, we propose that the additional pattern with λ_{b} is caused by a beating between the electronic contrast and the atomic lattice. Whenever periodic modulations of comparable, but not exactly the same, wavelengths interfere, Moiré patterns evolve [Oster and Nishijima, 1963]. It is clearly visible from

Figs. 7.2 and 7.3 that the spin spirals do not propagate along the $\langle 11\bar{2}\rangle$ directions, but rather at an angle of about $\pm 10°$ off the $\langle 11\bar{2}\rangle$ directions (see Fig. 7.3b). To validate the hypothesis of a Moiré pattern induced by the short wavelength electronic contrast, STM simulations were performed based on the model described in Refs. [Heinze, 2006; von Bergmann *et al.*, 2012] and in Section 1.2.2 of an assumed homogeneous cycloidal SS as example. We chose the wavelength as $\lambda_{\mathrm{hcp}} = 4.0$ nearest neighbor distances (NND = 2.715 Å) and its propagation direction tilted by $\alpha = +10°$ off the $[11\bar{2}]$ direction (Fig. 7.4c) with the prefactor of the TAMR part of the signal $\gamma_{\mathrm{T}} = 0.1$ and tip-sample distance $z_0 = 0.8$ nm. As evident from the simulation result (Fig. 7.4b), without any new assumptions, the experimental findings can be explained simply by a tilting of the SS propagation direction away from a high-symmetry direction and an interference of the short-range TAMR-contrast with the atomic close-packed rows.

This can be understood in more detail by taking some basic consideration about the TAMR and geometry into account. Fig. 7.4c shows a sketch of the atomic lattice with the typical unit parallelogram from Fig. 7.4b overlaid. The red and green arrows show the locations of up or down spin direction for a homogeneous SS, respectively. Since the TAMR-signal is proportional to $\cos^2(\theta)$, with θ being the polar angle of the spin, and is a local effect originating at the atom position, it becomes clear that at the corners of the parallelogram the maximum (minimum) TAMR-signal coincides with the close-packed rows. In between, the spin up or down positions do not coincide with equivalent atom positions and therefore result in a different TAMR-signal and thus a Moiré pattern evolves. Although this explanation of the Moiré pattern is based on the assumption of a homogeneous SS and the corresponding TAMR as the electronic contrast, it is also valid for any similarly periodic magnetic structure with an electronic contrast with half the magnetic period, because the explanation is merely considering geometry.

As Moiré patterns are known to be highly sensitive to small changes in angle or wavelength of the overlaid structures, they have been used in a variety of experimental techniques such as crystallography, metrology or optical alignment to obtain high-resolution data [Sciammarella, 1982; Reid, 1984; Halioua and Liu, 1989]. A close analysis of the Moiré pattern, represented by the unit parallelogram in Fig. 7.4a,b, also reveals a very sensitive dependence of its shape and size on the wavelength λ_{hcp} and the propagation direction determined by α, see Fig. 7.4d-k. Therefore we can conclude from Fig. 7.3, showing large domains with a singular Moiré pattern, that there must be some intrinsic interaction that forces the propagation direction of the SS to a certain angle away from the high-symmetry directions. An analysis of several islands reveals a typical tilting of the propagation direction of $\alpha = \pm(9 - 12)°$ with respect to the $\langle 11\bar{2}\rangle$ directions and $\lambda_{\mathrm{hcp}} = 3.90 - 4.15$ NND.

Once again using a homogeneous SS as an example, one possible explanation for the tilting of the propagation direction of the periodic magnetic structure can be found. The

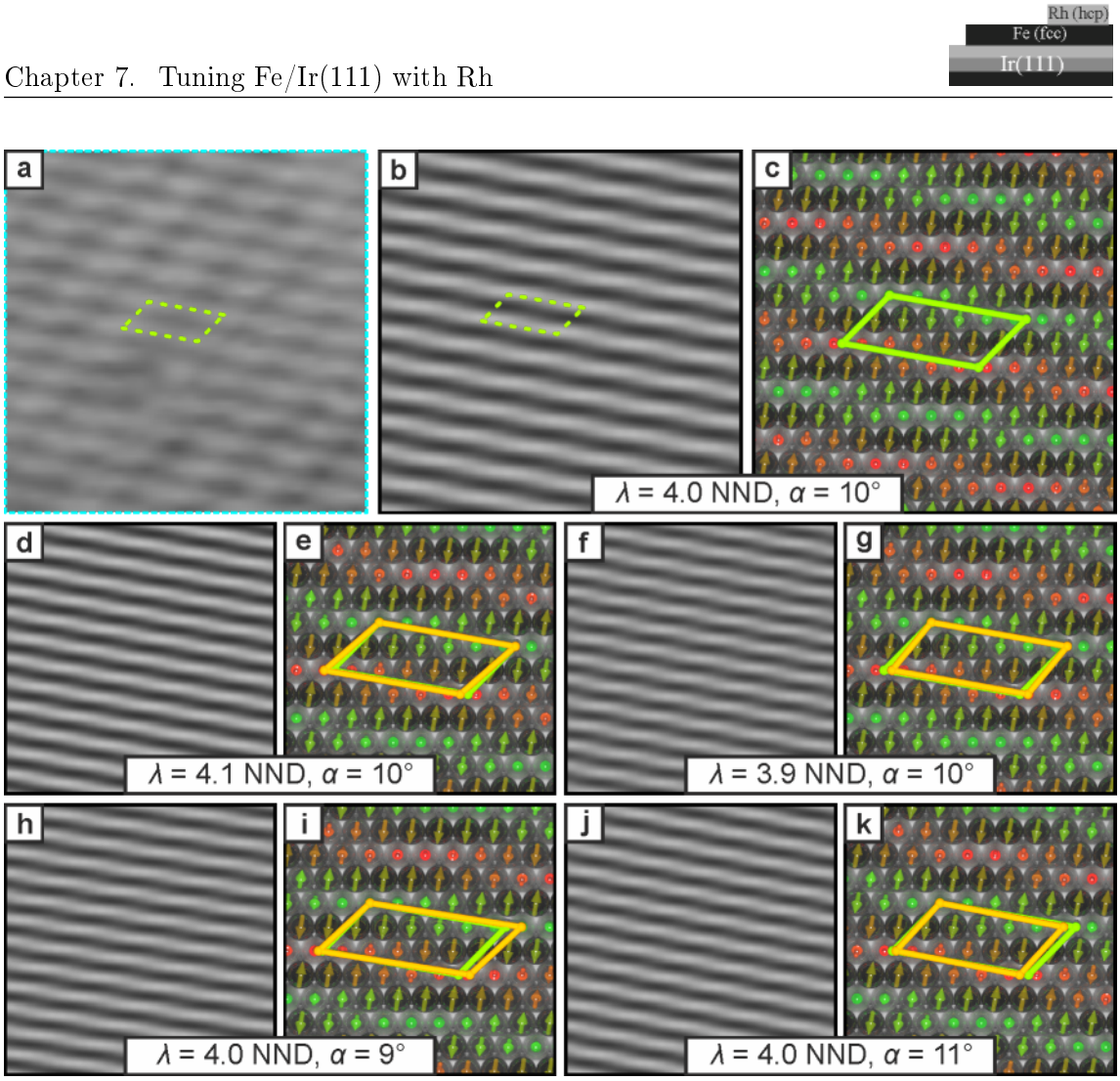

Figure 7.4.: Simulated contrast for hcp Rh/Fe/Ir(111). a Cut-out (dotted square) of data shown in Fig. 7.3a (6.6 × 6.6 nm). **b,d,f,h,j** STM-simulations of a homogeneous SS with λ_{hcp} and its propagation direction tilted by α off the $[11\bar{2}]$-direction, as indicated, with the prefactor of the TAMR part of the signal being $\gamma = +0.1$ and a tip-sample distance $z_0 = 0.8$ nm. Same size as in **a**. **c,e,g,i,k** Sketches of the corresponding magnetic structures, colourised according to the out-of-plane magnetisation component, with the TAMR unit cell overlaid on the atomic lattice (green for experimental one, yellow corresponding to simulation).

magnetic exchange interaction parameters J_{ij}, see Fig. 7.5a, not only influence the period λ but also the propagation direction of a certain SS. If only short-range interactions – short compared to λ – are taken into account, only energy minima along either $\bar{\Gamma} - \bar{\mathrm{M}}$ or $\bar{\Gamma} - \bar{\mathrm{K}}$ directions are possible (see yellow curve in Fig. 7.5d). Competing interactions, regarding their directional dependence, can only weaken directional minima of each other and not produce minima in between the high-symmetry directions, because their direction dependences have a similar cosine-like shape. Long-range, indirect exchange interactions, such as e.g. the RKKY exchange [Ruderman and Kittel, 1954; Kasuya, 1956; Yosida, 1957], which are mediated by the conduction electrons, can also have an impact on the

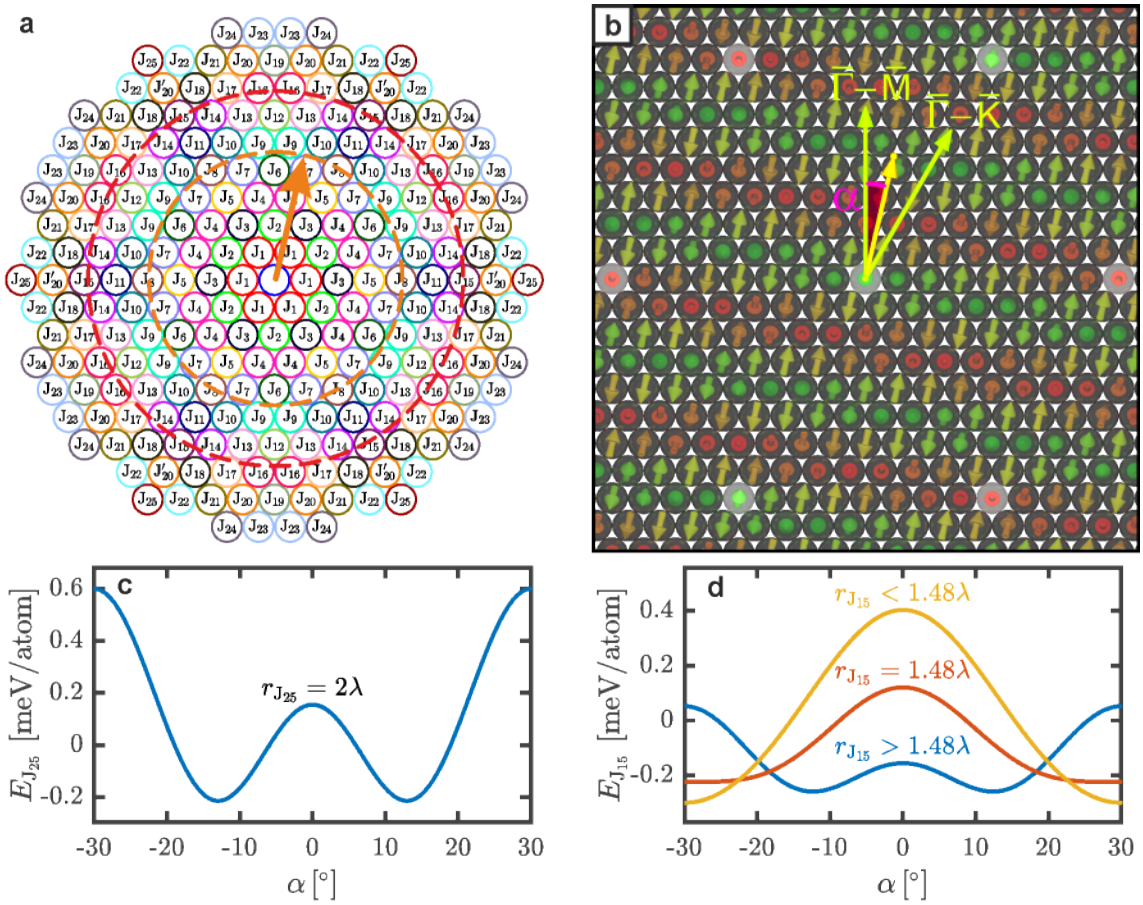

Figure 7.5.: Possible explanation for a propagation off high-symmetry directions in hcp Rh/Fe/Ir(111). **a** Sketch of the positions of spins corresponding to $J_{\leq 25}$. Orange dashed circle with radius $\lambda_{\text{hcp}} = 4.0\,\text{NND}$, with $\vec{q}$ marked by orange arrow. Red dashed circle with radius $1.48\lambda_{\text{hcp}}$. **b** Sketch of the positions of spins corresponding to J_{25} (highlighted) with a homogeneous SS with $\lambda_{\text{hcp}} = 4.0\,\text{NND}$ and $\alpha = 13°$ ($\vec{q}$ marked by orange arrow). **c** Direction dependence of the SS energy $E_{\text{SS},J_{25}}(\alpha)$ for $J_{25} = -0.1\,\text{meV}$, $\lambda_{\text{hcp}} = 4.0\,\text{NND}$, $0° \equiv \bar{\Gamma} - \bar{\text{M}}$ - direction. **d** Qualitative shapes of $E_{J_{15}}(\alpha)$ for different λ ($\lambda = 3.65\,\text{NND}$, $4.05\,\text{NND}$ and $4.46\,\text{NND}$ for the yellow, red and blue curve, respectively, $r_{J_{15}}$ is the distance to $J_{15} = 6\,\text{NND}$).

propagation direction of a SS, even generating local minima in between the high symmetry directions. It was shown that RKKY contributions to J_{ij} may have a strong directionality, which is induced by the anisotropy of the underlying Fermi-surface [Zhou *et al.*, 2010], and that it can have a strength of roughly 0.1 meV for adatoms on surfaces for a distance on the order of 2 nm [Wiebe *et al.*, 2011].

We use J_{25}, which acts between spins about 2.2 nm apart, as a simplified example to show how, in principle, a long-range exchange interaction of in our case $J_{i\gtrsim 15}$ could influence the propagation direction of the SS in hcp Rh/Fe/Ir(111) and be responsible for the tilting of the propagation direction away from high symmetry directions. Figure 7.5b depicts the

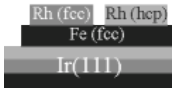

locations of the spins that contribute to the energy of J_{25}, overlaid on the spin structure of a homogeneous SS with $\lambda_{\mathrm{hcp}} = 4.0$ nearest neighbor distance (NND) at a propagation angle of $\alpha = 13°$. It becomes evident from the long distance to the involved spins compared to the SS wavelength that multiple different relative spin orientations are possible when the propagation direction is rotated. Indeed, an analysis of the energy of this homogeneous SS as a function of the propagation direction for all $J_{i\neq 25} = 0$ and $J_{25} = -0.1\,\mathrm{meV}$, Fig. 7.5c, shows distinct local minima at $\alpha = \pm 13°$ of a few $100\,\mu\mathrm{eV/atom}$. As seen from this simple exemplary calculation, a combination of weak non-isotropic long-range (compared to the magnetic period) interactions are a feasible explanation for the tilting of the propagation direction of the observed magnetic state in hcp Rh/Fe/Ir(111).

Figure 7.5d shows the qualitative function shapes of $E_{J_{15}}(\alpha)$ for different wavelengths λ. From numerical analyses, it becomes apparent that for $\lambda < r/1.4801$, with r being the distance to $E_{J_{15}}$, $E_{J_{15}}(\alpha)$ develops a minimum off the high-symmetry directions (0° and 30°) and changes its shape. Thus we conclude that for hcp Rh/Fe/Ir(111) with $\lambda_{\mathrm{hcp}} \approx 4.0\,\mathrm{NND}$ long-range exchange interactions of $J_{i\gtrsim 15}$ ($r \gtrsim 6\,\mathrm{NND}$), cf. red dashed circle in Fig. 7.5a, can tilt the propagation direction away from the high-symmetry direction. Acting in combination, they could then produce a minimum at the experimentally observed $\alpha = \pm 9°$ to 12°. Also this general trend is not restricted to homogeneous SSs, but should hold true for various periodic magnetic states.

In simple words, one possible explanation for the magnetic structure in hcp Rh/Fe/Ir(111) propagating in a direction that is not one of the high-symmetry axes of the crystal is proposed here. Long-range exchange interactions can result in such a tilting effect if the magnetic period is shorter than roughly 2/3 of the interaction distance. This is not the only possible explanation. In principle, it is plausible that also long-range DMI can have a similar effect. For other spin structures like inhomogeneous SSs or multi-Q states [Al-Zubi *et al.*, 2011], it cannot be excluded that a competition of higher-order interactions such as the 4-spin interaction or the biquadratic exchange interaction [Heinze *et al.*, 2011] with the Heisenberg exchange and/or DMI is responsible for the tilting.

7.3. DFT Calculations

To extract the exchange constants J_{ij} from first-principles calculations based on DFT, it is a common procedure to calculate the energy of several flat, homogeneous SS states with different periodicities and fit a Heisenberg spin model to the resulting energy dispersion. Figure 7.6 shows such spin spiral energy dispersion curves for the different stackings of Pd and Rh on Fe/Ir(111), calculated by the group of Prof. Stefan Heinze, Univ. Kiel. The exchange energy is given as a function of $q = 2\pi/\lambda$, with $q = 0$ ($\bar{\Gamma}$-point) representing the FM state and $q = 2\pi/\left(\sqrt{3}a\right)$ ($\bar{\mathrm{M}}$-point) referring to the row-wise AFM state. Since

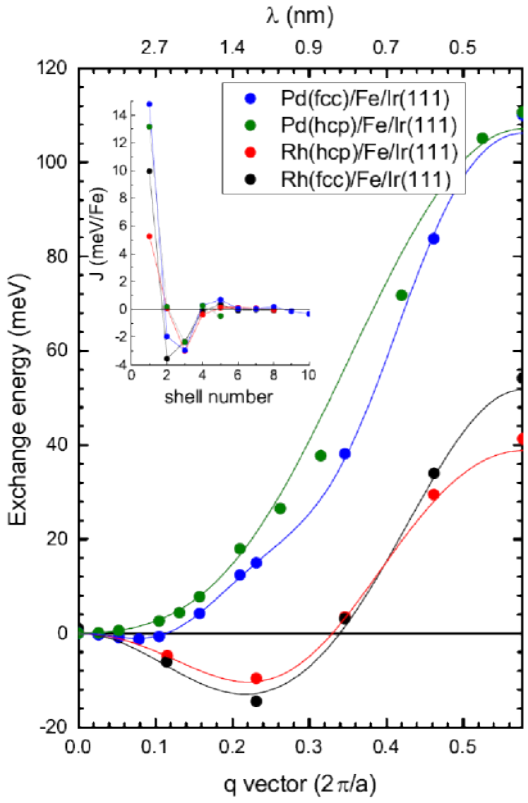

Figure 7.6.: Energy dispersion of spin spirals for Pd/Fe/Ir(111) and Rh/Fe/Ir(111). Spin spiral dispersion along the $\bar{\Gamma} - \bar{\mathrm{M}}$ direction of the 2D-Brillouin zone in both fcc and hcp stackings of the Pd or Rh overlayer, respectively. SOC has not been taken into account in these calculations. For Rh/Fe the magnetic exchange interaction stabilises a spin-spiral of $\lambda \approx 1.2$ nm period. The inset shows the exchange constants extracted from fitting of energy dispersions along both high symmetry directions; the solid lines show the fit results. Calculations were done by the group of Stefan Heinze using the full-potential augmented plane wave (FLAPW) method as implemented in the `FLEUR` code Heinze [2017] (taken from [Romming *et al.*, 2016, Fig. 1]).

SOC and, resulting from it, the DMI are not included in this calculation, any deviation of the curves from a cosine-shape with a minimum at a high-symmetry point, is a sign of frustration of exchange interactions. Indeed, the calculations show clear minima[1] for both stackings of Rh at around $\lambda \approx 1.2\,\mathrm{nm}$, driven by a weak J_1 combined with comparably strong J_2 or J_3 with the opposite sign. Additional calculations showed that also DMI is present and responsible for a cycloidal nature of the SSs and a unique rotational sense [Romming *et al.*, 2016]. However, the energy gain due to DMI is small compared to the deep energy minima of approx. 10 to 15 meV with respect to the FM state. The depth of the minima also corroborates the observed stability of the magnetic states against magnetic

[1] Although there is a minimum in the spin spiral dispersion for a certain wavelength, it does not necessarily infer that a SS is the actual ground state. Other magnetic states not considered here, such as multi-Q states, could have a lower energy.

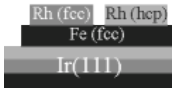

fields. An observation of magnetic field induced skyrmions within a reasonable magnetic field range is highly unlikely for Rh/Fe/Ir(111) (also confirmed experimentally up to 9 T [Romming, 2013]). Figure 7.6 also shows spin spiral dispersion curves for Pd/Fe/Ir(111). As has been shown in the previous chapters, the system Pd/Fe/Ir(111) is a better candidate for the experimental observation of skyrmions, due to their much steeper shape and without the deep minima.

7.4. Conclusions

Rh was used in this chapter as the element to tune the magnetic properties of fcc Fe/Ir(111) as an adlayer. The resulting magnetic structures in Rh/Fe/Ir(111) differ from the one observed in Fe/Ir(111) to a great extent, and the stacking of the adlayer plays a significant role, influencing the magnetic period and additional characteristic properties. On the one hand, in fcc Rh/Fe/Ir(111), a cycloidal SS ground state with a magnetic period of 1.5 nm along the three high-symmetry $\langle 11\bar{2} \rangle$ directions was found. In hcp Rh/Fe/Ir(111), on the other hand, the magnetic structure with a period of 1.1 nm propagates flexibly along a non-high-symmetry direction that is tilted by roughly $\alpha = \pm(9-12)^\circ$ with respect to the $\langle 11\bar{2} \rangle$ directions. This was confirmed with high accuracy by an analysis of Moiré patterns caused by a short range (half of the magnetic period) electronic contrast together with the atomic lattice that can also be observed with a non-magnetic tip. It was shown exemplarily that, in principle, long-range exchange interactions between spins at a distance of $\gtrapprox 1.6$ nm in this case can produce such a directional minimum in a non-high-symmetry direction.

DFT calculations showed that the short magnetic periodicities in Rh/Fe/Ir(111) are mainly caused by the frustration of exchange interactions, producing deep energy minima in the spin spiral dispersions of Rh/Fe/Ir(111). In comparison to Pd/Fe/Ir(111), presented in the previous chapters, the much shorter magnetic periods of 1.5 nm or 1.1 nm compared to 6 to 7 nm in Pd/Fe/Ir(111) primarily stem from weaker J_1 in Rh/Fe/Ir(111). In Rh/Fe/Ir(111), no skyrmions were observed experimentally up to magnetic fields of 9 T.

Summary

Throughout this thesis, different contrast modes of STM have been employed to investigate the influence of several configurations of Pd or Rh adlayers on the magnetism of Fe/Ir(111). Starting from the non-collinear nanoskyrmion lattice state in Fe/Ir(111) with a square symmetry and a period of 1 nm, the addition of the non-magnetic materials Pd or Rh on top leads to also non-collinear magnetic states in all cases studied here; the characteristic magnetic properties of these bilayer or triple-layer systems vary widely, depending on the adlayer material with periodicities ranging from 1 to 15 nm, and transition magnetic fields to skyrmion lattices ranging from <0.8 to >9 T. Another key factor, influencing the magnetic properties, is the stacking order of both the Fe and the first layer of non-magnetic Pd or Rh.

For the ML Pd on fcc Fe/Ir(111) systems, the magnetic ground state is a spin spiral with a period of roughly 7 nm with slight differences depending on the Pd stacking. Upon application of an external magnetic field, the PdFe systems undergo phase transitions to a skyrmion lattice state. At higher magnetic field, a mostly ferromagnetic state is obtained, facilitating the first experimental observation of interface-induced, isolated magnetic skyrmions in ultrathin films. It was shown how these skyrmions can be written and deleted individually in close vicinity to each other using the STM tip. The responsible tunnel parameters for switching the skyrmions were identified by analysing continuous switching signals. This yielded two possible explanations for the observed bias-dependent, preferred switching direction: STT due to the net spin-polarisation of the tunnel current, or asymmetric electronic relaxation processes due to major differences in the LDOS of skyrmion and FM state due to the NCMR.

Subsequently, this thesis focused on the details of the spin structure of isolated skyrmions. The high spatial resolution of SP-STM paired with the direct access to the spin structure of magnetic samples was used to prove the axial symmetry and fixed rotational sense of the spatially localised, solitonic magnetic whirls. By introducing a standard 360°-domain wall profile as an analytical function to describe the angular profile of magnetic skyrmions, it was possible to establish a connection to the micromagnetic model that was used to predict magnetic skyrmions [Bogdanov and Yablonsky, 1989]. Showing that the size and shape of isolated skyrmions scale with an external magnetic field as expected from the theory, a fitting procedure was implemented to extract the relevant material parameters from the field-dependent evolution of an isolated skyrmion in hcp Pd/Fe/Ir(111).

This fitting procedure was then extended to flexibly connect a variety of experimental observables with their theoretical counterparts, calculated in the micromagnetic model. Hence, it was possible to estimate the material parameters of effective exchange, DMI and uniaxial effective anisotropy for the various combinations of Pd adlayers on Fe/Ir(111). For hcp Pd/Fe/Ir(111), the model can very well describe the SS period, the field-dependent skyrmion size and shape and even the shape of 360°-DWs and magnetic phase transition fields for one set of distinct material parameters A, D, K and M. However, major discrepancies appear for the other systems. This, together with DFT calculations by the group of Prof. Stefan Heinze, Univ. Kiel, led to the conclusion that additional interactions - especially frustration of exchange interactions - need to be included for a full description of most of the Pd and Fe/Ir(111) based magnetic systems investigated here.

The good description of hcp Pd/Fe/Ir(111) was used in atomistic simulations, performed by the group of Prof. Hans Fangohr, Univ. Southampton (see Appendix A.2), to reproduce the experimental results. Within the framework of this thesis, the properties of the simulations regarding the topology were discussed in detail. In particular, the concept of classifying magnetic structures by the sign of the topological charge compared to the sign of the magnetic field into common (skyrmionic) and uncommon (induced by hysteresis) states was introduced and applied. Networks of 360°-DWs and target skyrmions are among the observed uncommon magnetic states, induced by magnetic field sweeps at low temperature and stabilised by confinement effects. Also, it was possible to experimentally verify the DMI-induced tilting of spins at open boundary island edges, which is another prediction by previous theoretical studies and by the atomistic simulations.

Finally, the characterisation of the magnetic structures observed in Rh/Fe/Ir(111) in comparison to Pd/Fe/Ir(111) emphasised, how sensitively ultrathin magnetic layer systems react to the microscopic morphology and stacking of each involved layer, including the non-magnetic ones. The periodicities of the uni-axial magnetic structures are 1.1 nm and 1.5 nm for the two stackings of Rh, respectively.

On the path towards the possible application of magnetic skyrmions in future spintronic devices, this thesis has covered some key aspects of the fundamental research necessary. Besides the discovery of individual, interface-induced skyrmions and the demonstration of their manipulability, the field-dependent structure of isolated skyrmions was connected to the micromagnetic theory, which was previously used for their prediction. Whereas it could be shown that the micromagnetic model exhibits excellent agreement for the model system hcp Pd/Fe/Ir(111), this thesis has shown that existing theories about skyrmionic systems need to be extended by further magnetic interactions for a complete description of the magnetic properties of all sample systems investigated here. Foremost, the frustration of exchange interactions should be incorporated, as there are strong experimental hints for its influence on the majority of the magnetic systems investigated in this work.

In conclusion, this thesis answered some fundamental questions about magnetic skyrmions and the tuning of interactions in thin films. Hopefully, it inspires more investigations and developments with the aim of skyrmion based memory or logic devices capable of handling the vast amount of data which is generated world-wide each year.

Appendix A.

Methods

A.1. Estimation of Tip-Sample Distance and Electric Field

The electric field between an STM tip and the sample surface can be estimated via the ratio of the applied sample bias voltage and the tip-sample distance, $E = U/d$ [Gerhard *et al.*, 2010; Brovko *et al.*, 2014]. As a result of the shape of the tip, the electric field derived in such a parallel-plate model is an upper bound for the electric field at the surface [Sonntag *et al.*, 2014]. Although U and relative tip–sample distances Δz are directly accessible in STM experiments, the absolute distance d is estimated by extrapolation, in a similar manner as in previous publications [Gerhard *et al.*, 2010; Hsu *et al.*, 2017]. Figure A.1a shows an $I(\Delta z)$-spectrum, recorded at $U = +650\,\mathrm{mV}$ with the same tip and on the same defect, mainly used in Section 3.3. The linear behaviour in this semi-logarithmic plot (see solid green line) is characteristic for the tunnel regime. An extrapolation to the point contact resistance of $12.9\,\mathrm{k\Omega}$ [Gerhard *et al.*, 2010; Hsu *et al.*, 2017] leads to the assignment of estimated absolute tip-sample distances for any current value at $U = +650\,\mathrm{mV}$. Together with the change of the relative tip height as a function of bias voltage U at $I = 300\,\mathrm{nA}$, see Fig. A.1b, all of the data sets shown in Fig. 3.6 can be assigned an absolute tip-sample distance d and with it an estimated electric field E. These results are used in Fig. 3.10 to rule out a major impact of the electric field on the switching mechanism of skyrmions in Pd/Fe/Ir(111).

A.2. Spin Dynamics Simulation Details

The atomistic simulations in Chapter 6 were performed by David Cortés-Ortuño in the group of Prof. Hans Fangohr, Univ. Southampton using the atomistic and micromagnetic simulations package Fidimag [Cortés-Ortuño *et al.*, 2016], which is written in C and Python. The atomistic code solves the Landau–Lifshitz–Gilbert equation at $T = 0$ using a Hamiltonian based on a discrete spin Heisenberg model, as described in Section 1.1.1, with a damping coefficient of 0.9.

The profile of the PdFe islands were obtained mapping black and white STM images

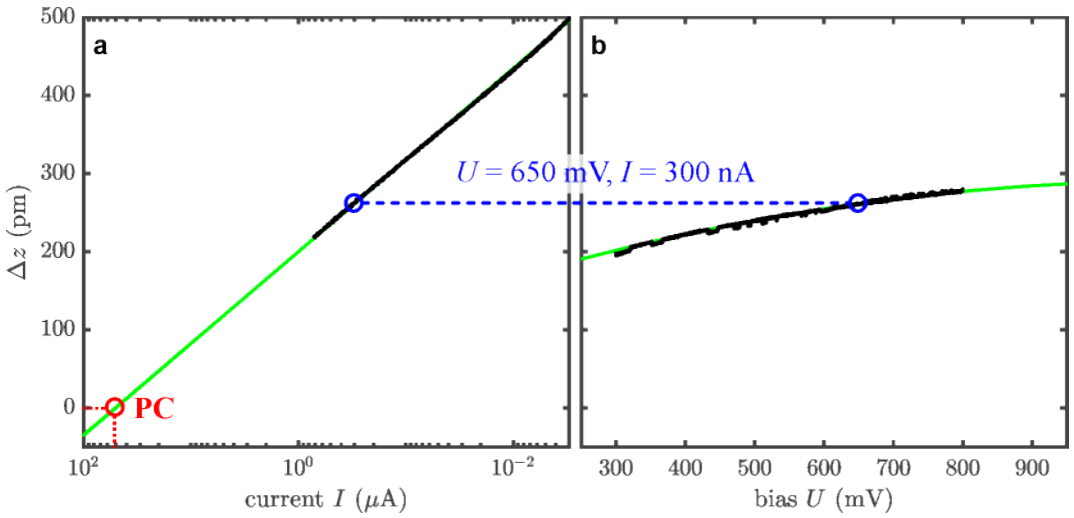

Figure A.1.: Estimation of the tip-sample distance with $z(I)$ and $z(U)$. **a** Black data points from $I(z)$-spectroscopy. $U = +650\,\mathrm{mV}$, $I_{\mathrm{stab}} = 700\,\mathrm{nA}$, $B = -2.8\,\mathrm{T}$. **b** Relative tip height Δz during a constant current sweep of the bias from $U_{\mathrm{s}} = +300\,\mathrm{mV}$ to $U_{\mathrm{e}} = +800\,\mathrm{mV}$ (same data is shown in Fig. 3.11a). Sweep recording duration: 50 s, $I_{\mathrm{set}} = 300\,\mathrm{nA}$, $U_{\mathrm{mod}} = 10\,\mathrm{mV}$, $B = +2.7\,\mathrm{T}$, $T = 4.2\,\mathrm{K}$. Both spectra are taken with the tip positioned over the defect shown in Fig. C.2 (Tip#1) (same tip and position as complete data set in Fig. 3.6). The absolute tip-sample distance is estimated from the extrapolation of $I(z)$-spectrum to the point contact (PC) resistance of $12.9\,\mathrm{k\Omega}$ ($I_{\mathrm{cont}} \approx 50\,\mu\mathrm{A}$). $\Delta z(U)$ is offset by matching the same values in **a** and **b** at $U = +650\,\mathrm{mV}$, $I = 300\,\mathrm{nA}$, see blue circles. Solid green lines depict the estimated absolute tip-sample distance d in the skyrmion state for the respective tunnel parameters.

into a hexagonally arranged lattice of spins in Fidimag. Magnetic parameters for the simulations are taken from Ref. [Romming *et al.*, 2015] and converted to atomistic values: $J_1 = 5.88\,\mathrm{meV}$, $D_1 = 1.56\,\mathrm{meV}$, $K = 0.41\,\mathrm{meV}$ and $\mu = 3.0\,\mu_{\mathrm{B}}$.

Simulations of a field sweep starting from different magnetic states are based on, firstly, relaxing artificially made magnetic configurations which resemble the ones observed experimentally, e.g. a skyrmion, target skyrmion, skyrmion and helicoid, etc., under a specific magnetic field. Secondly, the relaxed state is taken and the magnetic field is increased or decreased before relaxing the system for every field, like a hysteresis loop. As a result, different magnetic configurations are obtained on this field sweep depending on the starting magnetic configuration.

The 3D representation of the simulation results and their analysis regarding the topological charge was done by the author of this thesis.

A.3. Estimation of Saturation Magnetisation

The saturation magnetisation M_S of the PdFe bilayer was estimated by using values for the atomic magnetic moments from DFT calculations [Dupé *et al.*, 2014] and assuming a

uniform distribution of the magnetisation μ in the volume V:

$$M_S = \frac{\mu}{V} = \frac{3\mu_B}{\frac{\sqrt{3}}{2}a^2 \cdot t}, \tag{A.1}$$

with $a = 2.715\,\text{Å}$ and $t = 4.08\,\text{Å}$ as the DFT nearest-neighbor distance and bilayer thickness, respectively.

A.4. Different Error Weighting in Section 4.1

To obtain a larger influence of the error weighting procedure such that the experimental values with a small relative error have a much larger impact on the fitting procedure than the ones with higher relative uncertainties ($|B| > 2.6$ in Fig. 4.3), in [Romming *et al.*, 2015] an error-weighting different to the one in Eq. (1.21) was used:

$$\mathcal{S}(\mathcal{P}) = \sum_{\chi} \left\{ \text{median}(\chi_i) \cdot \sqrt{\sum_{i=1}^{N} (\chi_i - \Upsilon_i(\mathcal{P}))^2 \cdot \frac{w_i^2}{N^2}} \right\}, \tag{A.2}$$

with

$$w_i = \frac{\chi_i}{\xi_i}$$

as the error weight. The additional multiplication by the median of the experimental input values leads to an artificial over-weighting of c compared to w. This leads to a good fit to the important data points, neglecting the faulty ones.

A.5. Error Estimation for A, D, K

Based on the magnetic moment derived from DFT and assuming that it is homogeneously distributed over the PdFe bilayer, the error bars for A, D, K can be estimated in the following way. Both the standard deviations of the experimental values of $c(B)$ and $w(B)$ and their scattering around the fitted curves are within less than 5 % [1]. The error bars of A, D, K were obtained by applying the fitting procedure to four sets of $c(B)$ and $w(B)$, which were artificially increased or decreased by ±5 %. The maximal deviation of the material parameters during these fits was chosen as the reasonable error bar for each parameter A, D and K.

This procedure was applied in Section 4.1. In all other cases, the fit procedure was carried out numerous times while varying the experimental input parameters according to

[1] For $|B_z| > 2.5\,\text{T}$, a small jiggling of the skyrmion position at a fast time scale could be the reason for a systematic overestimation of w in the SP-STM-images. Due to the larger error bar of these values, they only have a small influence on the error weighted fitting procedure.

their error. The standard deviation of the resulting material parameters was then used as their respective error.

Appendix B.

Triple Layer Fe/Ir(111)

B.1. Distorted Skyrmion Model

In the framework of this thesis, the spin structure model of a skyrmion, as described in Chapter 4 with Eq. (4.2), was extended to also model distorted skyrmions, as seen in the TL Fe/Ir(111) [Hsu *et al.*, 2017]. The spin structure is modeled as a bent 360°-DW of length l on the perimeter of a circle with radius r and capped at each end with half of an axially symmetric skyrmion, see Fig. B.1a. The parameters of the 360°-DW as well as the skyrmion are $\pm c$ and w, the position and width of two equivalent 180°-DW, as defined by Eq. (1.19), and a rotational sense as shown (green/red indicates magnetisation up/down).

Throughout the work of Hsu *et al.*, three SP-STM simulations were compared to the experimental data and could explain the measured data with IP sensitivity. This way, it was possible to conclude that these entities indeed have the topology of a skyrmion. Figure B.1c shows a map of the topological charge of the modelled spin structure. Although there are clear kinks in the topological charge density at the border between the domain wall section and the skyrmion sections, the sum of the topological charge is exactly $Q = +1$ like for a normal skyrmion with axial symmetry. The topological charge of the bent 360°-DW-section sums up to zero.

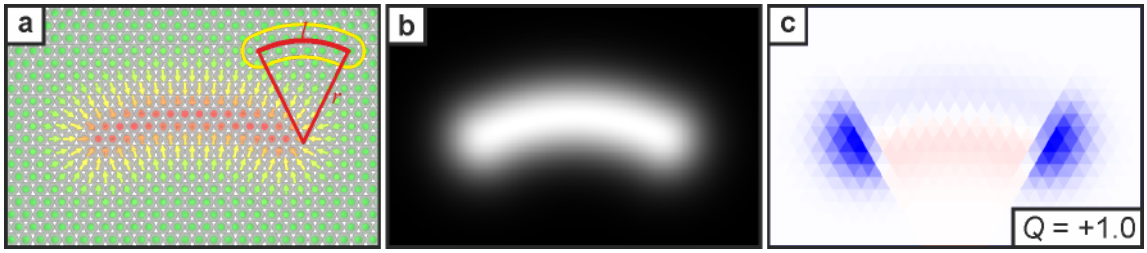

Figure B.1.: Model of a distorted skyrmion. **a** Spin structure as described in the text with $l = 3.5\,\mathrm{nm}$, $r = 3.8\,\mathrm{nm}$, $c = 0.45\,\mathrm{nm}$, $w = 1.0\,\mathrm{nm}$. **b** SP-STM-simulation of the spin structure in **a** according to Eq. (1.22) with OOP tip, $z_0 = 0.6\,\mathrm{nm}$, $\gamma_\mathrm{P} = 0.1$. **c** Map of the topological charge of the spin structure in **a**, obtained as described in Chapter 6 (colour code according to Fig. C.1b).

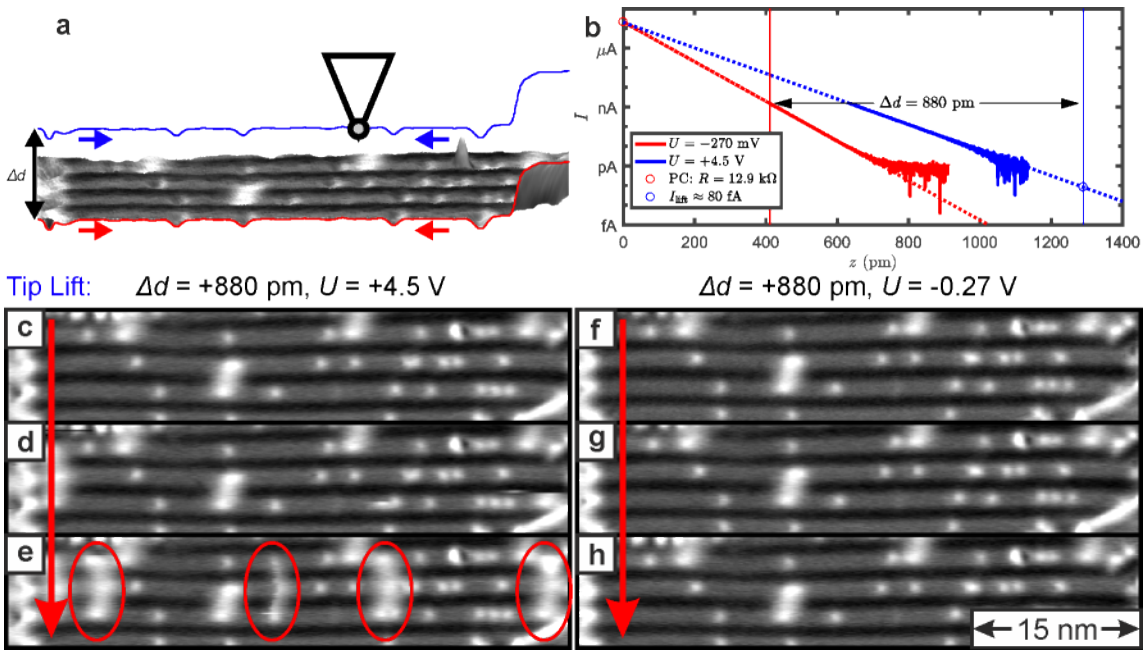

Figure B.2.: Low-current writing of skyrmions. **a** 3D sketch of the measurement procedure; for each line, the surface is first scanned (forward and backward, red trace) at low voltage before retracing the same line with an offset of $\Delta d = +880\,\mathrm{pm}$ (blue trace). **b** $I(z)$-spectroscopy at the two bias voltages of interest. The tip-sample distance is estimated from the extrapolation of $I\,(z, U = -270\,\mathrm{mV})$-spectrum to the point contact resistance of $12.9\,\mathrm{k\Omega}$. **c-h** SP-STM based $\mathrm{d}I/\mathrm{d}U$ maps of a TL Fe/Ir(111)-sample taken in subsequent order. The images are recorded during the first pass of the sample at $U = -270\,\mathrm{mV}$ and $I_{\mathrm{set}} = 1.5\,\mathrm{nA}$. After each line, the tip was lifted by $\Delta d = +880\,\mathrm{pm}$ while retracing the previously recorded lines at half-speed and applying $U = +4.5\,\mathrm{V}$ (**c-e**) or keeping the same voltage (**f-h**). Panels **f-h** serve as counter-experiment without the high voltage applied. Cr-bulk tip, $T = 4.2\,\mathrm{K}$, $B = +2.8\,\mathrm{T}$, $U_{\mathrm{mod}} = 34\,\mathrm{mV}$.

B.2. "Zero-Current" Switching of Skyrmions

In [Hsu *et al.*, 2017], the distorted skyrmions as described in the previous section were written and deleted by local electric fields. Although it was shown by Hsu *et al.* that the main mechanism responsible for switching the skyrmions is indeed the electric field, the nature of the shown experiments always involved a tunnel current of typically 1 nA or more. The high electric fields of $|E| > 2\,\mathrm{V\,nm^{-1}}$ typically require a tip-sample distance $z_0 < 1\,\mathrm{nm}$. This necessitates a considerable tunnel current flowing when bias voltages above 2 V are applied.

Figure B.2 shows a different approach to switching the skyrmions while minimising the tunnel current. An area mostly free of skyrmions, but where skyrmions are typically seen at the magnetic field of $B = +2.8\,\mathrm{T}$, is imaged with low bias voltage ($U_{\mathrm{m}} = -270\,\mathrm{mV}$, $I_{\mathrm{set}} = 1.5\,\mathrm{nA}$, leading to an estimated[1] absolute tip-sample distance $z_0 \approx 410\,\mathrm{pm}$). After

[1] To estimate the absolute tip-sample distance, the linear behaviour of the current vs. the distance in

each line being recorded in the forward and backward direction at the given set-point (red line in Fig. B.2a), the tip is lifted by $\Delta d = +880\,\mathrm{pm}$ and a higher voltage of $U_\mathrm{s} = +4.5\,\mathrm{V}$ is applied while retracing the previously recorded height-profiles of the forward and backward channel (blue line in Fig. B.2a). This way, a constant and relatively high electric field is applied without the need for a measurable tunnel current. Although the current flowing during the tip lift is below the detection limit of our STM, the tunnel current at a tip lift distance of $\Delta d = +880\,\mathrm{pm}$ can be estimated by extrapolating an $I(z)$-spectrum to $I(z = z_0 + 880\,\mathrm{pm}) < 100\,\mathrm{fA}$, see Fig. B.2b. Although this is a very low current, still on the order of 600 electrons flow every ms and could potentially activate a switching process.

Panels c-h of Fig. B.2 show the $\mathrm{d}I/\mathrm{d}U$-maps of such measurements, recorded at $U_\mathrm{m} = -270\,\mathrm{mV}$, $I_\mathrm{set} = 1.5\,\mathrm{nA}$, each with a second trace of the lines in between with a tip lift of $\Delta d = +880\,\mathrm{pm}$. For the left column, the bias applied during the tip lift is $U_\mathrm{s} = +4.5\,\mathrm{V}$, whereas for the right column, the bias stays at $U_\mathrm{s} = -270\,\mathrm{mV}$, serving as a counter-check experiment. Comparing the left and the right column, it is directly evident that during the measurements with $U_\mathrm{s} = +4.5\,\mathrm{V}$ single skyrmions are written (marked by the red ellipses in Fig. B.2e), whereas without the high bias, the magnetic state remains the same. This shows that the electric-field driven switching of distorted skyrmions in the TL Fe/Ir(111) still works with currents below 100 fA.

this semi-logarithmic plot is extrapolated to the point contact resistance of 12.9 kΩ (marked as PC in Fig. B.2b) [Gerhard *et al.*, 2010; Hsu *et al.*, 2017], similar to Appendix A.1.

Appendix C.

Additional Figures and Data

k	$h_1(k)$	$h_S(k)$	k	$h_1(k)$	$h_S(k)$	k	$h_1(k)$	$h_S(k)$
0.06	0.215	0.297	0.90	0.178	0.421	1.74	0.117	0.145
0.10	0.212	0.597	0.94	0.176	0.406	1.78	0.112	0.133
0.14	0.211	0.634	0.98	0.174	0.392	1.82	0.107	0.122
0.18	0.210	0.655	1.02	0.171	0.379	1.86	0.102	0.110
0.22	0.209	0.662	1.06	0.169	0.364	1.90	0.097	0.099
0.26	0.208	0.661	1.10	0.167	0.349	1.94	0.088	0.088
0.30	0.206	0.656	1.14	0.164	0.335	1.98	0.078	0.078
0.34	0.203	0.649	1.18	0.162	0.320	2.02	0.068	0.068
0.38	0.203	0.631	1.22	0.159	0.306	2.06	0.059	0.059
0.42	0.201	0.610	1.26	0.156	0.292	2.10	0.051	0.051
0.46	0.199	0.594	1.30	0.153	0.280	2.14	0.043	0.043
0.50	0.198	0.577	1.34	0.150	0.267	2.18	0.036	0.036
0.54	0.196	0.557	1.38	0.147	0.252	2.22	0.030	0.030
0.58	0.194	0.541	1.42	0.144	0.240	2.26	0.024	0.024
0.62	0.192	0.524	1.46	0.142	0.227	2.30	0.019	0.019
0.66	0.191	0.508	1.50	0.138	0.214	2.34	0.014	0.014
0.70	0.189	0.493	1.54	0.135	0.202	2.38	0.010	0.010
0.74	0.187	0.478	1.58	0.132	0.191	2.42	0.006	0.006
0.78	0.185	0.463	1.62	0.128	0.179	2.46	0.003	0.003
0.82	0.183	0.448	1.66	0.124	0.167	2.50	0.000	0.000
0.86	0.180	0.435	1.70	0.120	0.156			

Table C.1.: Values for $h_1(k)$ and $h_S(k)$. Values as used in the estimation of transition magnetic fields. Graphically extracted from Fig. 1.2b.

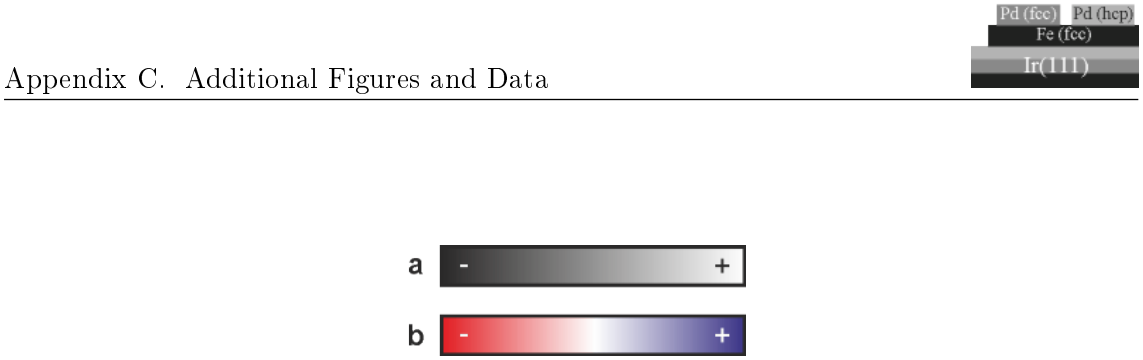

Figure C.1.: Colour bars used throughout this thesis. **a** Gray-scale colour bar. **b** Red-White-Blue Colour bar. The values indicated throughout the thesis correspond to the minimum and maximum value of the colour code used.

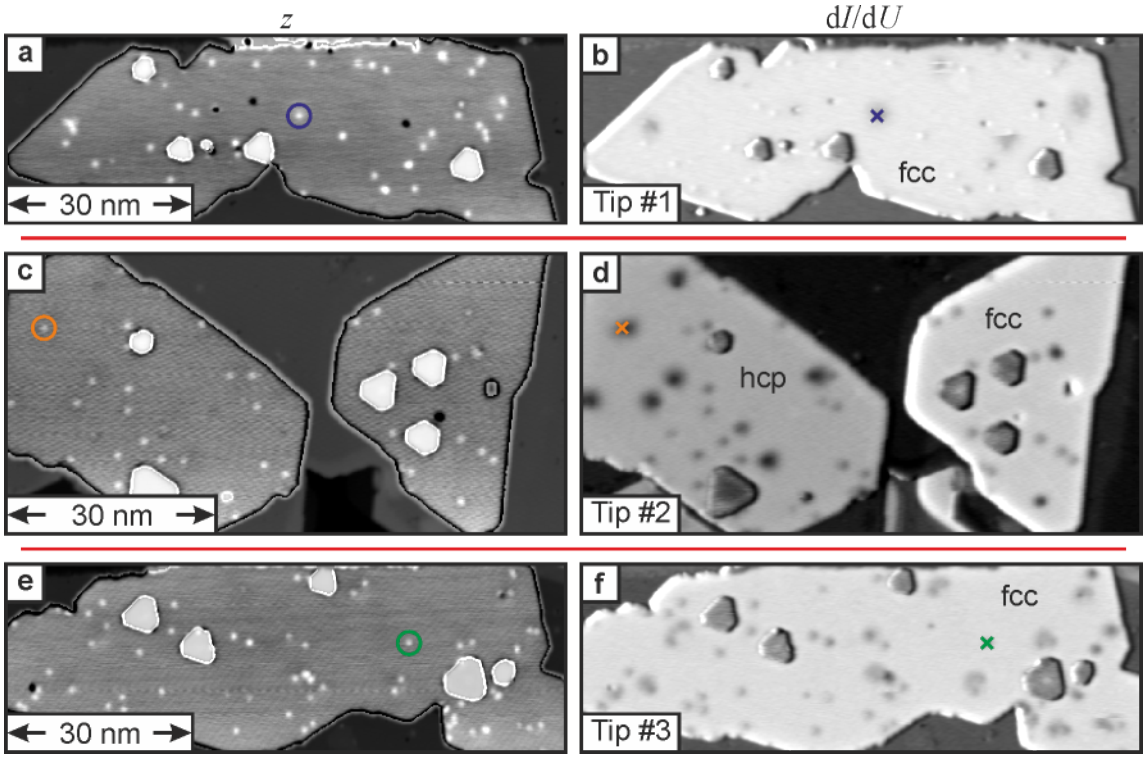

Figure C.2.: Positions of spectra. **a,c,e** SP-STM constant-current images (contrast adjusted locally to ±15 pm) and **b,d,f** simultaneously acquired dI/dU images of Pd/Fe/Ir(111) islands with the tip positions marked by circles/crosses, where telegraph noise signals and spectra were recorded. **a,b**: Tip position of data shown in Figs. 3.5 to 3.8 and 3.10 to 3.12. $B = +2.9\,\mathrm{T}$, $U = +600\,\mathrm{mV}$, $I_{\mathrm{set}} = 750\,\mathrm{pA}$. **c,d**: Tip position of data shown in Fig. 3.9. $B = +2.85\,\mathrm{T}$, $U = +700\,\mathrm{mV}$, $I_{\mathrm{set}} = 1\,\mathrm{nA}$. **e,f**: Tip position of data shown in Figs. C.3 to C.5. $B = +2.7\,\mathrm{T}$, $U = +700\,\mathrm{mV}$, $I_{\mathrm{set}} = 1\,\mathrm{nA}$. Between the acquired data series (horizontal red lines), major tip changes occured. Bulk Cr tip, $T = 4.2\,\mathrm{K}$, $U_{\mathrm{mod}} = 60\,\mathrm{mV}$.

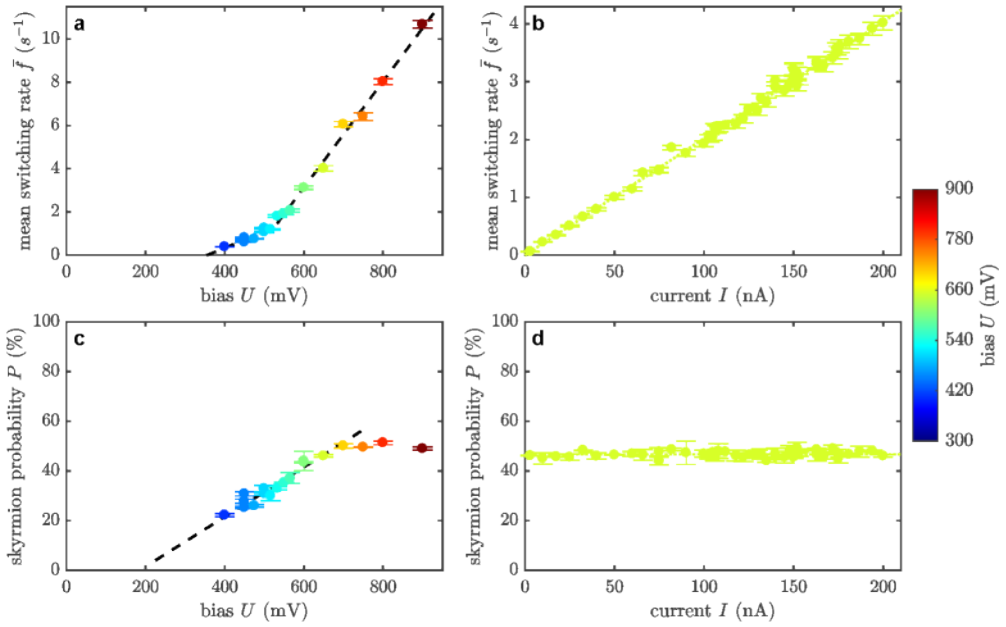

Figure C.3.: Additional data: U and I dependence of skyrmion switching. a,b Mean switching rate $\bar{f}$ as a function of U at constant $I_{\mathrm{set}} = 200\,\mathrm{nA}$ and as a function of I at $U = +650\,\mathrm{mV}$, respectively. **c,d** The corresponding skyrmion probabilities P. All data points were extracted from respective time-dependent switching signals, recorded on a defect hosting a skyrmion, see Tip#3 in Fig. C.2. $\bar{f}$ according to Eq. (3.5), P according to Eq. (3.3). Dashed lines in **a** and **c**, and coloured, dotted lines in **b** and **d** are linear guides to the eye. $T = 4.2\,\mathrm{K}$, $B = +2.9\,\mathrm{T}$.

C.1. Additional Data: Exploration of the Switching Mechanism

Figures C.3 to C.5 show data sets similar to the ones presented in Section 3.3, but recorded on a different defect hosting a skyrmion in fcc Pd/Fe/Ir(111) and with a different tip, see Tip#3 in Fig. C.2. Even though a major tip change occurred in between the data set presented in Section 3.3 and the one shown here and although a different skyrmion at a different defect is investigated, several of the experimental observations in Section 3.3 can be validated with the data shown in Figs. C.3 to C.5:

- Also for this data set, the mean switching yield per electron Υ is mainly influenced by the applied bias voltage U, see Fig. C.4a. Higher positive U leads to a higher Υ in two linear regimes with different slopes also separated at around $U \approx +500\,\mathrm{mV}$.
- Also the directionality of the switching process, represented as the skyrmion probability, has a similar dependency on U as in Fig. 3.6c, only shifted vertically. It also varies by about 30 % in the bias range investigated.
- The tunnel current I once again only changes the average switching rate $\bar{f}$ but not

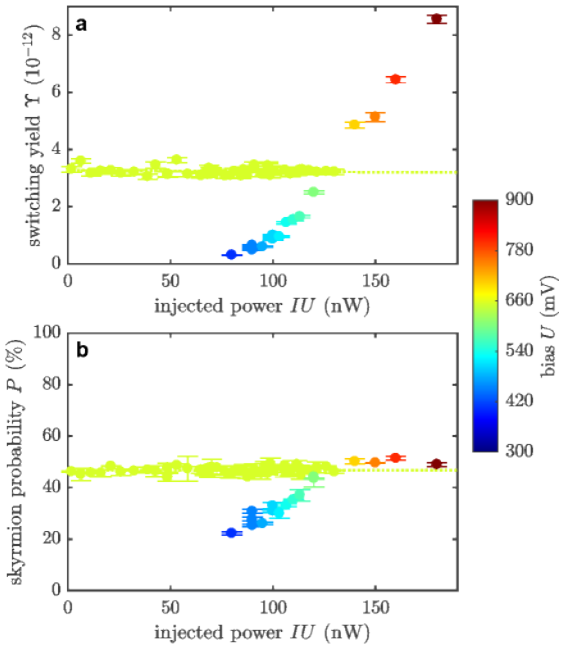

Figure C.4.: Additional data: injected power $I \cdot U$. **a** Mean switching yield Υ as a function of the injected power $I \cdot U$ for the full data set of Fig. C.3. **b** The corresponding skyrmion probabilities P as a function of $I \cdot U$. All data points were extracted from respective time-dependent switching signals, recorded on a defect hosting a skyrmion, see Tip#3 in Fig. C.2. Υ according to Eq. (3.6), P according to Eq. (3.3). Coloured, dotted lines serve as constant linear guides to the eye. $T = 4.2\,\mathrm{K}$, $B = +2.9\,\mathrm{T}$.

the switching yield Υ or the skyrmion probability P to a significant extent, also down to $I = 3\,\mathrm{nA}$, see Fig. 3.6b,d.

- The external magnetic field B influences the skyrmion probability as expected, leading to less skyrmion probability for higher magnetic fields, see vertical shift in Fig. 3.6c.

- Also the switching yield depends on the magnetic field, with generally a higher yield for higher magnetic field, compare the maximal yield here of $\Upsilon_{\mathrm{max},\#3} \approx 8.5 \times 10^{-12}$ at $B = +2.9\,\mathrm{T}$ to $\Upsilon_{\mathrm{max},\#1} \approx 3.5 \times 10^{-12}$ at $B = +2.7\,\mathrm{T}$.

- The skyrmion writing and deleting yields in Fig. C.5d exhibit similar shapes as the ones in Fig. 3.12b.

None of the observations made here contradict the interpretations offered in Section 3.3. But also from this additional data set, it is not possible to determine, which of the two given explanations in Section 3.3 is the dominating one.

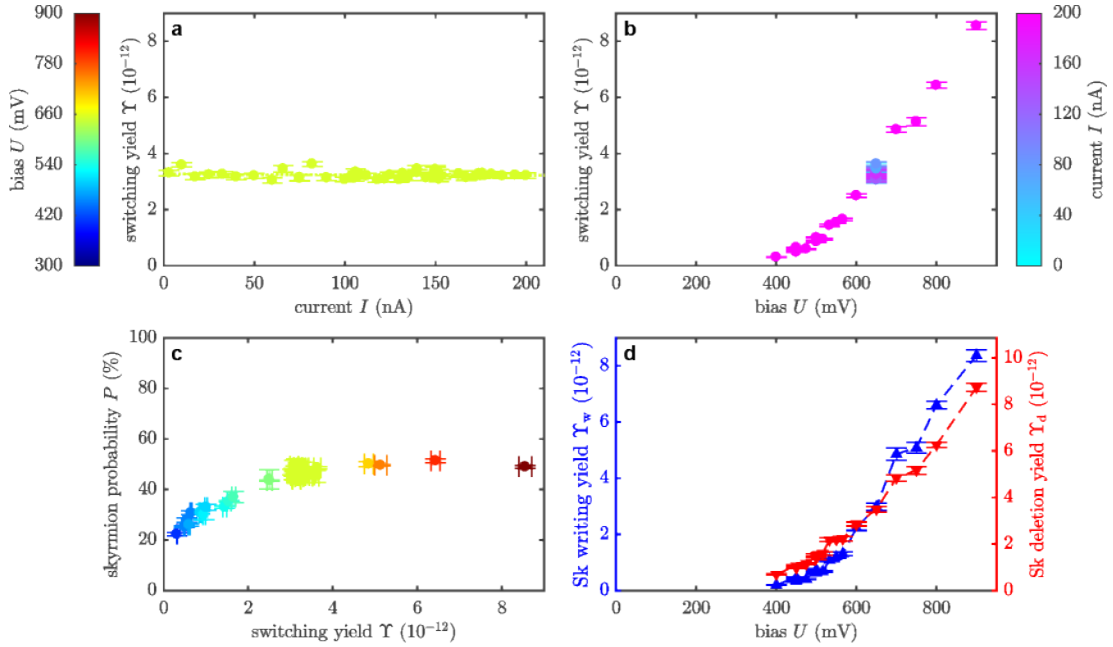

Figure C.5.: Additional data: switching yield Υ. **a** Mean switching yield Υ as a function of I at $U = +650\,\mathrm{mV}$. **b** Υ as a function of U for the full data set of Fig. C.3. **c** The corresponding skyrmion probabilities P of the complete data set plotted as a function of Υ. **d** The skyrmion writing and deletion yields Υ_w and Υ_d as a function of bias voltage, calculated from Eqs. (3.7) and (3.8) for the data points shown in Fig. C.3a, similar to Fig. 3.12b. y-scales are adapted to have Υ_w and Υ_d cross at $U_{inv} \approx +630\,\mathrm{mV}$. All data points were extracted from respective time-dependent switching signals, recorded on a defect hosting a skyrmion, see Tip#3 in Fig. C.2. Υ according to Eq. (3.6), P according to Eq. (3.3). Coloured, dotted line in **a** serve as constant guide to the eye. $T = 4.2\,\mathrm{K}$, $B = +2.9\,\mathrm{T}$.

List of Figures

1.1. Relative atom positions corresponding to exchange constants 6
1.2. Skyrmion and reduced phase diagram for skyrmionic systems 10
1.3. Example of a spin spiral profile 12
1.4. SP-STM geometry and spin-split LDOS 15
1.5. Different magnetic STM contrasts 17
1.6. Magnetic contrasts on 180°-domain walls 18

2.1. Clean Ir(111)-substrate 22
2.2. Nanoskyrmion lattice in fcc Fe/Ir(111) 23
2.3. Sample preparation of Pd/Fe/Ir(111) 24
2.4. Rh/Fe/Ir(111) - defects due to intermixing 25
2.5. Stacking of Rh/Fe/Ir(111) 26

3.1. Magnetic field dependence of Pd/Fe/Ir(111) 30
3.2. Influence of bias voltage in Pd/Fe/Ir(111) 32
3.3. Writing single skyrmions in Pd/Fe/Ir(111) 35
3.4. Writing and deleting single magnetic skyrmions 36
3.5. Exploration of the switching mechanism: telegraph noise 38
3.6. Exploration of the switching mechanism: U and I dependence 39
3.7. Exploration of the switching mechanism: switching yield Υ 40
3.8. Exploration of the switching mechanism: injected power $I \cdot U$ 41
3.9. Exploration of the switching mechanism: B-dependence 42
3.10. Exploration of the switching mechanism: d and E 47
3.11. z-spectroscopy for constant current 48
3.12. Different LDOS of skyrmion and ferromagnet 50

4.1. Spin structure of an individual skyrmion in PdFe/Ir(111) 54
4.2. Comparison of proposed skyrmion profile with numerical calculations 55
4.3. Evolution of the size and shape of skyrmions in PdFe/Ir(111) as a function of external magnetic field 56
4.4. Validation of material parameters via micromagnetic simulations 57
4.5. Uncertainty of the material parameter fit 60

4.6. Influence of the material parameters on the size and shape of an isolated skyrmion . . . 62

5.1. Magnetic field dependent evolution of ML Pd/Fe(fcc) . . . 66
5.2. ML Pd/Fe(fcc) at higher bias . . . 67
5.3. Line profiles of 360°-DWs in the ML Pd/Fe(fcc) . . . 69
5.4. Pd on hcp Fe . . . 70
5.5. Magnetic field dependent evolution of Pd on Pd(fcc)/Fe(fcc) . . . 72
5.6. Magnetic field dependent evolution of Pd on Pd(hcp)/Fe(fcc) . . . 75
5.7. Phase diagram by Wilson *et al.* – adapted version of Fig. 1.2b . . . 78
5.8. Comparison of the model with spin spiral dispersion calculations . . . 79

6.1. The concept of topology in discrete magnetism . . . 82
6.2. Pd(fcc)/Fe(fcc) at 2K: Meta-stable states at low T . . . 84
6.3. Pd(fcc)/Fe(fcc) at 2K: Spin spiral junctions . . . 85
6.4. Confined Pd(hcp)/Fe(fcc) . . . 86
6.5. Pd(hcp)/Fe(fcc): Topological charge of simulated magnetic states . . . 88
6.6. Pd on Pd(fcc)/Fe(fcc): Discovery of the target skyrmion . . . 90
6.7. Topological charge and STM contrast of a target skyrmion . . . 91
6.8. The role of edge conditions for the existence of target skyrmions . . . 93
6.9. Edge tilt in hcp Pd/Fe/Ir(111) . . . 94

7.1. Magnetism of fcc Rh/Fe/Ir(111)-islands . . . 98
7.2. Magnetism of hcp Rh/Fe/Ir(111)-islands . . . 99
7.3. hcp Rh/Fe/Ir(111)-islands with a non-magnetic tip . . . 100
7.4. Simulated contrast for hcp Rh/Fe/Ir(111) . . . 102
7.5. Possible explanation for a propagation off high-symmetry directions in hcp Rh/Fe/Ir(111) . . . 103
7.6. Energy dispersion of spin spirals for Pd/Fe/Ir(111) and Rh/Fe/Ir(111) . . . 105

A.1. Estimation of the tip-sample distance with $z(I)$ and $z(U)$ . . . 112

B.1. Model of a distorted skyrmion . . . 115
B.2. Low-current writing of skyrmions . . . 116

C.1. Colour bars used throughout this thesis . . . 120
C.2. Positions of spectra . . . 120
C.3. Additional data: U and I dependence of skyrmion switching . . . 121
C.4. Additional data: injected power $I \cdot U$ . . . 122
C.5. Additional data: switching yield Υ . . . 123

References

T. Adams, A. Chacon, M. Wagner, A. Bauer, G. Brandl, B. Pedersen, H. Berger, P. Lemmens and C. Pfleiderer, Long-Wavelength Helimagnetic Order and Skyrmion Lattice Phase in Cu_2OSeO_3. *Phys. Rev. Lett.* **108**, 237204 (2012). (Cited on page 62.)

A. Al-Zubi, G. Bihlmayer and S. Blügel, Modeling magnetism of hexagonal Fe monolayers on 4d substrates. *Phys. Status Solidi B* **248**, 2242 (2011). (Cited on pages 99, 100, and 104.)

J. Bardeen, Tunnelling From A Many-particle Point of View. *Phys. Rev. Lett.* **6**, 57 (1961). (Cited on page 14.)

I. Bat'ko and M. Bat'ková, Calorimetric tunneling study of heat generation in metal-vacuum-metal tunnel junctions. *Eur. Phys. J. Appl. Phys.* **31**, 191 (2005). (Cited on page 45.)

E. Bauer, Epitaxy of metals on metals. *Applications of Surface Science* **11**, 479 (1982). (Cited on page 22.)

M. Beg, R. Carey, W. Wang, D. Cortés-Ortuno, M. Vousden, M.-A. Bisotti, M. Albert, D. Chernyshenko, O. Hovorka, R. L. Stamps and et al., Ground state search, hysteretic behaviour, and reversal mechanism of skyrmionic textures in confined helimagnetic nanostructures. *Sci. Rep.* **5**, 17137 (2015). (Cited on pages 91 and 93.)

B. Berg and M. Lüscher, Definition and Statistical Distribution of a Topological Number in the Lattice O(3) σ-Model*. *Nucl. Phys. B* **190**, 412 (1981). (Cited on page 81.)

L. Berger, Emission of spin waves by a magnetic multilayer traversed by a current. *Phys. Rev. B* **54**, 9353 (1996). (Cited on page 48.)

K. von Bergmann, S. Heinze, M. Bode, G. Bihlmayer, S. Blügel and R. Wiesendanger, Complex magnetism of the Fe monolayer on Ir(111). *New J. Phys.* **9**, 396 (2007). (Cited on page 23.)

K. von Bergmann, S. Heinze, M. Bode, E. Y. Vedmedenko, G. Bihlmayer, S. Blügel and R. Wiesendanger, Observation of a complex nanoscale magnetic structure in a hexagonal Fe monolayer. *Phys. Rev. Lett.* **96**, 167203 (2006). (Cited on pages 23 and 65.)

K. von Bergmann, A. Kubetzka, O. Pietzsch and R. Wiesendanger, Interface-induced chiral domain walls, spin spirals and skyrmions revealed by spin-polarized scanning tunneling microscopy. *J. Phys. Condens. Matter* **26**, 394002 (2014). (Cited on pages 23, 53, and 97.)

K. von Bergmann, M. Menzel, A. Kubetzka and R. Wiesendanger, Influence of the Local Atom Configuration on a Hexagonal Skyrmion Lattice. *Nano Lett.* **15**, 3280 (2015). (Cited on pages 23 and 71.)

K. von Bergmann, M. Menzel, D. Serrate, Y. Yoshida, S. Schröder, P. Ferriani, A. Kubetzka, R. Wiesendanger and S. Heinze, Tunneling anisotropic magnetoresistance on the atomic scale. *Phys. Rev. B* **86**, 134422 (2012). (Cited on pages 15, 16, and 101.)

G. Binnig and H. Rohrer, Scanning Tunneling Microscopy. *Helv. Phys. Acta* **55**, 726 (1982). (Cited on page 14.)

S. Blundell, *Magnetism in Condensed Matter*. Oxford Master Series in Condensed Matter Physics (Oxford University Press, Oxford, 2001). (Cited on pages 5 and 7.)

M. Bode, M. Heide, K. von Bergmann, P. Ferriani, S. Heinze, G. Bihlmayer, a. Kubetzka, O. Pietzsch, S. Blügel and R. Wiesendanger, Chiral magnetic order at surfaces driven by inversion asymmetry. *Nature* **447**, 190 (2007). (Cited on page 31.)

A. Bogdanov and A. Hubert, The Properties of Isolated Magnetic Vortices. *Phys. Status Solidi B* **186**, 527 (1994a). (Cited on pages 9, 53, 55, 56, and 57.)

A. Bogdanov and A. Hubert, Thermodynamically stable magnetic vortex states in magnetic crystals. *J. Magn. Magn. Mater.* **138**, 255 (1994b). (Cited on pages 8, 9, 11, 53, 55, 57, and 91.)

A. Bogdanov and A. Hubert, The stability of vortex-like structures in uniaxial ferromagnets. *J. Magn. Magn. Mater.* **195**, 182 (1999). (Cited on pages 57 and 91.)

A. N. Bogdanov, U. K. Rößler, M. Wolf and K.-H. Müller, Magnetic structures and reorientation transitions in noncentrosymmetric uniaxial antiferromagnets. *Phys. Rev. B* **66**, 214410 (2002). (Cited on page 9.)

A. N. Bogdanov and D. A. Yablonsky, Thermodynamically stable "vortices" in magnetically ordered crystals. The mixed state of magnets. *Zh. Exsp. Teor. Fiz.* **68**, 101 (1989). (Cited on pages 2, 9, 29, 53, 57, 62, 77, 78, and 107.)

O. Boulle, J. Vogel, H. Yang, S. Pizzini, D. de Souza Chaves, A. Locatelli, T. O. Mentes, A. Sala, L. D. Buda-Prejbeanu, O. Klein, M. Belmeguenai, Y. Roussigné, A. Stashkevich, S. M. Chérif, L. Aballe, M. Foerster, M. Chshiev, S. Auffret, I. M. Miron and G. Gaudin,

Room-temperature chiral magnetic skyrmions in ultrathin magnetic nanostructures. *Nat. Nanotechnol.* **11**, 449 (2016). (Cited on pages 62 and 63.)

H.-B. Braun, Fluctuations and instabilities of ferromagnetic domain-wall pairs in an external magnetic field. *Phys. Rev. B* **50**, 16485 (1994). (Cited on pages 12, 13, and 55.)

H.-B. Braun, Nucleation in ferromagnetic nanowires - magnetostatics and topology. *J. Appl. Phys.* **85**, 6172 (1999). (Cited on page 9.)

O. O. Brovko, P. Ruiz-Díaz, T. R. Dasa and V. S. Stepanyuk, Controlling magnetism on metal surfaces with non-magnetic means: electric fields and surface charging. *J. Phys. Condens. Matter* **26**, 093001 (2014). (Cited on page 111.)

F. Büttner, I. Lemesh and G. S. D. Beach, Full phase diagram of isolated skyrmions in a ferromagnet, arXiv:1704.08489 (2017a). (Cited on pages 63 and 83.)

F. Büttner, I. Lemesh, M. Schneider, B. Pfau, C. M. Günther, P. Hessing, J. Geilhufe, L. Caretta, D. Engel, B. Krüger, J. Viefhaus, S. Eisebitt and G. S. D. Beach, Field-free deterministic ultra fast creation of skyrmions by spin orbit torques, arXiv:1705.01927 (2017b). (Cited on page 63.)

C. J. Chen, Theory of Scanning Tunneling Spectroscopy. *J. Vac. Sci. Technol. A: Vacuum, Surfaces and Films* **6**, 319 (1988). (Cited on page 14.)

C. J. Chen, Origin of Atomic Resolution On Metal-surfaces In Scanning Tunneling Microscopy. *Phys. Rev. Lett.* **65**, 448 (1990). (Cited on page 14.)

C. J. Chen, *Introduction to Scanning Tunneling Microscopy* (Oxford University Press, 1993). (Cited on pages 14 and 16.)

G. Chen, T. Ma, A. N'Diaye and H. Kwon, Tailoring the chirality of magnetic domain walls by interface engineering. *Nat. Commun.* **4**, 2671 (2013). (Cited on page 63.)

G. Chen, A. Mascaraque, A. T. N'Diaye and A. K. Schmid, Room temperature skyrmion ground state stabilized through interlayer exchange coupling. *Appl. Phys. Lett.* **106**, 242404 (2015). (Cited on page 63.)

D. Cortés-Ortuño, W. Wang, M. Beg, R. A. Pepper, M.-A. Bisotti, R. Carey, M. Vousden, T. Kluyver, O. Hovorka and H. Fangohr, Thermal stability and topological protection of skyrmions in nanotracks. *Scientific Reports* **7**, 4060 (2017). (Cited on page 83.)

D. Cortés-Ortuño, W. Wang, R. Pepper, M.-A. Bisotti, T. Kluyver, M. Vousden and H. Fangohr, Fidimag v2.0. https://doi.org/10.5281/zenodo.167858 (2016). (Cited on page 111.)

A. Crépieux and C. Lacroix, Dzyaloshinsky-Moriya interactions induced by symmetry breaking at a surface. *J. Magn. Magn. Mater.* **182**, 341 (1998). (Cited on pages 7 and 76.)

D. M. Crum, M. Bouhassoune, J. Bouaziz, B. Schweflinghaus, S. Blügel and S. Lounis, Perpendicular reading of single confined magnetic skyrmions. *Nat. Commun.* **6**, 8541 (2015). (Cited on pages 15, 16, 49, and 63.)

B. Dupé, G. Bihlmayer, M. Böttcher, S. Blügel and S. Heinze, Engineering skyrmions in transition-metal multilayers for spintronics. *Nat. Commun.* **7**, 11779 (2016). (Cited on pages 63 and 79.)

B. Dupé, M. Hoffmann, C. Paillard and S. Heinze, Tailoring magnetic skyrmions in ultra-thin transition metal films. *Nat. Commun.* **5**, 4030 (2014). (Cited on pages 31, 53, 58, 66, 79, 80, and 112.)

I. E. Dzyaloshinskii, Thermodynamic theory of weak ferromagnetism in antiferromagnetic substances. *Sov. Phys. JETP* **5**, 1259 (1957). (Cited on pages 7 and 31.)

P. Echenique, J. Pitarke, E. Chulkov and A. Rubio, Theory of inelastic lifetimes of low-energy electrons in metals. *Chem. Phys.* **251**, 1 (2000). (Cited on page 45.)

E. Feldtkeller, Mikromagnetisch stetige und unstetige Magnetisierungskonfigurationen. *Zeitschrift fur Angewandte Physik* **19**, 530 (1965). (Cited on page 83.)

P. Ferriani, K. von Bergmann, E. Y. Vedmedenko, S. Heinze, M. Bode, M. Heide, G. Bihlmayer, S. Bluegel and R. Wiesendanger, Atomic-scale spin spiral with a unique rotational sense: Mn monolayer on W(001). *Phys. Rev. Lett.* **101**, 027201 (2008). (Cited on page 31.)

A. Fert, Magnetic and Transport Properties of Metallic Multilayers. *Materials Science Forum* **59–60**, 439 (1990). (Cited on pages 7 and 31.)

A. Fert, V. Cros and J. Sampaio, Skyrmions on the track. *Nat. Nanotechnol.* **8**, 152 (2013). (Cited on pages 2, 30, 31, 61, 62, and 63.)

A. Fert and P. M. Levy, Role of Anisotropic Exchange Interactions in Determining the Properties of Spin-Glasses. *Phys. Rev. Lett.* **44**, 1538 (1980). (Cited on page 76.)

A. Fert, N. Reyren and V. Cros, Magnetic skyrmions: advances in physics and potential applications. *Nat. Rev. Mater.* **2**, 17031 (2017). (Cited on page 63.)

M. Finazzi, M. Savoini, A. R. Khorsand, A. Tsukamoto, A. Itoh, L. Duò, A. Kirilyuk, T. Rasing and M. Ezawa, Laser-Induced Magnetic Nanostructures with Tunable Topological Properties. *Phys. Rev. Lett.* **110**, 177205 (2013). (Cited on pages 63 and 91.)

A. Finco, P.-J. Hsu, A. Kubetzka, K. von Bergmann and R. Wiesendanger, Tailoring noncollinear magnetism by misfit dislocation lines. *Phys. Rev. B* **94**, 214402 (2016). (Cited on page 76.)

L. Gerhard, T. K. Yamada, T. Balashov, A. F. Takács, R. J. H. Wesselink, M. Däne, M. Fechner, S. Ostanin, A. Ernst, I. Mertig and W. Wulfhekel, Magnetoelectric coupling at metal surfaces. *Nat Nano* **5**, 792 (2010). (Cited on pages 111 and 117.)

J. Hagemeister, *Confinement effects and stability of spin-spirals and skyrmions in ultrathin magnetic films*. Ph.D. thesis, Universität Hamburg (2016). (Cited on pages 93 and 94.)

J. Hagemeister, D. Iaia, E. Y. Vedmedenko, K. von Bergmann, A. Kubetzka and R. Wiesendanger, Skyrmions at the Edge: Confinement Effects in Fe/Ir(111). *Phys. Rev. Lett.* **117**, 207202 (2016). (Cited on page 92.)

J. Hagemeister, N. Romming, K. von Bergmann, E. Y. Vedmedenko and R. Wiesendanger, Stability of single skyrmionic bits. *Nat. Commun.* **6**, 8455 (2015). (Cited on pages 34 and 43.)

M. Halioua and H.-C. Liu, Optical three-dimensional sensing by phase measuring profilometry. *Opt. Lasers Eng.* **11**, 185 (1989). (Cited on page 101.)

C. Hanneken, *Development and Characterization of Cr Bulk Tips for SP-STM*. Diplomarbeit, Universität Hamburg (2011). (Cited on page 46.)

C. Hanneken, *Observation of Non-Collinear Magnetoresistance by Scanning Tunneling Spectroscopy on Skyrmions in PdFe/Ir(111)*. Ph.D. thesis, Universität Hamburg (2015). (Cited on pages 21, 24, 33, 49, and 65.)

C. Hanneken, A. Kubetzka, K. von Bergmann and R. Wiesendanger, Pinning and movement of individual nanoscale magnetic skyrmions via defects. *New J. Phys.* **18**, 055009 (2016). (Cited on pages 25, 59, and 68.)

C. Hanneken, F. Otte, A. Kubetzka, B. Dupé, N. Romming, K. von Bergmann, R. Wiesendanger and S. Heinze, Electrical detection of magnetic skyrmions by tunnelling noncollinear magnetoresistance. *Nat. Nanotechnol.* **10**, 1039 (2015). (Cited on pages 15, 16, 17, 33, 49, 63, 72, and 86.)

Y. N. Harari, *Sapiens: A Brief History of Humankind* (Harper, 2014). (Cited on page 1.)

M. Heide, G. Bihlmayer and S. Blügel, Dzyaloshinskii-Moriya interaction accounting for the orientation of magnetic domains in ultrathin films: Fe/W(110). *Phys. Rev. B* **78**, 140403 (2008). (Cited on page 12.)

S. Heinze, Simulation of spin-polarized scanning tunneling microscopy images of nanoscale non-collinear magnetic structures. *Appl. Phys. A* **85**, 407 (2006). (Cited on pages 14, 15, 16, and 101.)

S. Heinze. www.flapw.de (2017). (Cited on page 105.)

S. Heinze, K. von Bergmann, M. Menzel, J. Brede, A. Kubetzka, R. Wiesendanger, G. Bihlmayer and S. Blügel, Spontaneous atomic-scale magnetic skyrmion lattice in two dimensions. *Nat. Phys.* **7**, 713 (2011). (Cited on pages 23, 62, 65, and 104.)

S. Heinze, S. Blugel, R. Pascal, M. Bode and R. Wiesendanger, Prediction of bias-voltage-dependent corrugation reversal for STM images of bcc (110) surfaces: W(110), Ta(110), and Fe(110). *Phys. Rev. B* **58**, 16432 (1998). (Cited on page 14.)

P.-J. Hsu, A. Finco, L. Schmidt, A. Kubetzka, K. von Bergmann and R. Wiesendanger, Guiding Spin Spirals by Local Uniaxial Strain Relief. *Phys. Rev. Lett.* **116**, 017201 (2016). (Cited on page 97.)

P.-J. Hsu, A. Kubetzka, A. Finco, N. Romming, K. von Bergmann and R. Wiesendanger, Electric-field-driven switching of individual magnetic skyrmions. *Nat. Nanotechnol.* **12**, 123 (2017). (Cited on pages 44, 46, 62, 63, 90, 111, 115, 116, and 117.)

A. Hubert and R. Schäfer, *Magnetic Domains* (Springer, 2000). (Cited on pages 5 and 12.)

J. Iwasaki, M. Mochizuki and N. Nagaosa, Current-induced skyrmion dynamics in constricted geometries. *Nat. Nanotechnol.* **8**, 742 (2013). (Cited on page 61.)

W. Jiang, P. Upadhyaya, W. Zhang, G. Yu, M. B. Jungfleisch, F. Y. Fradin, J. E. Pearson, Y. Tserkovnyak, K. L. Wang, O. Heinonen, S. G. E. te Velthuis and A. Hoffmann, Blowing magnetic skyrmion bubbles. *Science* **349**, 283 (2015). (Cited on pages 2, 62, and 63.)

F. Jonietz, S. Muehlbauer, C. Pfleiderer, A. Neubauer, W. Muenzer, A. Bauer, T. Adams, R. Georgii, P. Boeni, R. A. Duine, K. Everschor, M. Garst and A. Rosch, Spin Transfer Torques in MnSi at Ultralow Current Densities. *Science* **330**, 1648 (2010). (Cited on pages 2, 62, and 63.)

W. Kang, Y. Huang, X. Zhang, Y. Zhou and W. Zhao, Skyrmion-Electronics: An Overview and Outlook. *Proc. IEEE* **104**, 2040 (2016). (Cited on page 63.)

T. Kasuya, A Theory of Metallic Ferro- and Antiferromagnetism on Zener's Model. *Prog. Theor. Phys.* **16**, 45 (1956). (Cited on pages 6 and 102.)

I. Kezsmarki, S. Bordacs, P. Milde, E. Neuber, L. M. Eng, J. S. White, H. M. Ronnow, C. D. Dewhurst, M. Mochizuki, K. Yanai, H. Nakamura, D. Ehlers, V. Tsurkan and A. Loidl, Néel-type skyrmion lattice with confined orientation in the polar magnetic semiconductor GaV_4S_8. *Nat. Mater.* **14**, 1116 (2015). (Cited on page 62.)

A. A. Khajetoorians, B. Baxevanis, C. Huebner, T. Schlenk, S. Krause, T. O. Wehling, S. Lounis, A. Lichtenstein, D. Pfannkuche, J. Wiebe and R. Wiesendanger, Current-Driven Spin Dynamics of Artificially Constructed Quantum Magnets. *Science* **339**, 55 (2013). (Cited on pages 47 and 48.)

S. Komineas and N. Papanicolaou, Skyrmion dynamics in chiral ferromagnets under spin-transfer torque. *Phys. Rev. B* **92** (2015). (Cited on pages 91 and 92.)

S. Krause, *Thermal and Current-Induced Magnetization Switching of Fe/W(110) Nanoislands Investigated by Spin-Polarized Scanning Tunneling Microscopy*. Ph.D. thesis, Hamburg (2008). (Cited on page 47.)

S. Krause, L. Berbil-Bautista, G. Herzog, M. Bode and R. Wiesendanger, Current-induced magnetization switching with a spin-polarized scanning tunneling microscope. *Science* **317**, 1537 (2007). (Cited on pages 46 and 48.)

S. Krause, G. Herzog, A. Schlenhoff, A. Sonntag and R. Wiesendanger, Joule Heating and Spin-Transfer Torque Investigated on the Atomic Scale Using a Spin-Polarized Scanning Tunneling Microscope. *Physical Review Letters* **107**, 186601 (2011). (Cited on page 45.)

A. Kubetzka, M. Bode, O. Pietzsch and R. Wiesendanger, Spin-Polarized Scanning Tunneling Microscopy with Antiferromagnetic Probe Tips. *Phys. Rev. Lett.* **88**, 057201 (2002). (Cited on page 21.)

A. Kubetzka, C. Hanneken, R. Wiesendanger and K. von Bergmann, Impact of the skyrmion spin texture on magnetoresistance. *Phys. Rev. B* **95**, 104433 (2017). (Cited on pages 15, 16, 17, 33, 49, 50, 63, and 72.)

A. Kubetzka, O. Pietzsch, M. Bode and R. Wiesendanger, Spin-polarized scanning tunneling microscopy study of 360° walls in an external magnetic field . *Phys. Rev. B* **67**, 020401 (2003). (Cited on pages 12, 13, 55, and 69.)

W. Kutta, Beitrag zur näherungsweisen Integration totaler Differentialgleichungen. *Z. Math. Phys.* **46**, 435 (1901). (Cited on page 11.)

J. C. Lagarias, J. A. Reeds, M. H. Wright and P. E. Wright, Convergence Properties of the Nelder-Mead Simplex Method in low Dimensions. *SIAM J. Optim.* **9**, 112 (1998). (Cited on page 14.)

A. O. Leonov and M. Mostovoy, Multiply periodic states and isolated skyrmions in an anisotropic frustrated magnet. *Nat. Commun.* **6**, 8275 (2015). (Cited on page 9.)

A. O. Leonov, U. K. Rössler and M. Mostovoy, Target-skyrmions and skyrmion clusters in nanowires of chiral magnets. *EPJ Web of Conferences* **75**, 05002 (2014). (Cited on page 91.)

A. O. Leonov, Y. Togawa, T. L. Monchesky, A. N. Bogdanov, J. Kishine, Y. Kousaka, M. Miyagawa, T. Koyama, J. Akimitsu, T. Koyama, K. Harada, S. Mori, D. McGrouther, R. Lamb, M. Krajnak, S. McVitie, R. L. Stamps and K. Inoue, Chiral Surface Twists and Skyrmion Stability in Nanolayers of Cubic Helimagnets. *Phys. Rev. Lett.* **117**, 087202 (2016). (Cited on page 62.)

S.-Z. Lin and S. Hayami, Ginzburg-Landau theory for skyrmions in inversion-symmetric magnets with competing interactions. *Phys. Rev. B* **93**, 064430 (2016). (Cited on pages 8 and 9.)

Y. Liu, H. Du, M. Jia and A. Du, Switching of a target skyrmion by a spin-polarized current. *Phys. Rev. B* **91**, 094425 (2015). (Cited on page 91.)

MATLAB, *Release 2016b* (The MathWorks Inc., Natick, Massachusetts, 2016). (Cited on page 14.)

F. Matsukura, Y. Tokura and H. Ohno, Control of magnetism by electric fields. *Nat Nano* **10**, 209 (2015). (Cited on page 46.)

S. Meckler, N. Mikuszeit, A. Pressler, E. Y. Vedmedenko, O. Pietzsch and R. Wiesendanger, Real-Space Observation of a Right-Rotating Inhomogeneous Cycloidal Spin Spiral by Spin-Polarized Scanning Tunneling Microscopy in a Triple Axes Vector Magnet. *Phys. Rev. Lett.* **103**, 157201 (2009). (Cited on page 31.)

S. Meckler, O. Pietzsch, N. Mikuszeit and R. Wiesendanger, Micromagnetic description of the spin spiral in Fe double-layer stripes on W(110). *Phys. Rev. B* **85**, 024420 (2012). (Cited on page 12.)

M. Menzel, *Non-collinear magnetic ground states observed in iron nanostructures on iridium surfaces*. Ph.D. thesis, Universität Hamburg, Hamburg (2011). (Cited on page 21.)

M. Menzel, Y. Mokrousov, R. Wieser, J. E. Bickel, E. Vedmedenko, S. Blügel, S. Heinze, K. von Bergmann, A. Kubetzka and R. Wiesendanger, Information Transfer by Vector Spin Chirality in Finite Magnetic Chains. *Phys. Rev. Lett.* **108**, 197204 (2012). (Cited on page 9.)

P. Milde, D. Kohler, J. Seidel, L. M. Eng, A. Bauer, A. Chacon, J. Kindervater, S. Muhlbauer, C. Pfleiderer, S. Buhrandt, C. Schutte and A. Rosch, Unwinding of a Skyrmion Lattice by Magnetic Monopoles. *Science* **340**, 1076 (2013). (Cited on page 62.)

C. Moreau-Luchaire, C. Moutafis, N. Reyren, J. Sampaio, C. A. F. Vaz, N. Van Horne, K. Bouzehouane, K. Garcia, C. Deranlot, P. Warnicke, P. Wohlhüter, J.-M. George, M. Weigand, J. Raabe, V. Cros and A. Fert, Additive interfacial chiral interaction in multilayers for stabilization of small individual skyrmions at room temperature. *Nat. Nanotechnol.* **11**, 444 (2016). (Cited on pages 62 and 63.)

T. Moriya, Anisotropic superexchange interaction and weak ferromagnetism. *Phys. Rev.* **120**, 91 (1960). (Cited on pages 7, 31, and 53.)

S. Mühlbauer, B. Binz, F. Jonietz, C. Pfleiderer, A. Rosch, A. Neubauer, R. Georgii and P. Böni, Skyrmion Lattice in a Chiral Magnet. *Science* **323**, 915 (2009). (Cited on pages 2, 29, and 62.)

J. Müller, Magnetic skyrmions on a two-lane racetrack. *New J. Phys.* **19**, 025002 (2017). (Cited on page 61.)

M. Müller, K. Albe, C. Busse, A. Thoma and T. Michely, Island shapes, island densities, and stacking-fault formation on Ir(111): Kinetic Monte Carlo simulations and experiments. *Phys. Rev. B* **71**, 075407 (2005). (Cited on page 26.)

W. Münzer, A. Neubauer, T. Adams, S. Mühlbauer, C. Franz, F. Jonietz, R. Georgii, P. Böni, B. Pedersen, M. Schmidt, A. Rosch and C. Pfleiderer, Skyrmion lattice in the doped semiconductor $Fe_{1-x}Co_xSi$. *Phys. Rev. B* **81**, 041203 (2010). (Cited on page 62.)

A. K. Nayak, V. Kumar, T. Ma, P. Werner, E. Pippel, R. Sahoo, F. Damay, U. K. Rößler, C. Felser and S. S. Parkin, Magnetic antiskyrmions above room temperature in tetragonal Heusler materials. *Nature* **548**, 561 (2017). (Cited on page 63.)

J. A. Nelder and R. Mead, A Simplex Method for Function Minimization. *Comput. J.* **7**, 308 (1965). (Cited on page 14.)

OOMMF, *Release 1.2a5* (`http://math.nist.gov/oommf`, 2016). (Cited on page 58.)

A. van Oosterom and J. Strackee, The Solid Angle of a Plane Triangle. *IEEE Trans. Biomed. Eng.* **30**, 125 (1983). (Cited on pages 81 and 82.)

G. Oster and Y. Nishijima, Moiré Patterns. *Sci. Am.* **208**, 54 (1963). (Cited on page 100.)

S. S. P. Parkin, M. Hayashi and L. Thomas, Magnetic domain-wall racetrack memory. *Science* **320**, 190 (2008). (Cited on pages 2 and 63.)

C. Pfleiderer and A. Rosch, Condensed-matter physics: Single skyrmions spotted. *Nature* **465**, 880 (2010). (Cited on page 29.)

O. Pietzsch, A. Kubetzka, D. Haude, M. Bode and R. Wiesendanger, A low-temperature ultrahigh vacuum scanning tunneling microscope with a split-coil magnet and a rotary motion stepper motor for high spatial resolution studies of surface magnetism. *Rev. Sci. Instrum.* **71**, 424 (2000). (Cited on page 21.)

L. Pleth Nielsen, F. Besenbacher, I. Stensgaard, E. Laegsgaard, C. Engdahl, P. Stoltze, K. W. Jacobsen and J. K. Nørskov, Initial growth of Au on Ni(110): Surface alloying of immiscible metals. *Phys. Rev. Lett.* **71**, 754 (1993). (Cited on page 24.)

M. Plihal, D. L. Mills and J. Kirschner, Spin Wave Signature in the Spin Polarized Electron Energy Loss Spectrum of Ultrathin Fe Films: Theory and Experiment. *Phys. Rev. Lett.* **82**, 2579 (1999). (Cited on page 45.)

G. Reid, Moiré fringes in metrology. *Opt. Lasers Eng.* **5**, 63 (1984). (Cited on page 101.)

H. J. Richter, The transition from longitudinal to perpendicular recording. *J. Phys. D: Appl. Phys.* **40**, R149 (2007). (Cited on page 2.)

U. K. Rößler, A. N. Bogdanov and C. Pfleiderer, Spontaneous skyrmion ground states in magnetic metals. *Nature* **442**, 797 (2006). (Cited on page 9.)

U. K. Rößler, A. A. Leonov and A. N. Bogdanov, Chiral Skyrmionic matter in non-centrosymmetric magnets. *J. Phys: Conf. Ser.* **303**, 012105 (2011). (Cited on pages 9 and 53.)

S. Rohart and A. Thiaville, Skyrmion confinement in ultrathin film nanostructures in the presence of Dzyaloshinskii-Moriya interaction. *Phys. Rev. B* **88**, 184422 (2013). (Cited on pages 12, 57, 58, 84, 91, 93, and 94.)

N. Romming, *Tuning non-collinear magnetic states with non-magnetic adlayers*. Master's thesis, University of Hamburg (2013). (Cited on pages 29, 97, and 106.)

N. Romming, C. Hanneken, M. Menzel, J. E. Bickel, B. Wolter, K. von Bergmann, A. Kubetzka and R. Wiesendanger, Writing and Deleting Single Magnetic Skyrmions. *Science* **341**, 636 (2013). (Cited on pages 29, 36, 52, 62, 63, 66, 68, 87, 90, and 97.)

N. Romming, M. Hoffmann, B. Dupé, K. von Bergmann, S. von Malottki, A. Kubetzka, R. Wiesendanger and S. Heinze, Spin spirals in ultra-thin films driven by frustration of exchange interactions: Rh/Fe/Ir(111), arXiv:1610.07853 (2016). (Cited on pages 79 and 105.)

N. Romming, A. Kubetzka, C. Hanneken, K. von Bergmann and R. Wiesendanger, Field-dependent size and shape of single magnetic Skyrmions. *Phys. Rev. Lett.* **114**, 177203 (2015). (Cited on pages 12, 53, 56, 61, 62, 63, 86, 94, 112, and 113.)

R. E. Rottmayer, S. Batra, D. Buechel, W. A. Challener, J. Hohlfeld, Y. Kubota, L. Li, B. Lu, C. Mihalcea, K. Mountfield, K. Pelhos, C. Peng, T. Rausch, M. A. Seigler, D. Weller and X. M. Yang, Heat-Assisted Magnetic Recording. *IEEE Trans. Magn.* **42**, 2417 (2006). (Cited on page 2.)

S. Rousset, S. Chiang, D. E. Fowler and D. D. Chambliss, Intermixing and three-dimensional islands in the epitaxial growth of Au on Ag(110). *Phys. Rev. Lett.* **69**, 3200 (1992). (Cited on page 24.)

L. Rózsa, K. Palotás, A. Deák, E. Simon, R. Yanes, L. Udvardi, L. Szunyogh and U. Nowak, Formation and stability of metastable skyrmionic spin structures with various topologies in an ultrathin film. *Phys. Rev. B* **95**, 094423 (2017). (Cited on page 9.)

M. A. Ruderman and C. Kittel, Indirect Exchange Coupling of Nuclear Magnetic Moments by Conduction Electrons. *Phys. Rev.* **96**, 99 (1954). (Cited on pages 6 and 102.)

C. Runge, Über die numerische Auflösung von Differentialgleichungen. *Math. Ann.* **46**, 167 (1895). (Cited on page 11.)

J. Saßmannshausen, *Rastertunnelmikroskopie ultradünner Bleischichten auf Fe/Ir(111).* Master's thesis, Universität Hamburg (2016). (Cited on pages 24 and 25.)

J. Sampaio, V. Cros, S. Rohart, A. Thiaville and A. Fert, Nucleation, stability and current-induced motion of isolated magnetic skyrmions in nanostructures. *Nat. Nanotechnol.* **8**, 839 (2013). (Cited on pages 2 and 63.)

A. Schlenhoff, *Imaging and Switching Individual Nanomagnets with Spin-Polarized Scanning Field Emission Microscopy.* Ph.D. thesis, Universität Hamburg (2013). (Cited on page 45.)

A. Schlenhoff, S. Krause, G. Herzog and R. Wiesendanger, Bulk Cr tips with full spatial magnetic sensitivity for spin-polarized scanning tunneling microscopy. *Appl. Phys. Lett.* **97**, 083104 (2010). (Cited on page 21.)

L. Schmidt, J. Hagemeister, P.-J. Hsu, A. Kubetzka, K. von Bergmann and R. Wiesendanger, Symmetry breaking in spin spirals and skyrmions by in-plane and canted magnetic fields. *New J. Phys.* **18**, 075007 (2016). (Cited on pages 31, 66, 87, and 97.)

T. Schulz, R. Ritz, A. Bauer and M. Halder, Emergent electrodynamics of skyrmions in a chiral magnet. *Nat. Phys.* **8**, 301 (2012). (Cited on page 62.)

C. A. Sciammarella, The Moiré method—A review. *Exp. Mech.* **22**, 418 (1982). (Cited on page 101.)

Seagate, Prognose zum Volumen der jährlich generierten digitalen Datenmenge weltweit in den Jahren 2016 und 2025 (in Zettabyte). In *Statista - Das Statistik-Portal*, Retrieved 12th July, 2017 at https://de.statista.com/statistik/daten/studie/267974/umfrage/prognose-zum-weltweit-generierten-datenvolumen/ (2017). (Cited on page 1.)

S. Seki, X. Z. Yu, S. Ishiwata and Y. Tokura, Observation of Skyrmions in a Multiferroic Material. *Science* **336**, 198 (2012). (Cited on page 62.)

K. Shibata, X. Yu, T. Hara, D. Morikawa, N. Kanazawa, K. Kimoto, S. Ishiwata, Y. Matsui and Y. Tokura, Towards control of the size and helicity of skyrmions in helimagnetic alloys by spin-orbit coupling. *Nat. Nanotechnol.* **8**, 723 (2013). (Cited on page 63.)

A. Shilov, Western Digital Announces Ultrastar He12 12 TB and 14 TB HDDs. In *AnandTech*, Retrieved 12th July, 2017 at http://www.anandtech.com/show/10888/western-digital-announces-ultrastar-he12-12-tb-and-14-tb-hdds (2016). (Cited on page 1.)

E. A. da Silva Oliveira, R. Silva, R. Silva and A. Pereira, Effects of second neighbor interactions on skyrmion lattices in chiral magnets. *J. Phys. Condens. Matter* **29**, 205801 (2017). (Cited on page 9.)

E. Simon, K. Palotás, B. Ujfalussy, a. Deák, G. M. Stocks and L. Szunyogh, Spin-correlations and magnetic structure in an Fe monolayer on 5d transition metal surfaces. *J. Phys. Condens. Matter* **26**, 186001 (2014a). (Cited on page 58.)

E. Simon, K. Palotás, L. Rózsa, L. Udvardi and L. Szunyogh, Formation of magnetic skyrmions with tunable properties in PdFe bilayer deposited on Ir(111). *Phys. Rev. B* **90**, 094410 (2014b). (Cited on pages 66, 79, and 80.)

R. Skomski, A. Kashyap, J. Zhou and D. J. Sellmyer, Anisotropic exchange. *J. Appl. Phys.* **97**, 10B302 (2005). (Cited on page 8.)

T. H. R. Skyrme, A Unified Field Theory of Mesons and Baryons. *Nuclear Physics* **31**, 556 (1962). (Cited on page 9.)

J. Slonczewski, Current-driven excitation of magnetic multilayers. *Journal of Magnetism and Magnetic Materials* **159**, L1 (1996). (Cited on pages 47 and 48.)

A. Sonntag, J. Hermenau, A. Schlenhoff, J. Friedlein, S. Krause and R. Wiesendanger, Electric-Field-Induced Magnetic Anisotropy in a Nanomagnet Investigated on the Atomic Scale. *Phys. Rev. Lett.* **112**, 017204 (2014). (Cited on pages 44, 46, and 111.)

A. Soumyanarayanan, M. Raju, A. L. Gonzalez Oyarce, A. K. C. Tan, M.-Y. Im, A. P. Petrovic, P. Ho, K. H. Khoo, M. Tran, C. K. Gan, F. Ernult and C. Panagopoulos, Tunable room-temperature magnetic skyrmions in Ir/Fe/Co/Pt multilayers. *Nat. Mater.* **16**, 898 (2017). (Cited on page 63.)

J. Tersoff and D. R. Hamann, Theory and Application For the Scanning Tunneling Microscope. *Phys. Rev. Lett.* **50**, 1998 (1983). (Cited on page 14.)

J. Tersoff and D. R. Hamann, Theory of the Scanning Tunneling Microscope. *Phys. Rev. B* **31**, 805 (1985). (Cited on page 14.)

W. Weber, D. A. Wesner, G. Güntherodt and U. Linke, Direct observation of spin-split electronic states of Pd at the Pd(111)/Fe(110) interface. *Phys. Rev. Lett.* **66**, 942 (1991). (Cited on page 29.)

J. Wiebe, L. Zhou and R. Wiesendanger, Atomic magnetism revealed by spin-resolved scanning tunnelling spectroscopy. *J. Phys. D: Appl. Phys.* **44**, 464009 (2011). (Cited on page 103.)

R. Wiesendanger, *Scanning Probe Microscopy and Spectroscopy - Methods and Applications* (Cambridge University Press, 1994). (Cited on page 14.)

R. Wiesendanger, Spin mapping at the nanoscale and atomic scale. *Rev. Mod. Phys.* **81**, 1495 (2009). (Cited on pages 14, 16, and 97.)

R. Wiesendanger, Single-atom magnetometry. *Curr. Opin. Solid State Mater. Sci.* **15**, 1 (2011). (Cited on page 14.)

R. Wiesendanger, H. J. Guntherodt, G. Guntherodt, R. J. Gambino and R. Ruf, Measurement of the Local Electron-spin Polarization By the Scanning Tunneling Microscope. *Helv. Phys. Acta* **63**, 778 (1990a). (Cited on page 14.)

R. Wiesendanger, H. J. Guntherodt, G. Guntherodt, R. J. Gambino and R. Ruf, Scanning Tunneling Microscopy With Spin-polarized Electrons. *Z. Phys. B: Condens. Matter* **80**, 5 (1990b). (Cited on page 14.)

M. N. Wilson, A. B. Butenko, A. N. Bogdanov and T. L. Monchesky, Chiral skyrmions in cubic helimagnet films: The role of uniaxial anisotropy. *Phys. Rev. B* **89**, 094411 (2014). (Cited on pages 9, 10, 56, 57, 70, and 78.)

C. Witt, U. Mick, M. Bode and R. Wiesendanger, An ultrahigh vacuum scanning tunneling microscope for in situ studies of thin-film growth. *Rev. Sci. Instrum.* **68**, 1455 (1997). (Cited on page 21.)

S. Woo, K. Litzius, B. Krüger, M.-Y. Im, L. Caretta, K. Richter, M. Mann, A. Krone, R. M. Reeve, M. Weigand, P. Agrawal, I. Lemesh, M.-A. Mawass, P. Fischer, M. Kläui and G. S. D. Beach, Observation of room-temperature magnetic skyrmions and their current-driven dynamics in ultrathin metallic ferromagnets. *Nat. Mater.* **15**, 501 (2016). (Cited on pages 2, 62, and 63.)

D. Wortmann, S. Heinze, P. Kurz, G. Bihlmayer and S. Blügel, Resolving complex atomic-scale spin structures by spin-polarized scanning tunneling microscopy. *Phys. Rev. Lett.* **86**, 4132 (2001). (Cited on page 14.)

K. Yosida, Magnetic Properties of Cu-Mn Alloys. *Phys. Rev.* **106**, 893 (1957). (Cited on pages 6 and 102.)

X. Z. Yu, N. Kanazawa, Y. Onose, K. Kimoto, W. Z. Zhang, S. Ishiwata, Y. Matsui and Y. Tokura, Near room-temperature formation of a skyrmion crystal in thin-films of the helimagnet FeGe. *Nat. Mater.* **10**, 106 (2011). (Cited on page 62.)

X. Z. Yu, N. Kanazawa, W. Z. Zhang, T. Nagai, T. Hara, K. Kimoto, Y. Matsui, Y. Onose and Y. Tokura, Skyrmion flow near room temperature in an ultralow current density. *Nat. Commun.* **3**, 988 (2012). (Cited on pages 2, 62, and 63.)

X. Z. Yu, Y. Onose, N. Kanazawa, J. H. Park, J. H. Han, Y. Matsui, N. Nagaosa and Y. Tokura, Real-space observation of a two-dimensional skyrmion crystal. *Nature* **465**, 901 (2010). (Cited on pages 29 and 62.)

X. Zhang, M. Ezawa and Y. Zhou, Magnetic skyrmion logic gates: conversion, duplication and merging of skyrmions. *Sci. Rep.* **5** (2015a). (Cited on page 63.)

X. Zhang, J. Xia, Y. Zhou, D. Wang, X. Liu, W. Zhao and M. Ezawa, Control and manipulation of a magnetic skyrmionium in nanostructures. *Phys. Rev. B* **94** (2016). (Cited on pages 91 and 92.)

X. Zhang, G. P. Zhao, H. Fangohr, J. P. Liu, W. X. Xia, J. Xia and F. J. Morvan, Skyrmion-skyrmion and skyrmion-edge repulsions in skyrmion-based racetrack memory. *Sci. Rep.* **5**, 7643 (2015b). (Cited on pages 2, 61, and 63.)

X. Zhang, Y. Zhou, M. Ezawa, G. P. Zhao and W. Zhao, Magnetic skyrmion transistor: skyrmion motion in a voltage-gated nanotrack. *Sci. Rep.* **5**, 11369 (2015c). (Cited on pages 61 and 63.)

L. Zhou, J. Wiebe, S. Lounis, E. Vedmedenko, F. Meier, S. Blügel, P. H. Dederichs and R. Wiesendanger, Strength and directionality of surface Ruderman-Kittel-Kasuya-Yosida interaction mapped on the atomic scale. *Nat. Phys.* **6**, 187 (2010). (Cited on page 103.)

List of Publications

Research Articles

- N. Romming, C. Hanneken, M. Menzel, J. E. Bickel, B. Wolter, K. von Bergmann, A. Kubetzka and R. Wiesendanger, Writing and Deleting Single Magnetic Skyrmions. *Science* **341**, 636 (2013).
- C. Hanneken and N. Romming, Magnetische Knoten auf der Festplatte. *Spektrum der Wissenschaft* **Okt. 2013**, 22 (2013).
- N. Romming, A. Kubetzka, C. Hanneken, K. von Bergmann and R. Wiesendanger, Field-dependent size and shape of single magnetic Skyrmions. *Phys. Rev. Lett.* **114**, 177203 (2015).
- C. Hanneken, F. Otte, A. Kubetzka, B. Dupé, N. Romming, K. von Bergmann, R. Wiesendanger and S. Heinze, Electrical detection of magnetic skyrmions by tunnelling non-collinear magnetoresistance. *Nat. Nanotechnol.* **10**, 1039 (2015).
- J. Hagemeister, N. Romming, K. von Bergmann, E. Y. Vedmedenko and R. Wiesendanger, Stability of single skyrmionic bits. *Nat. Commun.* **6**, 8455 (2015).
- A. O. Leonov, T. L. Monchesky, N. Romming, A. Kubetzka, A. N. Bogdanov and R. Wiesendanger, The properties of isolated chiral skyrmions in thin magnetic films. *New J. Phys.* **18**, 065003 (2016).
- P.-J. Hsu, A. Kubetzka, A. Finco, N. Romming, K. von Bergmann and R. Wiesendanger, Electric-field-driven switching of individual magnetic skyrmions. *Nat. Nanotechnol.* **12**, 123 (2017).
- W. Paul, K. Yang, S. Baumann, N. Romming, T. Choi, C. P. Lutz and A. J. Heinrich, Control of the millisecond spin lifetime of an electrically probed atom. *Nat. Phys.* **13**, 403 (2017).

Invited Talks

- 07.01.2014:
  N. Romming, C. Hanneken, M. Menzel, J. E. Bickel, B. Wolter, K. von Bergmann, A. Kubetzka and R. Wiesendanger, *Writing and deleting single magnetic skyrmions.*
  Current-driven magnetisation dynamics workshop, Leeds (England).

- 18.08.2014:
  N. Romming, C. Hanneken, M. Menzel, J. E. Bickel, B. Wolter, K. von Bergmann, A. Kubetzka and R. Wiesendanger, *Writing and deleting single magnetic skyrmions.*
  SPIE NanoScience + Engineering, San Diego (CA, USA).

- 20.05.2015:
  N. Romming, A. Kubetzka, C. Hanneken, K. von Bergmann and R. Wiesendanger, *Field-dependent size and shape of single magnetic Skyrmions.*
  International Workshop on Topological Structures in Ferroic Materials, Sydney (Australia).

- 10.06.2015:
  N. Romming, A. Kubetzka, Ch. Hanneken, K. von Bergmann, F. Otte, B. Dupé, S. Heinze and R. Wiesendanger, *Spin-orbit coupling in surface or interface states.*
  SOCSIS 2015, Spetses (Greece).

- 07.07.2015:
  N. Romming, A. Kubetzka, C. Hanneken, K. von Bergmann and R. Wiesendanger, *Field-dependent size and shape of single magnetic Skyrmions.*
  20th International Conference on Magnetism, Barcelona (Spain).

Contributed Talks, Seminar Talks and Outreach

- 12.09.2013:
  N. Romming, C. Hanneken, M. Menzel, J. E. Bickel, B. Wolter, K. von Bergmann, A. Kubetzka and R. Wiesendanger, *Tuning non-collinear magnetic states with non-magnetic adlayers.*
  International Conference on Nanoscience and Technology, Paris (France).

- 12.11.2013:
  N. Romming, C. Hanneken, M. Menzel, J. E. Bickel, B. Wolter, K. von Bergmann, A. Kubetzka and R. Wiesendanger, *Writing and deleting single magnetic skyrmions.*
  544. WE-Heraeus-Seminar: Interactions with the Nanoworld, Bad Honnef (Germany).

- 03.09.2014:
  N. Romming, C. Hanneken, M. Menzel, J. E. Bickel, B. Wolter, K. von Bergmann, A. Kubetzka and R. Wiesendanger, *Writing and deleting single magnetic skyrmions.* ALS-CXRO Wednesday seminar, Berkeley, Berkeley (USA).

- 11.09.2014:
  N. Romming, C. Hanneken, M. Menzel, J. E. Bickel, B. Wolter, K. von Bergmann, A. Kubetzka and R. Wiesendanger, *Writing and deleting single magnetic skyrmions.* Special Seminar for S&T team, IBM Research - Almaden, San Jose (CA, USA).

- 16.03.2015:
  N. Romming, A. Kubetzka, C. Hanneken, K. von Bergmann and R. Wiesendanger, *Field-dependent size and shape of single magnetic Skyrmions.*
  79th Spring Conference, Deutsche Physikalische Gesellschaft, Berlin (Germany).

- 26.05.2015:
  N. Romming, A. Kubetzka, C. Hanneken, K. von Bergmann and R. Wiesendanger, *Investigation and Manipulation of Single Magnetic Skyrmions.*
  Seminar at the Centre for Quantum Computation and Communication Technology, Sydney (Australia).

- 18.09.2015:
  N. Romming, *Magnetische Knoten als Datenspeicher der Zukunft.*
  Neueröffnung der Ausstellung "Nanotechnologie - Aufbruch in neue Welten", Hamburg (Germany).

- 08.03.2016:
  N. Romming, M. Hoffmann, B. Dupé, A. Kubetzka, K. von Bergmann, S. Heinze and R. Wiesendanger, *Exchange driven spin spiral in Rh/Fe/Ir(111).*
  80th Spring Conference, Deutsche Physikalische Gesellschaft, Regensburg (Germany).

- 22.08.2016:
  N. Romming, K. von Bergmann, A. Kubetzka and R. Wiesendanger, *Complex Spin States and Skyrmions in confined geometries.*
  International Conference on Nanoscience and Technology, Busan (Republic of Korea).

Posters

- 09.04.2014:
  N. Romming, K. von Bergmann, A. Kubetzka and R. Wiesendanger, *Magnetic field dependent study of the skyrmion size.*
  SKYMAG 2014, Paris (France).

- 04.11.2015:
  N. Romming, A. Kubetzka, C. Hanneken, K. von Bergmann and R. Wiesendanger, *Investigation and Manipulation of Single Magnetic Skyrmions.*
  598. WE-Heraeus-Seminar, Bad Honnef (Germany).

Danksagung

Diese Doktorarbeit hätte nicht entstehen können ohne die Unterstützung einer Anzahl an Personen, bei denen ich mich hiermit gerne bedanken möchte:

- Prof. Dr. Roland Wiesendanger danke ich für die Möglichkeit, in seiner Arbeitsgruppe meine Doktorarbeit durchführen und die Ergebnisse auf internationalen Konferenzen präsentieren zu dürfen.

- PD Dr. Guido Meier und Dr. Vincent Cros danke ich für die Übernahme der Gutachten der Dissertation.

- Dr. Kirsten von Bergmann und Dr. André Kubetzka für die herausragende Betreuung, viele erhellende Diskussionen auch abseits der Physik, das detaillierte Korrekturlesen der Arbeit und viele lustige Abende nach Feierabend und auf Konferenzen.

- Des Weiteren danke ich Prof. Dr. Wolfgang Hansen, Prof. Dr. Stefan Heinze und Prof. Dr. Michael Thorwart als Gutachter der Disputation.

- Allen jetzigen und ehemaligen Kollegen aus Labor 013 gilt besonderer Dank für Jahre fruchtvoller und angenehmer Zusammenarbeit. Besonders erwähnen möchte ich dabei Dr. Christian Hanneken und Dr. Matthias Menzel.

- Viele Teile dieser Arbeit sind aus Kollaborationen mit anderen exzellenten Forschergruppen entstanden, deren Mitgliedern ich hiermit für viele wissenschaftliche Diskussionen und horizonterweiternde Gespräche danken möchte. Insbesondere den Gruppen von Prof. Stefan Heinze und von Prof. Hans Fangohr, die maßgeblich zu Ergebnissen dieser Arbeit beigetragen haben.

- Ich danke auch der gesamten Gruppe R für die angenehme Arbeitsatmosphäre.

- Allen Mitarbeitern der ehemaligen Gruppe von Dr. Andreas Heinrich bei IBM Research Almaden danke ich für die herzliche Aufnahme in ihre Arbeitsgruppe während meines Aufenthaltes in Kalifornien und die Unternehmungen außerhalb des Labors, insbesondere William Paul und Susanne Baumann.

- Ohne die (verwaltungs-)technische Unterstützung aller Mitarbeiter des Helium-Teams, der mechanischen und elektronischen Werkstatt und des technischen und administrativen Teams wäre die Fertigstellung dieser Arbeit nicht möglich gewesen.

- Der DFG via SFB668 und dem DAAD danke ich für die finanzielle Unterstützung während meiner letzten Jahre.

- Für viele witzige Mittagessen, Kaffeepausen, erneute Kaffeepausen und Unternehmungen außerhalb der Uni danke ich meinen liebsten Kommilitonen Vincent, Anka, Svenja und Philip.
- Ich bedanke mich bei all meinen Freunden, die mich in den letzten Jahren begleitet und unterstützt haben, insbesondere bei Janni, der mich auch gerne mal mit einem FIFA-Abend aufgebaut hat.
- Meiner Familie danke ich für die vielen Jahre der Unterstützung und des Vertrauens, danke dass ihr immer da seid.
- Schlussendlich danke ich meinen beiden Mädels, Doreen und Lotta, ihr macht es all den Aufwand wert.